Università degli Studi di Padova

Dipartimento di Ingegneria dell'Informazione

Population models for complex non-linear phenomena in biology: from mitochondrial dynamics to brain networks

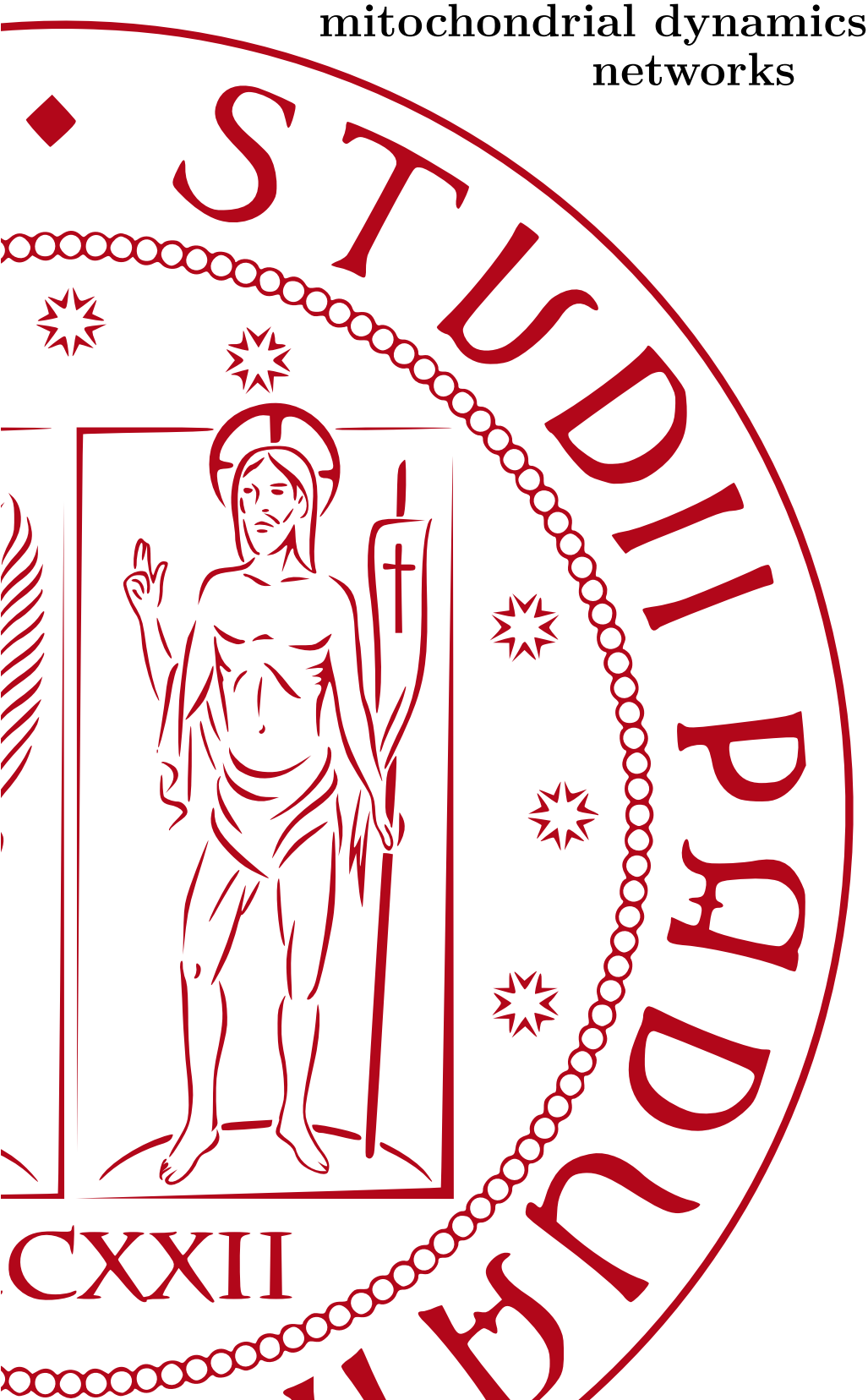

Ph.D. candidate
Chiara Favaretto

Advisor
Prof. Angelo Cenedese

Director & Coordinator
Prof. Andrea Neviani

Ph.D. School in
Information Engineering

Department of
Information Engineering
University of Padova
2017

"In fondo, si vive sempre e solo quello che si vuole vivere. È da lì che si deve ripartire. Per desiderare quello che si ha già. Senza passare il tempo a sperare che forse un giorno tutto sarà diverso. Perché tutto è già diverso, non appena si fa la pace con i propri ricordi. Quelli che smetteranno di accompagnarci solo quando avremo ritrovato quei profumi e quei rumori, la fine della fatica, l'inizio della gioia."

Michela Marzano, 'Volevo essere una farfalla', 2011

Abstract

The human brain is as much fascinating as complicated: this is the reason why it has always captured scientists' attention in several fields of research, from biology to medicine, from psychology to engineering. In this context various non-invasive technologies have been optimized in order to allow the measure of signals, able to describe brain activities. These data, derived from measurement methods that largely differ in their nature, have opened the door to new characterizations of this organ, that highlighted the main features of its operating principles. Brain signals indeed have revealed to be fluctuating during time, both during a specific task, and when we are not carrying on any activities. Furthermore, a selective coordination among different regions of the brain has emerged.

As engineers, we are particularly attracted by the description of our brain as a graph, whose nodes and edges can be representative of several different elements, at distinct spatial scales (from single neurons to large brain areas). In the last decades, wide attention has been devoted to reproduce and explain the complex dynamics of the brain elements by means of computational models. *Graph theory* tools, as well as the design of *population models*, allow the exploitation of many mathematical tools, helpful to enlarge the knowledge of healthy and damaged brains functioning, by means of *brain networks*.

Interestingly, the incapability of human brains to work properly in case of disease, has found to be correlated with dysfunctions in the activity of mitochondria, the organelles that produce large part of the cells' energy. In particular, specific relationships have been reported among neurological diseases and impairments in mitochondrial dynamics, which refers to the continuous change in shape of mitochondria, by means of fusion and fission processes. Although the existing link between brain and mitochondria is still ambiguous and under debate, the huge amount of energy required by our brain to work properly suggests a larger mitochondrial-dependence of the brain than of the other organs.

In this thesis we report the results of our research, aimed to investigate a few aspects of this complex brain-mitochondria relationship. We focus on mitochondrial dynamics and brain network, as well as on suitable mathematical models used to describe them. Specifically, the main topics handled in this work can be summarized as follows.

Population models for mitochondrial dynamics. We propose a modified prey-predator non-linear population model to simulate the main processes, which take part in the mitochondrial dynamics, and the ones that are strongly related to it, without neglecting the energy production process. We present two possible setups, which differ in the inclusion of a feedback link between the available energy and the formation of new mitochondria. We discuss their dynamics, and their potential in reproducing biological behaviors.

Brain signals: comparison of datasets derived through different technologies. We analyze two different datasets of brain signals, recorded with various methods (functional magnetic resonance imaging, fMRI, and magnetoencephalography, MEG), both in condition of no activity and during an attentional task. The aim of the analysis is twofold: the investigation of the spontaneous activity of the brain, and the exploration of possible relationships between the two different techniques.

Brain network: a Kuramoto-based description. We analyze empirical brain data by means of their oscillatory features, with the purpose of highlighting the characteristics that a computational phase-model should be able to reproduce. Hence, we use a modified version of the classic Kuramoto model to reproduce the empirical oscillatory characteristics.

Analysis and control of Kuramoto networks. Most of the theoretical contribution of this thesis refers to analytical results on Kuramoto networks. We analyze the topological and intrinsic conditions required to achieve a desired pattern of synchronization, represented by fully or clustered synchronized configuration of oscillators.

Sommario

Il cervello umano è tanto affascinante quanto complesso: questo è il motivo per cui ha sempre attirato l'attenzione degli scienziati in molteplici ambiti di ricerca, dalla biologia alla medicina, dalla psicologia all'ingegneria. In questo contesto, diverse tecnologie non invasive sono state ottimizzate per permettere la misurazione di segnali, atti a descrivere l'attività cerebrale. Questi dati, derivanti da metodi di misura che differiscono molto nella loro natura, hanno aperto la porta a nuove descrizioni di quest'organo, che a loro volta hanno evidenziato le caratteristiche principali delle sue funzionalità. In particolare, è emerso come i segnali cerebrali fluttuino nel tempo, sia durante lo svolgimento di una particolare operazione, sia nei periodo di completa inattività. Inoltre, è stata individuato un coordinamento specifico e selettivo tra le diverse regioni del cervello.

In quanto ingegneri, la nostra attenzione è principalmente focalizzata sulla descrizione del cervello umano come un grafo, i cui nodi ed archi possono assumere il ruolo di elementi diversi, a seconda della specifica scala spaziale di interesse (siano essi descrittivi di singoli neuroni o intere aree cerebrali). Negli ultimi decenni, un notevole impegno è stato applicato per riprodurre e spiegare le complesse dinamiche degli elementi cerebrali attraverso l'utilizzo di modelli matematici. Infatti, la *teoria dei grafi* e il design di *modelli di popolazione* permettono lo sfruttamento di molti strumenti matematici, utili per ampliare la conoscenza del funzionamento del nostro cervello, sia in stato di salute, sia in malattia, attraverso la definizione di *reti cerebrali*.

È affascinante come l'incapacità del cervello umano di operare correttamente in caso di malattia sembri essere correlato ad alcune disfunzioni dell'attività dei mitocondri, gli organelli che producono la maggior parte dell'energia cellulare. In particolare, sono state riportate delle relazioni specifiche tra alcune malattie neurologiche e il danneggiamento della dinamica mitocondriale, ossia il continuo cambio di forma e lunghezza dei mitocondri, tramite i processi di fusione e fissione. Nonostante l'effettiva esistenza di un collegamento tra il cervello e i mitocondri sia ancora ambiguo ed oggetto di dibattito tra gli scienziati, la considerevole quantità di energia richiesta dal cervello umano per lavorare correttamente suggerisce che il cervello, più degli altri organi, sia dipendente dall'attività mitocondriale.

In questo lavoro di tesi sono riportati i risultati della nostra ricerca, atta ad investigare alcuni aspetti di questa complessa relazione tra cervello e mitocondri. Ci siamo quindi concentrati sulla dinamica mitocondriale e sul concetto di rete cerebrale, oltre che sui modelli matematici idonei alla loro descrizione matematica. Qui di seguito sono riportati e riassunti i principali argomenti trattati in questo manoscritto.

Modelli di popolazione per la dinamica mitocondriale. Proporremo un modello di popolazione non lineare ispirato ai modelli preda-predatore per simulare tutti i processi principali che prendono parte alla dinamica mitocondriale e quelli che sono fortemente connessi ad essa, incluso il processo di produzione di energia. Nello specifico, presenteremo due possibili configurazioni, che si differenziano nella presenza o meno di un collegamento in retroazione tra la quantità di energia libera disponibile e la formazione di nuovi mitocondri. Verrà quindi discussa la dinamica di entrambe le configurazioni e la loro capacità di riprodurre i comportamenti biologici osservati nella realtà.

Segnali cerebrali: confronto tra dataset ottenuti tramite tecnologie differenti. Riporteremo l'analisi di due dataset di segnali cerebrali registrati con diversi metodi (risonanza magnetica funzionale, fMRI, e magnetoencefalografia, MEG), sia in assenza di attività, sia durante lo svolgimento di un compito di attenzione. Quest'analisi ha un duplice obiettivo: lo studio dell'attività cerebrale spontanea e l'esplorazione di possibile relazioni esistenti tra le due diverse tecniche di misura.

Rete cerebrale: una descrizione basata sul modello Kuramoto. Ci soffermeremo sull'analisi di dati cerebrali empirici evidenziando le loro proprietà oscillatorie, con lo scopo di sottolinearne le caratteristiche che un modello matematico di fase dovrebbe essere in grado di riprodurre. Quindi, riporteremo una versione modificata del modello Kuramoto classico che abbiamo utilizzato per riprodurre le caratteristiche oscillatorie osservate empiricamente.

Analisi e controllo di reti di Kuramoto. La maggior parte del contributo teorico di questo lavoro di tesi comprende alcuni risultati analitici riguardo reti di oscillatori Kuramoto. Riporteremo quindi l'analisi atta a determinare le condizioni intrinseche e topologiche necessarie per ottenere un desiderato pattern di sincronizzazione, relativo sia ad una configurazione di oscillatori interamente sincronizzata, sia sincronizzata a gruppi.

Acknowledgments

First, I would like to thank my advisor Prof. Angelo Cenedese for his supervision during the period of my PhD. He has always supported my ideas and my interests, even though they fall outside the classic automation engineering discipline. Overall, he passed down to me the love for the academic research and for the multidisciplinary scientific collaborations. Furthermore, he always took care of me, as a parent would have done.

I would like to deeply thank the broad-minded Prof. Maurizio Corbetta, who made me discovering the awesome world of the neuroscience and who gave me the opportunity to take part to his ambitious project.

A special thank goes to Prof. Fabio Pasqualetti, whom I had the pleasure to meet and work with during my period abroad at the University of California in Riverside. At UCR I have been supervised by Prof. Elisa Franco, whom I would like to thank for having given me this wonderful opportunity.

One thank goes to Prof. Stefania Della Penna and Dr. Sara Spadone from the University of Chieti, who have been really willing to collaborate with me and to introduce me to the MEG technique.

Furthermore, I would like to thank all the committee that patiently read and reviewed this thesis, with a particular thank to Prof. Franco and Prof. Della Penna, who examined the first version of this manuscript.

To conclude the research-side and begin the personal-side thanks, I cannot forget to mention my colleagues and (mainly) friends Giulia Michieletto and Giulia Prando. We shared a lot of experiences and we always supported one each other. My PhD experience would not have been such awesome without their friendship. I really wish them the best for their life and career and I hope to have the opportunity to spend a lot of time together also in the future.

One thought goes to all my other PhD colleagues, in particular I would like to mention Marco, Andrea, and Diego, who are older than me and (together with Giulia) welcomed

me when I started this experience, and Michele, Giacomo, Irene, Nicoletta and Yutao, who shared all the three years with me and Giulia. During my experiences I have never meet a research group as brought together as we have been.

Then I really want to recall all my colleagues met in Riverside, with a special thought to Gianluca, Rajasekhar, Tommaso, and Siddhart, with whom I had a great time. Last but not least I would like to thank Lorenzo: we had the pleasure to work together and to become real friends. He always managed to get a smile out of me.

A deep thank goes to all my buddies in Treviso (in particular to Beatrice, Laura and Giacomo). The physical distance between us cannot weaker our emotional bond.

My life in Padova would not have been as great as it has been without all my housemates: a particular thank goes to Miriam, Giulia, Enrico and Andrea.

A special mention goes to my parents, Rita and Marcello, my big brother Flavio and my extended family, Chiara, Liliana and Mario, who always supported me and I am sure will support me anyway in the future. If I was able to reach this result, it was mostly their credit, as they always taught me good and bad, right and wrong to grow up and to discover the love for research.

The last, most unique thank goes to the person, who let me grow up day by day and who taught me happiness and love in the every-day life. He made me understand that we don't have to be "perfect" to be happy, and let me see the beauty of our flaws, which color our life and characterize our uniqueness. I sincerely want to thank you, Luca.

Notation and acronyms

Notation	Description
Sans Serif font	algorithm name
$\mathcal{A}$	set
$\lvert\mathcal{A}\rvert$	cardinality of set $\mathcal{A}$
$\mathbf{x}$	vector
x_i or $[\mathbf{x}]_i$	i-th element of vector $\mathbf{x}$
$\mathbf{A}$ or $[a_{ij}]$ ($[a_{ijk}]$)	matrix or tensor
a_{ij} or $[\mathbf{A}]_{ij}$ ($[\mathbf{A}]_{ijk}$)	the $(i,\, j)$ ($(i,\, j,\, k)$) element of matrix (tensor) $\mathbf{A}$
$\mathbf{a}_i$	i-th column of matrix $\mathbf{A}$
$\mathbb{1}_d$	vector of ones of size $d \times 1$
$\mathbb{1}_d^{\perp}$	orthogonal complement of $\mathbb{1}_d$
$\mathbb{0}_d$	zero-vector of size $d \times 1$
$\mathbb{0}_{d_1,d_2}$	zero-matrix of size $d_1 \times d_2$
$\mathbb{I}_d$	identity matrix of dimension d
$A(t)$	amplitude of a complex signal
j	immaginary unit
$\mathbb{N}$	set of natural numbers
$\mathbb{R}$	set of real numbers
$\mathbb{R}_{\geq 0}$	set of positive real numbers ($\mathbb{R}_{\geq 0} := (0,\, +\infty)$)
$\mathbb{R}^d$	Euclidean d-dimensional space
$\mathbb{R}^{d_1 \times d_2}$	space of real matrices with d_1 rows and d_2 columns
$\mathbb{C}$	set of complex numbers
p_{ij}	path from i to j on a spanning tree
$\mathcal{N}(\mu,\, \Sigma)$	Gaussian distribution with mean μ and covariance Σ
$\mathcal{U}([u_{\min},\, u_{\max}])$	Uniform distribution within interval $u_{\min}, \ldots, u_{\max}$
$:=$ $(=:)$	the left (right) side is defined by the right (left) side
$\approx$	the left side is approximately equal to the right side
$\mathbf{A}^n$	the n-th power of a square matrix

$\mathbf{A}^\mathsf{T}$ ($\mathbf{x}^\mathsf{T}$)	transposed matrix (vector)
$\mathbf{A}^{-1}$	the inverse matrix of matrix $\mathbf{A}$
$\lvert\cdot\rvert$	absolute value
$\lVert\cdot\rVert_\mathrm{F}$	Frobenius norm
$\lVert\cdot\rVert_\infty$	infinite norm
$\circ$	outer product ($\mathbf{x}\circ\mathbf{y}=\mathbf{x}\mathbf{y}^\mathsf{T}$)
$\odot$	Hadamard product
$\oslash$	element-wise division
$\mathrm{Im}(\mathbf{A})$	image of the space spanned by the columns of $\mathbf{A}$
$\mathrm{Im}(\mathbf{A})^\perp$	orthogonal subspace of $\mathrm{Im}(\mathbf{A})$
$\sigma(\mathbf{A})$	set of the eigenvalues of matrix $\mathbf{A}$
$\ker(\mathbf{A})$	kernel of the space spanned by the columns of $\mathbf{A}$
$\det(\mathbf{A})$	determinant of matrix $\mathbf{A}$
$\Re[\cdot]$	real part
$\mathcal{H}[\cdot]$	Hilbert transform
$\mathbf{1}_v(\cdot)$	indicator function of variable v
$\dot{x}(\cdot)$	derivative of x
$\frac{\partial}{\partial t}x(t,\,s)$	partial derivative of x with respect to t
$D^+f(\cdot)$	right-hand derivative of f
$\frac{d^n}{dt^n}$	n-times differentiation
$f\lvert_{(a)}(t)$	value of function f evaluated at point $t=a$

Symbols	Description
$a_x(\cdot)$	analytical signal related to time series $x(\cdot)$
$\theta_{x_i}(\cdot)$ or $\theta_i(\cdot)$	phase referred to time series $x_i(\cdot)$
$V(\cdot)$	Lyapunov function
$\mathcal{G}$	graph
$\mathcal{V}$	set of nodes of a graph
$\mathcal{E}$	set of edges of a graph
$\mathcal{T}$	spanning tree
$\mathcal{P}$	partition
$\mathcal{L}(\cdot)$	Lagrangian function
$\mathbf{L}_{\mathcal{G}}$	Laplacian matrix of the graph $\mathcal{G}$
$\delta(\cdot,\,\cdot)$	Kronecker delta function
$\mathtt{P}(\cdot)$	probability function
p_{val}	significance p-value used in ANOVA or t-test
F	F-value of ANOVA test
$\#$	number of

Abbreviation	Description
AD	Alzheimer's Disease
ADP	adenosine diphosphate
ALS	Amyotrophic Lateral Sclerosis
AMPK	AMP-activated protein kinase
ATP	adenosine triphosphate
BLP	band-limited power
BOLD	blood oxygen level-dependent signal
Ca^{2+}	calcium ions
cAMP	cyclic adenosine 3',5'-monophosphate
CAPs	coactivation patterns
cKM	classic Kuramoto model
Coh	cross-coherence
$CMRO_2$	cerebral metabolic rate of oxygen
DAN	dorsal attention network
DBS	deep brain stimulation
DCM	dynamic causal model
$DJ-1$	Parkinsonism associated deglycase protein
DMN	default mode network
Dnm1l	dynamin 1-like protein
Drp1	dynamin-related protein 1
DTI	diffusion tensor imaging
EEG	electroencephalography
e.g.	for example
ERR α (γ)	estrogen-related receptor alpha (gamma))
ETC	electron transport chain
$FADH_2$	flavin adenine dinucleotide reduced form
FC	functional connectivity
FHN	FitzHugh-Nagumo model
FHUs	functional hereditary units
Fis1	fission 1 homologue protein
fMRI	functional magnetic resonance imaging
GC	Granger causality
GDAP1	anglioside-induced differentiation-associated protein 1
GH	Greenberg-Hastings model
GTP	guanosine triphospate

H^+	protons
HD	Huntington's Disease
HRF	heamodynamic response function
ICA	indipendent components analysis
i.e.	id est
INs	interneurons
KL	Kullback-Lieber divergence
KM	(modified version of) Kuramoto model
MAPK	mitogen-activated protein kinase
MEG	magnetoencephalography
Mfn1 (2)	mitofusin 1 (2) protein
MI	mutual information
Mid	immunoglobulin D-binding protein
Mff	mitochondrial fission factor
mtDNA	mitochondrial DNA
mTOR	mammalian target of rapamycin
NADH	nicotinamide adenine dinucleotide reduced form
NAMPT	nicotinamide phosphoribosyltransferase
n.c.	nullcline
NNTF	non-negative tensor factorization
NRF-1 (-2)	nuclear respiratory factor 1 (2)
ODE	ordinary differential equation
Oma1	metalloendopeptidase
Opa1	dynamin-like 120 kDa protein
OXPHOS	oxidative phosphorylation
p38	mitogen-activated protein kinases
PCA	principals components analysis
PD	Parkinson's Disease
p.d.f.	probability density function
PGC-1α	peroxisome proliferator-activated receptor gamma co-activator 1-alpha
Pink1	PTEN-induced putative kinase 1
PNs	pyramidal neurons
PPA	point process analysis
PPAR-γ	peroxisome proliferator-activated receptor gamma
resp.	respectively

RN	Rulkov neuron model
ROI	region of interest
ROS	reactive oxygen species
RS	resting state
rs-fMRI	resting state functional magnetic resonance imaging
RSNs	resting state networks
SAM	sorting and assembly machinery
SC	structural connectivity
SIRT1	sirtuin 1
SQUID	superconducting quantum interference device
s.t.	such that
TFAM	mitochondrial transcription factor A
TFB	transcription factor B
VIS	visual network
w.r.t.	with respect to

Contents

1
Motivation

"Nobody realizes that some people expend tremendous energy merely to be normal."
Albert Camus, Notebooks 1942-1951

Since the beginning of time, mankind has been attracted by the complexity of the world around them. Humans tried to shed light on the unknown, be it very small (as atoms and molecules), or extremely large (as the outer space). However, one of the most complex existing systems is the human body in itself, with its anatomical, physiological, and psychological natures. It is often said that our body is a perfect machine, where a huge number of different processes combine one each other in order to let us all live any instant of our life.

Research fields have majored in several topics related to the understanding of the human beings' functioning, in order to improve and extend people lifespans. So far, much progress has been done and nowadays we have the opportunity of knowing our anatomy and our behavior nature very well. Nevertheless, we still have to face some *monsters*, whose essence is not fully understood, yet. One of the main mysteries is represented by the neurodegenerative diseases, which still affect our society, without we can actively react. Let us think for instance to Parkinson's or Alzheimer's Diseases.

Everyone knows that the brain is an incredibly complex system: a human brain comprises about 100 billion neurons connected by about 100 trillion synapses, which

are anatomically organized over multiple scales of space and functionally interacting over multiple scales of time. All of this creates a humongous *network* of parallel and distributed computational units, that can be considered as a biological hardware from which all our thoughts, feelings, and behaviors emerge. Therefore, it is not surprising that the understanding of how brain works is one of the most interesting challenges that involve scientists from several fields, ranging from neuroscience, to engineering, from medicine, to psychology. However, relatively simple processes such as cognition, attention, and memory, are so complicated that despite decades of intense research we have not really solved the puzzle of how these mechanisms work, yet.

From the modern brain networks science, it emerged that some basic principles may be able to describe the complexity of brain structures, connections and processes. Thus, in the last years an improved collaboration among different scientific fields (from neuroscience, to engineering, from psychology, to physics) is developing, aimed to provide a deeper (even not complete) understanding of the brain.

What is more, many clinical diseases, that are still not fully understood and treatable, like Parkinson's Disease, Alzheimer's Disease, dementia and schizophrenia, are found to be interpreted as disorders of such human brain networks. Hence, new insights on useful therapies are pusher objectives of this modeling challenge.

Central to current thinking about brain networks is the concept of the *connectome*, which was coined in 2005 by Olaf Sporns, Giulio Tononi, and Rolf Kötter (Sporns et al. (2005)), and independently in a PhD dissertation by Patric Hagmann (Hagmann (2005)), to describe a matrix representing all possible pairwise anatomical connections among elements of the brain. Nowadays this term is used with a wider meaning, referring both to anatomical and functional connections within the brain. Despite it will be described in detail throughout this thesis, in short, *functional* links have to be thought as a measure of similarity among signals measured at different spatial areas of the brain. Then, the mathematical and conceptual developments in complex network science, together with the evolution of technologies for measuring nervous systems set the bases for a new conception of the study of the connectome in its whole. To this aim, different tools can be used (from mathematical, to behavioral methods), depending on the specific target, the different time and the spatial scale that we are interested in.

In particular, as researchers in automation engineering, we are especially attracted by the description of the human brain as a dynamical system evolving over a *graph*, and its analysis through the tools offered by control systems and graph theory. From our point of view, brain networks can be depicted as *populations* of neurons (or larger brain areas), whose dynamics depends on their internal structural and functional connections.

Specifically, we describe this ensemble as a population of agents, which are able to *synchronize* and *desynchronize* during time, by assuming more or less coherent pattern behaviors as time goes on and which cooperatively act towards a task accomplishment. This framework allows us to think of brain areas as a group of *oscillators*, whose dynamics can be described by their phases' dynamics.

We hence make extensive use of mathematical models useful to describe complex systems of oscillators. In particular we are interested in networks, whose agents behave like a single sub-network, where all elements have the same dynamics, or where groups or clusters of agents are characterized by similar within-group and different between-groups dynamics.

The theoretical description of these phenomena is motivated by evidences coming from experimental brain data. Indeed, we will analyse real neuronal data, in order to recognize in the empirical signals, characteristics and features that we would be able to reproduce by means of computational tools. In particular, we are interested in understand how the brain networks work in *resting-state*, that is when we are not doing anything (but neither sleeping), and how they are able to switch to a condition of *task-doing*, when we want to perform a specific action. With respect to the experimental data, different measurements of brain signals are now available, but they are very different one another, and they often describe only indirect measures of the true neural activity. Thus, the relationship among different data, and their possible combination is still unclear among neuroscientists. To discuss this aspect, in this work we present a comparison of two datasets referred to the same activity, but recorded with different technologies: we focus on pros and cons of each modality and on the consistency of information that can be derived, to identify which features are useful to achieve new insights on the large set of unresolved questions.

When we think of the brain as a network of interconnected nodes (that is a graph), we cannot neglect the huge budget of energy that it needs to work properly. To this aim, the neuron cells are equipped with a larger number of mitochondria than the other cells of our body. Mitochondria indeed are the organelles inside eukaryotic cells, whose most prominent roles are to produce ATP, the energy currency of the cell, through respiration, and to regulate cellular metabolism. We observe that there is a complex relation between mitochondria and brain. Although many sides of this link are still unknown, a number of evidences suggests a strong correlation among mitochondrial dysfunction and neurological diseases. Our interest in mitochondria analysis emerges from these aspects, and we focus on the description of the so-called *mitochondrial dynamics*, a process describing continuous change of shape and location of these organelles, which continuously fuse and

split up during time. Some mathematical models have already been proposed in the literature to describe this phenomenon; however, we believe that they do not account for some important properties, such as the analytic tractability, or the link between mitochondrial dynamics and the main mitochondrial function (that is energy production). Specifically, we focus on providing a mathematical framework, which is complete and analyzable at the same time, with a particular attention on the relationship between mitochondrial dynamics and energy demand.

In summary, this work is aimed to analyze and characterize some aspects of the complex relationship that exists among mitochondria and brain. This relation, indeed, emerges from empirical observations (such as the coexistence of mitochondrial and neuronal dysfunction in neurological disorders, and the large demand of mitochondrial-produced energy by the brain), but it is still unclear. Specifically, we make use of system theory applied on networks of coupled oscillators, to characterize brain networks and their synchronized, or desynchronized dynamics. Figure 1.1 depicts an overview of the main topics, which are discussed in this thesis, and whose direct or indirect links motivate all our research.

Undoubtedly, this is only a small tile of the whole set of relationships that characterizes this complex system. However, we hope that our work may be useful to complete a little part of this unresolved, amazing puzzle.

Contents

1.1 Contribution and outline

We refer to Figure 1.1 to describe the theoretical and empirical contributions of this thesis.

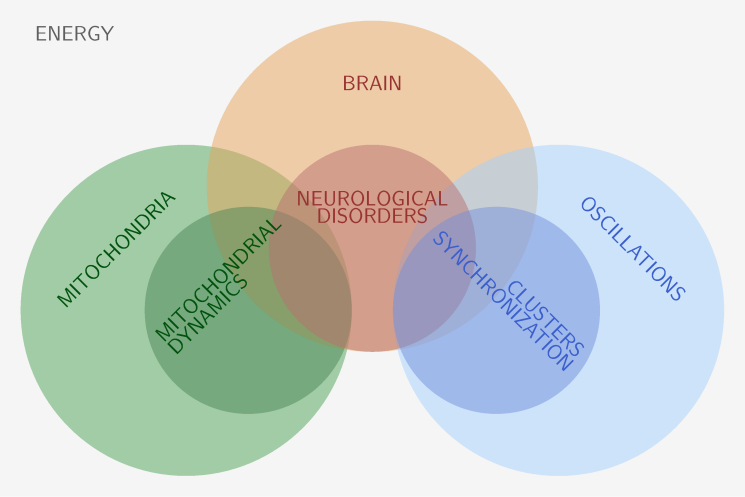

Figure 1.1: Overview of the main topics addressed throughout this work, and their interconnections. Refer to the main text for a detailed explanation.

This manuscript is aimed to investigate the complex relationship existing between the functioning of the human brain and the mitochondria, which populate our cells. In particular, we focus on the peculiarity of mitochondria, which allows them to continuously fuse and split up, namely the mitochondrial dynamics. On the other hand, several evidences have highlighted the presence of mitochondrial dysfunction (and, mitochondrial dynamics' impairment) in certain neurological diseases, such as Parkinson's, Alzheimer's, or Hunghtington's Diseases. Commonly, most of the neurological diseases characterized by mitochondrial pathology, are also affected by dysfunctions in the neuronal network activity. The human brain has been in fact often referred as a complex network of elements (group of neurons, or brain regions), which communicate each other through a particular network topology, which we will investigate throughout the following chapters. When this networking does not work properly, serious disorders may occur. Although the recent work of a large part of scientists has been focused on the investigation of this intricate relationship among mitochondria, brain disorders and brain networks, a lot of questions are still unanswered, and many biological evidences remain mysteries, so far. Thus, we addressed our research following two pathways. On the one side we described the brain as a population of small brain regions, whose dynamics evolves over a graph. Specifically, we characterized it as a system of Kuramoto oscillators (Kuramoto

(1975)), and we investigated the topological and intrinsic conditions that can lead to the formation of sub-networks within the whole population of nodes. On the other hand, we proposed a simple, yet complete, prey-predator population model for the mitochondrial dynamics and other phenomena related to it.
As the underling connection between these processes, we detected the availability of energy. Indeed, energy production is exactly the main function of these organelles, and this fact may be the most relevant connection with the brain, which requires a large amount of energy to fulfil all its tasks. In addition, the ongoing fluctuations and oscillations, which characterize the neuronal activity, and which lead to the formation of brain networks, induce a considerable expenditure of energy.

The remaining part of this chapter and the following ones are organized as described below, where we list also the already published contributions.

Chapter 1. Starting from the main motivations which guide our research, a large amount of attention is devoted to the concept of energy production and requirement, which is at the basis of the complex relationship among mitochondria, brain, and brain activity. In addition we report a brief description of two neurological diseases, characterized by the coexistence of mitochondrial and oscillatory dysfunctions.

Chapter 2. It describes mitochondria and mitochondrial dynamics from a biological point of view, and provides the preliminary information required to understand the hypotheses of the mathematical model presented in the following chapter.

Chapter 3. In this chapter we propose a modified prey-predator population model to simulate the main processes, which take part in the mitochondrial dynamics, and the ones that are strongly related to it. We present two possible setups, and we discuss their behavior at the equilibrium, as well as their sensitivity to the most important parameters.

Chapter 4. Chapter 4 contains an introduction to the activity of the brain, and the different techniques used to measure this activity. Then we focus on the graph representation of the brain, and the mathematical tools offered by information and systems theory, useful to analyze and characterize the signals of the brain.

Chapter 5. In this chapter we analyze two real datasets of brain signals recorded with different techniques and in different conditions, with the twofold aim of investigating the spontaneous activity of the brain, and exploring possible relationships between the two different techniques.

Chapter 6. After an introduction of the concept of synchronization among agents, in this chapter a subset of the empirical dataset analyzed in Chapter 5 are examined, from a synchronization point of view. The purpose is to highlight the features that a computational phase-model should be able to reproduce. In addition, we use the Kuramoto model to reproduce the oscillatory characteristics of the measured data.
Related publication:

- Favaretto, C. and Cenedese, A. (2016). On brain modeling in resting-state as a network of coupled oscillators. In *2016 IEEE 55th Conference on Decision and Control (CDC)*, pages 4190–4195.

Chapter 7. The most part of the theoretical contribution of this manuscript is contained in this chapter, which reports our analytical results on Kuramoto model and the topological and intrinsic conditions required to achieve a desired synchronized, or clustered synchronized configuration within a network of coupled oscillators.
Related publications:

- Cenedese, A. and Favaretto, C. (2015). On the synchronization of spatially coupled oscillators. In *2015 54th IEEE Conference on Decision and Control (CDC)*, pages 4836–4841.
- Favaretto, C., Bassett, D. S., Cenedese, A., and Pasqualetti, F. (2017a). Bode meets kuramoto: Synchronized clusters in oscillatory networks. In *2017 American Control Conference (ACC)*, pages 2799–2804.
- Favaretto, C., Cenedese, A., and Pasqualetti, F. (2017b). Cluster synchronization in networks of kuramoto oscillators. In *IFAC World Congress*.
- Tiberi, L., Favaretto, C., Innocenti, M., Bassett, D. S., and Pasqualetti, F. (2017). Synchronization patterns in networks of kuramoto oscillators: A geometric approach for analysis and control. *arXiv preprint arXiv:1709.06193*. [accepted for CDC 2017].

Chapter 8 This chapter offers some concluding remarks and some food for thought on possible future works.

Complementary work not included in the thesis:

- Cenedese, A., Favaretto, C., and Occioni, G. (2016). Multi-agent swarm control through kuramoto modeling. In *2016 IEEE 55th Conference on Decision and Control (CDC)*, pages 1820–1825.

- Pasqualetti, F., Favaretto, C., Zhao, S., and Zampieri, S. (2018). Fragility and controllability tradeoff in complex networks. [submitted to ACC 2018].

1.2 Brain, energy, and mitochondrial dynamics

In this section we address the physiological aspects that relate brain functioning and neurons oscillations with mitochondrial dynamics and energy supply. Specifically, we describe the complex network of relationships among these elements, in order to highlight the requirements for each part of the whole system to work properly. This section is hence aimed to define the common theme that motivates all the results presented in this manuscript, and that revolves around the production and the requirement of energy.

1.2.1 Brain and energy

Although it represents only the 2% of the total human body weight, the human brain consumes the 20% of the total oxygen consumption (McKenna et al. (2006)), and the neurons are one of the most metabolically active cell types in our body. However, despite the well-known facts about brain's large energy budget, a clear understanding of how it is apportioned among the many ongoing functional processes in neurons and glial cells (i.e. cells that surrounds and supports neurons in the central nervous system) is still missing. The metabolic activity of the brain consists largely in the oxidation of glucose to carbon dioxide and water, resulting in the production of large amounts of energy in the form of adenosine triphosphate (ATP). While spontaneous activity of the brain, in a condition of rest, has been previously considered merely to be *noise*, more recently, it has been revealed to be essential in order to understand the brain function. Indeed (and surprisingly), most of the brain energy consumption is related to intrinsic activity that is not driven by responses to external stimuli (Mitra and Raichle (2016)), while energy associated with evoked brain activity accounts for less than 5% of the total brain energy budget. Thus, the metabolic activity of the brain is remarkably constant over time (*baseline activity*), even though mental and motor activity widely vary (Raichle and Gusnard (2002)). Moreover, from functional analysis of brain signals during rest, it has emerged a significant correlation of the spontaneous infra-slow (less than 0.1 Hz) fluctuations within specific functional areas in the brain.

Hence, thanks to the modern imaging techniques (functional magnetic resonance imaging, fMRI, magnetoencephalography, MEG, and positron emission tomography, PET) used to analyse the functioning of the brain, it has emerged that there is a relationship between brain energy metabolism and cellular activity (Smith et al. (2002); Hyder et al.

(2002)). Specifically, the change in oxygen consumption induced by stimulation has shown to be proportional to the change in spike frequency. The nature of the ongoing intrinsic activity, that needs this large amount of brain's energy, is however not clear, yet. Moreover, the scenario is complicated by the cellular heterogeneity of the brain, where different cell types have distinctive metabolic profiles (Magistretti and Allaman (2015)), and a particular distinction exists between neurons and astrocytes (the most numerous and diverse neuroglial cells in the central nervous system). Over the last years, various approaches have been used to establish the *energy budget* of the brain (Attwell and Laughlin (2001); Harris et al. (2012); Hyder et al. (2013)), and it appears that the 75-80% of the energy is consumed by neurons, while the remaining part is used for glia-based processes. Specifically, most of the energy used by neurons for signaling (the ensemble of communication process that governs basic activities of cells and coordinates all cell actions) appears to be consumed at the synapse (Harris et al. (2012); Rangaraju et al. (2014)), the point at which a nervous impulse passes from one neuron to another.

1.2.2 Energy and mitochondria

Given that our brain needs a large amount of energy in order to work properly, we now report a brief description of the ATP production in human cells. Most commonly the cells use ADP (adenosine diphosphate) as a precursor molecule and then add a phosphorus to it. In eukaryotes this process can occur either in the soluble portion of the cytoplasm (cytosol) or in the energy-producing structures called *mitochondria*. In short, a mitochondrion is a double-membrane system, consisting of inner and outer mitochondrial membranes separated by an intermembrane space. The inner membrane forms numerous folds (cristae), which extend into the interior (or matrix) of the organelle. Each of these components plays distinct functional roles, with the matrix and inner membrane representing the major working compartments of mitochondria (see Chapter 2).

Cellular and mitochondrial energy production. Mitochondria consume about 90% of mammalian oxygen and use it to synthesize ATP. Specifically, mitochondria intervene in the last phase of cellular catabolism, after the enzymatic reactions of intermediate metabolism, which degrade carbohydrates, fats and proteins into smaller molecules such as pyruvate, fatty acids and amino acids, respectively. Through β-oxidation and the Krebs cycle, mitochondria then transform these energetic elements in NADH and $FADH_2$, which are next degraded by the mitochondrial respiratory chain in a process called oxidative phosphorylation (OXPHOS). During this process, the electrons liberated by the oxidation of NADH and $FADH_2$ are passed along a series of carriers,

which consists of four enzyme complexes (complexes I to IV), and two mobile electron carriers (coenzyme Q and cytochrome c), and finally transferred to molecular oxygen. The whole set of these carriers is referred as *respiratory chain* or *electron transport chain* (ETC). NADH and $FADH_2$ hence play the role of energy substrate, through which the transfer of electrons from complex I or II to complex IV mediates the extrusion of protons (H^+) from the mitochondrial matrix to the intermembrane space, leading to a proton electrochemical potential gradient across the inner mitochondrial membrane, which is known as the proton-motive force. The proton-motive force is used to drive gradient-dissipating activities, including the generation of ATP by ATP synthase, which is the main pathway for the return of protons into the matrix. This gradient is determined by two components, which are the membrane potential $\Delta\Psi_m$, which arises from the net movement of positive charge across the inner mitochondrial membrane, and a chemical potential (the pH gradient). Finally, ATP is transported outside the mitochondrion to the cytosol by the adenine nucleotide translocator (ANT) and exchanged for ADP. The membrane potential contributes most of the energy (typically $\sim 150\,\text{mV} \div 180\,\text{mV}$) that is stored in the gradient. Specifically, at any instant of time, $\Delta\Psi_m$ represents the balance between the processes that contribute to the generation of the proton gradient, and those that consume it.

The ATP turnover reactions (which includes its synthesis, consumption and translocation) and the protons leaks of the inner mitochondrial membrane regulate the respiration rate by affecting $\Delta\Psi_m$ (see Figure 1.2). When $\Delta\Psi_m$ increases, the rate of respiration is inhibited, whereas a decrease in $\Delta\Psi_m$ causes an acceleration in the respiration rate.

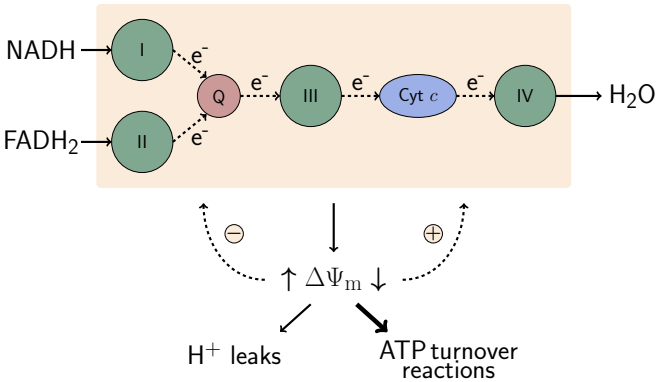

Figure 1.2: Electron transport chain. The ATP turnover reactions (synthesis, consumption and translocation) and the proton leaks of the inner mitochondrial membrane regulate the rate of respiration by affecting the mitochondrial membrane potential $\Delta\Psi_m$. An increase (↑) in $\Delta\Psi_m$ has an inhibitory effect (−) on the rate of respiration, whereas a decrease (↑) in $\Delta\Psi_m$ will accelerate the respiration rate (+). (Adapted from Moncada and Erusalimsky (2002) [Fig. 1]).

ATP regulation in the brain

A brief description of how the brain regulates its energy supply in response to different information processing tasks is here made available. To sustain neuronal function and the relative huge energy demand, the brain has developed neurovascular coupling mechanisms in order to increase the flow of blood to regions in which neurons are active. From recent studies it has emerged that neurotransmitter-mediated signaling (particularly by glutamate) has a major role in regulating cerebral blood flow, and that much of this control is mediated by astrocytes. The vascular energy supply by neural activity is largely mediated by feedforward mechanisms. During these processes, neurons either signal directly to blood vessels or activate astrocytes to release vasoactive agents onto the vessels (Attwell et al. (2010)).

Specifically, the regulation of ATP in the brain can be represented through a block diagram as in Figure 1.3. It is provided by the combination of two feedback loops: the outer one on its own would provide relatively poor control; it is a legacy from the control of glycolysis in simple cells. The main contribution is due to the inner feedback loop, which, together with the outer one, ensures a consistent homeostatic steady state level of ATP. However, this level is not sufficient in neurons, where extra ATP is required by signaling; thus, the brain energy metabolism has to accommodate rapid changes in ATP levels. This transient demand of energy is supplied by a fast feedforward loop, through which astrocytic lactate is released.

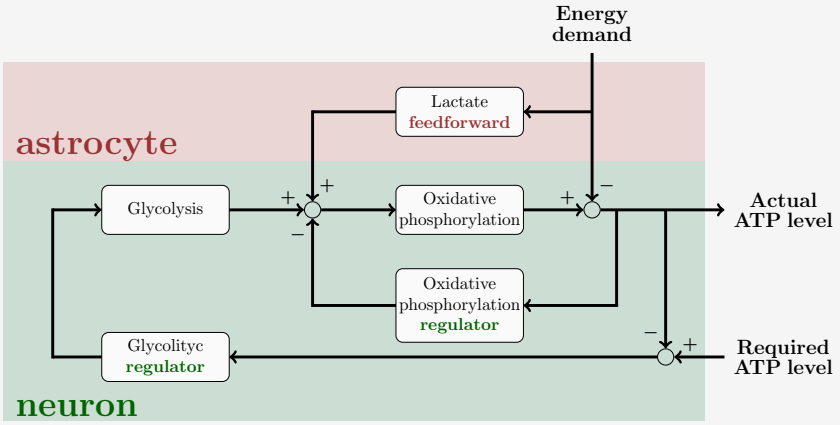

Figure 1.3: Energy regulation and control structure for brain energy metabolism. For most of the human cell types, the ATP supplies are regulated by a combination of two feedback loops (Glycolytic regulator, and Oxidative phosphorylation regulator). The *extra* ATP required by the neurons within the brain, associated with rapid transient ATP demands, is provided through a fast feedforward lactate loop. (Adapted from Wellstead and Cloutier (2012)).

1.2.3 Mitochondrial dynamics and energy metabolism

Accepted that a good functioning of the brain is strictly related to good mitochondrial performance in energy production, it is interesting now to explore the relationship between energy metabolism and *mitochondrial dynamics*. Indeed, as mobile organelles that are organized in dynamic networks, mitochondria continuously join by the process of fusion and divide by the process of fission. This *machinery* of fusion and fission is referred by biologists as *mitochondrial dynamics*. In Lu (2011), the authors discuss the possible bidirectionality of this relation, such that organelles' energy production depends on shape changes of the mitochondria, and meanwhile fusion and fission processes are regulated by the energy state of the cell. Here we summarize this bidirectional relation, which links the mitochondrial capability of ATP production, with the mitochondrial membrane potential $\Delta\Psi_m$, and with the proteins involved in fusion and fission processes. As we will see in Chapter 2, the proteins that regulate mitochondrial fusion at most are the mitofusins Mfn1 and Mfn2, and dynamin-like 120 kDa protein Opa1. They are dynamin-related proteins, anchored in the mitochondrial membranes, and show GTPase activity (GTPase is a large family of hydrolase enzymes that can bind and hydrolyze guanosine triphosphate, GTP), which is essential for their mitochondria-fusing activity. Instead, the most relevant proteins identified as fission mediators are Drp1 (dynamin-related protein 1), DNM1l (dynamin 1-like protein), and fission 1 homologue protein (Fis1).

Possible control of mitochondrial dynamics by energy metabolism. The idea that mitochondrial dynamics may be regulated by the energy state is supported by some studies that show that mitochondrial fusion is altered by the collapse of $\Delta\Psi_m$, through the cleavage of Opa1 (Legros et al. (2002); Ishihara et al. (2003); Duvezin-Caubet et al. (2006)). Furthermore, the phosphorylation of Drp1 by cAMP-dependent kinase activates mitochondrial fission. Other works proposed the idea that Opa1, Mfn1, Mfn2 and Drp1 all require GTP to be performing, thus supporting the hypothesis of a bioenergetic control of the mitochondrial dynamics. Indeed, the GTP formation by the Krebs cycle followed by GTP extrusion by the ANT could directly modulate mitochondrial fusion (Ježek and Plecitá-Hlavatá (2009); Ježek et al. (2010)). Moreover, Opa1 has shown to be $\Delta\Psi_m$-dependent, since a loss in mitochondrial membrane potential triggers the cleavage of long isoforms of Opa1 to shorter form, reducing the ability for mitochondrial fusion (Legros et al. (2002)). These are only some examples of evidences used to corroborate this first hypothesis. Yet, how these master regulators of energy metabolism interact with the mitochondrial fusion and fission proteins also remains to be investigated.

Possible control of energy metabolism by mitochondrial dynamics. Conversely to the hypothesis described above, other evidences validated the idea that mitochondrial dynamics may regulate energy metabolism, and not be regulated by it. For instance, Tondera et al. (2009) evidenced a rapid stress-induced mitochondrial hyperfusion, accompanied by an increase in mitochondrial ATP production. Although the mechanism was not completely clear, it may be hypothesized that mitochondrial fusion could increase the speed of diffusion of energy metabolites within the mitochondrial tubules. Similarly, the overexpression of Mfn2 causes the increase of ATP production and glucose oxidation (Bach et al. (2005)). Opa1 may contribute to control energy production, since the removal of m-AAA protease, which cleaves Opa1 in a $\Delta\Psi_m$-dependent manner, limits the ability of OXPHOS to supply ATP under conditions of high energy requirement (Ehses et al. (2009)). Therefore, this observation supposes that changes in mitochondrial membrane composition control energy metabolism, thus highlighting the complexity of the whole system.

Given the high level of complexity of these correlated phenomena, it is likely that no-one of the presented hypotheses is independent from the other, and that the relationship between mitochondrial dynamics and energy metabolism is actually bidirectional. However new investigations are needed to fill all the gaps.

1.2.4 Energy, mitochondria and neuronal oscillations

So far, we have introduced the existing link among brain, energy and mitochondria (and mitochondrial dynamics). However, we have not mentioned any possible connection of energy (and hence mitochondria) and the oscillatory activity of the brain, yet. Thus, in this section we highlight the complex set of relationships existing between mitochondria and brain signals' oscillations, going through the large amount of energy required to sustain neuronal oscillatory activity.

As we will discuss in Chapters 4, 5, and 6, functional magnetic resonance imaging (fMRI) allows to record brain signals from different regions at the same time, as an undirected measure of the electrical activity of the brain. Through these data, we are able to define the so-called functional connectivity (FC) maps, that describe how correlated the activity of different brain areas is. As we will discuss in Chapter 4, these maps lead to consider the human brain as a network of nodes (brain areas, for instance) with some specific topological characteristics that guarantee an optimal information sharing among each of its parts. Specifically, brain areas are not uniformly connected, but a small-world topology can be identified. That is, the network has clustering properties similar to a regular lattice and path length similar to a random network. Moreover,

in the complex system of brain, some regions act like hubs, since they have a number of connected neighbors that largely exceeds the average. The presence of these hubs increases the efficiency of the communication within brain areas. However, very less is known about the physiological significance of this particular topology (small-worldness and hubs presence). The link between different importance of nodes within the network and its meaning can be analyzed through the combination of fMRI with other sources of data, such as EEG (electroencephalography), which describe the frequency-specific electrophysiological dynamics underlying synchronous fMRI-derived fluctuations.

For instance, a collections of evidences of correlation between FC and oscillations in the gamma-band (γ-oscillations) have been summarized in Lord et al. (2013), where the authors remarked how the relationship between fMRI synchronization patterns and γ-band dynamics is coherent with the established role of this band's dynamics in supporting distributed neurocognitive phenomena, which require the coordination of large neuronal ensembles. Namely, high frequency oscillations are thought to support the sharing of information arising from distributed neural sources, thus enabling several mental operations. The generation of γ-frequency oscillations has been related to the reciprocal connectivity between membrane potentials of large ensambles of pyramidal neurons (PNs) and fast-spiking inhibitory interneurons (INs). In addition, the authors supported the idea that local γ-band activity may become synchronized across anatomically distant regions in the brain thanks to the self-organization of the brain activity into a critical state, thus enabling functional integration in large-scale networks.

Although there are several evidences of the correlation among mitochondrial dysfunction and abnormal patterns of synchronization in brain signals, the exact relationship between these two phenomena is still unknown. The direct link between network synchronization and energy demands may be found in the high local energy consumption in the brain due to the maintenance of ionic homeostasis across neuronal cell membrane during high frequency network oscillations. (Lord et al. (2013)). Thus, the retention of γ-oscillations likely requires strong mitochondrial performance in providing ATP.

At this point, it is reasonable to assert that the metabolic processes in the brain not only have the role to sustain basic physiological functions required in every tissues of the human body to the survival of the same tissue, but also may be necessary in order to shape the functional network topology of the brain.

Certainly, the mitochondrial function is not the only responsible for the network activity of the brain, and it cannot be separated from the glucose supply, critical to the sustain of high frequency oscillations. For instance, one hypothesis is that in specific disorders, the impaired glucose uptake may trigger the reorganization of synchronized

network activity in the brain to a topological configuration which is less metabolically expensive, but which also leads to the detriment of integration capacity (Lord et al. (2013)). In addition, the relationship could be bidirectional: this may be the case of schizophrenia, where the development of metabolic disorder may be the consequence (and not the cause) of abnormal network connectivity, which requires more glucose consumption by the brain, and a consequent reduced glucose uptake by peripheral tissues.

1.2.5 Mitochondria and the brain

At this point, a complex link between brain and mitochondrial function cannot be neglected. This relationship has emerged even more strongly during the last decades, when the idea that neurological disorders may be linked to mitochondrial dysfunction rose among scientists. The relationship between these two typologies of disorders is not unrealistic, if we consider the large energy consumption of the brain and the main role played by mitochondria, responsible for the ATP production. As mobile organelles, mitochondria undergo transport and trafficking to the areas of cells where they are most needed. Hence their number within the cells changes in relation to the amount of energy required in the specific tissue. Therefore, it is not surprising that neurons within the brain are highly populated by mitochondria and are sensitive to potential mitochondrial dysfunction in ATP producing.

Indeed, one evidence of this relationship between mitochondria and brain can be found in the neurological disorders that have been identified to have mitochondrial dysfunction as a component of their pathogenesis (Chan et al. (2016)). In addition to the primary mitochondrial disorders, which are due to mitochondrial or nuclear DNA mutations, and cause defects in the respiratory chain, other multi-organ diseases have been recently identified as secondary mitochondrial disorders. The most popular examples are Parkinson's Disease (PD) (Abou-Sleiman et al. (2006)), Alzheimer's Disease (AD) (Moreira et al. (2010)), Huntington's Disease (HD) (Oliveira (2010)), Amyotrophic Lateral Sclerosis (ALS) (Hervias et al. (2006)), and psychiatric disorders such as schizophrenia and bipolar disorder (Clay et al. (2011)). All of the mentioned disorders are examples of neurodegenerative diseases, thus confirming the hypothesis of a strong relation among the two biological fields. Furthermore, mitochondrial dysfunctions increase with age, and age is the most impairment risk factor for these neurodegenerative diseases.

Intriguingly, most of the neurological diseases that are classified as secondary mitochondrial disorders, are also affected by dysfunctions in neuronal network activity or neuronal oscillations.

Neurological diseases and mitochondrial dynamics. Recent studies have identified that several neurological diseases are not only related to the mitochondria, but specifically to mitochondrial dynamics (fission and fusion), biogenesis (formation of new mitochondria) and mitophagy (elimination of damaged mitochondria). In addition to their direct effects on mitochondrial shape, length, number, and location, mitochondrial dynamics are critical for the maintenance of the integrity and homogeneity of mitochondria. Indeed, impaired mitochondrial fusion has been reported to cause mutations and deletion in the mitochondrial DNA, thus resulting in the accumulation of dysfunctional mitochondria. Due to the lack of efficient DNA repair systems, mitochondria are relatively vulnerable to deleterious damage, thus defective mitochondria need to be cleared in a timely manner. Specifically, mitochondrial fission has been shown to participate in the elimination of damaged mitochondria by mitophagy. Moreover, as highlighted in the previous section, mitochondrial fusion and fission proteins could be directly involved in the assembly of respiratory complexes, underscoring the important role of mitochondrial dynamics in regulating mitochondrial function.

The deficiency of almost all mitochondrial fusion and fission regulators or the expression of dominant negative mutants of mitochondrial fusion and fission regulators impairs mitochondrial movement and proper localization, leading to mitochondrial depletion in neurites and synapses and eventually to dendritic spine and synaptic loss (Baloh (2008); MacAskill et al. (2009)).
The crucial role of mitochondrial dynamics for neuronal function is evidenced by the fact that genetic mutations in key regulators of mitochondrial dynamic cause dominantly inherited neurological diseases. Some examples can be found in Table 1.1, where the diseases are reported with the coexisting altered phenomena of mitochondrial dynamics.

Although the widespread presence of mitochondrial dynamic abnormalities and dysfunction in various neurodegenerative diseases suggests that the cause of altered mitochondrial dynamics could be multifactorial, emerging studies have implied that the manipulation of mitochondrial dynamics may be a common therapeutic approach to improve mitochondrial and neuronal function and prevent neurodegeneration. Thus our interest motivates the employment of a mathematical and control theoretic modeling approach to get new insights on the mechanisms of mitochondrial dynamics and their regulation.

Disorders	Impared phenomenon	Species	References
ALS	↑ fission	rat	Song et al. (2013)
AD	↑ fission	mouse	Cho et al. (2009)
HD	↑ fission	human, mouse, rat	Haun et al. (2013)
PD	↑ fission	human	Santos et al. (2015)
ARSACS	↓ fission	human, mouse	Bradshaw et al. (2016) Girard et al. (2012)
ARCMT2K	↓ fission	human	Niemann et al. (2009)
CMT4A	↓ fission	human	Cuesta et al. (2002) Niemann et al. (2009)
CMT2K	↓ fission	human	Sivera et al. (2010) Niemann et al. (2009)
CMT2A2	↓ fusion	human, rat	Misko et al. (2012) Züchner et al. (2004)
ADOA	↓ fusion	human, rat	Misko et al. (2012) Zanna et al. (2007)

Table 1.1: Examples of mitochondrial fusion and fission impairment in neurological diseases (see Flippo and Strack (2017), Table 1). Abbreviations: ALS, Amyotrophic lateral sclerosis; AD, Alzheimer's Disease; HD, Huntington's Disease; PD, Parkinson's Disease; ARSACS, Autosomal-recessive spastic ataxia of Charlevoix-Sanguenay; ARCMT2K, Autosomal recessive Charcot-Marie-Tooth Disease, type 2K; CMT4A, Autosomal recessive Charcot-Marie-Tooth Disease, type 4A; CMT2K, Autosomal dominant Charcot-Marie-Tooth disease; CMT2A2, Autosomal dominant Charcot-Marie-Tooth disease, type 2A2; ADOA, Autosomal dominant optic atrophy.

1.2.5.1 Motivational examples

To explain how mitochondrial and neurological dysfunctions occur together, and how network activity and neuronal oscillations are related to these pathologies, we briefly report some characteristics of Huntington's and Parkinson's Diseases.

Huntington's Disease (HD). Originally known as Huntington chorea due to the classic symptom of *dancing* movement (chorea), HD occurs as a consequence of a mutation in the huntingtin gene. It presents with cognitive and psychiatric disturbances and motor impairment (Sturrock and Leavitt (2010)). As other neurological disorders, HD is extremely difficult to nurse, since it is only at the larger stage of the disease, when it is very hard to reverse the degeneration process, that the main symptoms emerge. The evidence of mitochondrial dysfunction in HD are threefold: first, severe respiratory chain defects, especially in complex II-III (Gu et al. (1996)); second, there are evidence of regionally-specific damage in the mitochondrial DNA (mtDNA), especially within the parietal, frontal and temporal cortex of HD patients (Polidori et al. (1999); Horton

et al. (1995)). Finally, more recently, also links among HD and impaired mitochondrial dynamics have emerged through immunohistochemical analysis of mitochondria extracted from medium spiny neurons in patients' brain. Specifically, the analysis has shown disrupted mitochondrial morphology that results from increased fission and reduced fusion, creating fragmented mitochondria (Kim et al. (2010)). Mutant huntingtin binds to the mitochondrial fission protein Drp1 (Song et al. (2011)) and upregulates its enzymatic activity increasing mitochondrial fission, that leads to several downstream impairments, like reduced mitochondrial biogenesis, synaptic degeneration, and impaired mitochondrial trafficking (Shirendeb et al. (2011)).

From a neuronal network point of view, EEG analysis in HD patients revealed several, and sometime controversial, abnormal oscillatory patterns in EEG power, which correlates with neurological and neurocognitive impairment of the patients (see De Tommaso et al. (2003); Painold et al. (2010); Starr et al. (2008), just to mention a few).

Parkinson's Disease (PD). Another progressive disease that combines neurological and motor disorders is Parkinson's Disease. Indeed, PD patients present both motor symptoms, like tremor, rigidity, and bradykinesia, and cognitive impairments, as well as psychiatric symptoms (Aarsland et al. (2010); Forsaa et al. (2010)). PD has been related to the loss in dopaminergic neurons of substantia nigra pars compacta in the basal ganglia, and to the misfolding of the presynaptic protein, α-synuclein. Similarly to HD, the relationship between PD and mitochondrial dysfunction is widely accepted by scientists (Exner et al. (2012)). Specifically, PD not only correlates with significant impairment within the respiratory chain, but also with an high deletion in mitochondrial DNA in the substantia nigra (Bender et al. (2006)). Furthermore, the mutation of three specific genes (Parkin, Pink1 and DJ $-$ 1), associated with PD patients, highlights the relation of this disease with mitochondrial dynamics and mitophagy. Parkin encodes proteins needed to recruit damaged mitochondria and promote autophagy. Moreover it is also at the core of other mitochondrial functions, including prevention of mitochondrial swelling and protection against mitochondrial cell death. Pink1 mutation causes a fragmentation of mitochondria, which leads to the disruption of mitochondrial morphology. At physiologic levels, both mitochondrial fission and mitophagy are beneficial, working together to eliminate damaged and depolarized mitochondria, however, an impairments of either process can lead to increased oxidative stress and reduced ATP production (Archer (2013)). Finally, DJ $-$ 1 mutations cause increased vulnerability to oxidative stress (ROS) and hypersensitivity to complex I inhibition.
The link between PD and neuronal network activity emerges from abnormal EEG oscillatory activities observed in PD patients, characterized by a reduction in the alpha

and beta rhythm activity, concurrent with an increase in the slower delta and theta wave activity (Soikkeli et al. (1991)). Moreover, recent surgical procedures (see, for instance, Deep Brain Stimulation, DBS), have revealed excessive high frequency synchronization in subthalamic nucleus and basal ganglia, in patients with tremor (Levy et al. (2000, 2002)). However, the exact mechanism through which this network reorganization happens, is still unclear.

2

Background: mitochondria, energy and mitochondrial dynamics

"Over the long term, symbiosis is more useful than parasitism. More fun, too. Ask any mitochondria."
Larry Wall, 1997

First discovered in the 1800s, mitochondria are rod-shaped organelles, found in nearly all eukaryotes, including plants, animals, fungi, and protists. They are large enough to be observed with a light microscope, and the name *mitochondria* was coined to reflect the way they looked to the first scientists to observe them, stemming from the Greek words for *thread* and *granule*. For many years after their discovery, mitochondria were commonly believed to transmit hereditary information, until the mid-1950s, when a method for isolating the organelles intact was developed and the modern understanding of mitochondrial function was worked out.

The elaborate structure of a mitochondrion is very important to the functioning of the organelle (see Figure 2.1).
Two specialized membranes encircle each mitochondrion present in a cell, dividing the organelle into a narrow intermembrane space and a much larger internal matrix, each of which contains highly specialized proteins. The inner membrane is highly convoluted so

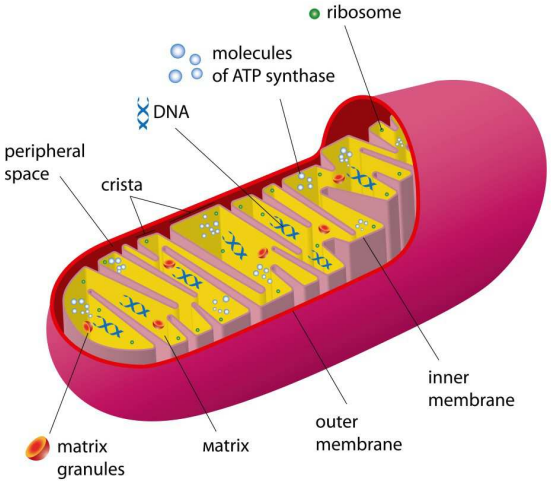

Figure 2.1: Cartoon of a mitochondrion and its parts. (Images from Semedo (2015)).

that a large number of folds called cristae are formed.

Mitochondria are multi-functional organelles of the eukaryotic cell, with a main function consisting in generating ATP through oxidative phosphorylation (OXPHOS) and a broader involvement into other processes like fatty acid oxidation, apoptosis, cell cycle and cell signaling (Tam et al. (2015)). However, mitochondria are also a main cause of cell destruction due to the production of reactive oxygen species (ROS) that can damage DNA and proteins (Disatnik et al. (2015)). Mitochondrial dysfunctions in regulating these concurrent and competing tasks are hence very dangerous for the whole organism and have been associated with aging and a large number of diseases, including cardiovascular, metabolic and neurological pathologies.

One of the main peculiarities of these organelles consists in possessing their own genome, the so-called mitochondrial DNA (mtDNA), which encodes proteins involved in OXPHOS and, as a consequence, in the ATP production. The composition of mtDNA can vary with respect to the different cell type and tissue, and, moreover, in the same cell a condition of heteroplasmy can be observed (Tam et al. (2015)), which corresponds to the coexistence of wild type and mutant mtDNA. It has been noted that age-related deficit in mitochondrial functions is associated with the accumulation of mutant mtDNA within the cells and more generally mutations in mtDNA (e.g. point mutations, rearrangements and deletions) can have drastic consequences in cell life.

Contents

2.1 Mitochondria and mitochondrial dynamics

Mitochondria are organized in a dynamic tubular network that is continuously reshaped by opposite processes of fusion and fission among mitochondria. This dynamics changes the morphology of the organelles and influences their sub-cellular location and function (Guo et al. (2013)). Specifically, mitochondrial fusion is the process by which two mitochondria merge in order to form a unique organelle, whereas fission describes the division of a fused mitochondrion into two organelles. This fusion/fission machinery, referred as *mitochondrial dynamics*, enables the exchange of mitochondrial components among different organelles in the cell, including metabolites, proteins and mtDNA: in this way, protein products of wild type mtDNA can complement missing and defective proteins due to mutant mtDNA (Tam et al. (2015)). Impairment in either fusion or fission can limit mitochondrial motility and energy production as well as increase oxidative stress and, more specifically, the failure of this machinery has been shown to be linked with neurodegenerative and metabolic diseases.

It is widely accepted that mitochondrial dynamics (fusion and fission), together with mitochondrial autophagy (mitophagy, i.e. the mitochondrial degradation) and biogenesis (the formation of new mitochondria) constitute a quality control process, which is able to maintain mitochondrial health by performing a segregation of the dysfunctional mitochondria. This process makes damaged mitochondria unable to fuse and subjected to elimination. Remarkably, mitochondria seem indeed equipped with the ability to regulate and adapt their metabolic capacity and mtDNA through this dynamic behaviour (Hyde et al. (2010)).

In this interplay scenario, understanding the process, through which mitochondria perform a quality control of mtDNA integrity and the preservation of their bioenergetic function, becomes important and of large interest among the scientists. Mitochondrial performance can be measured with respect to their bioenergetic capacity (i.e. ATP production), damage accumulation (ROS production and accumulation of mutant mtDNA) and metabolic fitness (Chauhan et al. (2014)). In addition, mitochondrial health is linked to the measurement of the membrane potential $\Delta\Psi_m$, which has been shown to be linearly related with the ATP production in an unstressed situation (Patel et al. (2013)).

More interestingly from our point of view, the central role of mitochondria in cell life justifies the existence of multiple (and robust) control layers ruled by the cell in order to coordinate the mitochondrial activity between bioenergetic demands and external stimuli. In particular, in (Hyde et al. (2010)) the authors differentiate between *local*

and *global* control, which play at individual mitochondrial level and at whole cell level, respectively. The former can yield to a loss of mitochondrial membrane potential $\Delta\Psi_m$ and stimulate the isolation of the mitochondrial units from the network in order to increase the probability of mitophagy, whereas the latter is related to the cell cycle. In this picture, mitochondrial biogenesis is a key phase of the cell cycle, which increase mitochondrial mass, respiratory capacity and energy production.

2.1.1 Phenomena description and regulation

Given these premises, the rationale behind our work is to design a mathematical model to analyze the full mitochondrial dynamics as a system of different phenomena that jointly yield quality control over the cell health. In general, such an approach can provide a systemic overview of the interplay among the several concurrent relations in order to gain a deeper comprehension of the cell self-regulation loops. In particular, this model can help to analytically study the role of each phenomenon and of a possible feedback link with the ATP demand to support the experiment design phase for more targeted studies.

In order to simplify the dynamics and highlight the regulation loops of interest, the main phenomena and reaction species that are considered in the model are summarized in the schematic picture of Fig. 2.2 and recalled in the following.

Biogenesis. Mitochondrial biogenesis can be defined as the growth and division of pre-existing mitochondria. Its functional purpose is to maintain mitochondrial quality and ensure sufficient ATP production (Nilsson et al. (2015)). Mitochondrial biogenesis is regulated in response to external stimuli and cellular stress through signaling cascades and transcriptional complexes that promote the formation and assembly of mitochondria (Dominy and Puigserver (2013); Tam et al. (2015)). It can be induced by exercise, fasting, thermogenesis, oxidative stress, and inflammatory cell stress (Cherry and Piantadosi (2015)). Furthermore, in order to maintain a correct mitochondrial biogenesis, a coordination of more than a thousand of proteins is needed. Since the majority of these proteins are encoded in the nucleus, there exists a process for targeting, importing and assembling[1] to ensure a correct mitochondrial dynamics (Jornayvaz and Shulman (2010)).

The activity of multiple transcription factors during the mitochondrial biogenic process is coordinately regulated by the transcriptional co-activator PPARγ (namely the peroxisome proliferator-activated receptor γ co-activator 1-α, PGC-1α).

PGC-1α is a co-transcriptional regulation factor, which plays a central role in the

[1]The sorting and assembly machinery (SAM) is a protein complex that operates after the translocase of the outer membrane, to mediate insertion of β-barrel proteins into the outer mitochondrial membrane.

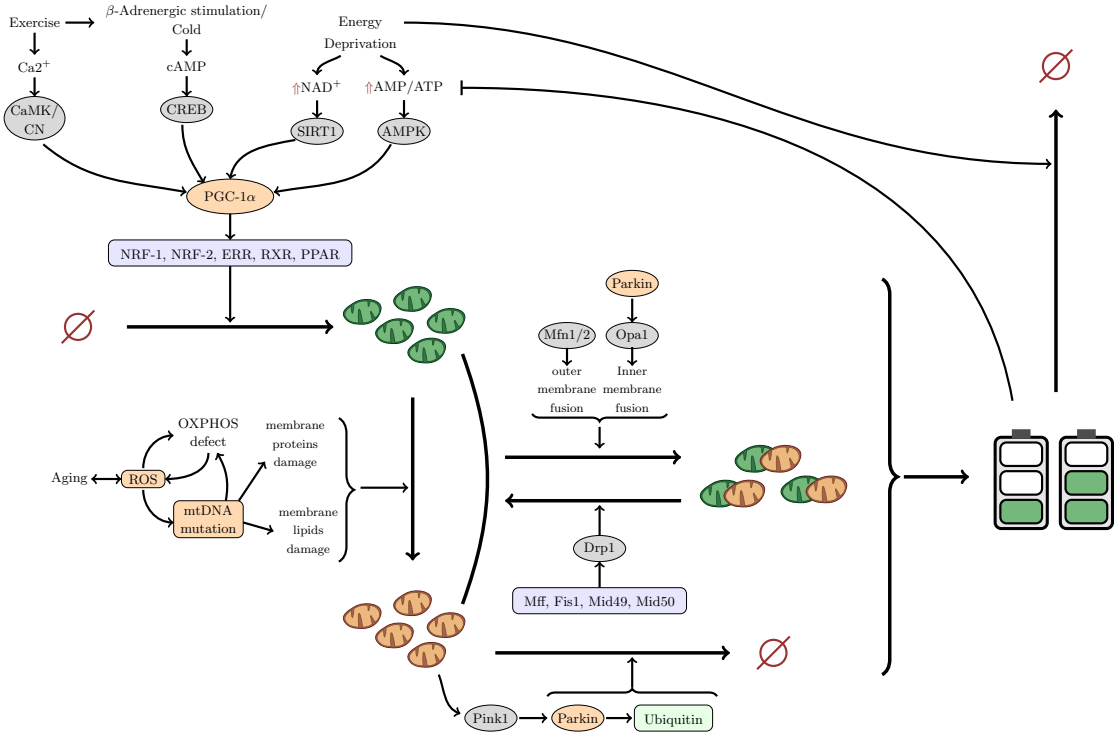

Figure 2.2: Schematic representation of mitochondrial dynamics. Healthy mitochondria are in green, damaged ones are brown and the free ATP level are depicted as batteries. Biogenesis (upper-left corner) is regulated by factor PGC-1α, which activates a set of transcription factors (NRF-1, NRF-2, ERR, RXR, PPAR), and is clearly depending on the ATP level (through energy deprivation and the ratio AMP/ATP). Fusion/fission machinery (center) is controlled by the balance of Pink1 and Parkin through Drp1, Opa1, Mfn1 and 2. Mitophagy (bottom-left corner) is driven by aging through ROS and OXPHOS and directly by mtDNA mutation. Damaged, healthy and fused mitochondria (obtained from fusion of damaged and healthy) contribute to the generation of energy.

regulation of mitochondrial biogenesis and is itself regulated by other factors, as AMPK and p38 MAPK. In particular, PGC-1α induces mitochondrial biogenesis by activating transcription factors, as NRF-1 and NRF-2, which promote and regulate the expression of TFAM and TFBs (Dominy and Puigserver (2013); Jornayvaz and Shulman (2010)), PPARs and ERRs α and γ. The two orphan nuclear receptors ERR α and γ target a common set of promoters involved in the uptake of energy substrates, production, and transport of ATP across the mitochondrial membranes (Ventura-Clapier et al. (2008)). With a structure and a function similar to those of PGC-1α, PGC-1β induces mitochondrial biogenesis and increases basal oxygen consumption (Jornayvaz and Shulman (2010)). The main signaling modules that control mitochondrial biogenesis are AMP-Activated Protein Kinase (AMPK), calcium signaling, cAMP pathway and mTOR pathway. Since we are particularly interested in the relationship between ATP and mitochondrial dynamics, we

focus on AMPK. In particular, AMPK regulates biogenesis by controlling intracellular energy metabolism in response to acute energy need. It is activated by the augmented ratio AMP/ATP led by β-GPA. Essential to this process there are the AMPK-mediated activation of PGC-1α and SIRT1. AMPK can directly phosphorylate and activate PGC-1α (Jäger et al. (2007)). On the other side, through NAMPT-dependent and -independent mechanisms, AMPK is also able to increase NAD^+ levels, which promotes SIRT1 activity and the activation of PGC-1α. Hence, AMPK, SIRT1 and PGC-1α together play a fundamental role in response of situations of caloric restriction and exercise (Dominy and Puigserver (2013)). It has been shown that a decrease in the AMPK activity appears during aging and can be related to mitochondrial dysfunction and impairment of intracellular lipid metabolism (Jornayvaz and Shulman (2010)).

Since most of the signaling involved in the regulation of biogenesis is very hard to be measured (when it can be measured at all), the biogenesis regulation loop is here modeled through an Hill function, a mathematical tool often used to describe several reactions steps by means of only one contribution term. Given our purpose of studying the relation between the mitochondrial dynamics and the energetic level, we assume that an Hill function depending on the free ATP level can be used to describe this biogenesis feedback regulation.

Mitophagy. Mitophagy refers to the degradation of mitochondria through lysosomes. It can be both random and selective, since it is related to two different cell states. In the first case, mitophagy takes part to whole cell autophagy, while in the second case, it selectively degrades only defective mitochondria. In particular, we are interested in the latter, since it enables a sort of quality control of the health level of the cell: through this process, damaged organelles are hence isolated and subsequently catabolized via lysosomal degradation.

One of the most analyzed mitophagy pathway involves two genes, Pink1 and Parkin. Specifically, Pink1 is a mitochondrial localized kinase, imported and degraded with the mitochondria. The accumulation of Pink1 phosphorylates several proteins to recruit and activate Parkin Okatsu et al. (2015). Then, Parkin targets the autophagic membrane and enables mitophagy. Since Parkin is selectively enriched on dysfunctional mitochondria, healthy organelles are less subjected to degradation.

Interestingly, the energetic state of the cell regulates also this phenomenon: namely, mitophagy increases during oxidative conditions, which promote ATP production. Although it can seem in contrast with the idea that ATP is produced by healthy mitochondria, it is worth to be noticed that enhanced respiratory chain activity may lead to an increased production of reactive oxygen species with detrimental effects on mitochondrial func-

tions. On the other side, in situations of energy demand, mitophagy promotes energetic efficiency through the degradation of dysfunctional organelles (Mishra and Chan (2016)).

It has been reported that mutations of Pink1 and Parkin are linked to Parkinson's disease (Jones (2010)) and a dysfunction of mitophagy has been related to Huntington's disease and other neurodegenerative diseases (Hwang et al. (2015)), although the mechanism is not well known yet.

Fusion-fission. Fusion and fission represents the two main processes of mitochondrial dynamics, and refers to the ability of these organelles to merge each other, and to split up. The opposite phenomena of fusion and fission help mitochondria to regulate the cellular ATP production and minimize the accumulation of mutant mtDNA during aging (Chauhan et al. (2014)).

As a matter of fact, the fusion process involves mitochondria with high mitochondrial membrane potential $\Delta\Psi_m$, which is related to healthy organelles, and it has been observed that approximately 30% of fusion events are followed by fission leading to a statistically significant difference in the $\Delta\Psi_m$ of the two daughter organelles. This asymmetry influences the relative capacity for ATP and reactive oxygen species (ROS) production of the two daughters, playing a main role in quality maintenance, although it is currently not well understood. Nonetheless, this fact suggests that mtDNA occurrences, which provoke bioenergetic dysfunction and loss of $\Delta\Psi_m$, would be selectively excluded from the mitochondrial network by fission and subjected to mitophagy (Hyde et al. (2010); Patel et al. (2013)).

Since mitochondria are supplied with two different membranes (outer and inner), two fusion steps are needed, mediated by three large GTPases of the dynamin superfamily: Mitofusin 1 and 2 (Mfn1 and Mfn2) and Optic Antrophy (Opa1) (Qi et al. (2013); Chauhan et al. (2014)). Specifically, Mfn1 and Mfn2 are responsible of the outer membrane fusion, whereas Opa1 allows the fusion of the inner membrane.

Fusion rate is not constant over the whole organism, yet it is cell type and tissue dependent. Similarly, this phenomenon seems to assume different levels of importance in different tissue: for example, since it influences the OXPHOS activity, through the regulation of mtDNA levels, mitochondrial fusion becomes particularly relevant in cerebellar mitochondria. Moreover, it has been shown that the morphology of the mitochondria within the cells induces different energetic states of the cells: elongated mitochondria increase ATP production, and, on the other way, conditions that increase mitochondrial ATP function enhance fusion (Mishra and Chan (2016)).

Conversely, a decrease in fusion rate causes mitochondrial fragmentation and reduces content exchange between mitochondria, which seems to be related to mitochondrial

dysfunctions. This situation of impaired fusion can be linked to issues of the membrane potential, namely, when the membrane potential dissipates, the long isoform of Opa1 is completely cleaved and inactivated by the activation of Oma1, led by several sources of cellular stress.

In the case of a mtDNA-related disease, cells defect in OXPHOS and this can cause defects in the inner membrane fusion. Then, dysfunctional mitochondria remain isolated mitochondria and are more likely subjected to mitophagy. In this way, cells implement a quality control strategy preventing the spread of mtDNA mutations to wild-type mitochondria.

In literature, other hypotheses on the regulation of fusion have been proposed: some studies showed that oxidative stress can enhance fusion (Shutt et al. (2012)), whereas other researchers linked MAPK pathway with Mfn1 (Pyakurel et al. (2015)). Moreover, other authors have suggested that fusion is controlled by local concentration of GTP (Boissan et al. (2014)).

On the other hand, mitochondrial fission is regulated by dynamin-related protein 1 (Drp1), a large GTPase obtained by the mitochondrial outer membrane through several receptor proteins (Mff, Fis1, Mid49, Mid50) (Mishra and Chan (2016)).

Drp1 regulation is a complex mechanism, which includes, among others, phosphorylation, that can both enhance and inhibit Drp1, depending on the site. Inhibition of Drp1 causes mitochondrial tubulation and, as a consequence, promotes ATP production and limits mitochondrial degradation. On the other side, inhibition of mitochondrial OXPHOS enhances fission phenomena.

Therefore, fission regulation can also happen at the level of the Drp1 receptor proteins. In particular, it has been observed that a loss of mitochondrial fission factor (Mff) results in a dramatic mitochondrial elongation (Losón et al. (2013)). The connection between energy deficiency and fission increase is due to the fact that Mff is a phosporylation substrate for AMP kinase, which in turn activates Mff and fission (Toyama et al. (2016)).

As a final remark, we report that the fission phenomenon is related not only to the organelles morphology, but also to mitochondrial transport, mitophagy and apoptosis. Most interestingly, several diseases, particularly neurodegenerative and cardiovascular ones, have been associated with a loss of mitochondrial fusion-fission balance.

Damage/aging. Under the term *damage* we gather several phenomena that can affect mitochondria health and, in particular, we focus on those that can be related to aging.

Aging has been widely correlated with the accumulation of ROS, which promotes an increase of mutations in mtDNA. In addition, dysfunctional mtDNA can induce

more oxidative stress, damaging mitochondrial membrane proteins and lipids, and hence compromising the ATP production capacity of mitochondria (Chauhan et al. (2014)).

Mutations in mtDNA can cause defects in the OXPHOS process. In a single cell both wild-type and mutant mtDNA can coexist and define a condition of heteroplasmy. Moreover, the mtDNA composition can vary with respect to different tissues. Mutant mtDNA molecules have been shown to accumulate with age in a variety of tissues and organisms, thus reinforcing the hypothesis that mutant mtDNA possibly contribute to the general age-related decline in mitochondrial function observed in almost all tissues (Chinnery et al. (2002)).

For what concerns ROS, it could be increased by the inhibition of the respiratory chain, which leads to a reduction of its electron-carrying components and a consequent increase in ROS production. Moreover, inhibition of ATP synthesis can also lead to a reduction of respiratory carriers and an increase in mitochondrial membrane potential, which also promotes radicals production.

3

Mitochondrial dynamics and energy: a mathematical model

"All models are wrong, but some are useful"
George E.P. Box

In this chapter we propose a prey-predator non-linear mathematical model to describe the dynamic relations between a population of healthy, damaged and fused mitochondria and the available ATP within a cell. We assume that the sub-population of fused mitochondria is composed by the organelles generated by the fusion between healthy and damaged mitochondria (a couple of damaged mitochondria cannot fuse together, while the product of the fusion of two healthy organelles remains in the healthy population). In particular, our objective is to design a model and to define an analysis procedure aimed to capture the essence of the population processes (easily associated to the observed phenomena), and to highlight the principal regulation loops that play a role into mitochondrial dynamics.

In this regard, we take into account the cell demand in response to some energetic stress and the ATP production by healthy, damaged and fused mitochondria.

In particular, we conjecture and model a feedback loop driven by ATP to regulate the mitochondrial biogenesis: loosely speaking, a decrease of the free ATP level implies

an increase in biogenesis, in order to enlarge the mitochondrial mass and make the cell able to respond to possible energy demands by the cell. Throughout the chapter, we will use the expression *free ATP level* to indicate the quantity of available ATP in the cell (measured in moles).

Although the effects of the dynamics on the free ATP level are the result of a complex reaction chain, we believe that modeling the ATP as the explicit output of the mitochondrial population system allows a significant insight into the energy production process for regulatory purposes.

To validate the relevance of this feedback loop, we employ tools from system theory to analyze both a model with fixed biogenesis rate, where the feedback is not present, and a more complex model where this link is enabled.

Both these models represent the interplay between biogenesis and mitophagy through damage/aging and the dynamic machinery of fusion and fission as two different processes. Also, the fluxes from healthy to damaged population due to damage-related phenomena (which incorporates both mutants mtDNA and ROS production) are quantitatively described through ODEs, together with the different ability in producing energy by healthy, damaged and fused classes. The ATP consumption by the cell is considered as a function of an external input u, which can be considered fixed or variable during time.

Each of these phenomena is described through a specific rate constant: we implement a sensitivity analysis of the populations' size and the available ATP level with respect to each parameter, in order to understand the particular role of each process into the complex mitochondrial quality control.

These models are here formalized and analyzed through system theoretical tools to prove that they are well-posed and to infer the parameters' condition that guarantees the system stability. In particular, our approach highlights that the presence of a feedback allows to regulate the mitochondrial dynamics even in presence of unexpected events or exogenous disturbances related to the energy demand by the cell. By means of stochastic and sensitivity analyses, we tested the capability of the model to account for different observed behaviors.

In this context, as a scenario example, it will be discussed how the phenomena of biogenesis, fission/fusion and mitophagy interact in a situation of increased damage affecting the nominal free ATP level produced by the mitochondria, in order to compensate for the damage and support the energy demand. As often appears in natural phenomena, this can be regarded as a robustness property of the system to improve the survival possibility. Conversely, from a translational medicine perspective, this may suggest the possible target of a specific control action in order to compensate for a situation of damage.

Contents

Notation

For sake of clarity and in order to avoid ambiguities, we now report the symbols used in this chapter. The parameters of the models are reported in Table 3.1.

x_{h} [mol]: state variable (quantity of healthy mitochondrial population)
x_{d} [mol]: state variable (quantity of damaged mitochondrial population)
x_{f} [mol]: state variable (quantity of fused mitochondrial population)
x_{ATP} [mol]: state variable (quantity of free available ATP)
$\mathbf{x} = [\ x_{\mathrm{h}} \quad x_{\mathrm{d}} \quad x_{\mathrm{f}} \quad x_{\mathrm{ATP}}\ ]^{\mathsf{T}}$: state vector variable
$\bar{\mathbf{x}} = [\ \bar{x}_{\mathrm{h}} \quad \bar{x}_{\mathrm{d}} \quad \bar{x}_{\mathrm{f}} \quad \bar{x}_{\mathrm{ATP}}\ ]^{\mathsf{T}}$: equilibrium state vector
$\bar{u}$ [s^{-1}]: steady state value for ATP consumption rate
$\sigma(\mathbf{F})$: set of the eigenvalues of matrix $\mathbf{F}$
λ: eigenvalue variable (λ_1, λ_2, λ_3: eigenvalues with the larger real part)
$\mathbf{\Pi_F}(\lambda)$: characteristic polynomial of matrix $\mathbf{F}$
A, B, C, D, E, F: constant values
r, ℓ: constant ratios among model parameters
$\mathscr{C}^{(1)}_{\mathrm{pos}}$, $\mathscr{C}^{(2)}_{\mathrm{pos}}$, $\mathscr{C}_{\psi_{12}}$: systems of conditions
x_*-n.c.: nullcline of state variable x_* ($* \in \{\mathrm{h}, \mathrm{d}, \mathrm{f}, \mathrm{ATP}\}$)
$\mathrm{den}(\bar{x}_{\mathrm{d}})$: denominator of x_{d}-n.c as a function of $\bar{x}_{\mathrm{d}}$
$\bar{x}_{\mathrm{ATP,u}}$: new steady state of x_{ATP}, when the input $u \neq \bar{u}$
$\Delta\bar{x}_{\mathrm{ATP}}$ and $\Delta\bar{u}$: variation of $\bar{x}_{\mathrm{ATP}}$ and u w.r.t. the nominal steady state
$W(s)$: transfer function (ω_0: natural frequency; ξ: damping coefficient)
T_r: rise time of the 2-nd order system
$T_{s,2\%}$: settling time (2%) of the 2-nd order system

3.1 The model

The approach proposed in this work consists in describing mitochondrial dynamics through a *prey-predator* model, where the roles of preys and predators are played by healthy mitochondria (x_{h}) and damaged mitochondria (x_{d}), respectively. These two classes are also allowed to fuse themselves and give raise to the healthy-damaged fused mitochondria (x_{f})[1]. Moreover, the model includes the dynamics of the free ATP within the cell, as produced by the whole mitochondrial population and consumed in response to some energetic stress.

With reference to the schematic of Fig. 3.1 we consider the main phenomena of interest as related to a specific dynamic rate.

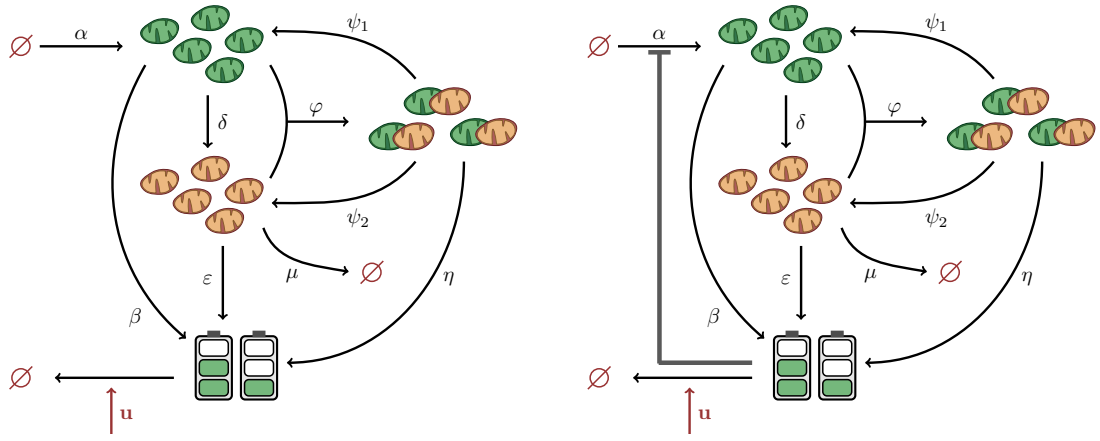

(a) without feedback (b) with feedback

Figure 3.1: Model of the mitochondrial dynamics of Fig. 2.2. The energetic stress input u is represented by the red arrow, while all the other phenomena are indicated by the black arrows. The characteristic rate parameters are indicated (α: biogenesis; δ: damage; μ: mitophagy; φ: fusion among healthy and damaged mitochondria; ψ_1: fission to healthy organelles; ψ_2: fission to damaged mitochondria; β, η, ε: ATP prodution by healthy, fused, and damaged mitochondria, respectively). Models **(a)** and **(b)** differ for the feedback loop from free ATP level to biogenesis (dark gray bold arrow).

Biogenesis (α [s^{-1}]) We consider that the biogenesis flux depends on rate α [s^{-1}]. At first, this parameter is chosen not to change in response to variation in the level of free ATP concentration (Fig. 3.1(a)): $\alpha = \alpha_0$. However, as motivated by the description in Sec. 2.1.1, we propose also a model in which the rate of the biogenesis flux is depending on the free ATP level (Fig. 3.1(b)): since we are interested in the

[1] We recall that we consider the fusion between healthy mitochondria as nourishing the healthy class, while damaged mitochondria cannot fuse within the damaged class.

activation of PGC-1α through AMPK (see Chapter 2 for details), we design the biogenesis rate as the sum of a constant rate α_0 and an Hill function of the ATP level (x_{ATP}), characterized by a constant value α, a constant k and a coefficient h: $\alpha = \alpha_0 + \alpha_1 / \left(k + x_{\text{ATP}}^h\right)$. In this way we introduce a feedback loop ATP-dependent, which itself includes several reaction steps.

The choice of using a non-constant biogenesis rate is common in literature, where different strategies can be found. Namely, whereas in Figge et al. (2012) it is described as a function of the mitophagy effect, in Patel et al. (2013) the biogenesis rate is characterized by a sigmoidal function with respect to the difference between the actual number of mitochondria and the nominal one. As a consequence, the formation of new mitochondria is subjected to a feedback control to avoid instability. The authors of Dalmasso et al. (2017) proposed to design mitochondrial biogenesis as an ATP-dependent function, as we do; nevertheless, we use a different model and an ATP-biogenesis link that can be analytically studied.

Mitophagy (μ [s^{-1}]) As suggested by Hoitzing et al. (2015) and Patel et al. (2013), we design the mitophagy rate, due to Pink1 and Parkin activation, through a constant rate. In order to include the selective enrichment of Parkin in dysfunctional isolated mitochondria, we assume that mitophagy can affect only unfused damaged organelles, whereas the other classes cannot be degraded.

Fusion (φ [$\text{mol}^{-1}\,\text{s}^{-1}$]) Because mitochondria spend the majority of their life cycle as solitary organelles Hyde et al. (2010), in our model fusion between healthy mitochondria is not described. On the other hand, the mechanism through which healthy and damaged mitochondria mix up and redistribute their health among the daughter-organelles is still not so clear and hence of research interest. Hence, fusion between healthy and damaged mitochondria together is represented explicitly in the model through a constant rate, following the idea proposed in Hoitzing et al. (2015) and Dalmasso et al. (2017).

Fission (ψ_1 [s^{-1}], ψ_2 [s^{-1}]) A fraction of fusion events is shown to be followed by statistically significant difference in the health level of the two daughters. This fact is due to the fission redistribution of the health quality within the cell, by the isolation of the damaged part: two different rate values ψ_1 and ψ_2 are used to describe the flux from fused to healthy mitochondria and from fused to damaged ones, respectively. This choice allows us to test the model behavior for different rates ratio.

Damage (δ [s^{-1}]) The possible mitochondrial damages caused by mutant mtDNA, ROS

production or aging are all included into the same process of damage.
Since we gather different sources of damage with the same rate, as a first approximation we assume that δ is constant as in Patel et al. (2013) and Dalmasso et al. (2017).

Energy: The energetic state of the cell is dependent on mitochondria morphologies Mishra and Chan (2016), therefore the ATP turnover is modelled as the sum of the ATP production by healthy (β [s^{-1}]), damaged (ε [s^{-1}]), and fused (η [s^{-1}]) mitochondria. Also, the bioenergetic demand from the cell is given as the input (u), which causes a decrease of the free ATP level.

The overall system dynamics follows as a set of non-linear ordinary differential equations (ODEs) referring to the size of healthy x_h, damaged x_d and fused x_f mitochondrial subpopulations, and the quantity of free energy (in form of ATP) x_ATP, which are summarized into the state vector $\mathbf{x} := [\ x_\mathrm{h} \quad x_\mathrm{d} \quad x_\mathrm{f} \quad x_\mathrm{ATP}\ ]^\mathsf{T}$:

$$\dot{x}_\mathrm{h} = \alpha x_\mathrm{h} + \psi_1 x_\mathrm{f} - \delta x_\mathrm{h} - \varphi x_\mathrm{h} x_\mathrm{d} \tag{3.1a}$$

$$\dot{x}_\mathrm{d} = \delta x_\mathrm{h} + \psi_2 x_\mathrm{f} - \varphi x_\mathrm{h} x_\mathrm{d} - \mu x_\mathrm{d} \tag{3.1b}$$

$$\dot{x}_\mathrm{f} = \varphi x_\mathrm{h} x_\mathrm{d} - (\psi_1 + \psi_2)\, x_\mathrm{f} \tag{3.1c}$$

$$\dot{x}_\mathrm{ATP} = \beta x_\mathrm{h} + \varepsilon x_\mathrm{d} + \eta x_\mathrm{f} - u \cdot x_\mathrm{ATP} \tag{3.1d}$$

where

$$\alpha = \alpha_0 \tag{3.2a}$$

in case of no energetic feedback (model (3.1)-(3.2a) as in Fig. 3.1(a)), and

$$\alpha = \alpha_0 + \frac{\alpha_1}{k + x_\mathrm{ATP}} \tag{3.2b}$$

in the case with energetic feedback (model (3.1)-(3.2b), Fig. 3.1(b)). A list of the nominal parameters' meaning and value is given in Table 3.1.

3.1.1 Equilibrium analysis without the ATP feedback loop

One of the main characteristics of a dynamical system is the description of its behavior around the equilibrium points (if any), defined as the steady state $\bar{\mathbf{x}} := [\ \bar{x}_\mathrm{h} \quad \bar{x}_\mathrm{d} \quad \bar{x}_\mathrm{f} \quad \bar{x}_\mathrm{ATP}\ ]^\mathsf{T}$ and constant input $\bar{u}$, such that $\dot{\mathbf{x}}\big|_{(\mathbf{x}=\bar{\mathbf{x}},\, u=\bar{u})} = \mathbb{0}_4$.

Specifically, model (3.1)-(3.2a) is characterized by two equilibria: the first (trivial equilibrium) with all species' dimensions equal to zero ($\bar{\mathbf{x}} = \mathbb{0}_4$) and any value for the

Parameters and description	Values (Tested Range)	Biological evidence and literature
δ [s^{-1}] damage rate	9.5×10^{-2} ($[0.05 - 0.2]$)	Variable w.r.t. internal/external factors
α_0 [s^{-1}] biogenesis rate	5.77×10^{-4} or 0	Optimized value in Dalmasso et al. (2017)
α_1 [mol s^{-1}] biogenesis rate	1×10^{-9} ($[0.01 - 2] \times 10^{-9}$)	Regulated by cellular stress (Boland et al. (2013))
k [mol] Hill constant of biogenesis rate	1×10^{-9}	
h Hill coefficient of biogenesis rate	1	
μ [s^{-1}] mitophagy rate	2×10^{-1} ($[0.01 - 0.5]$)	Optimized value in Dalmasso et al. (2017)
φ [$mol^{-1}\, s^{-1}$] fusion rate	8.3×10^{-2} ($[0.01 - 0.2]$)	Time scale of minutes (Twig et al. (2008))
ψ_1 [s^{-1}] fission rate (to healthy)	4.17×10^{-2} ($[0.001 - 0.1]$)	Time scale of minutes (Twig et al. (2008))
ψ_2 [s^{-1}] fission rate (to damaged)	4.17×10^{-2} ($[0.001 - 0.1]$)	Time scale of minutes (Twig et al. (2008))
β [s^{-1}] ATP production rate (by healthy)	0.1	
ε [s^{-1}] ATP production rate (by damaged)	0.01	
η [s^{-1}] ATP production rate (by fused)	0.5	
u [s^{-1}] ATP consumption rate	0.1 ($[0.001 - 0.25]$)	

Table 3.1: Description of the nominal parameters of the model (3.1) and (3.2).

input u, represents a situation where all population species disappear and it is of no interest for the study. The latter, instead, is not null and is given by a more complex expression:

$$\bar{x}_{\mathrm{h}} = \frac{\mu\,(\psi_1 + \psi_2)\,(\alpha_0 - \delta)}{\varphi\,[(\delta - \alpha_0)\,\psi_1 + \delta\psi_2]}, \qquad \bar{x}_{\mathrm{d}} = \frac{(\psi_1 + \psi_2)\,(\alpha_0 - \delta)}{\varphi\psi_2} \tag{3.3a}$$

$$\bar{x}_{\mathrm{f}} = \frac{\varphi}{\psi_1 + \psi_2}\bar{x}_{\mathrm{h}}\bar{x}_{\mathrm{d}}, \qquad \bar{x}_{\mathrm{ATP}} = \frac{\beta\bar{x}_{\mathrm{h}} + \varepsilon\bar{x}_{\mathrm{d}} + \eta\bar{x}_{\mathrm{f}}}{\bar{u}}. \tag{3.3b}$$

Beyond the specific value of the equilibrium point (3.3), its equations impose $\alpha_0 > \delta$ (yielding a biogenesis rate larger than the damage rate) and $\psi_2 > \frac{\alpha_0 - \delta}{\delta}\psi_1$ in order to keep the quantities positive.

Stability analysis of the equilibrium points. The stability of both equilibria of model (3.1)-(3.2a) can be studied through system linearization, which leads to the state matrices $\mathbf{F}_{(\bar{x},\bar{u})}$ and $\mathbf{G}_{(\bar{\mathbf{x}},\bar{u})}$:

$$\dot{\mathbf{x}-\bar{\mathbf{x}}} = \mathbf{F}_{(\bar{\mathbf{x}},\bar{u})}\,(\mathbf{x}-\bar{\mathbf{x}}) + \mathbf{G}_{(\bar{\mathbf{x}},\bar{u})}\,(u-\bar{u})\,, \tag{3.4}$$

with

$$\mathbf{F}_{(\bar{\mathbf{x}},\bar{u})} := \left[\begin{array}{ccc|c} \alpha_0-\delta-\varphi\bar{x}_{\mathrm{d}} & -\varphi\bar{x}_{\mathrm{h}} & \psi_1 & 0 \\ \delta-\varphi\bar{x}_{\mathrm{d}} & -\varphi\bar{x}_{\mathrm{h}}-\mu & \psi_2 & 0 \\ \varphi\bar{x}_{\mathrm{d}} & \varphi\bar{x}_{\mathrm{h}} & -(\psi_1+\psi_2) & 0 \\ \hline \beta & \varepsilon & \eta & -\bar{u} \end{array}\right] = \left[\begin{array}{c|c} \tilde{\mathbf{F}}_{(\bar{\mathbf{x}},\bar{u})} & \mathbb{0}_3 \\ \hline \star & -\bar{u} \end{array}\right],$$

$$\mathbf{G}_{(\bar{\mathbf{x}},\bar{u})} := \left[\begin{array}{c} 0 \\ 0 \\ 0 \\ \bar{x}_{\mathrm{ATP}} \end{array}\right].$$

Thanks to the lower-triangular structure of $\mathbf{F}_{(\bar{\mathbf{x}},\bar{u})}$, we can assert that the set of the eigenvalues of the matrix is defined as $\sigma(\mathbf{F}_{(\bar{\mathbf{x}},\bar{\mathbf{u}})}) = \{\sigma(\tilde{\mathbf{F}}_{(\bar{\mathbf{x}},\bar{\mathbf{u}})}),\ -\bar{u}\}$, and we can hence focus our analysis on $\sigma(\tilde{\mathbf{F}}_{(\bar{\mathbf{x}},\bar{\mathbf{u}})})$.
At first, we study the stability of the null equilibrium $\bar{x} = \mathbb{0}_4$. In this case, we have

$$\tilde{\mathbf{F}}_{(\mathbb{0}_4,\bar{u})} := \left[\begin{array}{cc|c} \alpha_0-\delta & 0 & \psi_1 \\ \delta & -\mu & \psi_2 \\ \hline 0 & 0 & -(\psi_1+\psi_2) \end{array}\right],$$

whose spectrum is $\sigma(\tilde{\mathbf{F}}_{(\mathbb{0}_4,\bar{u})}) = \{\alpha_0-\delta,\ -\mu,\ -(\psi_1+\psi_2)\}$. Hence, the stability of the zero steady state depends on the sign of $\alpha_0-\delta$.
For the nonzero equilibrium (3.3), the analytical expression of the eigenvalues of matrix $\tilde{\mathbf{F}}_{(\bar{x},\bar{u})}$ cannot be derived. However the stability of $\bar{x}$ can be analyzed by considering the sign of the characteristic polynomial's coefficients. Specifically we have:

$$\begin{aligned}\mathbf{\Pi}_{\tilde{\mathbf{F}}}(\lambda) = \lambda^3 + \lambda^2\left[\frac{\psi_1 B}{\psi_2} + \frac{\mu\alpha_0\psi_2}{A} + C\right] + \\ + \lambda\left[\frac{\mu}{A\psi_2}\left(-BC\psi_2^2 + \alpha_0\psi_1\psi_2 B + \delta\psi_2 BC - B^2C^2 + \alpha_0\psi_2^2 C\right)\right] + \mu BC,\end{aligned}$$

where $\mathbf{\Pi}_{\tilde{\mathbf{F}}}(\lambda) := \det(\lambda \mathbb{I}_3 - \tilde{\mathbf{F}}_{(\bar{x},\bar{u})})$, and we have defined

$$\begin{aligned} A &:= \delta(\psi_1 + \psi_2) - \alpha_0\psi_1 = \delta C - \alpha_0\psi_1 > 0, \\ B &:= \alpha_0 - \delta > 0, \\ C &:= \psi_1 + \psi_2 > 0, \end{aligned}$$

under the conditions due to the positiveness of species' size

$$\mathscr{C}^{(1)}_{\text{pos}} := \begin{cases} \alpha_0 > \delta \\ \psi_2 > \frac{\alpha_0 - \delta}{\delta}\psi_1 \end{cases} . \tag{3.5}$$

Since the coefficients of λ^3 and λ^2 and the constant term are all positive, according to Routh's Stability Criterion (Routh (1877)), the stability depends on the sign of the coefficient of the linear term λ. Specifically, we have that near the equilibrium point $(\bar{\mathbf{x}}, \bar{u})$, the non-linear system (3.3) is asymptotically stable if also that coefficient is positive, and it is unstable otherwise. Obviously, the sign depends on the choice of the parameters set and, specifically, it is positive if and only if the rate of fission to healthy mitochondria ψ_1 obeys the following equation:

$$\psi_1 > \frac{\delta(r-1)\left[r\left(\ell^2 - k + 1\right) + 2\ell^2 + 3\ell + 1\right]}{\ell^2(\ell+1)}, \tag{3.6}$$

where the two quantities $\ell > 0$ and $r > 1$ are such that

$$\psi_2 = \ell \cdot \psi_1, \qquad \text{and} \qquad \alpha_0 = r \cdot \delta.$$

By recalling condition (3.5), it has to be $k > \frac{\alpha_0 - \delta}{\delta}$. The value of the coefficient k can be tuned in order to favor either the healthy or the damaged mitochondria after fission. Specifically, the relationship $\psi_1 > \psi_2$ is achieved if and only if the following condition holds:

$$\mathscr{C}_{\psi_{12}} := \begin{cases} k \in \left]\frac{\alpha_0 - \delta}{\delta},\ 1\right[\\ 0 < \frac{\alpha_0 - \delta}{\delta} < 1 \ \Leftrightarrow\ 0 < \delta < \alpha_0 < 2\delta \end{cases}$$

To summarize, from the stability analysis of the equilibria, it follows that the null steady state is asymptotically stable if $\alpha_0 < \delta$, which means that the rate of new births caused by biogenesis is less than the rate of damage, with the consequent activation of mitophagy. Conversely, with respect to the more interesting non-null equilibrium, an opposite

condition $\alpha_0 > \delta$ is stated to ensure variables' positivity. This condition implies a continuous growth of the healthy population x_{h}. This growth drives the system to divergence if a balance condition (3.6) between fission to healthy and fission to damaged does not hold.
Indeed, in the specialized literature, some authors proposed to constrain the parameters of biogenesis and mitophagy through a relation such that the total number of mitochondria within the cell does not vary (Hoitzing et al. (2015)). With the similar aim of bounding the increase of population, in Patel et al. (2013) biogenesis is regulated by a feedback with respect to the total number of mitochondria, in such a manner that the larger the difference between the actual number and the nominal number becomes, the more the biogenesis parameter decreases.

However, the main drawback of this description is related to the incapability of the system to respond to a possible increase/decrease of the energy demand (input u), which reflects the level of stress of the cell and a consequent energy consumption. In fact, from the equilibrium expression (3.3), it can be noticed that the mitochondrial numerousness does not depend on the input at the equilibrium $\bar{u}$, while, instead, the free ATP level dynamics does:

$$\frac{\partial \bar{x}_{\mathrm{h}}}{\partial \bar{u}} = \frac{\partial \bar{x}_{\mathrm{d}}}{\partial \bar{u}} = \frac{\partial \bar{x}_{\mathrm{f}}}{\partial \bar{u}} = 0, \qquad \frac{\partial \bar{x}_{\mathrm{ATP}}}{\partial \bar{u}} = -\frac{\beta \bar{x}_{\mathrm{h}} + \varepsilon \bar{x}_{\mathrm{d}} + \eta \bar{x}_{\mathrm{f}}}{\bar{u}^2} < 0.$$

Specifically, an increased energy stress level at the equilibrium from $\bar{u}$ causes a decrease in the level of the free ATP of a factor $1/\bar{u}^2$: the system is not able to react to such variation, and the free ATP level rapidly goes to zero, leading the cell to termination. See Figure 3.2, where we consider

$$\Delta \bar{x}_{\mathrm{ATP}} := \bar{x}_{\mathrm{ATP},u} - \bar{x}_{\mathrm{ATP}}, \tag{3.7a}$$

$$\Delta \bar{u} := u - \bar{u}, \tag{3.7b}$$

where $\bar{x}_{\mathrm{ATP},u}$ is the new steady state value of free ATP when the input has a fixed value u different from $\bar{u}$.

However, biological evidence differs significantly from this description, since both biogenesis and mitophagy are regulated by the metabolic sensor AMP-activated protein kinase AMPK, which is in turn activated in response to biological stress (decreased ATP production) (Mihaylova and Shaw (2011)). Therefore, this link needs to be accounted for in the dynamical model by including a direct loop between the biogenesis rate and the level of free ATP within the cell. Furthermore, we choose not to add such dependence on the mitophagy process, since this latter phenomenon is implicitly considered by the

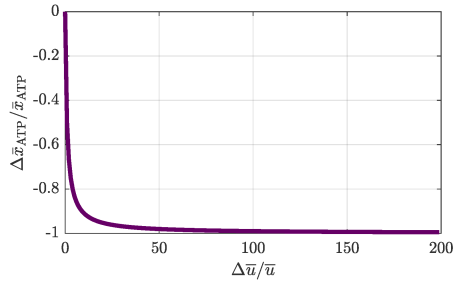

Figure 3.2: Sensitivity of the free ATP level at the equilibrium with respect to a variation in the input value u, which is considered fixed at its equilibrium state. Specifically, it is shown the relative variation of the free ATP as a function of the relative variation of the biological stress, at steady-state. Refer to equation (3.7) for the definition od $\Delta\bar{x}_{\mathrm{ATP}}$ and $\Delta\bar{u}$.

indirect link with the amount of healthy mitochondria.

3.1.2 Equilibrium analysis with ATP feedback loop

We consider here model (3.1)-(3.2b), where the biogenesis rate is composed by both a constant part α_0 and a variable part that depends on the level of the free ATP within the cell through an Hill function. With respect to the ATP role, α_0 is related to the steady-state biogenesis and it is here neglected to highlight the energy-dependent dynamics. Moreover, for sake of simplicity, it is assumed $h = 1$, so that the healthy equation (3.1a) becomes

$$\dot{x}_{\mathrm{h}} = \frac{\alpha_1}{k + x_{\mathrm{ATP}}} x_{\mathrm{h}} + \psi_1 x_{\mathrm{f}} - \delta x_{\mathrm{h}} - \varphi x_{\mathrm{h}} x_{\mathrm{d}}. \tag{3.8}$$

Fig. 3.3 shows a simulation of this model with a set of nominal parameters. This example highlights one main advantage of this representation: the initial condition is a non-zero equilibrium point with a nominal value for the input u. At time $t = 50\,\mathrm{s}$, the input changes and the system reacts in response to an augmented energy stress. Differently from the model with a fixed biogenesis rate, in this case the size of mitochondrial populations varies and reaches another equilibrium point in order to restore a level of free ATP similar to that of the nominal conditions.

Because of the non-linearity of the model, the exact computation of the non-trivial (interesting) equilibria becomes complicated. Nevertheless, through the nullclines[2] (n.c.) analysis, we can characterize the shape of the equilibria and the behavior of the system when it acts closed to them.

From Equations (3.1c) and (3.1d), we obtain the expression for $\bar{x}_{\mathrm{f}}$ and $\bar{x}_{\mathrm{ATP}}$ as follows:

[2] x_*-nullcline is a set of states $\{\mathbf{x}_{\mathrm{nc}_*}\}$ such that $\dot{x}_*\big|_{(\mathbf{x}=\mathbf{x}_{\mathrm{nc}_*})} = 0$.

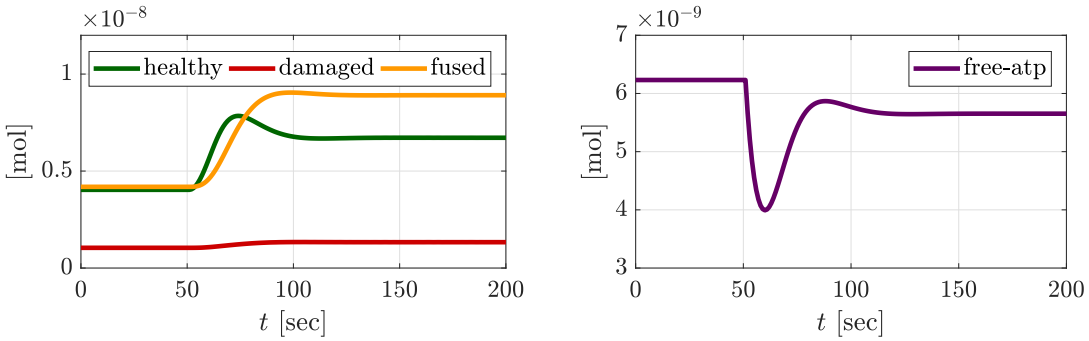

(a) State trajectory of the mitochondrial population (from equations (3.8)-(3.1b)-(3.1c))

(b) Trajectory of the free ATP level (from equation (3.1d))

Figure 3.3: State trajectory of system (3.1)-(3.2b): simulation with nominal parameters (see Table 3.1), with the steady state as initial conditions. At time $t = 50\,\mathrm{s}$ the biogenesis stress input u is doubled, yielding a suddenly decrease in the free ATP level: however, thanks to the feedback loop between ATP and $\dot{x}_\mathrm{h}$, the system reacts to this increased ATP consumption and reaches a new equilibrium point.

$$x_\mathrm{f}\text{-n.c.:} \qquad \bar{x}_\mathrm{f} = \frac{\varphi \bar{x}_\mathrm{h} \bar{x}_\mathrm{d}}{\psi_1 + \psi_2}, \tag{3.9a}$$

$$x_\mathrm{ATP}\text{-n.c.:} \qquad \bar{x}_\mathrm{ATP} = \frac{\beta \bar{x}_\mathrm{h} + \varepsilon \bar{x}_\mathrm{d} + \eta \bar{x}_\mathrm{f}}{\bar{u}} = \left(\beta \bar{x}_\mathrm{h} + \varepsilon \bar{x}_\mathrm{d} + \eta\varphi \frac{\bar{x}_\mathrm{h} \bar{x}_\mathrm{d}}{\psi_1 + \psi_2} \right) \frac{1}{\bar{u}}. \tag{3.9b}$$

Then, by combining Equations (3.8) and (3.1b), the nullclines for x_h and x_d assume the following forms:

$$x_\mathrm{h}\text{-n.c.:} \qquad \bar{x}_\mathrm{h} = -\left(\psi_1 + \psi_2\right) \frac{D \cdot \bar{x}_\mathrm{d}^2 + E \cdot \bar{x}_\mathrm{d} + F}{\mathrm{den}(\bar{x}_\mathrm{d})} \tag{3.10a}$$

$$x_\mathrm{d}\text{-n.c.:} \qquad \bar{x}_\mathrm{d} = \left(\psi_1 + \psi_2\right) \frac{\delta \bar{x}_\mathrm{h}}{\left(\psi_1 + \psi_2\right) \mu + \varphi \psi_1 \bar{x}_\mathrm{h}} \tag{3.10b}$$

where

$$\begin{aligned} D &:= \varphi \varepsilon \psi_2 > 0 \\ E &:= \varphi k \bar{u} \psi_2 + \delta \varepsilon \left(\psi_1 + \psi_2\right) > 0 \\ F &:= \bar{u} \left(\psi_1 + \psi_2\right) \left(\delta k - \alpha_1\right) \\ \mathrm{den}(\bar{x}_\mathrm{d}) &:= \varphi^2 \eta \psi_2 \bar{x}_\mathrm{d}^2 + \varphi \left(\psi_1 + \psi_2\right) \left(\beta \psi_2 + \delta \eta\right) \bar{x}_\mathrm{d} + \delta \left(\psi_1 + \psi_2\right)^2 \beta > 0 \end{aligned}$$

The shape of equations (3.10) is very useful to derive new insight on the dynamics of the system. Specifically, we can identify four main observations, summarized below.

o1. From equation (3.10b), we can note that the equilibrium value $\bar{x}_\mathrm{d}$ is always non-negative and x_d-nullcline is always monotonically increasing with respect to $\bar{x}_\mathrm{h}$, and it tends to $(\psi_1+\psi_2)\,\frac{\delta}{\varphi\psi_1}$ for $\bar{x}_\mathrm{h}\to+\infty$. As expected, its supremum value is directly proportional to damage and fission (from fused to damaged) rates, whereas it is inversely proportional with respect to the fusion rate.

o2. The nullclines of x_f and x_ATP are both monotonically increasing w.r.t. the other variables, but $\bar{x}_\mathrm{ATP}$ decreases in response of the increase of $\bar{u}$.

o3. As for x_h-nullcline, since the quantity $\mathrm{den}(\bar{x}_\mathrm{d})$ is always positive, the polynomial $D\cdot\bar{x}_\mathrm{d}^2+E\cdot\bar{x}_\mathrm{d}+F$ has to be negative, in order to ensure $\bar{x}_\mathrm{h}>0$. This condition induces a bound for the possible value of $\bar{x}_\mathrm{d}$, which has to be comprised between the two roots of the polynomial. Because the coefficients D and E are positive, for each parameters choice, we know that the sign of the roots of the polynomial depends on the sign of coefficient F. Specifically

1. if $F>0$ (which implies $\alpha_1<\delta k$), both the two roots are negative and hence there is no possible positive value of $\bar{x}_\mathrm{d}$ leading to a positive value of $\bar{x}_\mathrm{h}$;
2. if $F<0$ (which implies $\alpha_1>\delta k$), one root is negative and the other is positive and equal to $\frac{-E+\sqrt{E^2-4D\cdot F}}{2D}$. As a consequence, we have that

$$\bar{x}_\mathrm{h}>0 \quad\Longleftrightarrow\quad \mathscr{C}^{(2)}_\mathrm{pos}:\begin{cases}0<\bar{x}_\mathrm{d}<x_d^{\max}, & x_d^{\max}:=\frac{-E+\sqrt{E^2-4DF}}{2D}\\ \alpha_1>\delta k\end{cases}$$

Moreover, we have that $\bar{x}_\mathrm{h}$ tends to $\frac{u(\alpha_1-\delta k)}{\delta\beta}$ (which is positive if $\alpha_1>\delta k$) when $\bar{x}_\mathrm{d}$ tends to zero, and that $\bar{x}_\mathrm{h}$ tends to zeros as $\bar{x}_\mathrm{d}$ tends to $x_d^{\max}$.

o4. From the previous point and equation (3.10b), we can conclude that also $\bar{x}_\mathrm{h}$ should be bounded. If the bound is an upper or a lower bound depends on the choice of the set of parameters. Specifically, we have

$$\underbrace{[(\psi_1+\psi_2)\delta-x_d^{\max}\varphi\psi_1]}_{\substack{>0\\ \text{if } \delta(1+\ell)>\frac{\varphi k\bar{u}\ell+\delta\varepsilon(1+\ell)}{2\varepsilon K}}}\bar{x}_\mathrm{h}<x_d^{\max}(\psi_1+\psi_2)\mu, \qquad \text{where} \qquad \ell=\frac{\psi_2}{\psi_1}.$$

(See Appendix A.1 for details).

The nullclines for the non-trivial equilibrium ($\bar{\mathbf{x}}\neq\mathbb{0}_4$) obtained with nominal parameters can be observed in Figures 3.4, where the black dot represents the equilibrium point related to the chosen parameters.

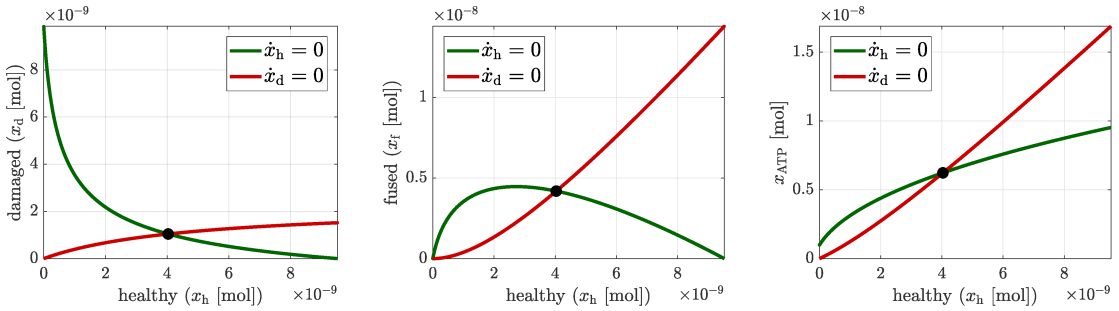

(a) Nullclines (x_d vs. x_h) (b) Nullclines (x_f vs. x_h) (c) Nullclines (x_{ATP} vs. x_h)

Figure 3.4: The Figures show the nullclines (3.10) of the healthy mitochondria dynamics (green line) and of the damaged one (red line), in three different spaces: **(a)** damaged versus healthy; **(b)** fused versus healthy; **(c)** available ATP versus healthy mitochondria.

As depicted in Figure 3.3, with the nominal set of parameters defined in Table 3.1, and a fixed input value $u = \bar{u} = 0.1\,\mathrm{s}^{-1}$, the non-zero equilibrium point is the following:

$$\bar{x}_h = 4.034 \times 10^{-9}\,\mathrm{mol}, \qquad \bar{x}_d = 1.043 \times 10^{-9}\,\mathrm{mol},$$
$$\bar{x}_f = 4.187 \times 10^{-8}\,\mathrm{mol}, \qquad \bar{x}_{ATP} = 6.231 \times 10^{-9}\,\mathrm{mol}.$$

However, it is important to note that in this work we are not trying to fit our model to a specific set of biological data, since we are more interested to discuss whether our model is able to qualitatively reproduce some observed behaviors, by varying the parameters in a specific manner. To this aim, the effective value of the equilibrium point is not particularly interesting itself, but it becomes relevant when the relative deviation from it are considered in situation of different level of stress input or varied parameters.

Stability analysis of the equilibrium points. With the same reasoning of Subsection 3.1.1, we can study the stability of the system with the ATP-feedback, around the equilibrium points:

$$\dot{\mathbf{x}} - \dot{\bar{\mathbf{x}}} = \mathbf{F_2}|_{(\bar{\mathbf{x}},\bar{u})}\,(\mathbf{x} - \bar{\mathbf{x}}) + \mathbf{G_2}|_{(\bar{\mathbf{x}},\bar{u})}\,(u - \bar{u})\,,$$

with

$$\mathbf{F_2} = \begin{bmatrix} \frac{\alpha_1}{k+x_{\mathrm{ATP}}} - \delta - \varphi x_{\mathrm{d}} & -\varphi x_{\mathrm{h}} & \psi_1 & -\frac{\alpha_1 x_{\mathrm{h}}}{(k+x_{\mathrm{ATP}})^2} \\ \delta - \varphi x_{\mathrm{d}} & -\varphi x_{\mathrm{h}} - \mu & \psi_2 & 0 \\ \varphi x_{\mathrm{d}} & \varphi x_{\mathrm{h}} & -(\psi_1 + \psi_2) & 0 \\ \beta & \varepsilon & \eta & -u \end{bmatrix},$$

$$\mathbf{G} = \begin{bmatrix} 0 \\ 0 \\ 0 \\ -x_{\mathrm{ATP}} \end{bmatrix}.$$

The stability of the trivial equilibrium, which describes the situation when all the species disappear, can be analyzed by evaluating $\mathbf{F_2}$ at $\bar{\mathbf{x}} = \mathbb{0}_4$. In that case, it is

$$\mathbf{F_2}|_{(\mathbb{0}_4,\bar{u})} = \left[\begin{array}{ccc|c} \frac{\alpha_1}{k} - \delta & 0 & \psi_1 & 0 \\ \delta & -\mu & \psi_2 & 0 \\ 0 & 0 & -(\psi_1 + \psi_2) & 0 \\ \hline \beta & \varepsilon & \eta & -u \end{array}\right],$$

whose eigenvalues are $\sigma\left(\mathbf{F_2}|_{(\mathbb{0}_4,\bar{u})}\right) = \{\alpha_1/k - \delta,\ -\mu,\ -(\psi_1 + \psi_2),\ -\bar{u}\}$. Hence the zero equilibrium is asymptotically stable if $\alpha_1/k < \delta$, and it is unstable if $\alpha_1/k < \delta$. We cannot affirm anything for $\alpha_1/k = \delta$. Furthermore, condition $\alpha_1/k < \delta$ is inconsistent with the existence of the non-trivial equilibrium, since it describes a situation where the new births rate is smaller than the damage rate.

To discuss the stability of the (more interesting) non-trivial equilibrium state, we consider:

$$\mathbf{F_2}|_{(\bar{\mathbf{x}},\bar{u})} = \begin{bmatrix} \frac{\alpha_1}{k+\bar{x}_{\mathrm{ATP}}} - \delta - \varphi \bar{x}_{\mathrm{d}} & -\varphi \bar{x}_{\mathrm{h}} & \psi 1 & -\frac{\alpha_1 \bar{x}_{\mathrm{h}}}{(k+\bar{x}_{\mathrm{ATP}})^2} \\ \delta - \varphi \bar{x}_{\mathrm{d}} & -\varphi x_{\mathrm{h}} - \mu & \psi_2 & 0 \\ \varphi \bar{x}_{\mathrm{d}} & \varphi \bar{x}_{\mathrm{h}} & -(\psi_1 + \psi_2) & 0 \\ \beta & \varepsilon & \eta & -\bar{u} \end{bmatrix}, \tag{3.12}$$

where $\bar{\mathbf{x}}$ obeys equations (3.9) and (3.10). As the analytical evaluation of the eigenvalues is impossible, due to the non-zero entry in position (1, 4), we discuss the stability of this equilibrium in a statistic manner, through an *eigenvalues random analysis*.

Eigenvalues of (3.12) random analysis. We considered the rate constants related to biogenesis (α_1), mitophagy (μ), fusion (φ) and fission (ψ_1 and ψ_2) and we let them

vary one by one within a reasonable interval. For each value assumed by the considered parameter, we evaluated the equilibrium value and the eigenvalues of the relative Jacobian, when varying all the other parameters in a random way, within an uniform interval centred in their nominal value, with a radius of 0.1% of the same nominal value. Then, we evaluated the asymptotic stability and the oscillations probabilities (as the mean over 100 simulations for each value of the parameter). Figure 3.5 shows the results.

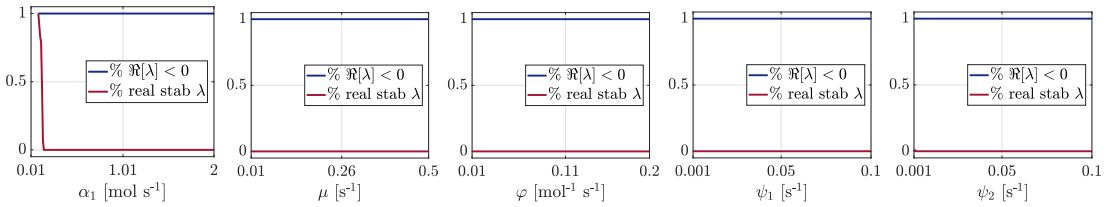

(a) Biogenesis (b) Mitophagy (c) Fusion (d) Fission to healty (e) Fission to damaged

Figure 3.5: Probability of asymptotic stability (blu line) and probability of all real (stable) eigenvalues of the Jacobian, with respect to the parameters of biogenesis (α_1), mitophagy (μ), fusion (φ), and fission (ψ_1, ψ_2). All the results are the mean values over one hundred simulations for each value of the examinated parameters. For each simulation all the other parameters are randomly chosen within an uniform interval around their nominal value (see the main text for the details).

Specifically, system stability is always preserved, except for $\alpha_1 < \delta k$, which refers to the case such that the non-trivial equilibrium does not exist. However, most of the time, the modes of the system are oscillatory stable, with the only exception for low values of biogenesis rate α_1, which lead to some cases of damping oscillatory behavior. In Section 3.2 we report the results of the sensitivity analysis of the eigenvalues in response to parameters' variations. Importantly, it has to be noticed that in all the spanned situation, the stability of the equilibrium state is always preserved. Thus we can suppose that the proposed model is well-posed.

3.2 Sensitivity analysis

The analysis of the sensitivity of the steady state with respect to the parameters' value is a very useful tool to quantify the role of each phenomenon within the complex machinery of mitochondrial dynamics. Specifically, the larger the relative value of the sensitivity, the more important the involved phenomenon.

3.2.1 Sensitivity analysis of species steady state

In Figure 3.6 the results of the sensitivity analysis of the steady state of the species is depicted, and specifically the scaled sensitivity values are shown. From these results, we can immediately assert the main roles of the parameters involved into the biogenesis phenomena to modulate the steady state of the proposed system. In particular, while

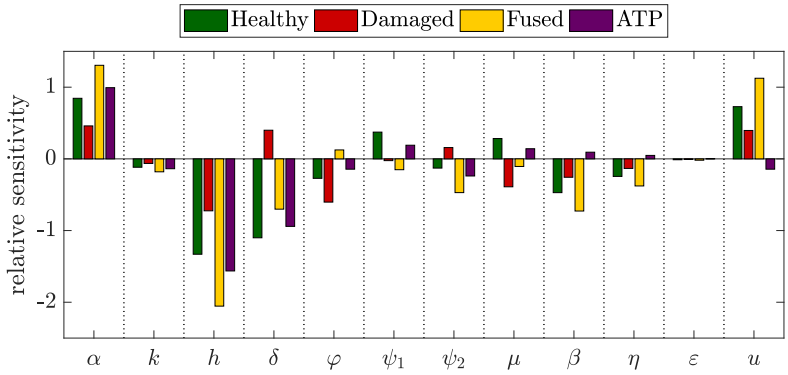

Figure 3.6: The figure shows the results of the scaled sensitivity analysis performed for the steady state value of all the state variables with respect to each fixed parameters and also with respect to the fixed input value u.

there is a positive correlation between α_1 and all the species at the equilibrium, a negative correlation involves the parameter h, which appears at the denominator of the Hill function. However, for sake of simplicity, we have assumed $h \equiv 1$. In both cases, it has to be noticed that the fused population of mitochondria is the more affected by these parameters, whereas the damaged one is the least. The value of the energetic stress u has a similar role, except for the ATP value, which obviously decreases when u increases. Moreover, since an augmented value of the free ATP level let the number of new birth decrease, all the parameters involved in the ATP production phenomenon (β, ε and η) are anti-correlated with the steady state values of the mitochondrial populations' size. The decrease of the damaged population numerousness caused by mitophagy (see rate μ) causes a reduction of fused mitochondria, but also an augmented number of the healthy population. This phenomenon finds its reason in biological evidences, from which it has been noticed than mitophagy and biogenesis are linked phenomena that enable a quality control within the cell. The role of both fusion and fission is easily understandable by the mathematical description of the model (3.1). An increase in fusion rate φ causes a drop in the healthy and damaged populations followed by a rise in the fused one. Fission to healthy (ψ_1) and fission to damaged (ψ_2) have an opposite role in the steady state values for what concerned the healthy and the damaged mitochondria, whereas they both make the fused population decrease. Intriguingly, φ, psi_1 and ψ_2 have different role with

respect to the free level of ATP at the equilibrium. While the first and the last cause an ATP reduction, the second one let it increase. However this fact can be easily interpreted as a consequence of the increased or decreased amount of healthy mitochondria caused by these phenomena.

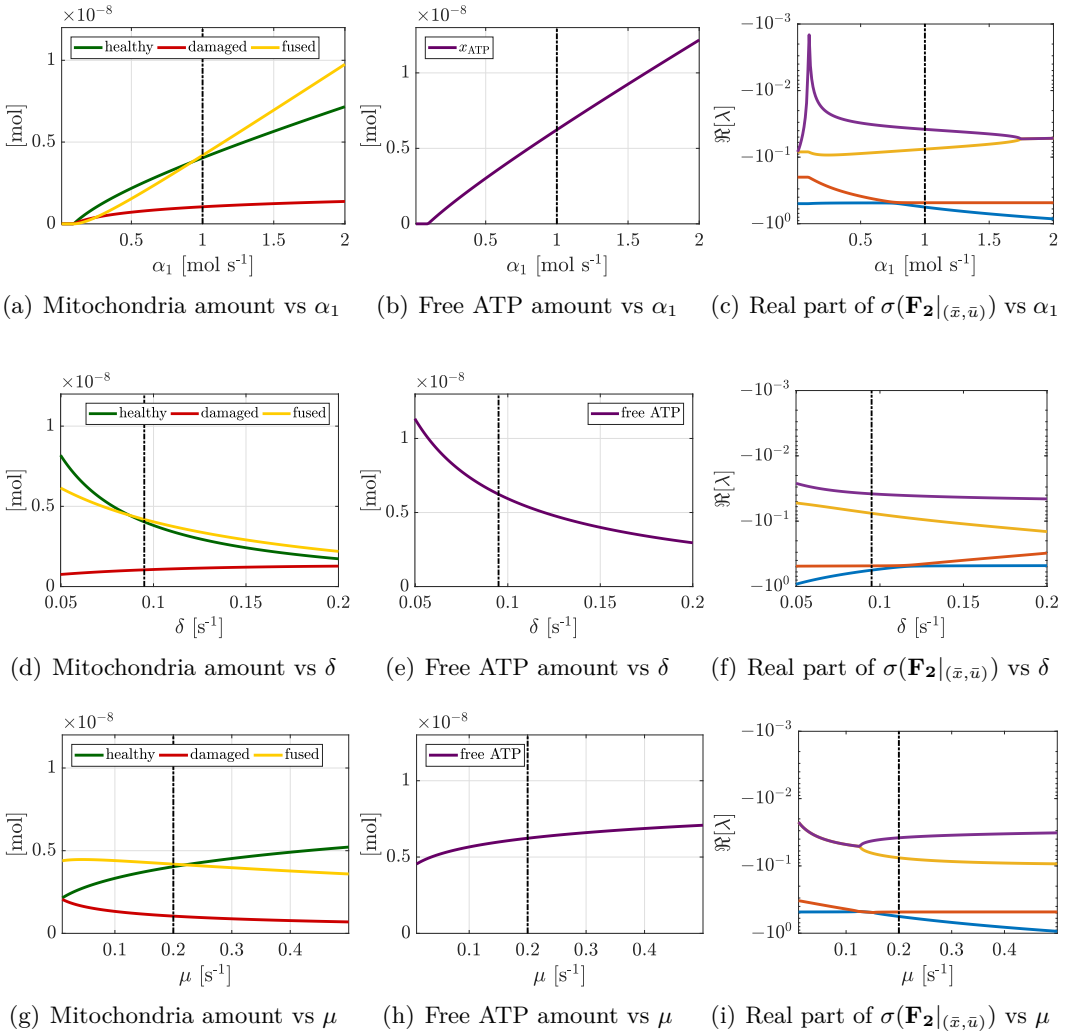

(a) Mitochondria amount vs α_1 (b) Free ATP amount vs α_1 (c) Real part of $\sigma(\mathbf{F_2}|_{(\bar{x},\bar{u})})$ vs α_1

(d) Mitochondria amount vs δ (e) Free ATP amount vs δ (f) Real part of $\sigma(\mathbf{F_2}|_{(\bar{x},\bar{u})})$ vs δ

(g) Mitochondria amount vs μ (h) Free ATP amount vs μ (i) Real part of $\sigma(\mathbf{F_2}|_{(\bar{x},\bar{u})})$ vs μ

Figure 3.7: The first two columns show the steady state values of the mitochondrial population size when the parameters related to biogenesis α_1, damage δ, and mitophagy μ vary. The right column instead shows, in a logarithmic scale, the real part of the eigenvalues of the Jacobian evaluated at the non-trivial equilibrium point, as a function of the variable parameters. The dotted and dashed lines highlight the nominal value of each parameter.

The analysis of the role of each parameter relatively to the steady state behavior of the model continues in Figures 3.7 and 3.8, where we report the values achieved at the equilibrium point by all the state variables, together with the real part of the eigenvalues

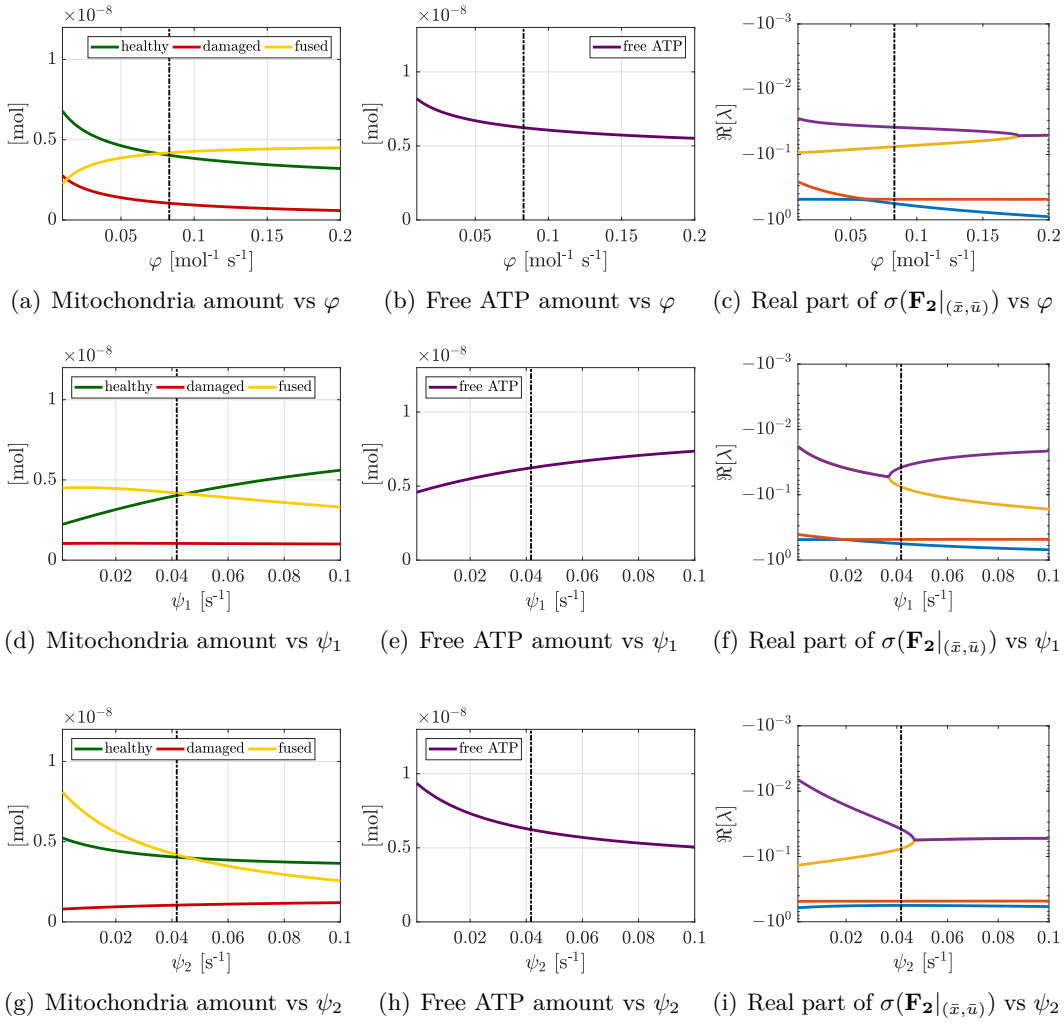

(a) Mitochondria amount vs φ (b) Free ATP amount vs φ (c) Real part of $\sigma(\mathbf{F_2}|_{(\bar{x},\bar{u})})$ vs φ

(d) Mitochondria amount vs ψ_1 (e) Free ATP amount vs ψ_1 (f) Real part of $\sigma(\mathbf{F_2}|_{(\bar{x},\bar{u})})$ vs ψ_1

(g) Mitochondria amount vs ψ_2 (h) Free ATP amount vs ψ_2 (i) Real part of $\sigma(\mathbf{F_2}|_{(\bar{x},\bar{u})})$ vs ψ_2

Figure 3.8: The first two columns show the steady state values of the mitochondrial population size when the parameters related to fusion φ, fission to healthy ψ_1, and fission to damaged ψ_2 vary. The right column instead shows, in a logarithmic scale, the real part of the eigenvalues of the Jacobian evaluated at the non-trivial equilibrium point, as a function of the variable parameters. The dotted and dashed lines highlight the nominal value of each parameter.

of the Jacobian matrix evaluated at the equilibrium, as a function of one parameter at a time, while the other parameters are fixed to their nominal value. Specifically, we let parameters α_1, δ and μ vary as regards Figure 3.7, while Figure 3.8 refers to parameters φ, ψ_1 and ψ_2. For all the observed behaviors, the shape of the steady state variables reflects the sensitivity analysis performed above (see Figure 3.6). However here we can also observe the shape of the sensitivity, and the effective reached steady state values. The real part of the eigenvalues are always negative, thus confirming the asymptotic

stability of the system around the different equilibria points. In particular, it is worth to be noted the role of parameter α_1 (see Figures 3.7(a), 3.7(b), and 3.7(c)): for very low values of this rate, which refers to the situation $\alpha_1 < \delta k$, the system directs to the zero (stable) equilibrium, since the other one is unstable (as discuss in Subsection 3.1.2).

To summarize, we can assert that this sensitivity analysis validates our choice of using a feedback relationship among the free ATP level and biogenesis rate, in the sense that the value of this rate has the most effect on the health level of the cell and on the free ATP availability within it.

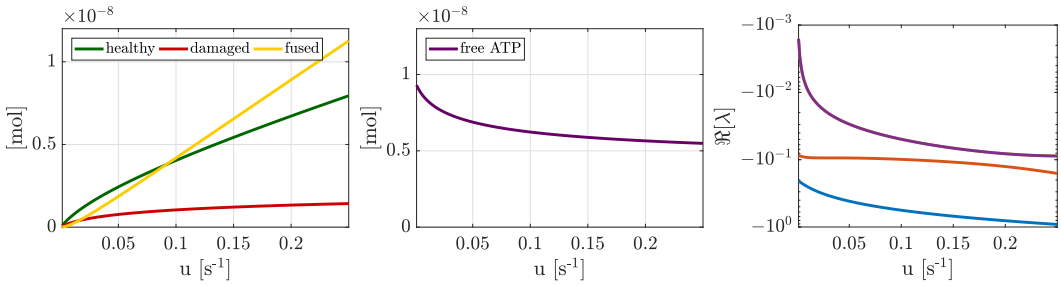

(a) Mitochondria amount vs u (b) Free ATP amount vs u (c) Real part of $\sigma(\mathbf{F_2}|_{(\bar{\mathbf{x}},\bar{u})})$ vs u

Figure 3.9: The first two columns show the steady state values of the mitochondrial population size when the energetic stress input u varies. The right column instead shows, in a logarithmic scale, the real part of the eigenvalues of the Jacobian evaluated at the non-trivial equilibrium point, as a function of the variable input. The dotted and dashed lines highlight the nominal value of u.

Finally, to analyse how the system reacts in response to different values of energy stress by the cell, the previous plots have been generated also with respect to the input signal u variation. By observing Fig. 3.9 we can see that when the level of stress is very low, the free level of ATP achieves its maximum value, but the mitochondrial populations tend all to zero, and the equilibrium tends to the instability. In fact, the case $u = 0$ is not depicted, since the zero equilibrium with the nominal parameters (with $\alpha_1 > \delta k$) is not stable, as previously discussed. However, when the energetic stress increases, the system is able to react and let the mitochondrial populations increase, in order to maintain a sufficiently large level for free ATP. If compared with Figure 3.2, referred to the model with fixed biogenesis rate, where the augmented u causes a total disappearance of the free ATP, in this case, we have only a slight decrease. This fact is also appreciated in the simulation example seen in Figure 3.3(b). As the input u tends to infinity, however, the level of free ATP goes to zero and the system equations for the dynamics of the mitochondrial populations (3.1a), (3.1b) and (3.1c) tend to assume the same form of system (3.1), when α_1 is replaced with α_1/k.

3.2.2 Sensitivity analysis of reactions' fluxes steady state

The sensitivity analysis task is a useful tool also to discuss the variation in fluxes of the biological reactions at the equilibrium when the parameters vary. Following a similar investigation process performed for the sensitivity analysis of the steady state values of the species, in this subsection we present the results of the fluxes sensitivity at the equilibrium.

Figure 3.10 shows the results of the analysis divided for groups of reactions. Specifically, in Fig. 3.10(a) the scaled sensitivity of the steady state fluxes of biogenesis, damage and mitophagy are depicted. As imaginable, all the fluxes increase when parameters α_1 and μ, related to biogenesis and mitophagy, respectively, increase. Interestingly, an increase in the damage rate δ does not imply an increased flux of damage, since the decreasing in biogenesis causes also a decreased damage flux. However, the flux of mitochondria depletion increases when δ become larger. Moreover, an augmented value of μ implies a larger flux for all the three reactions, since a smaller amount of mitochondria produces a lower level of free ATP and a consequent need of new births. The role of fusion and fission rates with respect to these reactions are different. At first, we can observe that a larger value of φ can increase the quality of the cell, in the sense that the mitophagy phenomenon decreases. Nevertheless, since it is also anti-correlated with the flux of biogenesis, parameters φ and $\psi_{1,2}$ should be accurately tuned, in order to maintain a required quality level.

The manner by which the variation of the parameters influences the fluxes of fusion and fission is presented in Figure 3.10(b). Similarly to the previous analyses, also these variable are sensitive to α_1, h and u at most. Again, they are all negatively correlated with the increase of ATP production (see β, η and ε effects). Intriguingly, all these reactions are negatively sensitive to damage and mitophagy rates, thus suggesting that a situation of high damage within the cell can cause a decrease in the fusion-fission machinery efficiency. The rate of fusion and fission are related in a direct way to their fluxes, however it is worth noting that an augmented rate of fission (both to healthy and damaged population) cause a (more or less significant) increasing in the flux of fusion at the equilibrium.

Finally, Figure 3.10(c) reports the scaled sensitivity of the fluxes related to production and consumption of ATP. Even if a complex set of phenomena can be observed in this image, we can note again that the most relevant parameters are the ones related to biogenesis and ATP consumption phenomena. Here, as expected, it can be found also an increased relevance of β, η an ε, due to their direct relationship with the observed fluxes. Among the other parameters, the most important is δ, which causes a decreased

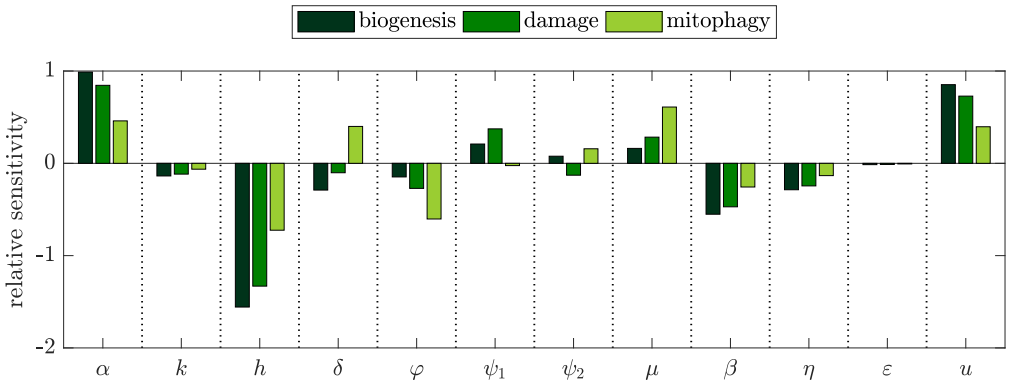

(a) Biogenesis, damage and mitophagy

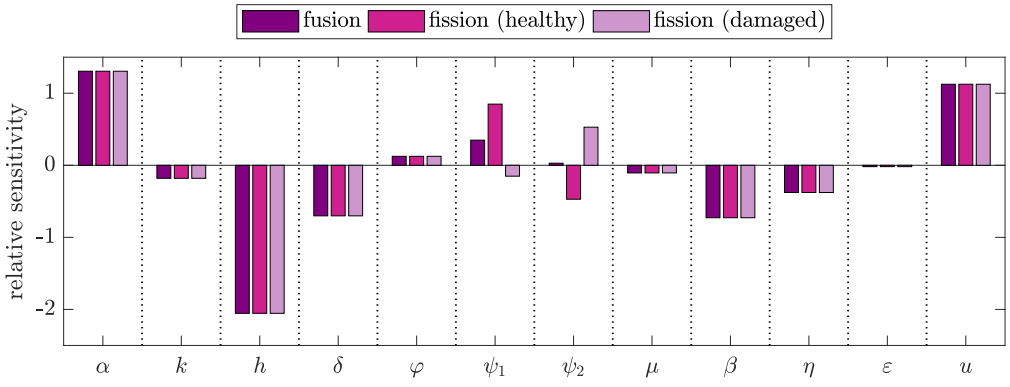

(b) Fusion and fission

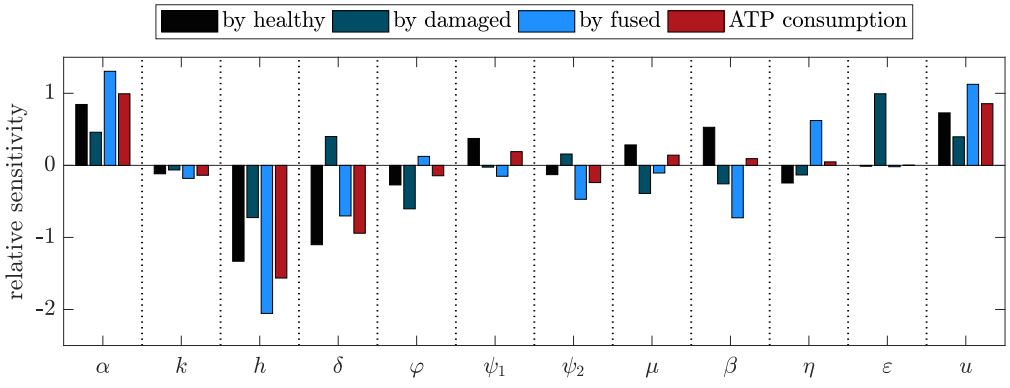

(c) ATP production and consumption

Figure 3.10: The figures show the results of the scaled sensitivity analysis performed for the steady state fluxes value of all the biological reactions with respect to each fixed parameters and with respect to the fixed input value u. Specifically, **(a)** refers to the processes of biogenesis, damage and mitophagy; **(b)** is related to fusion and fission processes; **(c)** focuses on the processes that involve the free ATP state variable.

production of ATP by healthy and fused mitochondria, and a consequent drop in the ATP production, since the size of free ATP will be decreased. From the remaining results, we can observe that the production of ATP can be enhanced differently by the tuning of φ and the fission rates, as for the ATP production. However, the role of these parameters is not very sizeable, if compared with the others.

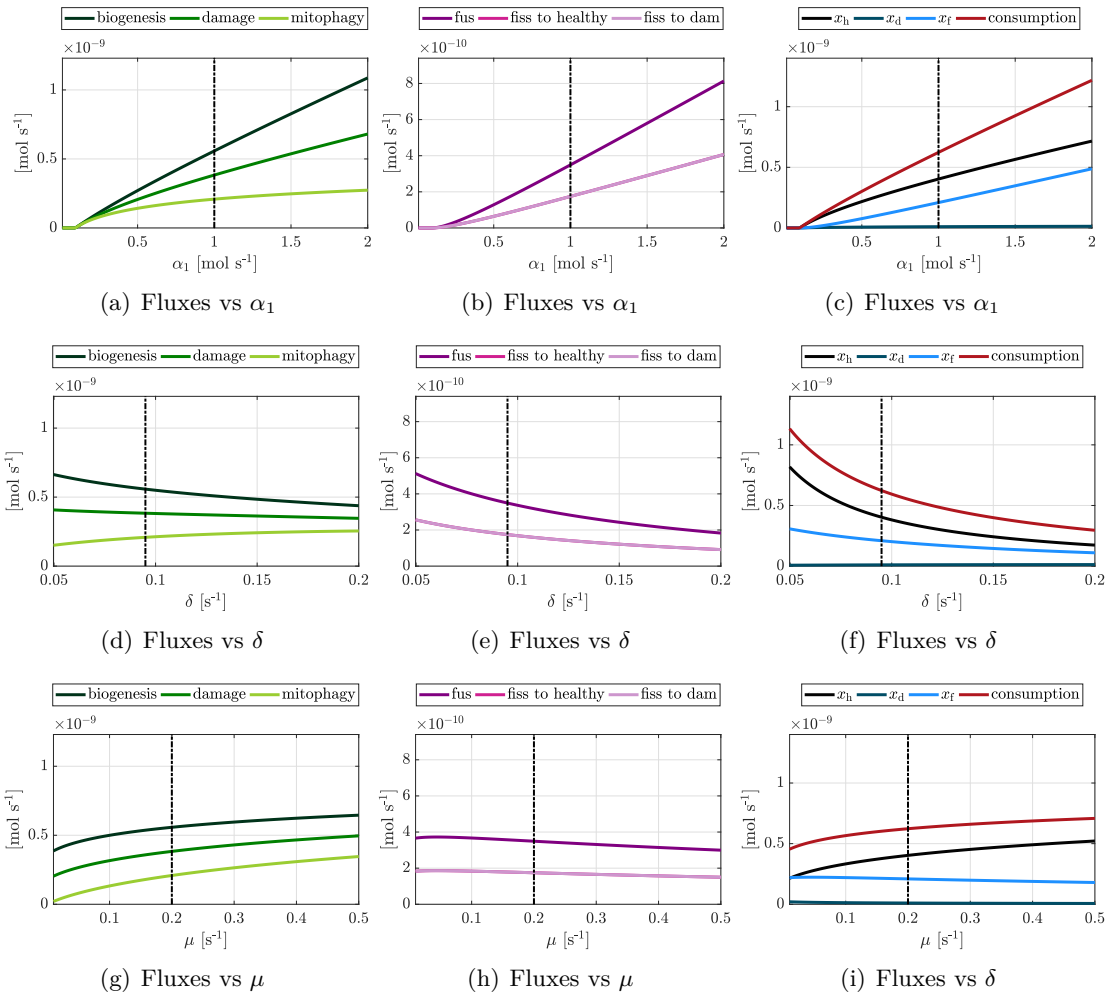

(a) Fluxes vs α_1 (b) Fluxes vs α_1 (c) Fluxes vs α_1

(d) Fluxes vs δ (e) Fluxes vs δ (f) Fluxes vs δ

(g) Fluxes vs μ (h) Fluxes vs μ (i) Fluxes vs δ

Figure 3.11: The figures show the steady state fluxes values of the biological reactions when the parameters related to biogenesis α_1, damage δ, and mitophagy μ vary. Specifically, the first column refers to the phenomena of biogenesis, damage and mitophagy, the central columns focuses on fusion and fission fluxes, and finally the left column regards the fluxes related to the ATP level. The dotted and dashed lines highlight the nominal value of each parameter.

Figures 3.11 and 3.12 report the values of the reactions' fluxes at the equilibrium as a function of the varied parameters. All the plots reflect the results discussed above,

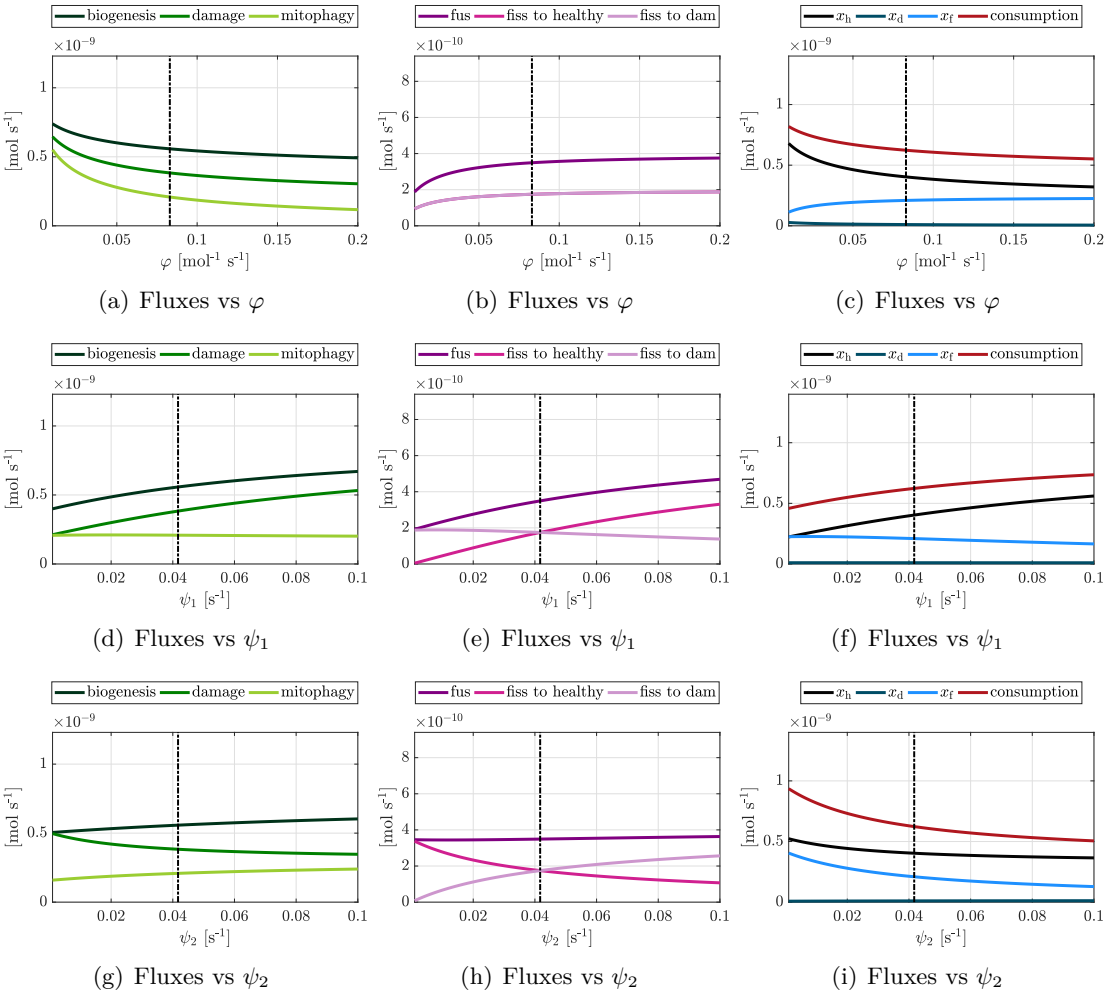

(a) Fluxes vs φ (b) Fluxes vs φ (c) Fluxes vs φ

(d) Fluxes vs ψ_1 (e) Fluxes vs ψ_1 (f) Fluxes vs ψ_1

(g) Fluxes vs ψ_2 (h) Fluxes vs ψ_2 (i) Fluxes vs ψ_2

Figure 3.12: The figures show the steady state fluxes values of the biological reactions when the parameters related to fusion φ, fission to healthy ψ_1, and fission to damaged ψ_2 vary. Specifically, the first column refers to the phenomena of biogenesis, damage and mitophagy, the central columns focuses on fusion and fission fluxes, and finally the left column regards the fluxes related to the ATP level. The dotted and dashed lines highlight the nominal value of each parameter.

but they also depicted the specific values assumed by the fluxes and the shape of their variation in response to the change of each analyzed parameter. The main role of α_1 observed in Figure 3.10 can be noted also in these plots, where the variation of α_1 causes the most rapid change of all the fluxes' value.

Given the considerable sensitivity of the fluxes with respect to energetic stress observed in Figure 3.10, we report also the values of the fluxes when u varies (see Figure 3.13). As expected, all the equilibrium fluxes increase as the value of u increases. This is one of

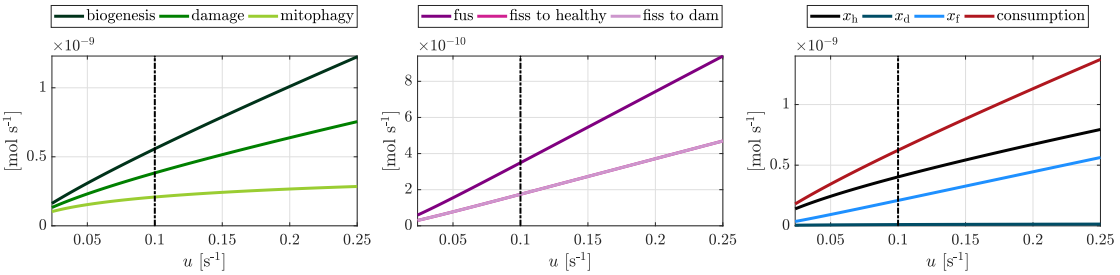

(a) Fluxes vs u (b) Fluxes vs u (c) Fluxes vs u

Figure 3.13: The figures show the steady state fluxes values of the biological reactions when the fixed value of the bioenergetic stress u varies with respect to its nominal value. Specifically, the first column refers to the phenomena of biogenesis, damage and mitophagy, the central columns focuses on fusion and fission fluxes, and finally the left column regards the fluxes related to the ATP level. The dotted and dashed line highlights the nominal value of the ATP consumption rate.

the strong point of this proposed dynamical system, with respect to the one with fixed biogenesis rate.

3.2.3 Sensitivity analysis of the transient response

The analysis of an high order non-linear model is often performed through its approximation to a second-order linear model around an equilibrium point. Specifically, this strategy can be useful to evaluate some transient characteristics of the system, that describe how fast it is to respond to a step input. However, this kind of analysis is as useful as good the approximation is. Thus, if the low-order linear system is sufficient to describe the non-linear complex dynamics, it can be a warning alarm that the latter is actually too complex to describe the desired phenomenon. In this subsection we present an analysis of the transient response and we show that the complexity of our non-linear system is not overdone, since the linear approximation is not able to fully describe the phenomena observed through the more complex one.

One of the most interesting aspect of a biological system refers to its performances in responding to an input signal arrived from the cell. In particular, in a mitochondrial dynamic framework, it can be useful to understand how quickly the systems reaches a new equilibrium in response to a sudden increase of the ATP request from the cell. This property can be studied through a transient analysis of the model step response.

To analytically evaluate the transient response, we can approximate the fourth-order linearized system (3.4) with a second-order one, by considering only the slower modes related to the eigenvalues with the larger real part, λ_1, λ_2 ($\Re[\lambda_1] \geq \Re[\lambda_2]$). The transfer

function $W(s)$ from the input to the output of the system is:

$$W(s) = \frac{W_0}{s^2 + 2\xi\omega_0 s + \omega_0^2}, \tag{3.13}$$

where $\omega_0 = \sqrt{\Re[\lambda_1]\Re[\lambda_2]}$ is the natural frequency and $\xi = -\frac{\Re[\lambda_1]+\Re[\lambda_2]}{2\omega_0}$ is the damping coefficient.

In order to characterize the transient response, we consider two quantities, the rise time T_r, defined as the time required for the response to rise from 10% to 90% of its final value, and the settling time $T_{s,2\%}$, which is the time required for the response curve to reach and stay within a range of certain percentage (here 2%) of the final value. These two quantities can be approximated as follows:

$$T_r \approx \frac{\ln(9)}{|\Re[\lambda_1]|}, \qquad T_{s,2\%} \approx \begin{cases} \frac{4}{|\Re[\lambda_1]|}, & \text{if } \lambda_2 \text{ and } \lambda_3 \text{ complex conjugated} \\ \frac{4}{\xi\omega_0}, & \text{otherwise} \end{cases},$$

where λ_3 is the third eigenvalue with the largest real part.

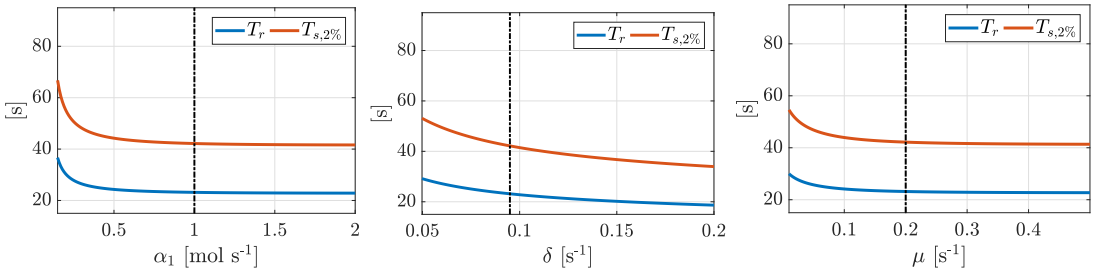

(a) Transient quantities vs α_1 (b) Transient quantities vs δ (c) Transient quantities vs μ

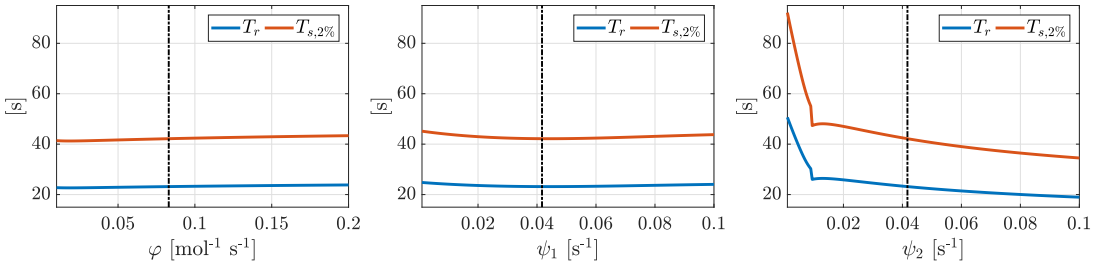

(d) Transient quantities vs φ (e) Transient quantities vs ψ_1 (f) Transient quantities vs ψ_2

Figure 3.14: The figures show the rise time (blue line) and the transient time (red line) evaluated through the approximation of the non-linear fourth order model (3.1) with a second-order linear model around the equilibrium state (3.13), as a function of the main parameters of the models. As in the previous figures, the dotted and dashed line highlights the nominal values of the considered parameters.

Figure 3.14 shows the values of the approximated rise time and settling time when each of the most relevant parameters is varied, one at a time. In particular, we can observe that the two values vary very similarly one each other, and they use to decrease as the parameters increase, except for φ and ψ_1. However, the transient quantities are not particularly sensitive to these two parameters, since they remain almost constant as φ and ψ_1 vary. From this figures, we can hence note that a more rapid response of the system does not mean a healthier cell, in fact both T_r and T_s decrease when δ, and ψ_2 increase, which yields a larger number of damaged mitochondria within the cell.

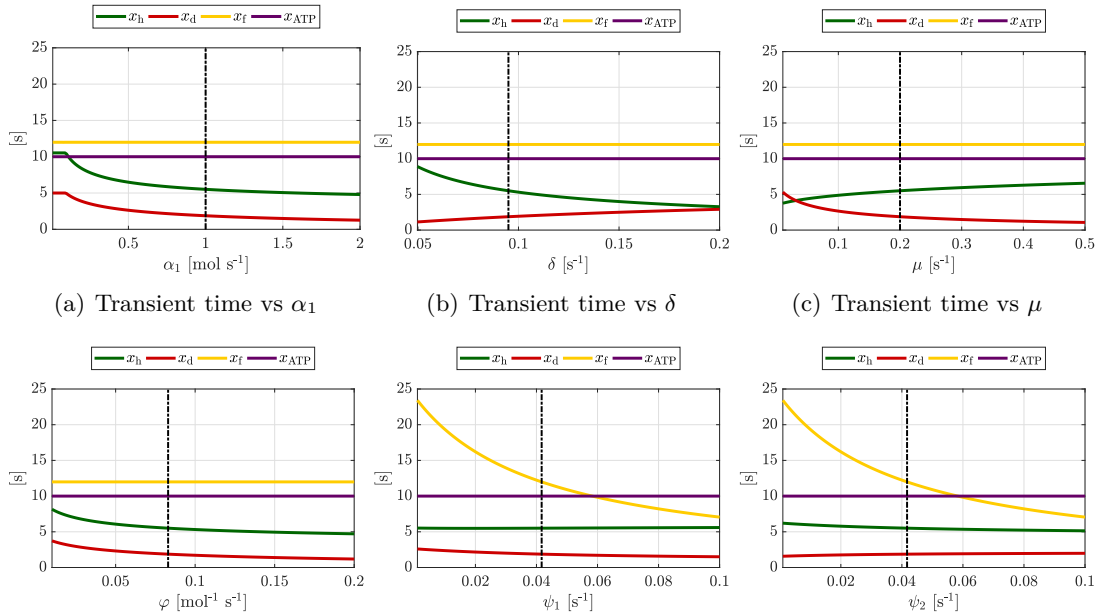

(a) Transient time vs α_1 (b) Transient time vs δ (c) Transient time vs μ

(d) Transient Time vs φ (e) Transient time vs ψ_1 (f) Transient time vs ψ_2

Figure 3.15: The figures show the transient time of all the state variables (x_h green, x_d red, x_f yellow, x_{ATP} purple) as a function of the main parameters of the models. These quantities have been evaluated through the software Copasi® 4.19. As in the previous figures, the dotted and dashed line highlights the nominal values of the considered parameters.

A less approximated values of these quantity, as a function of the system parameters, can be observed in Figure 3.15, derived through the software Copasi® 4.19. These pictures show the transient time for each state variable, evaluated through simulations. Intriguingly, the transient time of free ATP is always fixed to 10 s, independently of the values of the parameters, whereas different behavior can be observed for the other system variables. Specifically, the fused population has a transient time, which is free-standing with respect to all parameters, except for fission parameters ψ_1 and ψ_2, whose decrease causes a strong increase of the fused transient time. For what concerning the healthy and damaged mitochondria, their characteristic times decrease together when α_1 or

φ increase, while they are differently influenced by the other parameters' change. In particular the larger δ, the smaller the transient time for healthy mitochondria, and the larger the damaged one, until they become equivalent when δ reaches twofold its nominal value. A similar (but slower) behavior can be observed in consequence of ψ_2 changes. The opposite can instead be noticed when the mitophagy rate μ increases. An augmented value of ψ_1 causes only a slightly decrease in the transient time of damaged population, while the one of the healthy is independent.
Even if an interpretation of these sensitivity analysis is not easy to derive, two main facts should be highlighted: at first, in all cases, we can observe that the fused mitochondria are slower to react than the other sub-populations. This fact can be actually explained if considering that the size of the fused sub-population depends on how many healthy and damaged mitochondria are available at the same time. Second, if we compare Figures 3.14 and 3.15, we can assert that the second-order linear system approximation cannot describe the actual transient characteristics of the fourth-order non-linear system with a sufficient precision. Thus confirming that the complexity of our model is required, in order to describe the interested phenomena.

3.3 How to apply a control action?

One of the main advantages of devising and using synthetic systems to describe specific biological phenomena is the opportunity to test and predict the system behavior in response to a model change, be it endogenous (e.g. change of parameters) or exogenous (e.g. external stimuli). In particular, one main issue to be solved in this context can be expressed as follows.

How can we control a situation of "disorder" in mitochondrial dynamics by means of an external input? Which target should we choose for a possible control action?

To try and answer these open questions we attempt to predict which rate constants should be better to regulate so as to ensure a behavior similar to the healthy one as more as possible. To this aim, we present a combined sensitivity analysis with respect to a situation of increased damage rate. In particular, the nominal rate constant δ is here replaced with $\tilde{\delta} = 10 \times \delta$ and it is observed how the equilibrium point changes w.r.t. variations of every possible pair of the other main parameters. Specifically, we let α_1, μ, φ, ψ_1 and ψ_2 vary.

Figure 3.16 represents the ratio between the free ATP level at the equilibrium in the modified setting and the free ATP level reached with the nominal parameters, as a function of the parameters. In other words, it consists in a double sensitivity analysis to

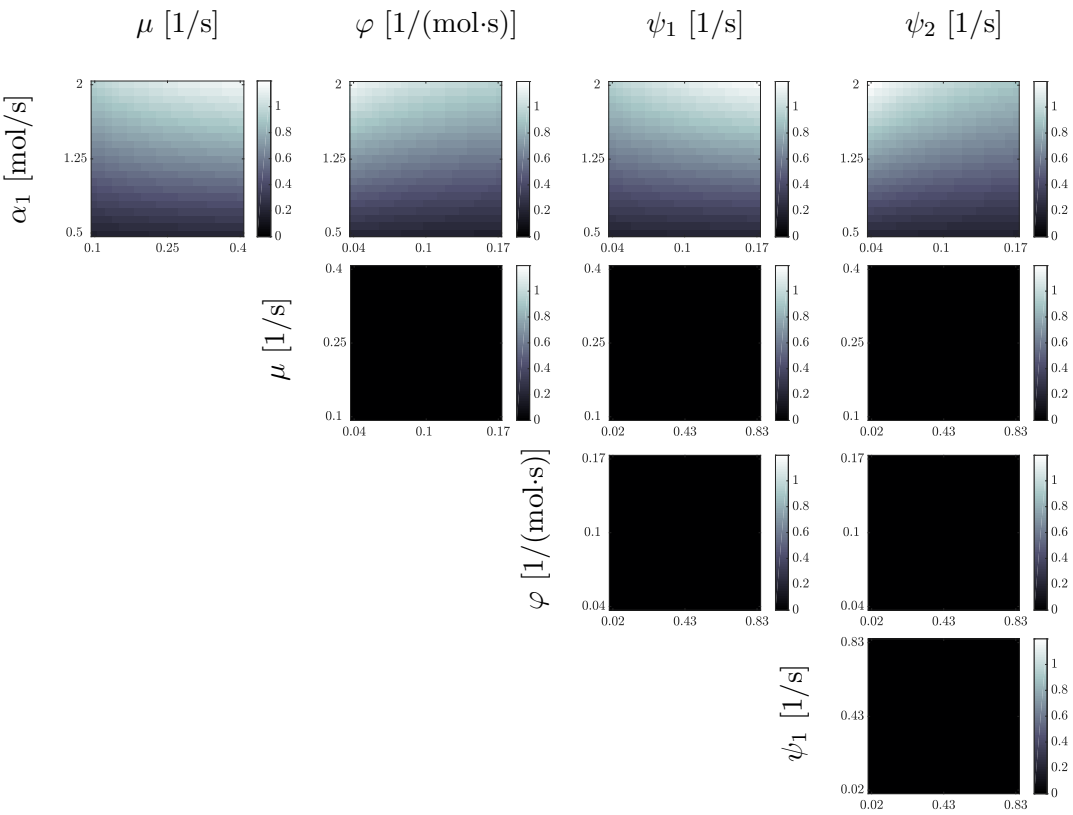

Figure 3.16: Heat maps of $\bar{x}_{\text{ATP}}/\bar{x}_{\text{ATP,nom}}$ in a situation of $\tilde{\delta} = 10 \times \delta$. The panel shows the ratio between the free ATP level at the equilibrium in the modified setting and the free ATP level reached with the nominal parameters, as a function of each pair of parameters, considered one at a time. The closer to one the ratio is, the more useful the choice of that specific pair of the parameters is, in order to restore a level of free ATP similar to the one obtained in a nominal background, even in an abnormal situation.

highlight the rate constants that mostly influence this ratio: as we can see from the heat map plots, the free ATP level is more sensitive to variations in biogenesis rate (α_1) than to variations in all the other analyzed parameters (first plot row). Moreover, a specific choice of α_1 let the system reach a level of free ATP equivalent to the one reached in a nominal setting, even in condition of increased damage. In practice, this discussion can be useful to set the direction to take in order to implement a control law and bring the ATP availability back to the nominal value. In this case, we can conjecture that the control law should target the biogenesis phenomenon, so as to increase its rate. Moreover, this results reinforce our conjecture on the role of biogenesis rate in mitochondrial dynamics, and the choice of relate the ATP level with this phenomenon.

3.4 Discussion and contribution

Our study follows the line of research in modeling mitochondrial dynamics of the last decades.

In this sense, in order to provide a first taxonomy of the related works and place our contribution in this context, the models that have appeared in literature can be categorized w.r.t. the presence or not of the spatial framework. Indeed, the movement of mitochondria along the microtubules network is one of the factors that influence the phenomenon of fusion-fission within the mitochondrial population. However, depending on the scale and the scope of each model, authors have chosen whether to take this aspect into account (Dalmasso et al. (2017); Tam et al. (2015, 2013); Patel et al. (2013); Sukhorukov et al. (2012)) or not (Figge et al. (2012); Mouli et al. (2009); Kowald and Kirkwood (2011); Hoitzing et al. (2015)). Our model, in particular, does not represent the spatial dynamics of the mitochondria, since it describes the phenomena on a larger scale, where the factors that influence the fusion-fission properties are not examined at the specific scale of single mitochondria but at the population level.

Many authors address the issue of the *mitochondria quality level* for the benefit of the hosting cells. In order to highlight how the quality of a cell can vary within a range of different levels, Figge et al. (2012) proposes a probabilistic model, which uses a master equation approach to describe the evolution of the probability $\mathtt{P}(q,t)$ during time, where $q = 0, 1, \ldots, Q$ represents the quality level and Q is the highest possible level. To analyze the mitochondrial function during aging, the author modeled the phenomena of fusion-fission (as a single one), mitophagy, biogenesis and two different types of damage (a random molecular damage and an infectious molecular one, which includes mutations of mtDNA). By representing each mitochondrion as a vector of ten functional hereditary units (FHUs), which can be intact or damaged, Mouli et al. (2009) in practice uses a sort of quality range level within 0 and 10 for each mitochondrion. This description lets the author implement selective fusion and mitophagy phenomena with respect to the level of activity of each organelle and it proves that the choice of a selective fusion improves the performance, especially in the case of higher fusion-fission frequencies. Differently from Figge et al. (2012), here the dynamics evolves along a life cycle for each mitochondria, even if each phenomenon is characterized by a respective probability. Moreover, fusion and fission are treated as distinct phenomena, where fission always follows a fusion event and can redistribute the intact and damaged FHUs among the daughters mitochondria.

More detailed models, which use the discrete range for the health quality, have been proposed in Dalmasso et al. (2017), Tam et al. (2015, 2013), Patel et al. (2013), where the

spatial description is also included. The former considers a static 2D spatial framework, represented as a circle with a fixed diameter containing a central nucleus, and a variable number of mitochondria. The mobility of each mitochondria depends on its position inside the cell. Specifically, the author defines the perinuclear area, where mitochondria have low velocity magnitude, and the bulk cytosolic area, characterized by the high velocity magnitudes of the mitochondria. Moreover, that work assumes that small mitochondria move faster than large ones. Dalmasso et al. (2017) describes the mitochondrial dynamics through an agent-based discrete model characterized by a complex fusion-fission cycle simulated for each mitochondrion, integrated with the phenomena of biogenesis and degradation and with the description of energetic stress. The dynamical rules are all updated at each cycle; for instance, the fusion phenomenon can hence take place even if two mitochondria are sufficiently closed one each other and if their masses are upper bounded. Also Tam et al. (2015, 2013) consider a static spatial framework by partitioning a 2D circular cell into a certain number of compartments. Fusion is hence influenced by the space because only mitochondria within the same or adjacent compartments can fuse each other. Even more complex is the model proposed in Patel et al. (2013), where unfused mitochondria are supposed to move along cytoskeletan filaments with a certain rate, such that the rate of fusion changes depending on the fact that none, one or both the two mitochondria that are experiencing fusion are moving at the time of the event.

Even if all these models may appear to convey more details than that proposed in our work, they suffer from the limitation of not being analytically treatable and they cannot be described by systems and control tools, which are required to allow the design of a control framework. This observation allows us to better state our contribution as follows.

c1. Being inspired by these aforementioned models (and by other simpler ones as in Hoitzing et al. (2015); Kowald and Kirkwood (2011)), we propose a prey-predator mathematical model, which at the same time is able to describe all the major phenomena of the mitochondrial dynamics and the damage degradation, and is also analytically treatable and coherent with observed phenomena.

c2. Moreover, our model differs from many of the other ones for taking into account the energetic framework, which plays a key role in the mitochondrial quality control. Inspired by Patel et al. (2013), which describes the biogenesis rate as a function of the total number of mitochondria, we include a feedback loop between the available ATP level within the cell and the biogenesis rate. This approach results in helping to understand how mitochondria behave in order to guarantee a sufficiently free ATP level, available to be consumed in response to a certain cell signal.

c3. The structure of the dynamical equations that are formulated yields the definition of a sensitivity analysis of the state variables with respect to all the parameters (including the input term), similarly to Dalmasso et al. (2017), as well as a study of the transient response to a step input due to an unexpected energetic stress, which affects the cell. In particular, a situation of impaired phenomenon can be tested by manipulating one of the nominal parameters related to the respective phenomenon: our proposed model can hence suggest in which part of the dynamics mechanism we should intervene in order to restore a normal (nominal) condition.

To mimic the complex set of phenomena that compose mitochondrial dynamics, our mathematical model exploits a prey-predator description in order to allow for an easy reading of the dynamical behavior of the mitochondrial population and to promote a tool to be used to simulate and test different hypotheses during an experimental design phase in biology. This model can be particularly useful to provide an insight into the relationship between biogenesis and ATP availability, an issue that is still not be completely understood, and into the mechanism of exchange that happens during fission.

Moreover, the presence of the feedback link between free ATP and biogenesis can easily describe how the cell is able to maintain a desired level of bioenergetic function, whereas the rate constants of fusion and fission can be analyzed to test different possible fission protocols. This concept is inherent in many biological system to provide self-healing capabilities to such systems. Since a wide number of neurodegenerative diseases have been referred in literature with mitochondrial dysfunctions, from a control theory point of view, this mathematical tool can support a qualitative understanding of which direction should be taken in order to improve the health level of cells in case of undesired situations. This is one of the most open and interesting question nowadays (Boland et al. (2013)).

Future work. In line with the recently discoveries on the role of mitochondrial dynamics into several cell's functions and its influence in a number of diseases, control system theory can provide helpful tools for the formulation and the discussion of models and controls, which can support the understanding of different mechanisms and suggest a regulatory loop for dysfunctional frameworks.

There are several improvements that can be envisaged and applied in order to make these tools more targeted and useful. First, with respect to the proposed model, we think of an extension of our prey-predator model into a set of multiple sub-classes, which can play as prey and predator for other different sub-classes at the same time.
Moreover, it could be surely interesting to implement a feedback loop for each rate constant (not only w.r.t. biogenesis), which links the available quantity of ATP with all

steps in mitochondrial dynamics and approaches the problem as a sort of Multi-Input Single-Output (MISO) system.
Indeed, one of the most interesting aspect is the design of specifically customized control laws that can provide a substantial help to suggest and predict treatments and therapy of different diseases.
Finally, this model and its derivations to follow should be clearly tested and validated against the experimental evidences, for example through measurements of mitochondrial dynamics, as data related to the mitochondrial membrane potential $\Delta\Psi_{\mathrm{m}}$ or measurements of the mitochondrial biogenesis and mitophagy phenomena rates.

4

Background: brain physiology and brain networks

"The chief function of the body is to carry the brain around."
T. A. Edison

There are a number of physiological processes that happen in the brain, and go on beyond the anatomy. What happens when a neuron is active is that it is receiving an input through its dendrites and then it is sending out information electrically through the axons (it is sending out little pulse of electrical activity or spikes, which travel down the axon into the axon terminals that then connect into the dendrites of other neurons which process that information). Refer to Figure 4.1 to follow this description. There is also a chemical activity which happens at the end of the axon terminals during the connections event, that happens at the synapse cleft (a tiny opening between two neurons). Thus, it is not an electrical conduction which happens between those two, but it is chemically based. Specifically, there are neurotrasmitters which are released from the axon terminal and they are taken up by the dendrites. This communication process requires other cells to support that activity and the introduction of oxygen and glucose in order to give enough energy for all of these processes to happen. Most of this metabolic demand is associated with the post synaptic changes.

Oxygen and glucose are required to be delivered in order to support these processes and they come from the blood, which is characterized by two different oxygenation

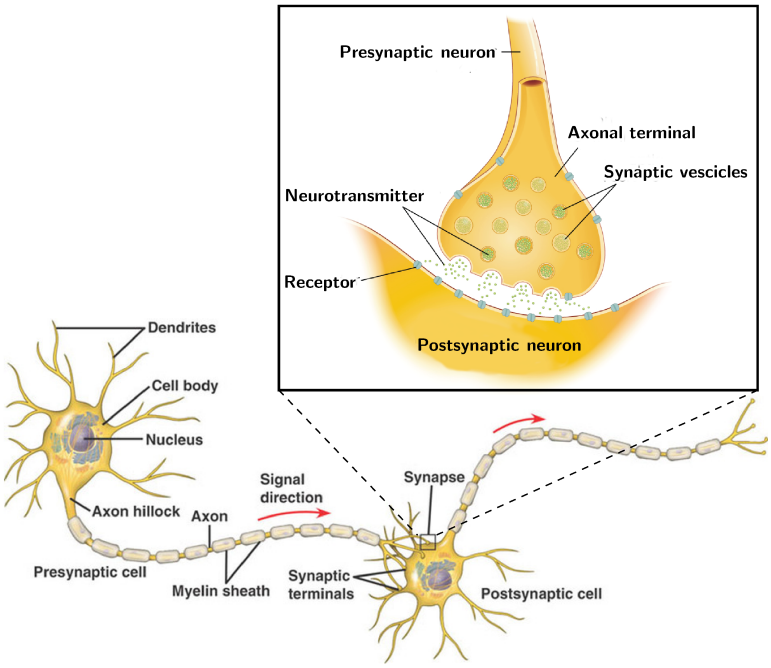

Figure 4.1: Representation of the electrical and chemical activity involving a neuron. Axons send electrical messages that are fired when neurotransmitters (chemicals specific to the nervous system) reach the dendrite of that neuron. Then, the chemical transmission among pre- and postsynaptic neurons take place. (Images modified from Betts et al. (2013)).

states that are magnetically different: the oxygenated hemoglobin or the deoxygeneted hemoglobin state. This magnetic difference between the two states allows us to see activity with the magnetic resonance imaging (MRI) scanner. Indeed, the changing in the magnetic properties is detected through the manner in which the water molecules near those blood cells are affected.

Rest and task-induced electrical activity Electrical activity in the brain may be differentiated into two modalities, by means of their temporal appearance.

m1. We refer to the so-called *resting-state* (RS) (or *baseline*) activity, to indicate a sustained activity mode, related to a condition of rest (i.e. a constant condition without imposed stimuli or other behaviorally salient events), and which may transiently decrease when the other modality is activated. RS activity has been related as *post-processing of information* mode (Magistretti (2006)), and it is referred to as the bulk of brain energy metabolism in term of quantity.

m2. The *task-specific* activation mode is instead transient in nature, and relates to *on-line processing of information* (Magistretti (2006)). In its whole, this modality

requires about 10% of RS energy, thus it is often referred as *the tip of the iceberg of brain metabolism* (Raichle (2003)).

This chapter has the purpose of presenting the preliminary notions on the different typologies of brain activity and some specific measurement techniques often used to record brain signals. Moreover, we report several mathematical tools useful when describing and analyzing these empirical data.

To this aim we cannot help but introduce the *connectome*, namely the description of the human brain as a graph of nodes, where these nodes can be interpreted at different scale, from single neurons, to large brain areas. This approach let us make use of systems and network theory in order to characterize the brain, both anatomically and functionally.

Contents

4.1 Different data to describe brain activity

In recent years, researchers from different fields have used several neuroimaging techniques (as fMRI, MEG, EEG, and PET) to get new insights on human brain functions. However, such non-invasive techniques are an indirect measure of the actual brain activity, which can only be estimated from the data. The combination of different modalities may be a useful tool to overcome this limitation and to be more confident of the results. On the other hand, this combination can bring to new discoveries only if the relationship among the modalities itself is well known. In Figure 4.2 we report the spatio-temporal resolution of several measurement methods (see the gray box for a brief description of the whole set of methods).

Among all the techniques used to measure the activity of the brain, we are particularly interested in functional magnetic resonance imaging (fMRI) and magnetoencephalography (MEG), since we had the opportunity to analyze real datasets derived from these techniques and we have addressed the problem of finding the possible relationship among them in some specific situations. Moreover, while fMRI data are usually measured to evaluate resting-state networks, MEG data may be more useful when specific tasks are performed. Here we report a brief description of these two signals and some results on their combination already reported in the literature.

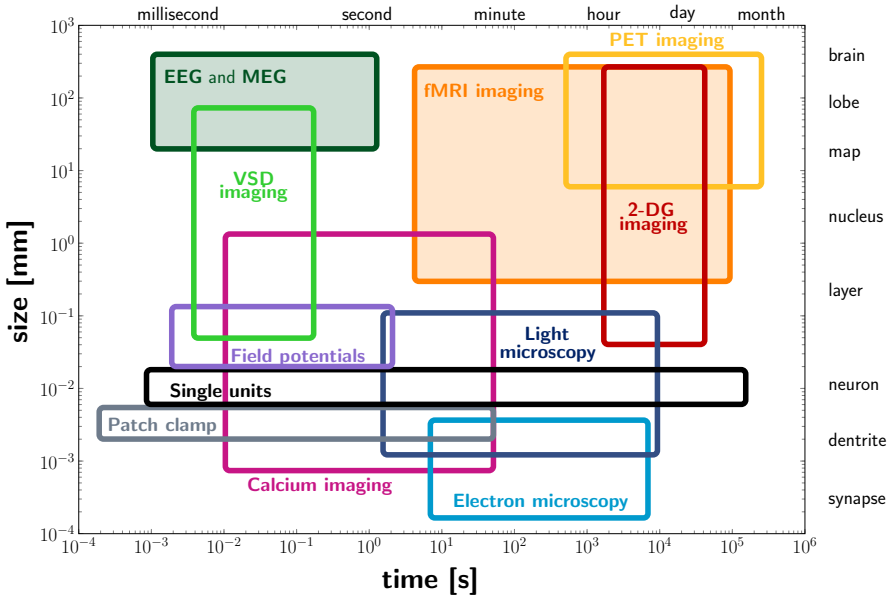

Figure 4.2: Spatio-temporal resolution of some of the most used methods for measuring brain activity. As noted, high-precision, invasive methods such as single unit recordings have high spatial and temporal resolution, but are not scalable to large-scale neural systems. On the other hand, non-invasive methods, such as EEG, MEG and functional MRI, are scalable but have poor spatial resolution. Filled areas refer to the technologies discussed throughout this thesis. **Abbreviations:** EEG, electroencephalography; fMRI, functional magnetic resonance imaging; MEG, magnetoencephalography; PET, positron emission tomography; VSD, voltage-sensitive dye; 2-DG, 2-deoxyglucose. See the main text and the gray box for a description of the measurement techniques. (Inspired by Fornito et al. (2016) [Fig. 2.1.1]).

4.1.1 fMRI data

Functional magnetic resonance imaging (fMRI) measures brain activity by detecting changes associated with blood flow that follows the changes in neuronal activity. Oxygen-rich blood and oxygen-poor blood have different magnetic properties, related to the hemoglobin that binds oxygen in blood. This fact causes a small effect on the MR signal, which is slightly stronger if the blood is more oxygenated. Moreover, an increase in neural activity leads to the blood being more oxygenated. These two aspects together make the blood-oxygen-level dependent (BOLD) signal detected by fMRI an indirect measure of the brain activity. (See Figure 4.3(a) for a description of the BOLD signal generation). This transient increase in MR signal is usually termed the BOLD hemodynamic response function (HRF). An example of the impulsive HRF is reported in Figure 4.3(b). Since it relies on the same principles as MRI, fMRI features a very high *spatial resolution* ($\sim$ 1mm). However, the hemodynamic response is much slower than the neuronal response and it takes several seconds for the HRF to peak in response to a stimulus

onset, and likewise several seconds to return to baseline following stimulus cessation. As a consequence, BOLD signals are characterized by low *temporal resolution*, due to physiological limitations themselves. Another drawback of fMRI signals consists in their susceptibility to physiological noise (as cardiac and respiratory cycles), and measurement parameters, like magnetic field strength, echo time, repetition time, and the imaging sequence used.

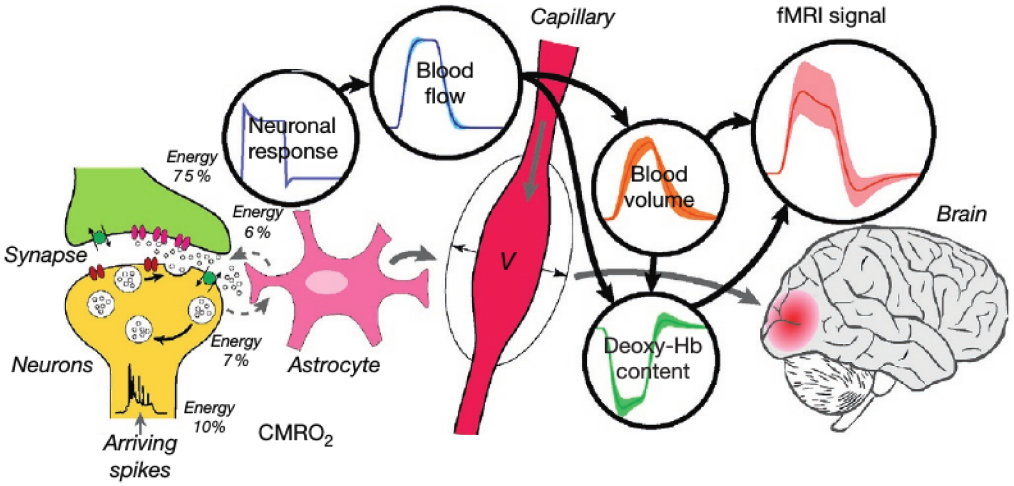

(a) BOLD signal generation. (Image from Toga (2015))

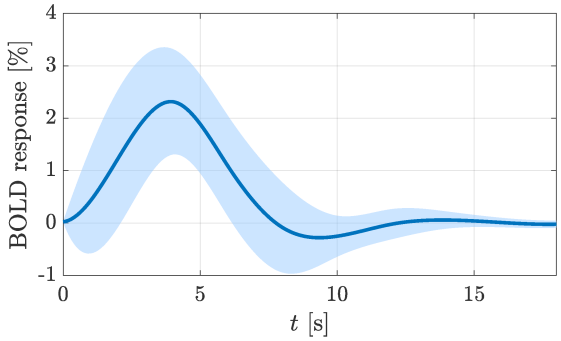

(b) Impulsive HRF

Figure 4.3: (a) Cartoon of the chain of physiological and physical event leading to the fMRI signal. Neuronal activity is associated with the cerebral metabolic rate of oxygen ($CMRO_2$) and induces chenges in cerebral blood flow. Such increase evokes increase in cerebral blood volume, and changes the amount of deoxygeneated blood. Finally, the blood oxygenation and the cerebral blood volume in a localized brain area are detected by the fMRI signal. **(b)** Example of the HRF to an impulse input, estimated[1] from the same empirical fMRI dataset used in Appendix A.8, referred to one subject. The light-blue coloured area represents two standard deviations of the estimated value.

4.1.2 MEG data

Magnetoencephalography (MEG) measures the magnetic fields induced above the scalp surface generated by the ionic currents flowing inside and outside neurons, driven mainly by excitatory postsynaptic activity (Figure 4.4). Specifically, these currents can be modelled as current dipoles, that are short segments along which the current flows from a source to a sink. For a detectable field, hundreds of thousands dentrites must be active synchronously. In theory, by using MEG devices, the sum of magnetic fields produced both by primary and volume currents are measured. However, in some brain regions, which can be approximated as a sphere with homeogeneous conductivity, the effect of volume currents may be negligible, and we can assume that the measured signal represents mainly the true neuronal activity (Pizzella et al. (2014)).

The magnetic sensors used to measure MEG signals are the superconducting quantum interference devices (SQUIDs), which are superconducting magnetic flux-to-voltage transducers featuring extremely low noise, with a field sensibility of about $1\,\mathrm{fT\,Hz^{1/2}}$. We remand to Clarke and Braginski (2006) for an extensive description. The sensor array is rigid and cannot be adjustable to the patient's head. A typical MEG system is composed by several hundred channels arranged on an helmet surface, and it measures simultaneously the magnetic field at multiple points over the scalp. See Della Penna et al. (2014) for a review of the existing MEG systems.

Since the MEG signals are measured outside the brain, a so-called MEG inverse problem has to be solved in order to estimate the source locations and their amplitudes as a function of time/frequency. Differently from the forward problem, aiming to predict the electromagnetic field generated by an arbitrary source configuration, the inverse problem is *ill-posed*, because a set of observations can be associated with infinite solutions. However, some information on source the configuration, and the use of suitable constraints make possible to define a problem with a unique solution (see Figure 4.5).

The *spatial resolution* of MEG technique is limited to about 5 mm, however its high *temporal resolution* of ∼1 ms makes possible the study of the dynamics of brain activity during time (see Figure 4.2).

[1]The estimation of the HRF has been performed with the method reported in Prando et al. (2017), and it goes beyond the scope of this manuscript.

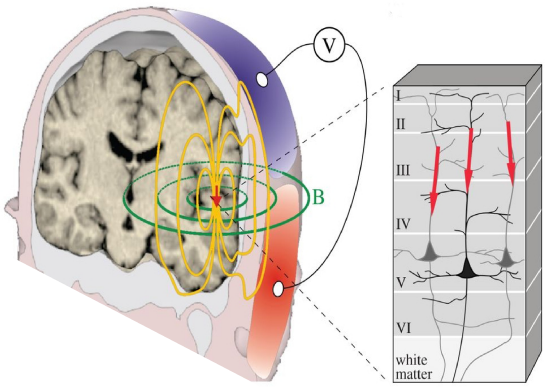

Figure 4.4: Genesis of EEG and MEG signals. **Left:** electric currents (red arrow) in active neurons drive volume currents (yellow lines) within the head, which gives rise to a potential distribution (V) on the scalp. The currents also generate a magnetic field (green lines; B) outside of the head; here the direction of the magnetic field follows (according to the right-hand rule) the direction of the net intracellular currents. **Right:** the main contribution to EEG and MEG signals comes from post-synaptic currents (red arrows) in the apical dendrites of pyramidal neurons. (Image adapted from Hari and Parkkonen (2015) [Fig. 1])

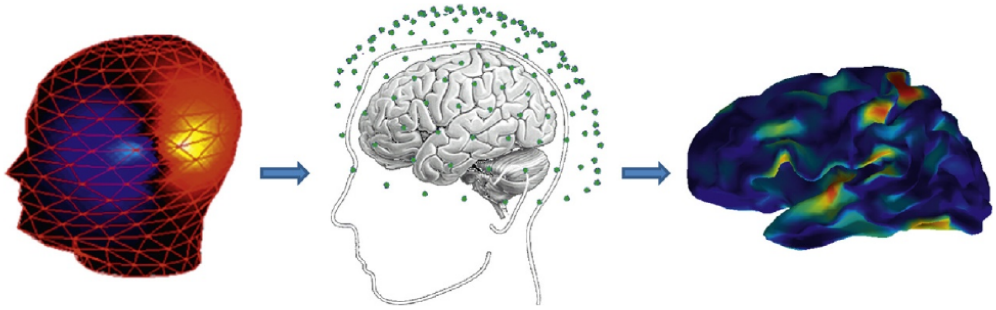

Figure 4.5: MEG signals measurement and inverse problem. **Left:** distribution of magnetic field measured outside the head. **Middle:** distribution of these magnetic field measurements relative to the head and cortical surface. **Right:** an estimate (based on additional prior information) of the current flow that gave rise to the magnetic field change. (Image adapted from Toga (2015))

Other brain activity measurement techniques mentioned in Figure 4.2

Calcium imaging is a powerful method to map neuronal interactions across large distances with cellular resolution. It measures intracellular calcium levels by introducing specific molecules, called calcium indicators, to neural tissue either by injection or transgenic methods. Since action potentials cause the cellular influx of calcium through voltage-dependent calcium channels, intracellular calcium can be used as a very accurate marker of spiking activity.

Electroencephalography measures brain signals through electrodes placed along the scalp,

by means of voltage fluctuations resulting from ionic current within the neurons of the brain.
Electron microscopy images the passage of electrons through a tissue specimen that has been stained with heavy metal elements. Some electrons pass through the tissue while others are scattered, creating a contrast that can be used to resolve anatomical features.
Light microscopy is an optical imaging technique that uses visible light to image small structures. Its resolution is thus limited by the visible wavelength of light.
Local field potential from an array of electrodes embedded in the culture surface provides a rich measure of activity with spatial resolution in the order of a few neurons per electrode.
Patch clamp techniques are laboratory techniques in electrophysiology used to study ionic currents in individual living cells, tissue sections, or patches of cell membrane. This method is especially useful in the study of excitable cells, such as neurons.
Positron-emission tomography is a technique used to observe metabolic processes in the body. Specifically, it detects pairs of gamma rays emitted indirectly by a positron-emitting radionuclide, which is introduced into the body on a biologically active molecule.
Voltage-sensitive dyes are dyes that change their spectral properties in response to voltage changes. They are able to provide linear measurements of firing activity of single neurons, large neuronal populations or activity of myocytes.
2-deoxyglucose imaging makes use of 2-DG, a known surrogate molecule that is useful for inferring glucose uptake and metabolism. Changes in 2-DG are used to identify changes in regional brain activity.

4.2 Graph theory and the brain

Graph theory plays a main role to understand the structure and function of several complex systems. The human brain is extremely complex, and naturally described by an interconnected distributed system. Thus it is natural to assume that graph theory may also be very useful for neuroscience. Specifically, brain networks may be graph-based represented in terms of square connectivity matrices, where each row (column) represents a different brain region (node in the graph) and each matrix element refers to an edge of the graph, indicating how connected each couple of areas is.

Graph theory have been taken part in neuroscience at different scales: from the microscopic scale of *C. elegans* (1998), to the macroscopic scale of human neuroimaging (from ∼2005), passing through the mesoscopic scale of tract-tracing data on the cat and the macaque (∼2001).

Thanks to this graph-based representation of brain networks, we can exploit several tools of graph theory in order to analyze, model and understand the functioning of the

whole brain or of a part of it. Depending on the specific application we are interested in, the matrix representation of the brain may change and describe a different *connectivity map* among the defined nodes.

Although it cannot be used to model every single detail of the brain, one of the main advantages of the use of graph theory for neuroscience is the simplicity. A graph is indeed able to reduce the myriad intricacies of the brain to a collection of nodes and edges, which can either be static or dynamic, and which can be implemented using an accessible mathematical language. However, the challenge is still to link topological metrics on abstract, simple graphs to biological mechanisms at cellular and molecular levels. Moreover, graph theoretical methods have the amazing characteristic of being generalizable to study complex systems of very different nature and scales. Multiscale measurements of brain networks indeed allow to recognize the same topological or dynamical features of the brain at different levels of analysis.

In summary, graph theory is a powerful tool for developing a coherent understanding of brain network organization that cuts across spatial and temporal scales, and which allows an understanding of how the connectome relates to a much broader class of complex systems.

In our research, we have focused on the meso- and macroscales of brain networks, and we neglect microscale analysis. Thus, in all what follows, only few information on the study of the brain at microscale is reported, while larger attention is devoted to larger scales analyses.

4.2.1 Connectivity maps

Three classes of brain connectivity are usually considered: structural connectivity (**SC**), functional connectivity (**FC**), and effective connectivity (**EC**) (Bullmore and Sporns (2009); Fornito et al. (2013); Friston (2011)). Each of these different connectivity maps can be evaluated through a specific set of data typology (see Figure4.6).

Structural connectivity. **SC** refers to the anatomical connections among neural elements. At different scales, these connections may assume distinct forms, such as axons and synapses between neurons at the microscale, or large-scale fiber bundles or fasciculi linking cortical and subcortical areas at meso- and macroscales. The structural connectivity maps can hence be measured using techniques as electron microscopy (micro), axonal tract-tracing (meso), and diffusion MRI (macro). In theory, structural connectivity should be directed, since each axon has a source and a target. However, it is often represented as undirected, as some measures are not able to resolve the directionality,

Figure 4.6: Schematic relationship between the various connectivity maps used to describe brain networks. **SC**: structural connectivity; **FC**: functional connectivity, **EC**: effective connectivity. (Modified images from ©1999-2017 Getty Image, Fornito et al. (2016), Xia et al. (2013)).

but only the existence and strength of the connections.

Functional connectivity. **FC** refers to a statistical dependence among data recorded at different neural elements. It is different from the anatomical connectivity, because it is not necessary to have a direct wiring between two elements of the brain for them to be functionally connected (for example, they can be connected through a third one). In the literature, several statistical measures have been used in different domains (time, frequency or wavelet domain). Depending on the source of data used to quantify the functional link among elements (nodes, or brain areas), this connectivity map assumes different meaning. Useful data to define **FC** maps are the recording of neurons' spikes (at microscale), hemodynamic signals, MEG, EEG (at larger scales). Moreover, one can also differentiate among resting-state **FC** (**rsFC**) and task-induced **FC**. When a meso-

or macroscale is considered, the interpretation of the **FC** map can be summarized as follows:

> **task-induced FC:** it refers to a condition such that the participant is doing a particular task, seeing what areas of the brain respond when the task is being performed, in a different way from when the task is not being performed;
>
> **rsFC:** it is a representation of which areas in the brain seem to respond functionally similarly in a spontaneous way. In the context of resting-state activity, it is more convenient to go beyond the cellular scale and focus on the mesoscale, where groups of several neurons are considered together and define brain areas.
> From coordinated analyses of **rsFC** and **SC**, a direct relationship among the two maps has emerged. Specifically, if two brain areas are structurally connected, then it is likely possible that they are also functionally linked during RS (Damoiseaux and Greicius (2009); Greicius et al. (2009); Van Den Heuvel and Pol (2010); Van Den Heuvel et al. (009a)). However, the opposite is not necessarily true, since the functional communication among areas does not imply that there is a direct anatomical link among them (Koch et al. (2002)).

FC map can be either directed or undirected, depending of the measure used to estimate it. For instance, in case of Pearson's correlation coefficient, the resulted **FC** is undirected, whereas Granger causality analysis yields a directed functional connectivity map (These measures will be described in Section 4.3.3).

Effective connectivity. While **FC** connectivity is estimated at the level of measured data, **EC** refers to the neuronal, sometime not measurable, level, and it includes information about the causality and direction of the connections. Therefore, it is always a directed map among the nodes. Specifically, the functional connectivity map may be considered as the consequence of the effective connectivity. The same data used to estimate **FC** can be used to infer **EC**, however, the analysis can be computationally very expensive.

4.2.2 The connectome network

Apparently, a lot of different ways may be used to associate a network to the connectome (i.e. the description of the human brain as a graph of nodes). However, if we want to represent the brain as a graph, we have to ensure that this graph matches with the known characteristics of the brain, that we report here. At first, in general, the nodes we define should be spatially embedded, since nervous systems exist in physical space

and spatial constraints have an important influence on network topology (Bullmore and Sporns (2012)). Then, they should be intrinsically homogeneous, and represent a coherent functional entity. On the other hand, they should also be extrinsically distinct or heterogeneous, allowing a differentiation among them based on some relevant characteristics. Second, to be realistic, the edges may reflect the connectivity feature of the brain areas. Both structural and functional connections are inherently directed: as mentioned in the previous section, structurally speaking, each connection has a source and a target, while functionally, there is a causal relationship among brain areas. However, some measurement techniques do not allow to resolve the directionality in **SC**, and several metrics used to define **FC** are symmetric. Then, we have to take into account the variability of the edges in terms of weights and type. In **SC** the strength of links varies in terms of the number of connecting fibers, the cross-sectional area, conduction speed and numerous other physical parameters. Functionally, different pairs of brain regions vary over time in their propensity for synchronization. In addition, the communication among pairs of nodes may have very different nature, such as chemical or electric, and function, e.g. excitatory and inhibitory interactions, or positive and negative correlations.

Another very important property that has to be considered when projecting the brain into a network is its dynamics, which obviously changes with respect to the scale we are considering. Since we are specifically interested in meso- and macroscale descriptions, structural connectivity changes over periods spanning days to years in accordance with developmental programs or experience-dependent plasticity (Zatorre et al. (2012)), thus it is usually considered as constant. **FC**s instead display different dynamics, depending on the measured data. Even though it is slower than the fast dynamics of neuronal ensembles that rapidly synchronize and desynchronize, the larger sales' dynamics are also evident. Faster time-scales are readily accessible with invasive recording techniques or non-invasively with EEG and MEG (Figure 4.2). Functional MRI represents only slower dynamics, although computational modeling suggests that rapid dynamics contribute to BOLD signal fluctuations (Deco et al. (2008)).
As reported in Fornito et al. (2016), the ideal brain graph should have the following fingerprint:

1. spatial embedding,
2. heterogeneity of node properties,
3. directionality of connectivity,
4. weight of connectivity,
5. heterogeneity of edge types,
6. dynamic changes in network organization.

Nevertheless, this is an ideal representation of the brain, which is very hard to implement. Hence, current maps and models capture some of these properties and do not capture others. We take this description into account in Chapters 5 and 6, where brain networks and models are built and discussed.

4.3 The activity of the brain

Brain rhythms. The combined electrical signals produced by neurons in the brain generate oscillations (brain waves). Thus, the brain activity is related with the concept of *synchronization*, which, in first place, can be thought as a measure of how coherent the behavior of different agents is. Synchronized activity between and within neuronal assemblies produce *brain rhythms*, that are fully described by their amplitude, frequency and phase. Traditionally, brain rhythms have been classified with respect to their frequency content, since the different frequency bands of brain oscillations are supposed to have functional significance, and to represent the brain strategy for processing parallel information and controlling co-occurrent processes at different spatial and temporal scales.

Specifically, as measured through MEG, a significant *delta* band activity (1-4 Hz) has been related to sleep activity in healthy subjects, while *theta* band power (4-7.5 Hz) has been shown to increase in arousal and working memory tasks. The best known frequency band is *alpha* (8-12 Hz), which correlates with rest condition. For instance, alpha suppression during the execution of a task is correlated with the activation of the recruited cortical areas (Pfurtscheller and Da Silva (1999)). Motor processing, sensorimotor control, sensory-motor integration, corticospinal coupling and proprioception are instead correlated with *beta* frequency band (15-25 Hz). Finally, oscillations above 30 Hz (*gamma* band) have been related to activity of limited cortical areas for stimulus selection, feature integration, pattern recognition, attention, multisensory integration, sensorimotor integration, pain processing, empathy and memory (Pizzella et al. (2014)). Figure 4.7 shows an example of a filtered time series extracted from a dataset of MEG signals.

4.3.1 Resting state (RS) activity

For several years, the existence of slow correlated fluctuations during rest has not been considered, and only task-induced activity was investigated. However, this kind of slow activity was particularly disturbing for studies aiming to detect only task-related (evoked) neuronal activations, since this ongoing activity was found to contribute for the variance

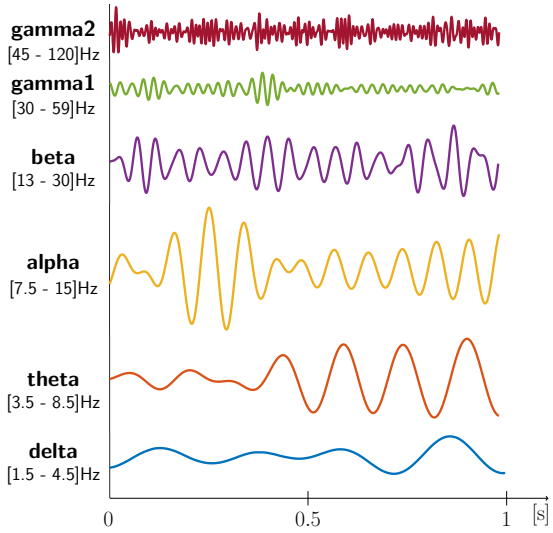

Figure 4.7: Example of filtered MEG data at different frequency bands. The used dataset and the selected bands are the same which will be considered in Chapter 5.

observed in evoked cortical responses (Arieli et al. (1996)). Thus, it became necessary to define a *baseline* (or *default-mode*) activity, which confirms that it exists a spontaneous activity of the brain, that cannot be considered simply as noise. Hence, when switching from rest to a particular task, not only activation of the task-related areas is observed, but also deactivation in certain other areas, suggesting that those ones are areas actively engaged during RS. In particular, further analyses provided evidence for the existence of a cohesive default mode network (DMN) (Greicius et al. (2003)), which involved a specific set of brain areas that are more functionally connected during resting-state than during any other tasks. Moreover, in this regime, also other groups of brain regions exhibit correlated activations, even if revealed to be more connected during some specific task than in rest.

The investigation on the nature of the mechanism underlying baseline brain activity has attracted considerable attention in the last years from several perspectives. The reason is that not only resting-state activity represents 90% of brain metabolism, but also the baseline activity appears to be dynamically regulated and varying under a wide range of physiological and pathological conditions (Raichle (2003); Shulman et al. (1997)). The function of the RS activity is not still completely understood, however one of the most intriguing hypotheses is that it reflects, at least in part, ongoing processes of synaptic plasticity, which are related to the post-processing of incoming information.

The interest on studying resting-state behaviors increases even more, if we consider that a large number of studies have reported altered resting brain activity in a wide range

of mental illness. Among all, these results have provided new insights on dysfunctional mechanisms and possible treatments of them. For instance, from functional analyses of the brain networks in Alzheimer's Disease it emerged that some topological features of healthy **rsFC**, like small-world properties, are not recovered in case of AD. On the other hand, schizophrenia seems to be related to a general decrease in **rsFC** values, suggesting that schizophrenia may arise from the disrupted functional integration of segregated brain areas. Many other mental diseases result to be correlated with abnormal functional connectivity in rest; however, the research in this field is still in process and a lot of new moves might be done.

One of the most used technique to analyze functional dynamics during resting-state is fMRI. However it is worth noting that, as an indirect measure of the brain activity, the BOLD signal cannot accurately assessed the exact neural mechanism at the origin of the observed fluctuations. Furthermore, this measure is sensitive to physiological noise, like heart and respiratory signals, which is nowadays not completely removable.

4.3.2 Task-induced activity

When studying task-induced activity in the brain, the aim is to identify the brain mechanism elicited by the specific task-related stimulus. Thus, one of the most widely used strategies consists in selecting a battery of stimuli that reflect very specific tasks for the brain and defining the baseline activity of the brain before the onset of each stimulus. Many repetitions of the same tasks are typically considered, so that, it is possible to identify and characterize the spatial and temporal response of the brain with respect to a rest condition.

Moreover, event-related cortical activity can be divided into *evoked* and *induced* components, which have different functional descriptions. The functional role of induced activity is assigned to top-down modulation through backward connections and lateral interaction, whereas in evoked components the bottom-up driving processes predominate (Tallon-Baudry and Bertrand (1999)). The difference between evoked and induced components can be in practice identified in their phase-response to timed event: while evoked responses are phase-locked to the stimulus, induced responses show trial-to-trial variation in latency (Chen et al. (2012)). However, this distinction goes beyond the object of this thesis, and we will use the two terms *evoked* and *induced* as synonyms.

4.3.3 Mathematical tools to describe brain's activities

In the previous sections we have introduced the different typologies of brain activity, and we have mentioned that functional or effective connectivity maps may be useful to

describe the existing relationship among the activity of different brain areas. However, we have not presented the mathematical tools usually implemented in order to derive such connectivity maps, so far. In this Section we report a brief exploration of the main mathematical measures used to define **FC** maps, since we will refer to this kind of maps in the following chapters. Nevertheless, some of these tools can be used also to infer **EC** maps, when the data refers to the source level.

4.3.3.1 Functional connectivity maps and RSNs estimation

To define **FC** networks during resting-state it is not possible to use the same strategies used to infer *evoked* functional networks (see subsection 4.3.2), during which they are captured by comparing a measure of brain activity during a particular task with baseline data sets. However, several approaches have been used to define resting-state networks (RSNs), such as correlation measures, coherence analysis, independent components analysis (ICA), principal component analysis (PCA), mutual information (MI), and phase locking evaluation (PLV).

Among all the aforementioned measures, we describe here how to evaluate *linear correlation* and *phase locking value*, since we will refer to these particular quantities in the following chapters. However, an illustration of the other measures is reported in Appendix A.2.

One of the most widely applied method to infer functional interactions is the estimation of the **Pearson's linear correlation coefficient** between each pair of temporal signals $x(\cdot)$ and $y(\cdot)$, which is defined by

$$\rho_{xy} := \frac{\sum_{t=1}^{T}\left[(x(t)-\bar{x})(y(t)-\bar{y})\right]}{\sqrt{\sum_{t=1}^{T}(x(t)-\bar{x})^2}\sqrt{\sum_{t=1}^{T}(y(t)-\bar{y})^2}} = \frac{\sigma_{xy}^2}{\sigma_x\sigma_y} \in [-1,\ 1], \tag{4.1}$$

where T is the number of time instant used to estimate the correlation coefficient, $\bar{x} = \sum_{t=1}^{T} x(t)/T$ is the mean value of signal $x(\cdot)$ across time, $\sigma_x = \sqrt{\sum_{t=1}^{T}(x(t)-\bar{x})^2/T}$ is the standard deviation of $x(\cdot)$, and finally $\sigma_{xy}^2 = \sum_{t=1}^{T}\left[(x(t)-\bar{x})(y(t)-\bar{y})\right]/T$ is the cross-covariance among signals $x(\cdot)$ and $y(\cdot)$. A high positive correlation indicates cooperation and integration between the signals; a correlation close to zero indicates no linear relationship; a negative correlation (or anticorrelation) indicates antagonism and segregation. By shifting one of the two time series with respect to the other, it is possible

to infer the lagged correlation $\rho_{xy}(\tau)$ as follows:

$$\rho_{xy}(\tau) = \frac{\sum_{t=1}^{T}\left[(x(t)-\bar{x})(y(t-\tau)-\bar{y})\right]}{\sqrt{\sum_{t=1}^{T}(x(t)-\bar{x})^2}\sqrt{\sum_{t=1}^{T}(y(t)-\bar{y})^2}} \in [-1,\ 1]. \tag{4.2}$$

Note that equations (4.1) and (4.2) are such that $\rho_{xy}(0) = \rho_{xy}$. In particular, two levels of analysis are possible through this metrics:

1. *seed-based correlation*, which looks at the correlation between one specific region and the rest of the network. This kind of analysis requires some information on the main activation sites of a certain RSN, and then, the co-activations seed map can be built by overlapping the correlation maps of each seed;
2. *correlation matrix*, which estimates all possible functional connections among each pair of region, and which can be analyzed through graph theory to evaluate the topological properties of such matrix, and to infer its functional modules and hubs.

When using (4.1) to quantify the functional connectivity map, some key properties are to be considered. First of all, ρ_{xy} only estimate the *linear* dependence among signals, discarding possible non-linear correlations, that are instead captured by other measures, as MI or synchronization analysis. Second, the correlation coefficient is sensitive to indirect effects, which arise when two nodes show correlated activity even in absence of a direct anatomical connection (Rubinov and Sporns (2010); Smith et al. (2011); Zalesky et al. (2012)), thanks to a third, intermediary node, or to a common driving stimulus (co-activation), or fluctuations in physiological and neuromodulatory processes. One of the main drawback of this functional measure is that it does not distinguish between the two principal coupling modalities hypothesized to underline brain function, that are phase coupling, and amplitude coupling. Phase coupling quantifies the consistency of the relative phase between two signals that oscillate with the same frequency[2], whereas amplitude coupling is typically quantified as the correlation of the amplitude envelopes of the signals (Figure 4.8).

A different measure to describe functional relationships among signals, by means of phase cohesiveness, is the **phase locking value** (PLV), which indicates how locked are the phases of two signals during time. Given two signals $x_i(\cdot)$ and $x_k(\cdot)$, and their respectively phases $\theta_i(t)$ and $\theta_k(t)$, their PLV is estimated as:

$$\mathrm{PLV}_{\theta_i\theta_k} = \left|\frac{1}{T}\sum_{t=1}^{T} e^{\mathrm{j}[\theta_k(t)-\theta_i(t)]}\right| \in [0,\ 1], \tag{4.3}$$

[2] As discussed in Chapter 7, phase synchronization requires frequency synchronization to be achieved.

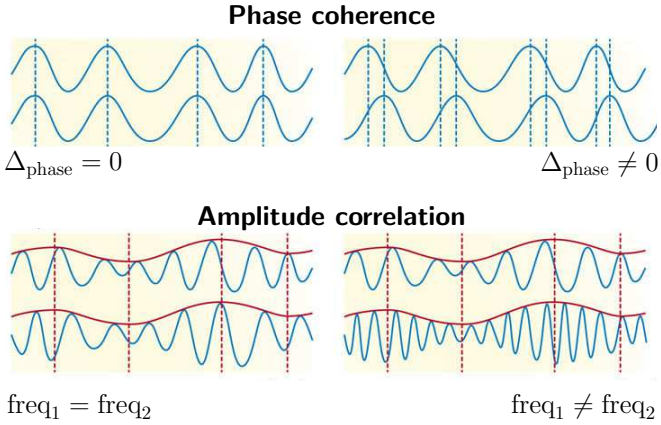

Figure 4.8: Examples of the two principal coupling modes of neurophysiological signals: phase and amplitude coupling. **Top:** phase coupling between two electrophysiological signals. Left shows an example of two signals in perfect phase synchrony with zero lag. The peaks and troughs of the oscillations occur at the same time. Right shows an example of phase synchrony with a non-zero lag. In this case, the phase of one signal is shifted with respect to the other, but the relationship is consistent across the recording period. **Bottom:** amplitude correlation is a measure of the correlation of the envelopes (shown in red) of two simultaneous oscillatory signals. Amplitude correlation can be measured between oscillatory signals of the same or different underlying carrier frequencies. Amplitudes can be positively correlated or negatively correlated. Here there is positive amplitude correlation between two oscillatory signals of the same (left) and different (right) underlying carrier frequencies. Phase coherence and amplitude correlation are *independent* of one another. This is exemplified in the bottom-left panel, in which the amplitudes of the two oscillations are correlated but the underlying oscillations are not phase coherent. (Images adapted from Siegel et al. (2012) [Fig. 1])

where T is the number of time instants used to estimate the PLV. Its value is always bounded by 0 and 1, and specifically, it is equal to 0 if the two phases are fully unlocked, while it is equal to 1 if they mantain the same distance at each instant of time ($|\theta_j(t) - \theta_i(t)| = \gamma$, for all $t = 1, \ldots, T$).

In addition to define a complete functional relation among each pairs of nodes, the aim is also to find a method in order to divide all the brain areas (nodes) in a certain number of subsets (groups, clusters), such that each node has a behavior coherent with the other nodes in the same cluster, but different from the nodes of the other groups. We use terms *module*, *cluster*, *group* and *community* interchangeably throughout this and following sections. Given a set of observations during time, there are several data clustering methods, among which we differentiate between **hierarchical algorithms** and **centroid-based algorithms**. The hierarchical algorithms may in turn be categorized into two broad classes: agglomerative and divisive. The first group includes methods that start with individual data points and group them together into larger clusters, while the latter includes methods starting with all nodes in a single cluster and attempt to find

divisions that delineate cohesive subsets of observations. The basic idea of centroid-based clustering instead is to define clusters based on the distance of each member of the group and the so-called centroid of the cluster itself, which is considered as representative for the whole community. Even though an exhaustive review of all the proposed clustering methods goes beyond the scope of this thesis, in Appendix A.4.1 we report a brief description of the most widely used algorithms in brain network, that we will exploit in the following sections.

While agglomerative hierarchical clustering requires the definition of rules used to aggregate element based on similarity measures, divisive hierarchical clustering does not, since it can be computed using standard graph theoretic methods, and it may be used to distinguish between communities consistently at each resolution scale (see Appendix A.4.1 for further details).

The main advantage of hierarchical clustering methods is that they do not need prior information on the number of groups that should be found from the data. However, they do not even give any information to determine whether the clustering solution obtained at one level is more valid or reliable than another.

In order to overcome this problem, in Newman and Girvan (2004) a modularity-based approach has been proposed, which should be able to measure also the quality of a partition at each scale of the clustering solution. Without going into the details of the algorithm, in Appendix A.4.1 we report the definition of the so-called *modularity index*, which can be evaluated once a partition of nodes has been defined.

The modularity index can either be used to quantify the quality of a partition that has been defined using any method for community detection, as a post-hoc test, or it can been incorporated into the clustering algorithm itself. Among several computational algorithms that have been proposed to implement a method to identify directly the best partition of a graph, the Louvain algorithm (Blondel et al. (2008)) is one of the most widely used methods, thanks to its computational low cost and accuracy.

Co-activation patterns of synchronized areas Rather then applying a clustering algorithm to the brain areas, other approaches are based on clustering time-frame instead of nodes, in order to define a certain number of co-activation patterns involving many (possible overlapping) brain regions (Tagliazucchi et al. (2012); Liu and Duyn (2013); Liu et al. (2013)). To do that, two similar (but different) methods have been proposed in the literature.

In Tagliazucchi et al. (2012), the authors support the idea that important information is compressed in few timing points, which are sufficient to derive the RSNs and their activation maps. After having normalized each measured BOLD signal by its own

standard deviation, they select the time points at which the signal is higher then a selected threshold (they specifically used one standard deviation as threshold). Then, they use an algorithm implemented in MATLAB®, based on the detection of connected components in co-activated first neighbors graph, in order to detect spatial clusters of activated voxels. This method, although simple, has been proved to recognised networks of areas coherent with the ones reported in literature. Furthermore, it allows not only the detection of networks, but also the specific time period during which they are more or less active. This method is referred as point process analysis (PPA).

Not long after, a similar method has been proposed (Liu and Duyn (2013); Liu et al. (2013)), which, rather than selectively averaging time points of activity increase in a seed region, classifies and averages time points with similar spatial distributions of activity using the k-means clustering algorithm to define co-activation patterns (CAPs). Specifically, after clustering, the time frames assigned to the same cluster are simply averaged, resulting in K maps (or CAPs). These CAPs are then normalized by the standard error (within cluster and across time frames) to generate Z-statistic maps, which quantify the degree of significance to which the CAP map values (for each voxel) deviate from zero. The idea under this strategy is that by averaging selectively frames, finer details regarding spontaneous co-activations of multiple brain regions may be extracted.

4.3.3.2 Clusters' dynamics estimate

All the functional connectivity measures described above are static measures, which can be used to detect the RSNs, but not their dynamics. As one of our aims is the analysis of spatio-temporal patterns of synchronization during time, we need to introduce some tools to handle this task. Specifically, we will employ two different methods, which have been both used to describe synchronization patterns in brain networks (Ponce-Alvarez et al. (2015); Allen et al. (2014)), both based on the definition of tensor matrices of dynamic functional connectivity. These modalities are based on methods to derive patterns of synchronization.

Tensor-FC definition. The basis idea to analyze the variability of functional connectivity consists in defining a tensor (or three-dimensional matrix) $\mathbf{T} \in \mathbb{R}^{N \times N \times L}$, which describes the functional connectivity map among regions at $L \leq T$ instants of time, being T the total time steps of the measured signals. In literature, several definitions of tensors can be found. Specifically we considered two cases, the first of which (**t1**) is applicable during phase coupling analysis only, whereas the latter (**t2**) can be employed during any kinds of analysis, by selecting a suitable **FC** metric.

t1. By considering $L = T$, tensor $\mathbf{T} \in \mathbb{R}^{N \times N \times T}$ can quantify the phase distance among nodes, in such a way that

$$[\mathbf{T}]_{ijt} = |\theta_j(t) - \theta_i(t)|, \qquad \forall\, i, j = 1, \ldots, N \qquad \forall\, t = 1, \ldots, T, \tag{4.4}$$

or its binary version $\mathbf{T^b} \in \mathbb{R}^{N \times N \times T}$:

$$[\mathbf{T^b}]_{ijt} = \begin{cases} 1, & \text{if } |\theta_j(t) - \theta_i(t)| < \phi, \\ 0, & \text{otherwise} \end{cases} \quad \forall\, i, j = 1, \ldots, N \quad \forall\, t = 1, \ldots, T, \tag{4.5}$$

where ϕ is a selected threshold angle within the interval $[0,\ \pi]$.

t2. Otherwise, the sliding windows method can be applied: it divides the whole set of time instants into L windows of W time points each, used to evaluate the functional connectivity (with respect to a desired metrics) at time point l ($\mathbf{FC}(l)$) through the values of the signals within the time interval $[l - W/2,\ l + W/2]$, with $l = 1, \ldots, L$. In this way, a tensor $\mathbf{T} \in \mathbb{R}^{N \times N \times L}$ of $\mathbf{FC}$s is defined, such that $[\mathbf{T}]_{ijl} = [\mathbf{FC}(l)]_{ij}$.

While the sliding windows-based tensor is analyzable through both the methods, which we are going to describe, a tensor defined with respect to the instantaneous phase difference is preferably to be referred only to the fist method.

Non-negative tensor factorization (NNTF). Non-negative tensor factorization can be seen as an higher-order Principal component analysis (PCA), as it is based on the canonical decomposition of a tensor representing the synchronization networks during time. The aim is hence to find an approximation $\widetilde{\mathbf{T}}$ (or $\widetilde{\mathbf{T}}^{\mathbf{b}}$) of tensors $\mathbf{T}$ (or $\mathbf{T^b}$), which can be decomposed into K rank-one positive tensors in the form:

$$\mathbf{T} \approx \widetilde{\mathbf{T}} = \sum_{i=1}^{K} \mathbf{a}_i \circ \mathbf{b}_i \circ \mathbf{c}_i, \qquad \mathbf{a}_i \in \mathbb{R}^N, \qquad \mathbf{b}_i \in \mathbb{R}^N, \qquad \mathbf{c}_i \in \mathbb{R}^T, \tag{4.6}$$

where $\circ$ is the outer product of vectors ($\mathbf{x} \circ \mathbf{y} = \mathbf{x}\mathbf{y}^\mathsf{T}$). The idea is to find the integer K and the set of *positive factor matrices* $\mathbf{A} = [\mathbf{a}_1, \ldots, \mathbf{a}_K] \in \mathbb{R}^{N \times K}$, $\mathbf{B} = [\mathbf{b}_1, \ldots, \mathbf{b}_K] \in \mathbb{R}^{N \times K}$, and $\mathbf{C} = [\mathbf{c}_1, \ldots, \mathbf{c}_K] \in \mathbb{R}^{T \times K}$, which best approximate the original tensor with respect

to a specific norm (in this case we consider the Frobenius norm $\|\cdot\|_{\mathrm{F}}$):

$$\{K, \mathbf{A}, \mathbf{B}, \mathbf{C}\} = \arg \min_{K,\mathbf{A},\mathbf{B},\mathbf{C}} \|\mathbf{T} - \widetilde{\mathbf{T}}\|_{\mathrm{F}}^2, \tag{4.7a}$$

$$\text{s.t.} \begin{cases} \mathbf{A}, \mathbf{B}, \mathbf{C} \geq 0 \\ K \in \mathbb{N} \end{cases}, \tag{4.7b}$$

where the symbol $\geq$ means that each element of matrices $\mathbf{A}$, $\mathbf{B}$, and $\mathbf{C}$ is non-negative. Since at each time step t, it is $[\mathbf{T}]_{ijt} = [\mathbf{T}]_{jit}$, we have $\mathbf{A} = \mathbf{B}$. The interesting part of this decomposition is its interpretation in terms of synchronization patterns' dynamics. In particular, the column vectors of $\mathbf{A}$ represent the K communities, and the i-th element of vector $\mathbf{a}_j$, $[\mathbf{a}_j]_i$ can be interpreted as the participation weight of node i to the community j. On the other hand, the K columns of matrix $\mathbf{C}$ are a measure of the activation level of the K communities during time (the t-th element of vector $\mathbf{c}_j$, $[\mathbf{c}_j]_t$, is the activation level of cluster j at time step t). This particular configuration allows the definition of clusters of nodes different from a partition, since each node may take part to different communities, with different participation weights. Moreover, each community is not static, but its activity level may change during time. Finally, at each time step t, the strength of community i is defined as the sum of all the participation weights of the community multiplied by its activation level at time t:

$$s_i(t) = [\mathbf{c}_i]_t \sum_{j=1}^{N} [\mathbf{a}_i]_j \in \mathbb{R}, \qquad \forall\, i = 1, \ldots, K, \qquad \forall\, t = 1, \ldots, T. \tag{4.8}$$

A measure of the global strength of the network during time is directly derived as the sum over all the single $s_i(t)$:

$$S(t) = \sum_{i=1}^{K} s_i(t), \qquad \forall\, t = 1, \ldots, T. \tag{4.9}$$

Dynamic-FC clustering. Given a tensor of **FC** maps, for each $l = 1, \ldots, L$, the upper triangular part of the symmetric $\mathbf{FC}(l)$ matrix can be vectorized, in order to achieve a matrix of dimension $N(N-1)/2 \times L$, whose column l is the functional connectivity at time l, and whose row i is the evolution of link i during time. In other words, in this way we are characterizing the dynamics of the edges of the brain graph, rather than the dynamics of the nodes. Then different strategies can be chosen. For instance, clustering methods can be applied to clusterize instants of time with similar functional coupling together, and to define a set of states given by the centroids of each cluster. Otherwise, a

correlation matrix among each of the L columns can be evaluated, and used as an input for a modularity clustering as described above, to define a set of modules with similar characteristics. Again, the average across the columns which participate to the same module can be used to describe the synchronized networks.

By evaluating the occurrence of each pattern during the whole period, a description of the dynamics of the RSNs is quantified. However, unlike NNFT, this method assumes that at each time point l only one pattern is active, and it does not admit the co-activation of different networks with different activity level in the same time. Moreover, as other clustering methods, this approach needs some a priori information on the correct number of clusters, or at least some metrics to quantify the goodness of each different choice.

4.3.4 Task-induced activity estimation

When comparing task-induced response with resting-state activity, we can suppose that task and ongoing conditions sum linearly and we can evaluate the first by subtracting the baseline from the measured signal during task. Otherwise, a more sophisticated method to estimate the non-linear relationship among the two components can be used, such as the dynamic causal model (DCM) (Friston et al. (2003)). The central idea behind DCM is to treat the brain as a deterministic non-linear system that is subjected to inputs describing a specific task. More recently a stochastic version of DCM has been proposed to describe the resting-state dynamics rather than the task-induced one (Friston et al. (2014)). In that case, the deterministic input is replaced with a stochastic input, which refers to endogenous fluctuations. As during our research we have not dealt with DCM, we remand to Friston et al. (1995, 2014) for further details about this computational technique.

5

fMRI and MEG: a task-induced comparison

"The human brain produces in 30 seconds as much data as the Hubble Space Telescope has produced in its lifetime."
K. Kording

In Section 4.1 we mentioned the great role that a combination of different technologies may have in finding new insights on the activity of our brain. However, before combining results obtained from different data, it is necessary to analyze the peculiarity of both modalities and highlight similarities and differences.

We are specifically interested in fMRI and MEG technique (see Sections 4.1.1 and 4.1.2), whose relationship is still under debate. A comparison among them focused only on resting-state dynamics can be misleading, due to the physiological differences of the two signals. Thus, we address this problem by observing the response to a specific task, when it is measured by means of fMRI or MEG techniques.

In this chapter we treat this problem focusing on a specific visual-attentional task. After a brief introduction on the relationship between fMRI and MEG signals, and a recall of the main results on the same task experiment reported in Spadone et al. (2015) obtained only with fMRI data, the aim of this chapter is twofold and it is summarized in what follows.

RSNs: prior for task, or idling state? First of all, starting from the results reported in Spadone et al. (2015) for what concerns fMRI data, here we carry on with the analysis and we investigate whether similar results emerge from MEG data. To this aim, we measure how slow fluctuations of MEG signals change from rest to task and across different frequency bands. Specifically, two hypotheses on the role of resting-state networks have to be tested.

h1a. RSNs represent spatio-temporal *priors* for task networks, and their modulation contributes to task-evoked responses. This means that the **FC** during rest recalls task-dependent behavior, thus providing a sort of prediction about coming stimuli. This hypothesis is supported by several works, which report the stability of the RSNs topography across behavioral states (Arfanakis et al. (2000); Fransson (2006)), and an high level of similarity between RSNs and task networks involved by common cognitive tasks (Smith et al. (2009); Cole et al. (2014)).

h1b. RSNs reflect a state of *idling* of the brain, which has to be reorganized in order to let task-dependent interactions emerge. Other works (Gao et al. (2013); Fornito et al. (2012)), which show the reconfiguration of resting-state connectivity during task are taken as support for this second hypothesis.

MEG and fMRI relationship: investigation on task-induced correlation As second purpose, we investigate the relationship among BOLD signals and electrophysiological fluctuations when switching from resting-state to a specific task. Specifically we test two possibilities:

h2a. MEG and fMRI signals respond to a visual-attentional stimulus in a fully independent manner. This idea is supported by the different nature of these brain signals, which describe distinct physiological phenomena evoked by the same stimuli.

h2b. Although their different nature, fMRI and slow (amplitude) MEG fluctuations reflect the same evoked neural activity. Thus, a larger correlation (be it positive or negative) emerges during task, than at rest. This hypothesis is supported by an emerging consensus that BOLD signal fluctuations correlate with band-limited power (BLP) fluctuations, especially in α and β frequency bands (Brookes et al. (2011); Stevenson et al. (2011)).

The several analyses reported in this chapter have been performed using MATLAB® 2017b and RStudio® software.

Contents

Notation

Throughout this chapter we will adopt the following notation in order to discern the functional connectivity matrices obtained from $N > 0$ time series, w.r.t. the technology (fMRI, or MEG), the considered subject, the frequency band (only for MEG), and the condition (rest, task, or the difference matrix task-rest).

> $\mathbf{FC}_{\text{fMRI}}(s,\ c) \in \mathbb{R}^{N\times N}$ represents the **FC** matrix obtained from the fMRI dataset of subject $s \in \{1,\dots,N_s\}$ in condition $c \in \{\mathsf{R},\ \mathsf{T},\ \mathsf{T}-\mathsf{R}\}$, where R, T and $\mathsf{T}-\mathsf{R}$ indicates rest, task, and task-rest conditions, respectively.
>
> $\mathbf{FC}_{\text{fMRI}}(c) \in \mathbb{R}^{N\times N}$ represents the **FC** matrix obtained from the fMRI dataset, as the average over the **FC**s of all the N_s subjects in condition $c \in \{\mathsf{R}, \mathsf{T}, \mathsf{T}-\mathsf{R}\}$.
>
> $\mathbf{FC}_{\text{MEG}}(s,\ f,\ c) \in \mathbb{R}^{N\times N}$ represents the **FC** matrix obtained from the MEG dataset of subject $s \in \{1,\dots,N_s\}$, within frequency band $f \in \{\delta, \theta, \alpha, \beta, \gamma_1, \gamma_2\}$, in condition $c \in \{\mathsf{R},\ \mathsf{T},\ \mathsf{T}-\mathsf{R}\}$.
>
> $\mathbf{FC}_{\text{MEG}}(f,\ c) \in \mathbb{R}^{N\times N}$ represents the **FC** matrix obtained from the MEG dataset within frequency band $f \in \{\delta,\ \theta,\ \alpha,\ \beta,\ \gamma_1,\ \gamma_2\}$, as the average over the **FC**s of all the N_s subjects, in condition $c \in \{\mathsf{R},\ \mathsf{T},\ \mathsf{T}-\mathsf{R}\}$.

Moreover, $\mathbf{FC}^n_* \in \mathbb{R}^{N_n\times N_n}$ represents the sub-matrix related to the sub-network $n \in \{\mathsf{D},\ \mathsf{V},\ \mathsf{DV}\}$, where D, V, DV stand for DAN, VIS, and DAN-VIS, respectively, and $\mathbf{FC}_*$ indicates one of the matrices defined above. (See Section 5.2.1 for the sub-networks' definition). $[\mathbf{FC}_*]_{ij}$ refers to the element at row i and column j of matrix $\mathbf{FC}_*$. Finally, the notation $\mathbf{FC}_{\text{fMRI}}$, $\mathbf{FC}_{\text{MEG}}$, or $\mathbf{FC}_{\text{MEG}}(f)$, without the condition argument, is used in general to distinguish among the different technologies and/or frequencies used to infer the **FC** matrix. $\mathbf{FC}(c)$ instead, refers to the functional connectivity matrix in condition c, without discerning among fMRI and MEG.

5.1 MEG and fMRI

Despite the two signals MEG and fMRI have fundamentally different properties, they are likely to originate from similar underlying physiological processes, thus suggesting that a relationship among them is highly probable. Unfortunately, a direct comparison between the two signals can be very tricky, considering the spatial limitation of MEG, and the temporal limitation of fMRI.

A comparison among modalities has been performed with task-driven studies and through functional connectivity approaches. The first one regards the BOLD and MEG signals response to specific stimuli, and it has been implemented at two levels: spatial or temporal. On the other hand, functional connectivity approaches try to find some relationship among functional networks obtained from fMRI or MEG data. Far from the idea of furnishing an exhaustive review of the evidences reported in literature, here we report a brief summary of the main results on spatial and temporal cross-modality relation.

Task-driven studies Spatial comparison between BOLD and MEG is corrupted by a high level of ambiguity due to the fact that errors of different nature are involved when the co-registration of MEG and fMRI functional data at the same anatomical coordinate space is implemented. Despite all the difficulties, some evidences of a close spatial relationship among the two modalities have been reported in previous works, including task induced changes in fMRI and oscillatory power in multiple frequencies MEG signals (Stevenson et al. (2011, 2012); Winterer et al. (2007)). These and other evidences encouraged some authors to use fMRI spatial information as a prior to the reconstruction of MEG data during the resolution to the inverse problem (see Henson et al. (2010); Ahlfors and Simpson (2004) as an example).
To overcome the ambiguities of spatial relationship among modalities, it can be useful to consider also a temporal comparison among them. From different works (Zumer et al. (2010); Mukamel et al. (2005)) it has emerged an high degree of negative correlation between stimulus-induced BOLD responses and induced changes in neuronal oscillatory amplitude in alpha and beta frequency bands, while a positive correlation has been observed in higher bands. This fact may suggest a difference in functionality, e.g. low frequency responses may present long range thalamo-cortical or cortico-cortical interaction, whereas high frequency responses may represent localised networks (Hall et al. (2014)). Overall, evidence suggests that this relationship is very complex, and it is unlikely that a simple one-to-one correspondence exists between BOLD and oscillations in any individual frequency band (Winterer et al. (2007)).

5.2 Task description and preliminary notions

Task description. We report here the description of the considered task as described in Spadone et al. (2015).
Stimuli were generated using the MATLAB Psychtoolbox-3 (Brainard (1997); Pelli (1997); Kleiner et al. (2007)) and consisted of two drifting Gabor patches with the following parameters: 2 cycle/° spatial frequency, 0.7 °/s drift rate, and 3° diameter. The two gratings were presented at opposite symmetrical locations on the horizontal meridian at an eccentricity of 5.5° from central fixation for the whole duration of the experiment. Participants were instructed to maintain central fixation on a central cross while covertly directing attention to one of the two patches to briefly detect the presented targets. The targets consisted of a brief (150 ms) change of the patch orientation in either clockwise or anticlockwise direction, which occurred, on average, every 9 s. The to-be-attended location was indicated by the appearance of a peripheral cue consisting of a 300 ms isoluminant change in the color (pink and cyan) simultaneously applied to the two patches. The relevant cue color (e.g., pink) to be attended for a whole block of trials was shown at the beginning of each block at fixation and counterbalanced across blocks. A cue could appear in the same location as the previous one (stay cue) or in the opposite location (shift cue), indicating that the attention had to be shifted. A pseudo-random stimulus sequence was designed to obtain short periods of consecutive cues (two, three, or four cues) of the same type (stay or shift). Cues appeared randomly every two, three, or four sampling times within a temporal window of ±400 ms centred on the sampling time. After each cue, either zero, one, or two targets could be presented (see Figure 5.1 for an example of the display sequence). The cue correctly predicted the location of the target with 80% probability (valid trials) but did not predict when the target would appear, thus providing no temporal information. In 20% of the trials, the target appeared at the uncued location (invalid trials). Participants were instructed to discriminate orientation changes as fast as possible by pressing a key of a response pad with their right middle or index finger to indicate clockwise or anticlockwise changes, respectively. The subjects selection has been performed by means a preliminary behavioral session. Then the selected subjects performed the actual fMRI session, which included 15 min of resting-state scans followed by $\sim$ 45 min of the experimental task (the task session was composed by 12 fMRI runs of 3.5 min each).

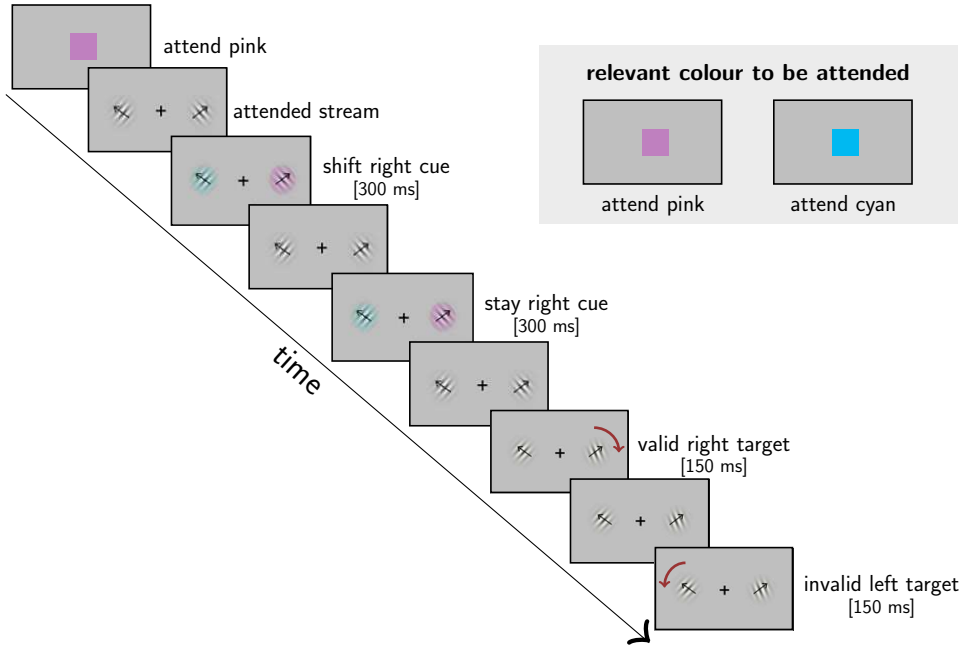

Figure 5.1: Example of the display sequence in the visuospatial attention task. At the beginning of the block, the relevant color to be attended is shown (pink). After an attended stream, the isoluminant change in the color appears: since the pink appears on the right, the cue indicates that the target would probably be on the right (shift right cue). The permanence of pink color on the right side, during the following isoluminant cue, indicates to keep attention on likely right-targets. Indeed, after another attended stream, the patch on the right changes orientation (valid target). However, the target which follows takes place in the uncued location (left), and it is referred as an invalid target. (The illustration of a single pair of Gabor patches is taken from Capotosto et al. (2013), [Fig.1])

5.2.1 Methods

fMRI data acquisition. The data used to perform our analysis refer to 16[1] right-handed healthy subjects, and they have been kindly shared by the University of Chieti. All the information related to the fMRI signals acquisition and the ROIs definition can be found in Spadone et al. (2015). Specifically, the regions of interest (ROIs) are $N = 14$, and 12 of them belong to two specific resting-state networks: the dorsal attention (DAN), and the visual network (VIS). Specifically there are $N^{\mathrm{D}} = 6$ ROIs within DAN and $N^{\mathrm{V}} = 6$ ROIs within VIS. Table 5.1 shows the selected ROIs (which represent the nodes of our graph) together with the MNI coordinates of their centres. BOLD images were motion-corrected within and between runs, corrected for across-slice timing differences, resampled into 3-mm isotropic voxels, and warped into 711–2C space, a standardized

[1] In Spadone et al. (2015) 18 subjects have been used to derive the reported fMRI-based results. However, we used only 16 of these 18 subjects.

atlas space (Talairach and Tournoux (1988); Van Essen (2005)). Preprocessing included a whole brain normalization correcting for changes in overall image intensity between BOLD runs. Each ROI reported in Table 5.1 is composed of a set of voxels (whose number varies across different ROI), and a time series of $T = 480$ time points during rest and $T = 1368$ during task (sampling time $dt = 1/F_s$, $F_s = 0.535\,\text{Hz}$) has been recorded from each voxel. Finally, the dynamics of the single ROI has been evaluated as the mean over the time series of all the voxels that belong to the considered region of interest.

network	label	name (hemisphere)	MNI coordinates		
			x	y	z
DAN	L-dFEF	dorsal frontal eye fields (left)	-25	-6	67
	L-pIPS	posterior intraparietal sulcus (left)	-23	-81	45
	L-SPL	superior parietal lobule (left)	-19	-68	57
	R-dFEF	dorsal frontal eye fields (right)	23	-8	63
	R-pIPS	posterior intraparietal sulcus (right)	33	-78	35
	R-SPL	superior parietal lobule (right)	11	-68	60
none	PreCu	precuneus	-1	-64	49
	R-vTPJ	ventral temporoparietal junction (right)	44	-53	16
VIS	L-MT	middle temporal visual area (left)	-40	-76	-7
	L-V3AV7	dorsal occipital visual cortex (left)	-26	-86	6
	L-V4V8	ventral occipital visual cortex (left)	-24	-81	-19
	R-MT	middle temporal visual area (right)	40	-80	1
	R-V3AV7	dorsal occipital visual cortex (right)	31	-86	10
	R-V4V8	ventral occipital visual cortex (right)	35	-72	-12

Table 5.1: ROIs selected as nodes of the network and their MNI coordinates. See Figure 5.2 for a spatial characterization.

Data filtering. The fMRI signals have been low-pass filtered within the band $[0, 0.17]$Hz, since no significant differences in the power spectral density after 0.17 Hz have been revealed (Spadone et al. (2015)).

Functional connectivity maps evaluation for fMRI data. For each subject $s \in \{1, \dots, N_s\}$ and each condition $c \in \{\mathsf{R},\ \mathsf{T},\ \mathsf{T} - \mathsf{R}\}$, $\mathbf{FC}_{\text{fMRI}}(s,\ c)$ is defined as the cross-correlation matrix (see Equation (4.1)) computed between all of the time series related to the selected ROIs. For the task dataset, the connectivity between each ROI pair was assessed by computing the Pearson's correlation coefficients (4.1) between all ROIs voxel pairs for each run and averaging across runs. Then, the correlation matrices were

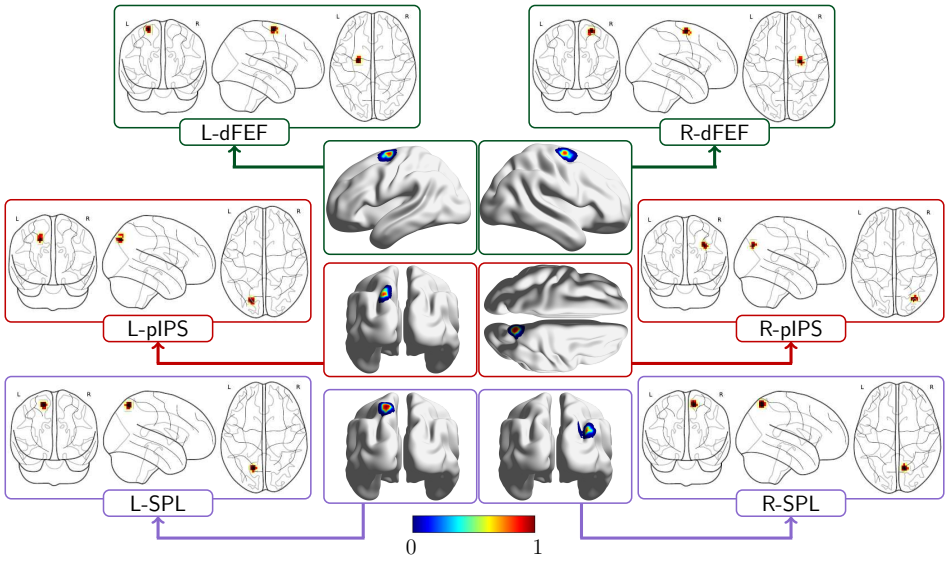

(a) DAN network

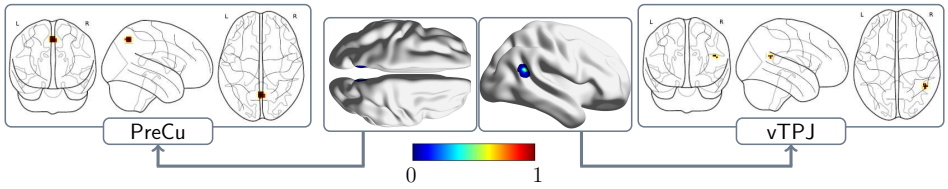

(b) None

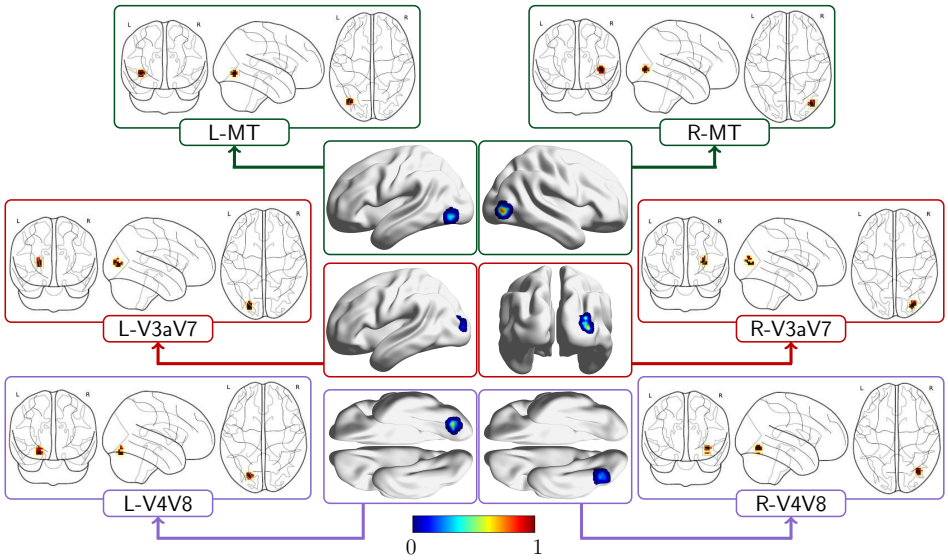

(c) VIS network

Figure 5.2: ROIs representation by sub-networks: **(a)** DAN, **(b)** none, **(c)** VIS.

Frequency band	Symbol	Range [Hz]
delta	δ	[1.5, 4.5]
theta	θ	[3.5, 8.5]
alpha	α	[7.5, 15]
beta	β	[13, 31]
gamma1	γ_1	[29, 51]
gamma2	γ_2	[49, 121]

Table 5.2: Frequency bands definition used in the analysis of MEG signals.

transformed by means of the Fisher z transform:

$$z(\rho) = \frac{1}{2} \ln \left[\frac{1+\rho}{1-\rho} \right]. \tag{5.1}$$

The same procedure was used for the resting-state dataset using the same window length as for the task runs and overlapping windows to obtain the same number of averages. Finally, $\mathbf{FC}_{\text{fMRI}}$ matrices for individual ROIs pairs during rest and task execution were obtained by averaging correlation values of all subjects and voxels within the analyzed ROIs pair.

MEG data acquisition. The MEG activity was measured at the University of Chieti, and refers to the same 16 healthy subjects as in the fMRI data, even if it has been recorded in different sessions. Participants performed three sessions of resting-state scan and two sessions of task scan. After ICA (independent component analysis) decomposition, MEG signals were reconstructed in the source-space domain with a sampling frequency $F_s = 1025\,\text{Hz}$. Then each of the three components of the source-space current density vector at every voxels has been filtered with Chebyshev Type II filters in six frequency bands (see Table 5.2).

Band limited power (BLP) has hence been computed for the filtered data as in De Pasquale et al. (2010):

$$p_i(t) = \frac{1}{T_p} \int_{t-T_p/2}^{t+T_p/2} |\mathbf{q}_i(u)|^2 du, \qquad \mathbf{q}_i(t) = [\ q_{i,x}(t) \quad q_{i,y}(t) \quad q_{i,z}(t)\ ]^{\mathsf{T}} \in \mathbb{R}^3, \tag{5.2}$$

where $\mathbf{q}_i(t)$ is the source-current density vector at ROI i at time t, and T_p =150 ms is the width of the sliding window used to evaluate the BLP. This averaging applies a low-pass filter with a stop-band which begins at frequency 6.7 Hz to $|\mathbf{q}_i(\cdot)|^2$. This frequency has been selected by considering the power spectrum density of the signal

and selecting the frequency above which the spectral density was flat, that indicates only white noise contribution. BLP has been evaluated at successive time increments of $dt = 20\,\text{ms}$, with a sliding window overlapping of 87%. The BLP signal is characterized by a slower dynamics than the original signal (see Figure 5.3 as an example), and it has been shown to be more related to the fMRI dynamics (Betti et al. (2013)).

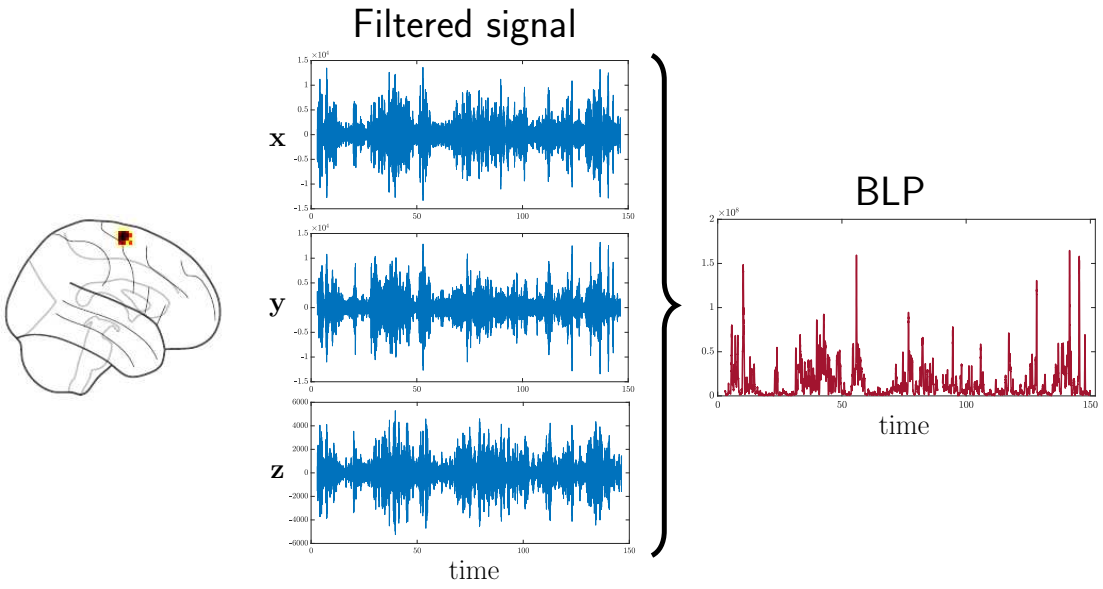

Figure 5.3: Representation of the MEG signal related to the region L-dFEF. **Left:** depiction of the selected ROI in the brain. **Centre:** x, y, and z components of α-band filtered source-current density signal $\mathbf{q}_i(\cdot)$. **Right:** band limited power of the filtered signal, evaluated as Equation (5.2).

Functional connectivity maps evaluation for MEG data. Similarly to $\mathbf{FC}_{\text{fMRI}}$, $\mathbf{FC}_{\text{MEG}}$ matrices are defined as cross-correlation matrices for all frequency bands. For each session (3 sessions of rest, 2 sessions of task), the connectivity between each ROIs pair was assessed by computing the Pearson's correlation coefficients (4.1) between the BLP signals in sliding windows of $\sim 40\,\text{s}$, that are non-overlapping during task and with 50% of overlapping in rest (to achieve a similar number of windows in both conditions). Then, the correlation matrices were transformed by means of the Fisher z transform (5.1). Finally, frequency-dependent $\mathbf{FC}_{\text{MEG}}$ matrices for individual ROIs pairs were obtained by averaging correlation values of all sliding windows and subjects within the considered ROIs pair. Importantly, to avoid misleading correlations due to the ROIs proximity, a mask matrix has been applied to discard inaccurate functional connections among too close nodes (see Figure 5.6).

Inter-subjects intra-modality coherence To quantify the intra-modality coherence among different subjects, we evaluate two quantities, namely a similarity and a dissimilarity measure.

Similarity measure: the similarity between the **FC** matrices of different subjects, we evaluated the Pearson's correlation coefficient among the vectorized **FC** maps of every possible pairs of subjects, thus obtaining a vector of $N_s \times (N_s - 1)$ correlation coefficient for each condition (R, T), or T-R), for each techniques (MEG, fMRI) and, in case of MEG, for each frequency bands. Then the mean coherence value for each combination of factors has been evaluated as the mean over the $N_s \times (N_s - 1)$ elements (see Figure 5.9), and a t-test has been used to test the non-zero correlation hypotheses. The relatively small dimension of the single sub-networks allows the evaluation of the coherence value only at the whole network level, since a correlation among a small set of data would not be significant (However, to be thorough, in Figure A.1 the results on the sub-networks are reported).

Dissimilarity measure: to quantify the difference between the **FC** matrices derived from different subjects, we consider each pair of subject and we performed the following steps:

1. we selected the techniques, sub-network, frequency and condition of interest and we normalized the full population selected matrices by dividing each matrix by the maximum entry among all of them;

2. then, for each pair of subjects, we evaluated the Hamming distance between the two normalized sub-networks, and we divided it by the number of entries of the interested sub-network. In this way, a vector of $N_s \times (N_s - 1)$ distance values is obtained.

Finally, we analyzed the resulted values by means of boxplots (see Figures 5.9 and A.2), to visualize the median and the sparsity of this dissimilarity quantity across different combination of factors.

Structural comparison among fMRI and MEG maps The structure of matrices $\mathbf{FC}_{\text{fMRI}}$ and $\mathbf{FC}_{\text{MEG}}$ are compared by means of two different measure, namely the matrix density and the Hamming distance. In order to evaluate both these measures, we first consider a vector of threshold values $\mathbf{t_r} = [\ 0 \quad 0.05 \quad \cdots \quad 1\ ]^{\mathsf{T}}$. For each entry $t_{r,i}$ of this vector, we define a *sign matrix* associated to $\mathbf{FC}_{\text{fMRI}}$ and one associated to each $\mathbf{FC}_{\text{MEG}}(f)$, both during rest and during task. Given a value $t_{r,i}$ and a **FC**, the relative *sign matrix* $\widetilde{\mathbf{FC}}$ is defined as follows:

s1. Evaluate the maximum value $M := \max_{ij}[\mathbf{FC}]_{ij}$, and the minimum value $m := \min_{ij}[\mathbf{FC}]_{ij}$.

s2. Define the *sign matrix* $\widetilde{\mathbf{FC}}$, such that

$$[\widetilde{\mathbf{FC}}(t_{r,i})]_{ij} = \begin{cases} +1, & \text{if } ([\mathbf{FC}]_{ij} > 0) \text{ and } ([\mathbf{FC}]_{ij} \geq t_{r,i} \times M) \\ -1, & \text{if } ([\mathbf{FC}]_{ij} < 0) \text{ and } ([\mathbf{FC}]_{ij} \leq t_{r,i} \times m) \\ 0, & \text{otherwise} \end{cases} \tag{5.3}$$

In this manner, for each modality, and for each frequency, we obtain a *sign matrix* for every threshold value $t_{r,i}$. These matrices are used to estimate the two measures mentioned above.

Matrix density Given a sign matrix, its density is defined as the number of non-zero entry of the matrix divided by the total number of the entries of the same matrix $\#\widetilde{\mathbf{FC}}$ (disregarding the masked elements). In other words, for each threshold value $t_{r,i}$, and for each condition (rest and task), the density is defined as:

$$d\left(\mathbf{FC}_{\text{fMRI}}(c),\, t_{r,i}\right) := \frac{\#\left(\widetilde{\mathbf{FC}}_{\text{fMRI}}(c, t_{r,i}) \neq 0\right)}{\#\widetilde{\mathbf{FC}}_{\text{fMRI}}} \in [0,\, 1], \tag{5.4a}$$

$$d\left(\mathbf{FC}_{\text{MEG}}(f, c),\, t_{r,i}\right) := \frac{\#\left(\widetilde{\mathbf{FC}}_{\text{MEG}}(f, c, t_{r,i} \neq 0)\right)}{\#\widetilde{\mathbf{FC}}_{\text{MEG}}} \in [0,\, 1]. \tag{5.4b}$$

This quantity measures the distribution of the relative weights of the considered matrix. Specifically, we estimated this quantity for each of the 16 subjects, and we considered the mean over them.

Hamming distance In order to evaluate the structural difference between $\mathbf{FC}_{\text{fMRI}}$ and $\mathbf{FC}_{\text{MEG}}$ matrices, for each condition (rest, task), for each frequency, and for each threshold value, we computed the Hamming distance between the relative sign matrices, as follows:

$$h\left(f, c, t_{r,i}\right) := \frac{\sum_{ij} \left|[\widetilde{\mathbf{FC}}_{\text{fMRI}}(c, t_{r,i})]_{ij} - [\widetilde{\mathbf{FC}}_{\text{MEG}}(f, c, t_{r,i})]_{ij}\right|}{\#\widetilde{\mathbf{FC}}} \in [0,\, 2]. \tag{5.5}$$

The smaller the Hamming distance, the more similar are the two considered matrices.

5.2.2 fMRI results reported in Spadone et al. (2015)

In this paragraph we briefly report the results obtained through the analysis of fMRI data in Spadone et al. (2015) that we would like to compare with results obtained with MEG data. In summary, the authors reported that in the transition from rest to task the functional architecture of the VIS and DAN was relatively preserved. However, during the visuospatial attention task (requiring either maintenance of the focus of processing on a stream of visual stimuli or a shift of attention to a competing visual stream) a decrease of correlation in the VIS and an increase of temporal correlation between frontoparietal regions of the DAN and visual regions bilaterally has been shown. Relatively to the hypotheses **h1a.** and **h1b.**, these results are consistent with a dynamic reorganization of active visual connections from task to rest and the *idling* hypothesis of RSNs. The resting connectivity in the DAN was instead relatively unaffected during attention, potentially indicating a role for spontaneous ongoing activity as a *prior* for attention selection (see Figure 5.4 for a representation of the $\mathbf{FC}_{\text{fMRI}}$ matrices). Note that these changes in functional connectivity have not been analyzed trial by trial, but they reflect adjustments of connectivity that occur during a task block or a series of trials, such as in our shift/stay cue analysis.

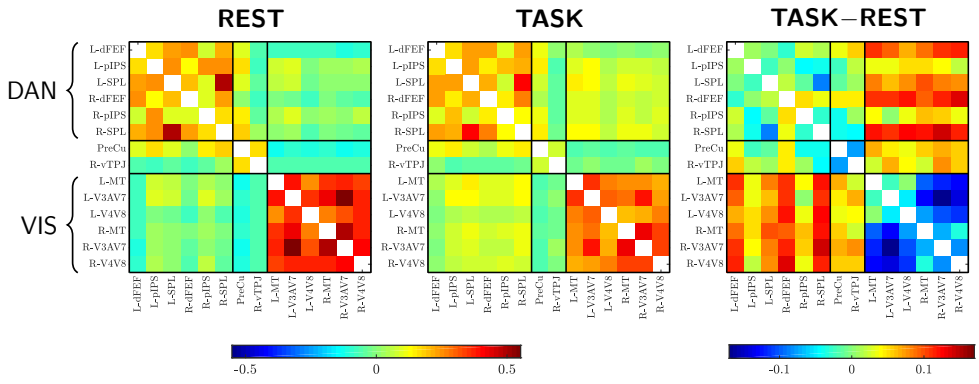

Figure 5.4: Functional connectivity map during rest (left), task (centre) and the difference between $\mathbf{FC}_{\text{fMRI}}(\mathsf{T})$ and $\mathbf{FC}_{\text{fMRI}}(\mathsf{R})$. $\mathbf{FC}(\cdot)$ matrices are obtained from the average across voxels pairs and subjects of the z-Fisher-transformed Pearson's correlation coefficients[2]. The nodes are in the same order as in Table 5.1.

[2]The $\mathbf{FC}_{\text{fMRI}}$'s reported here have been obtained with data from 16 subjects, while the matrices shown in Spadone et al. (2015) refer to 18 subjects.

5.3 Task-induced modulation of MEG data

In order to investigate hypotheses **h1a.** and **h1b.** on the role of resting-state oscillations with respect to the considered set of ROIs, by means of MEG BLP signals, we first test task-induced modulation of frequency-dependent $\mathbf{FC}_{\mathrm{MEG}}(f)$ matrices. Before performing this analysis, we report a test on the BLP modulation, to be considered as a control measure to verify the goodness of MEG data's quality. Specifically, in line with current literature, we expect larger BLP values in the α and β bands (Wen and Liu (2016)), when compared with the others. Moreover no significant change in the BLP is foreseen when switching from rest to task condition.

5.3.1 Task-induced modulation of BLP

As a control measure to verify the goodness of MEG data, we focus now on the mean value of the BLP signals, in order to test if there is a significant effect of the frequency band, rest or task condition, and network membership. Therefore, we applied a Three-Ways ANOVA with *network* (DAN, VIS, none), *frequency* (δ, θ, α, β, γ_1, γ_2) and *condition* (rest, task) as factors and the *mean BLP value* of each ROI as variable. The results indicate a non-significant three-ways interaction, but a significant interaction of network and frequency ($F = 7.71$; $p_{\mathrm{val}} < 3 \times 10^{-12}$) (see Figure 5.5(a)). No significant interaction among frequency and condition ($F = 0.88$; $p_{\mathrm{val}} = \text{n.s.}$) or network and condition ($F = 2.17$; $p_{\mathrm{val}} = \text{n.s.}$) emerges. Finally, there is no significant main effect of condition ($F = 0.52$; $p_{\mathrm{val}} = \text{n.s.}$), but a significant main effect both of network ($F = 72.75$; $p_{\mathrm{val}} < 2 \times 10^{-31}$) and frequency ($F = 84.21$; $p_{\mathrm{val}} < 3 \times 10^{-82}$). See Figures 5.5(b) and 5.5(c).
Post-hoc analyses show that the mean BLP is larger in the α-band than in the other frequencies, followed by the β-band (all $p_{\mathrm{val}} < 5 \times 10^{-2}$, Bonferroni corrected). Specifically, the BLP signal in ROIs belonging to the DAN network, or to neither networks in α-band is significant higher than other combinations of network and frequency (all $p_{\mathrm{val}} < 5 \times 10^{-2}$, Bonferroni corrected). The DAN network finally resulted to be characterized by a greater mean BLP than the VIS network and the nodes outside the networks (both $p_{\mathrm{val}} < 5 \times 10^{-2}$, Bonferroni corrected).

In summary, the task condition does not modulate significantly the mean BLP values of the ROIs, although a non-significant increase during task is observed in all frequency bands, but in the α-band. The signals, whose sources belong to the DAN network, has a larger mean power than the others, both in rest and in task. Finally, α and β bands are characterized by the larger values of power in both conditions.

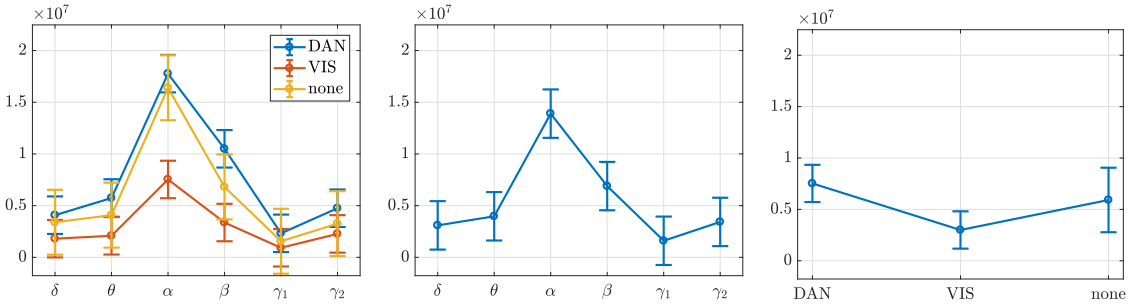

(a) Frequency-network interaction (b) Frequency main factor (c) Network main factor

Figure 5.5: Representation of the two- and one-level significant interactions resulted from a Three-Ways ANOVA with network (DAN, VIS, none), frequency (δ, θ, α, β, γ_1, γ_2) and condition (rest, task) as factors and the mean BLP value of each ROI as variable (y-axis).

5.3.2 Task-induced modulation of $\mathbf{FC}_{\mathrm{MEG}}$

A qualitative analysis of the matrices $\mathbf{FC}_{\mathrm{MEG}}$ (see Figure 5.6) in resting state and during task (as well as their differences) in the six frequency bands leads to some considerations. First, α and β bands seem to be characterized by higher $\mathbf{FC}_{\mathrm{MEG}}$ values than the other bands, both in rest and during task. Second, it can be observed a general decrease in correlation from rest to task, especially in α frequency band. Third, stronger intra-hemisphere than inter-hemisphere connections are conjectured. Finally, as an interesting insight, it can be observed that switching from rest to task seems to produce an increase in the $\mathbf{FC}_{\mathrm{MEG}}$ values between specific regions (R-dFEF/R-SPL, R-pIPS/R-SPL, L-V4V8/R-V4V8) both in higher (strongly) and lower (slightly) bands.

In order to verify the correctness of these observations, we performed several Two-Ways ANOVA tests to analyze the *condition* factor (rest, task) modulation of $\mathbf{FC}_{\mathrm{MEG}}$ value of each pair of ROIs belonging to DAN and VIS networks[3], when it interacts with *frequency* (δ, θ, α, β, γ_1, γ_2), *hemisphere* (intra-hemispheric or inter-hemispheric connections), or *network* (within or between network correlations) factors. The results indicate a significant interaction between frequency and condition ($F = 35.99$; $p_{\mathrm{val}} < 3 \times 10^{-16}$) and a significant interaction between network and condition ($F = 11.92$; $p_{\mathrm{val}} < 6 \times 10^{-4}$). See Figures 5.7(a) and 5.7(b), respectively. No significance emerges from condition and hemisphere factors interaction ($F = 0.1132$; $p_{\mathrm{val}} = \text{n.s.}$), where only the main factors hemisphere ($F = 608.09$; $p_{\mathrm{val}} < 2 \times 10^{-16}$) and condition ($F = 446.42$; $p_{\mathrm{val}} < 2 \times 10^{-16}$) are significant.

Post-hoc analyses indicate that stronger correlations are found in the α and β bands (with higher values in α), as expected ($p_{\mathrm{val}} < 5 \times 10^{-2}$, Bonferroni corrected). Interestingly,

[3] Three-Ways ANOVA tests has been performed as well, but they all resulted to be not significant.

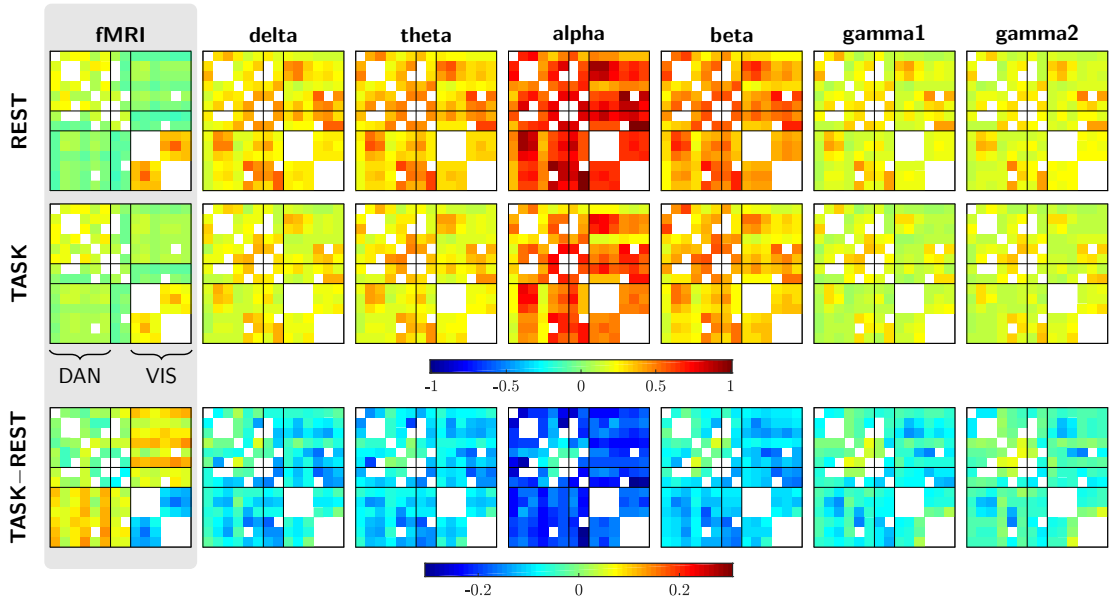

Figure 5.6: Functional connectivity maps during rest, task and their difference (task-rest) obtained with fMRI data and MEG data at different frequency bands. The matrices $\mathbf{FC}_{\text{fMRI}}$ and $\mathbf{FC}_{\text{MEG}}$ are obtained from the average across voxels' pairs and subjects of the z-Fisher-transformed Pearson's correlation coefficients. A mask matrix has been applied to discard inaccurate connections among too close ROIs (white cells). The nodes are in the same order as in Table 5.1.

the α-band emerges among the others (see Figure 5.7(a)): the more relevant decrease of $\mathbf{FC}_{\text{MEG}}$ during task with respect to the condition of rest is observed in the α-band ($p_{\text{val}} < 5 \times 10^{-2}$, Bonferroni corrected). Furthermore, as presumed, while at rest condition no significant difference emerges when within- and between-networks interactions are compared, during task, cross-network (DAN-VIS) connections are significantly weaker than within network links (see Figure 5.7(b)), thus confirming the networked structure of the matrices $\mathbf{FC}_{\text{MEG}}(\mathsf{T})$.

In summary, while a general decrease of correlation has been detected in all the bands, the α-band (which is characterized by the highest connectivity both in rest and in task) differs from the others for the magnitude of this decrease. Moreover, this analysis highlights networked specificity of the connections induced by task.

5.3.2.1 Temporal vs spatial modulation of $\mathbf{FC}_{\text{MEG}}$

From the results presented above, it emerges a weak networked structure, which becomes significant only during task, and an hemispheric main factor modulation. However, by observing Figure 5.6, the cross-network DAN-VIS seems to be particularly affected by

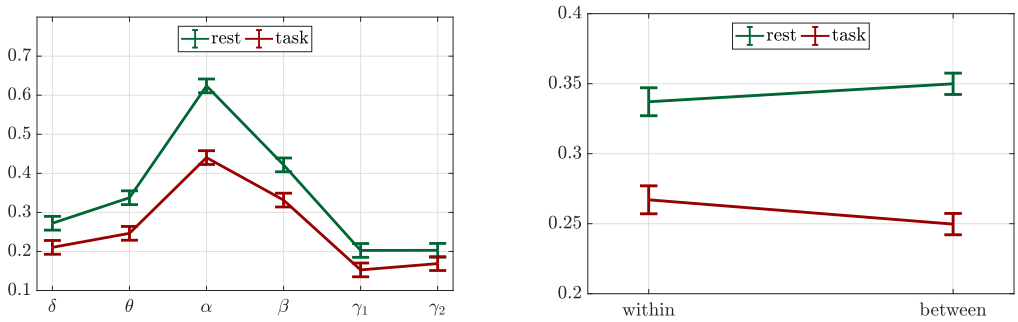

(a) Frequency-condition interaction (b) Network-condition interaction

Figure 5.7: Representation of the two-levels significant interactions resulted from two Two-Ways ANOVA tests with $\mathbf{FC}_{\mathrm{MEG}}$ value of each pair of ROIs belonging to DAN or VIS networks as variable (y-axis). **(a)** Two-Ways ANOVA with *frequency* (δ, θ, α, β, γ_1, γ_2), and *condition* (rest, task) as factors. **(b)** Two-Ways ANOVA with *network* (within or between network correlations), and *condition* (rest, task) as factors.

hemispheric modulation. On the other hand, both Figure 5.6 and the previous results suggest a significant temporal modulation of the FC networks, which interacts with other factors.

In order to investigate the relationship among spatial and temporal $\mathbf{FC}_{\mathrm{MEG}}$ modulation, we performed a Three-Ways ANOVA test with $\mathbf{FC}_{\mathrm{MEG}}$ value of each pair of ROIs belonging to DAN or VIS networks as variable and *frequency* (δ, θ, α, β, γ_1, γ_2), *hemisphere* (intra-hemispheric or inter-hemispheric connections), and *network* (within or between network correlations) as factors. The results indicate a non-significant three-level interaction ($F = 0.98$; $p_{\mathrm{val}} = \text{n.s.}$), whereas all two-level interactions are significant: network-hemisphere ($F = 40.65$; $p_{\mathrm{val}} < 2 \times 10^{-10}$), frequency-hemisphere ($F = 6.23$; $p_{\mathrm{val}} < 9 \times 10^{-6}$), and frequency-network ($F = 3.62$; $p_{\mathrm{val}} < 3 \times 10^{-3}$).
Post-hoc analyses confirm our conjecture regarding the DAN-VIS cross network, indeed the difference between intra- and inter-hemispheric connections (where intra connections are generally stronger than inter links) significantly enlarge ($p_{\mathrm{val}} < 5 \times 10^{-2}$, Bonferroni corrected) in DAN-VIS with respect to within network interactions (see Figure 5.8(a)). As shown in Figure 5.8(b), the interaction among hemisphere and frequency factors reinforces the role of α band, which is characterized by a significantly larger difference between intra- and inter-hemispheric connections, than the other frequency bands ($p_{\mathrm{val}} < 5 \times 10^{-2}$, Bonferroni corrected). Finally, from post-hoc analyses on the interaction between frequency and network factors in the $\mathbf{FC}_{\mathrm{MEG}}$ modulation, it emerges the stronger temporal modulation, if compared with the spatial-network characterization. Indeed, even if a significant interaction has been resulted, the most modulation is frequency-driven, as can be noted in Figure 5.8(c). To confirm this, the Three-Ways ANOVA test shows significant

main factors of frequency and hemisphere, but not significant network main factor.

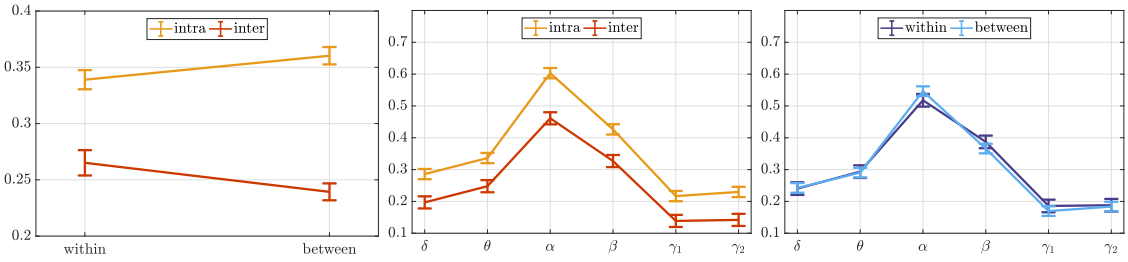

(a) Network-hemisphere interaction (b) Hemisphere-frequency interaction (c) Frequency-network interaction

Figure 5.8: Representation of the two-levels significant interactions resulted from a Three-Ways ANOVA test with $\mathbf{FC}_{\mathrm{MEG}}$ value of each pair of ROIs belonging to DAN or VIS networks as variable (y-axis), and *frequency* (δ, θ, α, β, γ_1, γ_2), *hemisphere* (intra-hemispheric or inter-hemispheric connections), and *network* (within or between network correlations) as factors.

In summary, the hemisphere factor modulation strengthens the difference both between within- and cross-network interactions, as well as the frequency-dependent **FC** links. Specifically, the DAN-VIS cross-network and the α-band are characterized by higher hemisphere specificity.

5.3.2.2 Task-induced variation in inter-subjects coherence

Inter-subjects differences among each frequency-dependent $\mathbf{FC}_{\mathrm{MEG}}(f)$ matrix highlight one of the main limitation of these data, where the use of population models to describe the behavior of a set of subjects is still questionable.

To quantify the intra-modality coherence, we have evaluated the Pearson's correlation coefficient among the vectorized functional connectivity maps of each possible pair of subjects, thus obtaining a vector of $N_s \times (N_s - 1)$ correlation coefficients for each frequency band. Then we performed a t-test for each band to evaluate if the mean over all the coefficients is significant larger than zero. The same approach has been used for fMRI data. Figure 5.9(a) illustrates the mean and the confidence interval of the intra-modal coherence value for rest and task when the whole network is considered (See Figures A.1 for the DAN and the VIS networks, and for the DAN-VIS cross-network). In both conditions, but the VIS network, all the values are significant larger than zero, but, as expected, they vary from rest to task. Specifically, central bands (within θ and γ_1) results more inter-subjects coherent during task, while, δ and γ_2 has almost the same behavior.

The high spatial resolution of fMRI technique induces a larger coherence among inter-subjects functional connectivity during task, when only the task-related sub-networks

are considered. On the contrary, when the whole network is analyzed, switching from resting-state to the task activity induces a general decreasing in population coherence. This fact is confirmed from the analyzed fMRI data, which are characterized by a task-induced decreased coherence in the whole network, while the sub-networks specific **FC** are more similar across subjects during task (the (dis)similarity is evaluated in terms of the normalized Frobenius norm of the matrix difference. See Figure A.2(f)).

MEG technique, however, is characterized by lower spatial resolution, thus a different behavior may be noticed. Specifically, as mentioned above, a general population alignment during task is observed at the level of the whole network, both in terms of increased correlation, and of reduced distance (see Figure A.2). Nevertheless, due to the higher temporal resolution of MEG technique, as expected, we can distinguish among frequency-specific behavior. In particular, as shown in Figures 5.9 and A.2, a larger consistency and a smaller difference among the subjects' **FC** are to be noticed in α and β frequency bands than in the other bands. However, from Figures 5.9(b), 5.9(c) and 5.9(d) it emerges that β band is characterized by larger distance across subject within single networks and cross-networks during task, than at rest, while higher frequency bands show opposite behaviors. Thus confirming that β is more active during resting-state than during task (Betti et al. (2013)).

From rest to task: no modulation of BLP but a significant modulation of $\mathbf{FC}_{\mathrm{MEG}}$. Our results indicate that the analyzed task does not modulate the BLP value itself, but it modulates the functional relationship among each pair of BLP signals, if compared with the functional correlation values obtained during rest.
This fact confirms that the analyzed networks (DAN and VIS), which have been selected through their fMRI response profile during the attention task (Spadone et al. (2015)), are still task-related when MEG signals are considered, thus confirming the analyses described in Betti et al. (2013). Specifically, the attention task causes a general decrease in the $\mathbf{FC}_{\mathrm{MEG}}$ in all the analyzed frequency bands. This result is in line with those obtained in Betti et al. (2013), where a visual task of natural scenes viewing is considered. Coherently with our findings, in that work a decrease in the within-network BLP correlation is observed especially in the α and β bands. The modulation of the $\mathbf{FC}_{\mathrm{MEG}}$ matrices induced by task reflects also a general decrease of the variability of each functional correlation value across subjects. This result suggests that beyond the individual variability of the resting state, which is generally larger in MEG than in fMRI, the task induces a decrease of this variability, since all the subjects are asked to perform the same visual-attentional action.

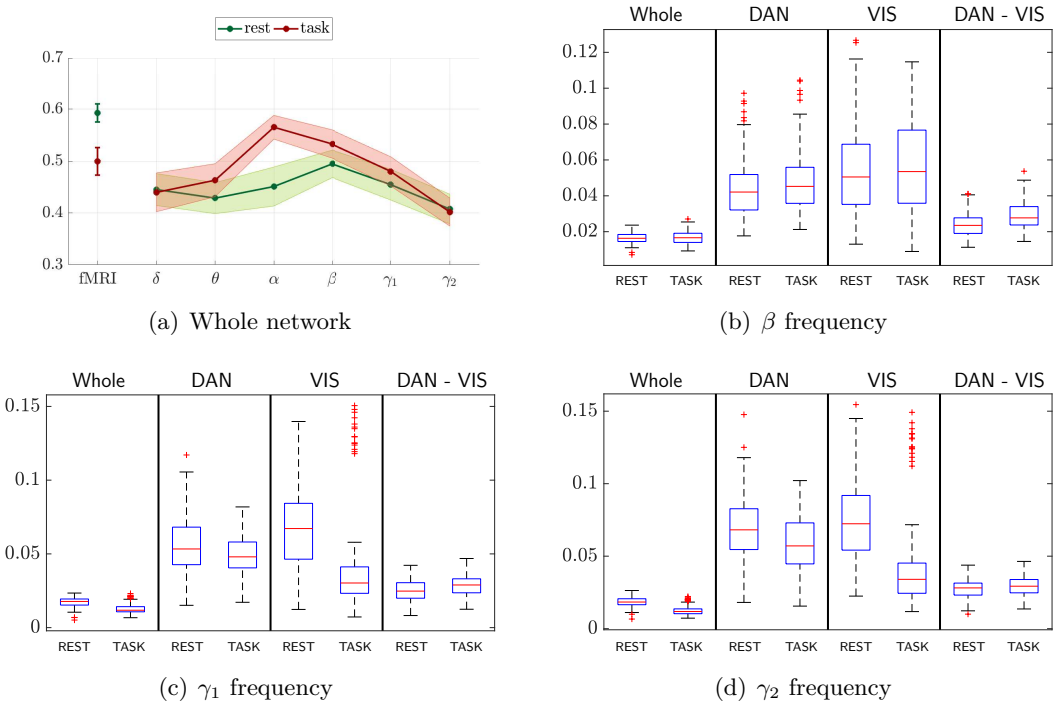

(a) Whole network

(b) β frequency

(c) γ_1 frequency

(d) γ_2 frequency

Figure 5.9: Intra-modality coherence among subjects. **(a)** Average and confidence interval of the Pearson's correlation coefficients evaluated between the vectorized **FC** of each pair of subjects in the whole network. **(b)÷(d)** Boxplots of the Frobenius norm of the difference among each pair of **FC** matrices at different frequencies (normalized w.r.t. to the maximum value of the entries among all the population) derived from different subjects, normalized by the number of matrix' entries.

Hemisphere-dependent behavior: intra-hemispheric connections are stronger than inter-hemispheric ones. As already discussed in De Pasquale et al. (2010) for what concerned the DAN network, our results show a significant difference between intra and inter-hemispheric functional correlation of BLP signals in all the analyzed frequency bands. In particular, stronger correlations have been found between regions of the same hemisphere.
Moreover, both frequency and network factors combine singularly with the hemisphere factor: the intra- or inter-hemispheric condition indeed strengthens the divergence among different frequencies, and among within or between networks interactions.

As observed in De Pasquale et al. (2010), fMRI networks are largely stationary and bilateral, with no relevant differences among within and across-hemispheres couplings; this difference between fMRI and MEG results is probably due to the non-stationarity showed by MEG networks.

Frequency-dependent behavior: the main role of temporal modulation. One of the main advantages of using MEG data is the high temporal resolution, which allows a frequency-specific analysis, that is not doable with fMRI signals. Our results indeed confirm the significance of the frequency factor both in power and in functional connectivity values. Specifically, what emerges from this study is the specificity of α and β frequency bands, when compared with the others.
First of all, the BLP signals are significantly higher in α than in the other frequencies. Interestingly, whereas all the BLP mean values generally increase during task (even if not significantly), a (non-significant) decrease is instead observed in α-band. However, the relevant role of α-band is strongly remarked when the $\mathbf{FC}_{\mathrm{MEG}}$'s are considered. This specific band is hence characterized by a general stronger connectivity among ROIs, and by a more relevant decrease of connection than all the other frequencies, during task. These results are coherent with a large part of the literature about $\mathbf{FC}_{\mathrm{MEG}}$ results (Pizzella et al. (2014); Marzetti et al. (2013); Hipp et al. (2012); De Pasquale et al. (2010); Betti et al. (2013); Engel et al. (2013)), where the strongest correlation in the α-band has been generally observed (sometimes in conjunction with the β-band, see Hipp et al. (2012)). In other works the increase of $\mathbf{FC}_{\mathrm{MEG}}(\alpha)$ is shown to be related to specific networks as in this case (DAN Pizzella et al. (2014); Marzetti et al. (2013); De Pasquale et al. (2010); VIS Engel et al. (2013); or DAN-VIS Pizzella et al. (2014); Engel et al. (2013)), whereas it is shown to decrease during task in the VIS network (see Betti et al. (2013)). This general strong connectivity of the α-band, which importantly decreases during task, is also combined with the absence of the networked structure (between-network connections are stronger than within-network links in this frequency), which is conversely observable in the other frequencies.

Overall, the functional analysis performed to MEG data highlights the larger role of temporal/frequency modulation than spatial modulation, with a significant hemispheric factor.

Idling state or prior: multiple answers. Regarding the tested hypotheses **(h1a)** and **(h1b)**, our results suggest different answers with respect to different frequency bands and networks. Specifically, while hypothesis **(h1a)** prevails in the highest bands (γ_1 and γ_2), which do not show a significant condition factor, lower bands report a significant decrease in functional connections, especially in α. This task-modulation in lower frequencies hence suggests that resting-state patterns describe a state of brain inactivity, which has to be reorganized to perform this specific task. On the other hand, the distinction between within and between function connections' strength becomes more evident during task than during rest (where the condition is not a significant factor) in β

and γ_1 frequencies. Specifically, within DAN connections become significantly stronger than DAN-VIS cross-interactions. This fact confirms assumption **(h1a)** for the DAN network at these frequencies, thus verifying what observed with fMRI analysis. Indeed, in Spadone et al. (2015), the resulted relative stability of the connection pattern in the DAN has been related to a possible centrality of this network, far away from the influence of sensory stimuli.

5.4 MEG vs fMRI: FC-based comparison

The relationship between the results obtained with fMRI and MEG data has been analyzed at different levels: at first, we compared the pattern within the matrices $\mathbf{FC}_{\text{fMRI}}$ and $\mathbf{FC}_{\text{MEG}}$ by means of Pearson's correlation. Then we considered the **FC** matrices as adjacency matrices that describe the relations among nodes (the ROIs) and compared them with respect to structural measures. Specifically, we evaluated the full network similarity and the single sub-network similarity, in a manner similar to that adopted in Garcés et al. (2016).

Note: Importantly, to achieve a meaningful comparison, we applied to each $\mathbf{FC}_{\text{fMRI}}(c)$ matrix the same mask used to describe all the MEG derived matrices, and we considered the non-masked values only (see Figure 5.6).

5.4.1 Overall and network-based comparison

From a qualitative analysis of Figure 5.6 and from the analysis of MEG data presented above, we speculate that the global networked architecture of the functional connectivity maps remains the same from fMRI and MEG, both in rest and in task. However, some dissimilarities can be distinguished between the two modalities. Specifically, the significant increase in cross-network correlation, observed with fMRI data, does not emerge by means of MEG data in any frequency band, where a decrease in $\mathbf{FC}^{\mathsf{DV}}_{\text{MEG}}$ is always observed when switching from rest to task. Nevertheless, in higher bands (γ_1 and γ_2) this decrease of cross-network functional connections is smaller than in other bands (see Figure 5.7(a)). Thus, we speculate that such lower decrease may drive to a positive correlation with fMRI results. Moreover, in α band this reduction of cross-network functional connections from rest to task is significantly larger than in the other frequencies. Therefore, our hypothesis is that a negative correlation may exist between $\mathbf{FC}^{\mathsf{DV}}_{\text{fMRI}}(\mathsf{T}-\mathsf{R})$ and $\mathbf{FC}^{\mathsf{DV}}_{\text{MEG}}(\alpha, (\mathsf{T}-\mathsf{R}))$.

Finally, from the difference among functional connectivities during task and rest in the DAN network $\mathbf{FC}^{\mathsf{DV}}(\mathsf{T}-\mathsf{R})$ (Figure 5.6), it can be hypothesized a positive correlation among fMRI and δ, β and γ's frequency bands, where an increase in the intra-right-

hemispheric connections emerges, similarly to what happens with BOLD data.

In what follows we report the statistical tests used to investigate our speculations.

To quantify the similarity among the results obtained from fMRI and MEG data, for every frequency band f, we considered all possible pairs of subjects $(s,\ r)$, and for each of them, we estimated the Pearson's correlation $\rho(\cdot,\cdot)$ among the upper-diagonal of $\mathbf{FC}_{\text{fMRI}}(s,\ c)$ and $\mathbf{FC}_{\text{MEG}}(r,\ f,\ c)$, with $s,\ r = 1,\dots,N_s$. Note that

$$\rho\left(\mathbf{FC}_{\text{fMRI}}(s,\ c),\ \mathbf{FC}_{\text{MEG}}(r,\ f,\ c)\right) \neq \rho\left(\mathbf{FC}_{\text{fMRI}}(r,\ c),\ \mathbf{FC}_{\text{MEG}}(s,\ f,\ c)\right).$$

In this manner, we obtained a vector of ${N_s}^2$ correlation values $\boldsymbol{\rho}$, whose average $\bar{\rho}_{\text{fMRI,MEG}}$ has been used to define the cross-modal correlation of the functional connectivity for the whole population:

$$\bar{\rho}_{\text{fMRI,MEG}}(f,\ c) = \frac{1}{N_s^2}\sum_{s=1}^{N_s}\sum_{r=1}^{N_s}\rho\left(\mathbf{FC}_{\text{fMRI}}(s,\ c),\ \mathbf{FC}_{\text{MEG}}(r,\ f,\ c)\right), \tag{5.6}$$

with $f \in \{\delta,\ \theta,\ \alpha,\ \beta,\ \gamma_1,\ \gamma_2\}$ and $c \in \{\mathsf{R},\ \mathsf{T},\ \mathsf{T}-\mathsf{R}\}$. This quantity was evaluated for the whole network (5.6), and for each separated network (DAN, D-$\bar{\rho}_{\text{fMRI,MEG}}$; VIS, V-$\bar{\rho}_{\text{fMRI,MEG}}$; DAN-VIS, DV-$\bar{\rho}_{\text{fMRI,MEG}}$):

$$\mathsf{D}\text{-}\bar{\rho}_{\text{fMRI,MEG}}(f,\ c) = \frac{1}{N_s^2}\sum_{s=1}^{N_s}\sum_{r=1}^{N_s}\rho\left(\mathbf{FC}^{\mathsf{D}}_{\text{fMRI}}(s,\ c),\ \mathbf{FC}^{\mathsf{D}}_{\text{MEG}}(r,\ f,\ c)\right),$$

$$\mathsf{V}\text{-}\bar{\rho}_{\text{fMRI,MEG}}(f,\ c) = \frac{1}{N_s^2}\sum_{s=1}^{N_s}\sum_{r=1}^{N_s}\rho\left(\mathbf{FC}^{\mathsf{V}}_{\text{fMRI}}(s,\ c),\ \mathbf{FC}^{\mathsf{V}}_{\text{MEG}}(r,\ f,\ c)\right),$$

$$\mathsf{DV}\text{-}\bar{\rho}_{\text{fMRI,MEG}}(f,\ c) = \frac{1}{N_s^2}\sum_{s=1}^{N_s}\sum_{r=1}^{N_s}\rho\left(\mathbf{FC}^{\mathsf{DV}}_{\text{fMRI}}(s,\ c),\ \mathbf{FC}^{\mathsf{DV}}_{\text{MEG}}(r,\ f,\ c)\right).$$

The first hypothesis that we have tested is the similarity among the general architecture of the **FC** matrices both in rest and in task. To test it, we considered $\bar{\rho}_{\text{fMRI,MEG}}(f,\ \cdot)$ for the whole network as a measure of this similarity. See Figure 5.10, where the mean values are reported with their confidence level, for each frequency band. As shown, $\bar{\rho}_{\text{fMRI,MEG}}(f,\cdot)$ in rest and task are positive at each frequency band, with larger values at task than at rest. To test the significance of this result, for each band we performed a t-test to determine whether these values are significant greater than zero. The results show that this similarity measure is significantly greater than zero ($p_{\text{val}} < 5 \times 10^{-2}$) in both conditions (rest and task) and for all frequency bands, but for δ band at rest.

To investigate our second hypothesis regarding fMRI-MEG relationship in the DAN-

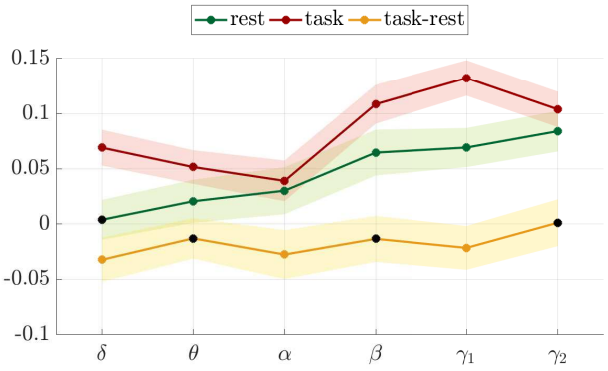

Figure 5.10: Averaged correlation among fMRI and MEG functional connectivity maps $\bar{\rho}_{\text{fMRI,MEG}}(f, c)$, evaluated as described in the main text, regarding the whole network. Coloured markers represent significantly positive (or negative) values, while black markers stand for non significant results.

VIS cross-network, we focused on DV-$\bar{\rho}_{\text{fMRI,MEG}}(\cdot, \mathsf{T}-\mathsf{R})$ (see Figure 5.11(c), yellow line). Among all the values, the more interesting results show a negative correlation fMRI-MEG in α band and a positive one at γ's, as expected. Again, to test the significance for DV-$\bar{\rho}_{\text{fMRI,MEG}}(\alpha, \mathsf{T}-\mathsf{R})$ and DV-$\bar{\rho}_{\text{fMRI,MEG}}(\gamma_i, \mathsf{T}-\mathsf{R})$ (with i equal to 1 or 2) to be negative and positive, respectively, we performed a t-test over all the values. All the interesting tests gave a $p_{\text{val}} < 5 \times 10^{-2}$, thus confirming our hypothesis.
Furthermore, a One-Way ANOVA test applied to the cross-modality correlation in task−rest **FC** in DAN-VIS (DV-$\bar{\rho}_{\text{fMRI,MEG}}(\cdot, \mathsf{T}-\mathsf{R})$) shows a significant frequency factor ($F = 5.12$; $p_{\text{val}} < 1.2 \times 10^{-4}$), with a significant lower correlation with α band than with γ_1 and γ_2 ($p_{\text{val}} < 5 \times 10^{-2}$, Bonferroni corrected) (see Figure 5.12).
Finally, with the same reasoning we tested the supposed positive correlation among fMRI and δ, β and γ's frequency bands in the DAN network, when considering the difference among task- and rest-functional connectivities. In this case, specific t-test analyses show a significant positive D-$\bar{\rho}_{\text{fMRI,MEG}}(\theta, \mathsf{T}-\mathsf{R})$, D-$\bar{\rho}_{\text{fMRI,MEG}}(\beta, \mathsf{T}-\mathsf{R})$, and D-$\bar{\rho}_{\text{fMRI,MEG}}(\gamma_1, \mathsf{T}-\mathsf{R})$, while the null hypothesis of zero correlation with γ_2 cannot be rejected.

In summary, our analysis confirmed what was initially believed. At first, we observed a global conservation in the MEG functional connectivities of the architecture of the network observed during fMRI analysis (both at rest and during task). This result is coherent with other works where topography of fMRI and MEG networks have been shown to be similar during rest (Brookes et al. (2011)) and movie observation (Betti et al. (2013); Muthukumaraswamy and Singh (2008)). Second, a different fMRI-MEG relationship across different networks and different frequencies has emerged. Specifically,

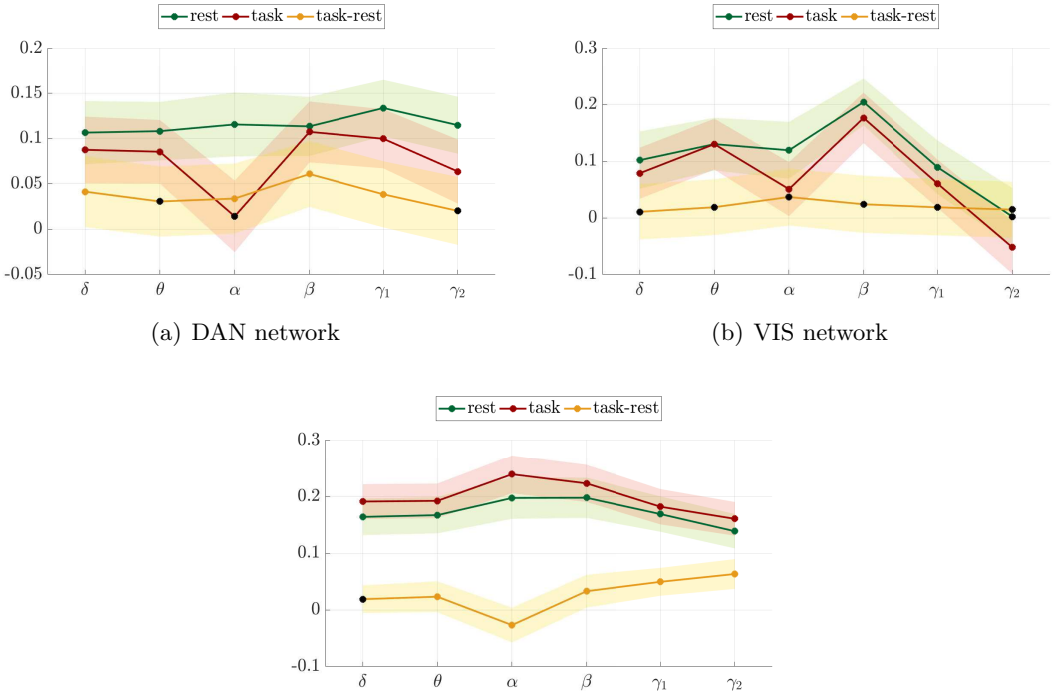

(a) DAN network

(b) VIS network

(c) DAN-VIS network

Figure 5.11: (a)÷(c) Averaged correlation among fMRI and MEG functional connectivity maps $\bar{\rho}_{\text{fMRI,MEG}}(f, \cdot)$, evaluated as described in the main text, regarding the DAN **(a)**, VIS **(b)**, or DAN-VIS **(c)** networks. Coloured markers represents significantly positive (or negative) values, while black markers stand for non significant results.

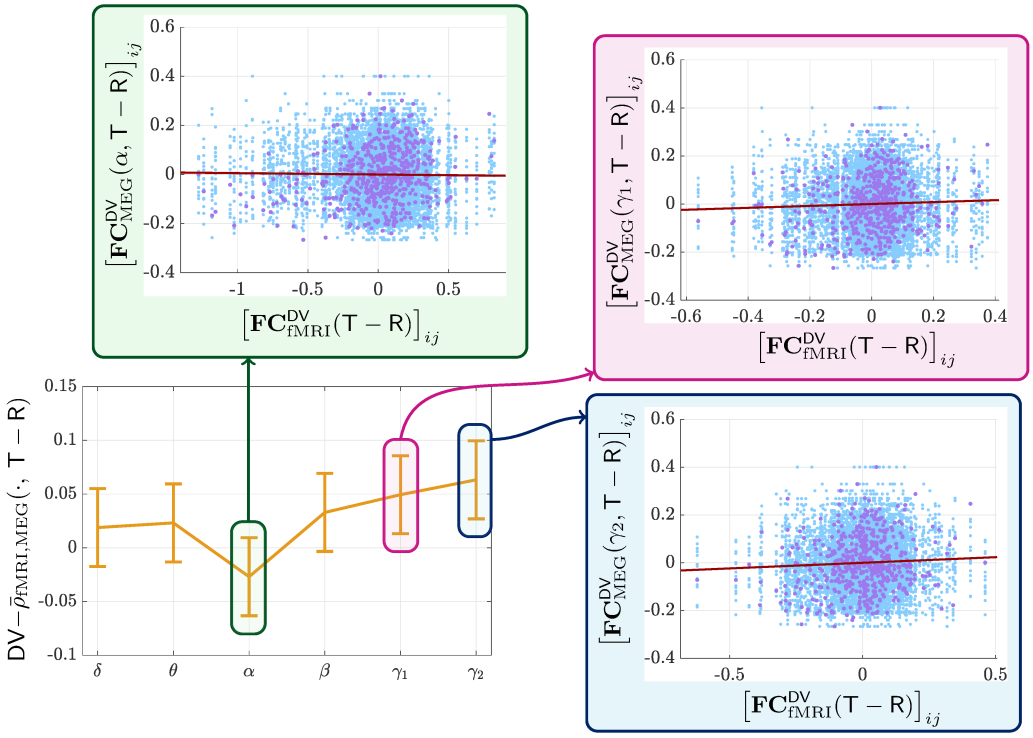

Figure 5.12: Bottom left: Result of the One-Way ANOVA test applied to the cross-modality correlations in task−rest FC in DAN-VIS with frequency as factor. The bars represent the confidence intervals. **Boxes:** scatter plots of the relationship between $\mathbf{FC}^{\mathrm{DV}}_{\mathrm{fMRI}}(\mathsf{T}-\mathsf{R})$ and **(green)** $\mathbf{FC}^{\mathrm{DV}}_{\mathrm{MEG}}(\alpha, \mathsf{T}-\mathsf{R})$, **(pink)** $\mathbf{FC}^{\mathrm{DV}}_{\mathrm{MEG}}(\gamma_1, \mathsf{T}-\mathsf{R})$ and **(blue)** $\mathbf{FC}^{\mathrm{DV}}_{\mathrm{MEG}}(\gamma_2, \mathsf{T}-\mathsf{R})$, after having removed the mean. Violets dots represent within-subjects relationships, while light blue dots stand for cross-subjects relations. The red line is the linear regression curve obtained with these points: note the (slightly) negative slope obtained with α, and the positive slopes resulted with γ's bands.

we reported a significant anti-correlation between fMRI and α band when switching from a condition of rest to task, together with a positive significant correlation in higher frequency bands (γ_1 and γ_2), which is in line with Betti et al. (2013).

5.4.2 Frequency and/or condition modulation

At this point, we wanted to test whether the general cross-modality correlation increases during task than during rest, and whether this fact happens differently with respect to the frequency band. This is supported by the idea that the specificity of this task should align the results obtained with different technologies, at least for what concerns the cross-network relationship (DAN-VIS), since the task involves a co-activation of the two networks.

To test this possible frequency and/or condition modulation, a Two-Ways ANOVA test was performed on the inter-modality correlation variables, with *frequency band* and *condition* (rest, or task) as factors. The test was applied both for the whole network, and for the single networks (DAN, VIS, DAN-VIS).

As reported in Figure 5.13(a), the results show a significant interaction of frequency and condition in the whole network ($F = 3.63$; $p_{\text{val}} < 2.79 \times 10^{-3}$), with a general significant ($p_{\text{val}} < 5 \times 10^{-2}$, Bonferroni corrected) larger correlation among fMRI results and higher (from β to γ_2) frequency bands than lower ones (from δ to α). Moreover a significant increase in cross-modality similarity in task than in rest results in δ, β and γ_1 bands (all $p_{\text{val}} < 5 \times 10^{-2}$, Bonferroni corrected).
No significant interaction of factors or condition modulation emerges in the VIS network, whereas both the main factors are significant: frequency ($F = 18.6753$; $p_{\text{val}} < 2 \times 10^{-16}$), with β band significantly more correlated with fMRI than γ_2 ($p_{\text{val}} < 5 \times 10^{-2}$, Bonferroni corrected); condition ($F = 4.5085$; $p_{\text{val}} < 3.39 \times 10^{-2}$), with a significantly larger correlation at rest than at task ($p_{\text{val}} < 5 \times 10^{-2}$, Bonferroni corrected).

Finally, interestingly, in the cross-network DAN-VIS, no significant interaction among factors is observed, but both significant main effects of condition ($F = 15.7898$; $p_{\text{val}} < 7.25 \times 10^{-5}$) and frequency ($F = 4.9189$; $p_{\text{val}} < 1.74 \times 10^{-4}$) emerge (see Figures 5.13(c) and 5.13(d)). Specifically, a larger alignment among fMRI and MEG results can be observed during task if compared with rest ($p_{\text{val}} < 5 \times 10^{-2}$, Bonferroni corrected). Moreover α band is significantly more correlated with fMRI than γ_2 ($p_{\text{val}} < 5 \times 10^{-2}$, Bonferroni corrected).

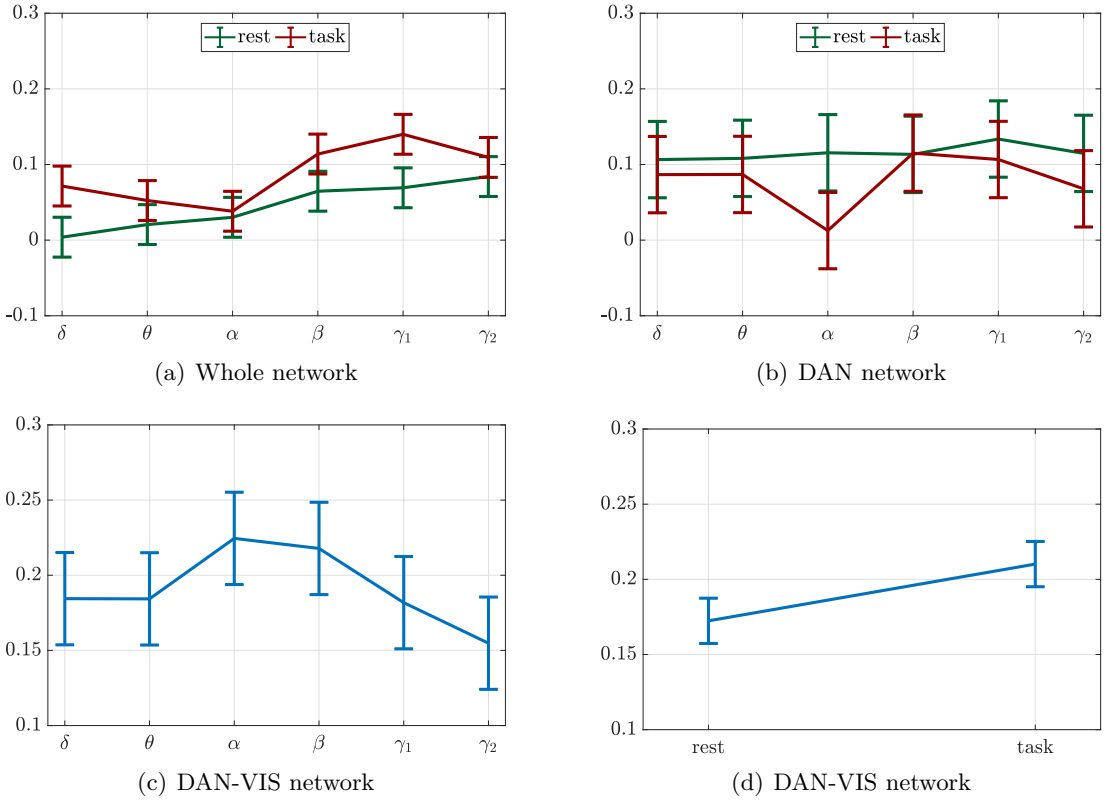

(a) Whole network

(b) DAN network

(c) DAN-VIS network

(d) DAN-VIS network

Figure 5.13: **(a)-(b)** Result of the Two-Way ANOVA test applied to the cross-modality correlation in rest and task FC in the whole **(a)** or in the DAN **(b)** network with frequency and condition as factor. The bars represent the confidence intervals. **(c)-(d)** Main factors evidence of the Two-Way ANOVA test applied to the cross-modality correlation in rest and task FC in the DAN-VIS network with frequency and condition as factor. The bars represent the confidence intervals.

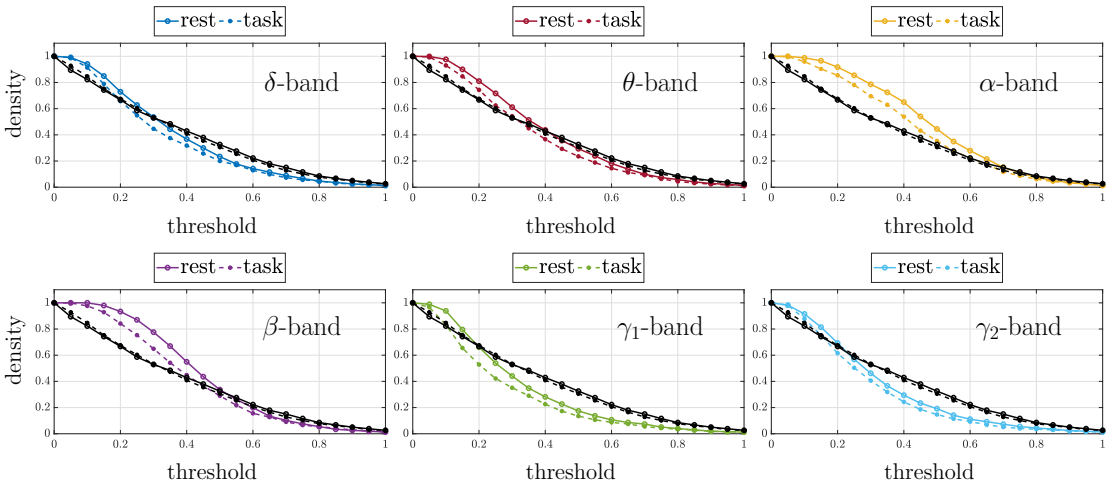

Figure 5.14: Density of the **FC** matrices, estimated as described in Section 5.2.1, as a function of the threshold vector $\mathbf{t_r}$. Each plot represents the density of $\mathbf{FC}_{\text{MEG}}$ of a specific frequency band evaluated during rest (colored continuous line) and during task (colored dotted line), compared with the density of $\mathbf{FC}_{\text{fMRI}}(\mathsf{R})$ (black continuous line) and $\mathbf{FC}_{\text{fMRI}}(\mathsf{T})$ (black dotted line).

5.4.3 Structural comparison

In order to compare the **FC** maps obtained through the two modalities, in different condition of rest or task, we analyzed the density of these matrices as a function of a threshold value (see Section 5.2.1). The results show that fMRI-derived **FC**'s do not vary in their density when switching from resting-state to task, while in all frequency-band, $d\left(\mathbf{FC}_{\text{MEG}}(f,\mathsf{R}),\, t_{r,i}\right) \geq d\left(\mathbf{FC}_{\text{MEG}}(f,\mathsf{T}),\, t_{r,i}\right)$ (see Figures 5.14, and A.3÷A.5). This fact is observed both when the whole network is considered, and when only a sub-network (DAN, VIS, or DAN-VIS) is visualized. From this analysis it emerges that in α and β bands the **FC** are characterized by larger relative weights, if compared with higher frequency bands: indeed, $d\left(\mathbf{FC}_{\text{MEG}}(\alpha),\, t_{r,i}\right)$ and $d\left(\mathbf{FC}_{\text{MEG}}(\beta),\, t_{r,i}\right)$ tend to decrease only when a certain threshold is reached. Moreover, the shape of the density functions obtained at lowest bands (δ and θ) are the most comparable with the ones obtained with fMRI data, at least when the whole network is observed.

A quantitative comparison between the structure of the **FC**'s obtained with fMRI and MEG data has been addressed by means of Hamming distance (see Section 5.2.1), as a function of the threshold vector $\mathbf{t_r}$. Two main observations emerge from this analysis: firstly, the shape of these functions is very different among different sub-network (see Figures 5.15 and A.6÷A.8), and secondly, this distance largely decreases when switching from rest to task, if we consider either the whole network or the DAN-VIS cross-network. Specifically, while the distance between $\mathbf{FC}_{\text{fMRI}}$ and $\mathbf{FC}_{\text{MEG}}$, or between $\mathbf{FC}^{\mathsf{DV}}_{\text{fMRI}}$ and

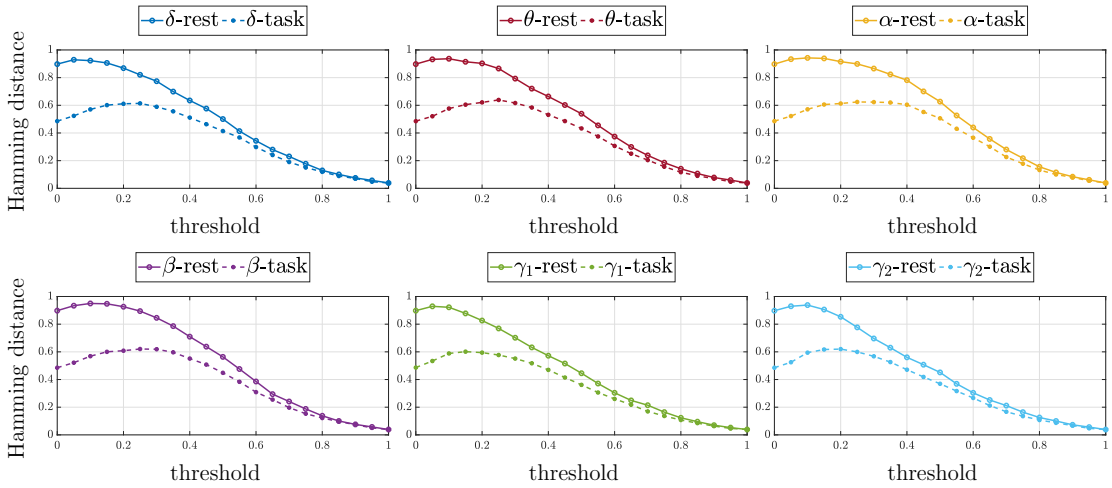

Figure 5.15: Hamming distance between $\mathbf{FC}_{\text{fMRI}}$ and $\mathbf{FC}_{\text{MEG}}$ in resting-state (continuous line) and during task (dashed lines), evaluated as described in Section 5.2.1, as a function of the threshold vector $\mathbf{t_r}$. The different boxes and colors represent different frequency bands. In this figure, the case of whole network is represented.

$\mathbf{FC}^{\text{DV}}_{\text{MEG}}$ reaches its maximum value when almost every entries are considered (i.e. low threshold values), a different behavior is observed in the DAN and VIS networks. In particular, in these networks an opposite behavior emerges, which is characterized by large distance when few entries are considered (high threshold values) and very low distance otherwise. A second aspect to be noticed regards the relevant distance decrease during task in the DAN-VIS cross-network, and the consequent decrease observed also in the whole network. Since the density values do not vary largely from rest to task at low threshold values, this decrease in distance cannot be owing to the density value. More likely, this fact can be related to a task-induced increase in similarity between different modalities. Interestingly, this behavior is not frequency-specific, but it is observed in all the different bands.

MEG vs fMRI: correlated task-induced frequency-dependent behavior. In summary, our results lead to the confirmation of hypothesis **(h2b)**, at the expense of its opposite **(h2b)**. However, as expected, the answer is not unique, but it is frequency-dependent, since the temporal modulation of the $\mathbf{FC}_{\text{MEG}}$'s leads to different MEG-fMRI relationship w.r.t. the considered frequency band. Indeed, we confirm that during task inter-modal similarity significantly increases in the cross-network interaction, while a significant decrease is observed within the DAN network, especially in α band. This is coherent with Betti et al. (2013) and in line with our speculative hypothesis that the specificity of the task should align the results obtained with different technologies, for

what concerns the cross-network relationship (DAN-VIS). This result is confirmed both by an overall comparison among the functional connectivities, and by a structural comparison performed through the definition of two metrics, namely the matrix density and the Hamming distance between fMRI- and MEG-derived **FC**. The structural analysis indeed highlights a strong distance decrease from rest to task in the cross-network (DAN-VIS), independently from the considered frequency.

5.5 Conclusion

In this chapter we addressed the problem of fMRI and MEG comparison, with a twofold purpose. Specifically, we used MEG frequency-dependent BLP signals to test different hypotheses on the role of resting-state functional correlation evidence, similarly to what reported in Spadone et al. (2015) for fMRI data. The two assumptions to be tested (**(h1a)** and **(h1b)**) consisted in assigning to the RSNs the role of *prior* for task-induced activity networks, or the role of *idling* state, respectively. Similarly to the results of Spadone et al. (2015), our answer is network-specific, since the relative stability of the DAN network is confirmed by our tests, especially in β and γ_1 bands. However, from our analysis also a frequency-dependent answer emerged. Indeed, $\mathbf{FC}_{\mathrm{MEG}}$ values in lower bands (with most evidences in α band) have been shown to be significantly modulated by task-condition, thus suggesting a reorganization of the brain functional connections in response to the considered task.

These preliminary results, together with a qualitative analysis of frequency-dependent $\mathbf{FC}_{\mathrm{MEG}}$ and $\mathbf{FC}_{\mathrm{fMRI}}$ matrices (Figure 5.6), suggest that fMRI and MEG signals are not fully independent one each other, but they may be explained by correlated task-evoked effects. Specifically, the global networked architecture of the functional connectivity maps remains the same from fMRI to MEG, especially during task, with some dissimilarities between the modalities. In particular, the significant increase in cross-network correlation, observed with fMRI data, does not emerge by means of MEG data in any frequency bands, where a decrease in DAN-VIS cross-network correlation is always observed when switching from rest to task. However, the lower decrease in γ's frequencies positively correlates with fMRI results. On the other hand, the significantly larger reduction of cross-network functional connection from rest to task in α band shows negative correlation with fMRI task-induced modulation. To summarize, we interpret the increased inter-modalities relationship (positive or negative) during task, when compared with rest, by proposing that they are not completely unconnected, but they are differently modulated by the same stimuli.

This analysis is only a preliminary study on the relationship between fMRI and MEG response in this interesting visuospatial attention task. Indeed, the detailed investigation of these different measured signals is the first step in order to design a suitable mathematical model, that should be able to reproduce the observed behaviors.

In Chapter 6 we will propose a different strategy to analyze the same fMRI data used in this chapter during resting-state from a synchronization point of view. In our opinion, this is another useful investigation to implement in order to achieve even more insights on the human brain activity.

6

Synchronization: a motivational evidence

"Figure out the rhythm of life and live in harmony with it."
Lao Tzu

Over the last decades a large number of theoretical and experimental studies have been aimed to investigate the nature of correlated patterns during resting state (RSNs). However, the significance of functional connectivity in brain activity during rest is still under debate, and it cannot be completely understood. One aspect which is widely accepted is the remarkable match between the resting-state functional connectivity matrix (**rsFC**) and the neuroanatomical (or structural) network (**SC**). This is the reason why various computational models have been used in order to predict the functional connectivity structure starting from the knowledge of the anatomical connections among different brain areas (see Cabral et al. (2014) for a recent review).

The *explorative dynamics* of the resting-state regime, during which different states (the RSNs) are visited over time, and subsequently deactivated, makes this regime very appealing from a dynamical system point of view. Indeed, it can be considered as a non-stationary dynamical process, where a fixed point cannot be defined. The aim of mathematical models is hence to understand how this kind of behavior can emerge from the anatomical architecture of the brain. Specifically, the brain can be described as a complex system, where collective dynamics of groups of neurons define a dynamical

unit, which obeys some specific dynamical equations, in the spontaneous state. The parameters of these *population models* can be tuned in order to describe different kinds of brain regimes. Therefore, computational models may be helpful to bridge the gap between structural and functional connectivity.

In Section 4.3 we have introduced the idea that the brain can be interpreted as a generator of brain waves. Thus, in literature, it has been described as a system of oscillators, whose dynamics can be characterized by the dynamics of their phases. This kind of brain network description introduces us to the *synchronization* phenomenon, which has been of great interest among scientists of several fields during the last decades. Synchronization over networks depends on the oscillators' dynamics, the interaction topology, and the coupling strengths, and the combination of these various factors can be quite intricate.

In order to characterize the complex oscillatory dynamics of the brain, different typologies of computational models have been used in literature to describe the RS dynamics. Among all these models, thanks to its compactness, *Kuramoto model* (KM) stands out.

Before modeling the brain dynamics (especially in resting-state) by means of computational models, a clear understanding of the oscillatory characteristic of the brain (or some specific brain areas) is necessary. To this aim, in the first part of this chapter we analyze the resting-state subset of the fMRI dataset described in Chapter 5, in order to recognized the oscillatory features of the network and to identify the peculiarities that a mathematical model should be able to reproduce. Specifically, we use some of the previously introduced measures (see 4.3.3), together with other quantities, to analytically and qualitatively describe the synchronization patterns emerging among the nodes of the network.

In the second part of this chapter, we will show how a modified version of the KM may be used in order to reproduce the oscillatory behavior of the considered brain regions, thus highlighting the great potential power of this population phase-model as a tool to gain new insights on the dynamic activity of the brain.

Contents

Notation

In this chapter we will deal only with datasets recorded through fMRI technique, during a resting-state condition. As a consequence, we simplify the notation used in Chapter 5 as follow:

> $\mathbf{FC}(s) := \mathbf{FC}_{\text{fMRI}}(s, \mathsf{R}) \in \mathbb{R}^{N \times N}$ represents the **FC** matrix obtained from the fMRI dataset of subject $s \in \{1, \dots, N_s\}$ at rest.
>
> $\mathbf{FC} := \mathbf{FC}_{\text{fMRI}}(\mathsf{R}) \in \mathbb{R}^{N \times N}$ represents the FC matrix obtained from the fMRI dataset, as the average over the **FC**'s of all the N_s subjects at rest.

Since different mathematical measures can be used to evaluate the functional connectivity maps, we will refer to $\mathbf{FC}_{(m)}(\cdot)$, or $\mathbf{FC}_{(m)}$, to highlight that the measure m has been selected to infer the functional connections among nodes. As described later, $m \in \{\mathsf{PLV}, \rho\}$. As in the previous chapter, $\mathbf{FC}^n_* \in \mathbb{R}^{N_n \times N_n}$ represent the sub-matrix related to the sub-network $n \in \{\mathsf{D}, \mathsf{V}, \mathsf{DV}\}$, where D, V, DV stand for DAN, VIS, and DAN-VIS, respectively, and $\mathbf{FC}_*$ indicates one of the matrices defined above. (See Section 5.2.1 for the sub-networks' definition). $[\mathbf{FC}_*]_{ij}$ refers to the element at row i and column j of matrix $\mathbf{FC}_*$.

Moreover, to describe the functional connectivities dynamics, we make use of three-dimensional tensors, with the following notation:

> $\mathbf{T}^{\mathbf{b}}_s \in \mathbb{R}^{N \times N \times T}$ represents the binary tensor referred to $\mathbf{FC}(s)$, as described by equation (4.5), where T is the number of time steps and $s \in \{1, \dots, N_s\}$.
>
> $\widetilde{\mathbf{T}}^{\mathbf{b}}_s(K) \in \mathbb{R}^{N \times N \times T}$ represents the best rank-K approximation of $\mathbf{T}^{\mathbf{b}}_s$, by means of the NNFT algorithm (see Section 4.3.3.2).

6.1 Synchronization: an introduction

The scientific interest in synchronization of coupled oscillators can be traced back a long time ago, when the Dutch mathematician and physicist Christiaan Huygens (1629-95) used the phrase *odd sympathy* in a letter to the Royal Society of London (Huygens (1897)), to describe the tendency of two pendulums to synchronize, or desynchronize, when mounted together on the same beam. This was one of the first observations of the phenomenon of coupled harmonic oscillators, which have many applications in physics

(see Pikovsky et al. (2003); Blekhman (1988) for a detailed historical review). Indeed, synchronization of coupled oscillators is ubiquitous in nature (Lewis et al. (2014); Strogatz (2000)), from the cohesive flocking of birds (Giardina (2008)) to the orchestrated firing of neurons (Nordenfelt et al. (2013); Ferrari et al. (2015)) to the dynamics of man-made networks, including power grids and computer networks (Nishikawa and Motter (2015)).

Research on synchronization phenomena focuses on ascertaining the main mechanisms responsible for collective synchronous behavior among members of a given population. To attain a global coherent activity, interacting oscillatory elements are required. Both internal and external stimuli may drive the rhythmical activity of each element. Despite the complexity that can be at the basis of these (sometime very different in nature) phenomena, a lot of effort has been done in the last decades to understand the essence of synchronization in terms of a few basic principles. As reported in Acebrón et al. (2005), two main ideas can be exploited in order to tackle this problem.

(i) In several biological phenomena, the rhythmical activity of each element is described in terms of a physical variable that evolves regularly in time until reaching a specific threshold. When this threshold is reached, the element emits a pulse, which is transmitted to the neighborhood. This is, for instance, the case of the action potential for neurons in the brain, or for cardiac cells). After the onset of this action potential, the system resets the state of the element, and a new *cycle* starts. In other word, the behavior of this element can be seen as the dynamics of an oscillator, characterized by a specific period. In this context, the concept of phase is directly defined, and it refers to a periodic measure of the elapsed time after the beginning of the cycle. When a single element produces a pulse, then the periods of its neighbors modify, becoming shorter or longer than their nominal duration. Thus a complex population-level behavior emerges, due to the contribution of *pulse-coupled* oscillators.

(ii) Consider now an ensemble of non-linear *phase-oscillators* (i.e. a population of non-linear oscillators moving in a globally attracting limit cycle of constant amplitude), and suppose that they are coupled sufficiently weakly to ensure that they will not be taken away from the global limit cycle. Thus, the evolution of the whole system is completely described through only one degree of freedom: the phase dynamics of each element.

Although the higher level of intuition given by the framework **(i)**, the second one is easier to be described by means of mathematical models, especially in case of large populations of oscillators. Thus, large part of the existing literature focused on the

description of *phase-oscillators*' networks with the purpose of characterizing existing phenomena. Even thought the *Winfree model* (Winfree (1967)) was too hard to be solved in its general version, it was Winfree, who realized that synchronization can be understood as a threshold process. Specifically, he showed that when the coupling among oscillators is strong enough, a macroscopic fraction of them synchronizes to a common frequency.

However, the difficulties on the tractability of Winfree model allowed the introduction of other simplified models. In this context, the model proposed by Kuramoto (Kuramoto (1975)) emerged. He analyzed a model of phase oscillators running at arbitrary intrinsic frequencies and coupled through the sine of their phases difference. Kuramoto model has the twofold advantage, of being simple enough to me mathematical tractable, yet sufficiently complex to describe non-trivial existing phenomena.

6.2 Useful synchronization measures

In order to extract the amplitude and the phase from fMRI data, or simulated data, let us consider the *analytic signal representation* $a_x(t)$ of each time series $x(t)$, whose definition is here reported.

Definition 6.2.1 (***Analytic signal representation***)**.** Given a real signal $x: \mathbb{R} \to \mathbb{R}$, its analytic representation $a_x(\cdot)$ is a complex signal defined as

$$\begin{aligned} a_x: \ & \mathbb{R} \to \mathbb{C} \\ & t \mapsto a_x(t) = x(t) + \mathrm{j}\mathcal{H}[x(t)] = A_x(t)e^{\mathrm{j}\theta_x(t)}, \end{aligned} \tag{6.1a}$$

where $\mathcal{H}[\cdot]$ is the Hilbert transform (Papoulis (1960)) of $x(\cdot)$:

$$\begin{aligned} \mathcal{H}: \ & \mathbb{R} \to \mathbb{R} \\ & x(t) \mapsto \mathcal{H}[x(t)] = \lim_{\varepsilon \to 0} \frac{1}{\pi} \int_{|\tau - t| > \varepsilon} \frac{x(\tau)}{t - \tau} d\tau. \end{aligned} \tag{6.1b}$$

□

The amplitude and the phase related to the signal x are hence defined as the amplitude A_x and phase θ_x of its analytic representation.

At the network level, the synchrony among the phases θ_i of a group of N oscillators

can be evaluated by means of the *order parameters* R and Φ, jointly defined as

$$R(t)e^{\mathrm{j}\Phi(t)} = \frac{1}{N}\sum_{i=1}^{N} e^{\mathrm{j}\theta_i(t)}, \tag{6.2}$$

where $R(t)$ measures phase uniformity at time t, and varies between 0 (fully desynchronized state) and 1 (fully synchronized state), and $\Phi(t)$ represents the phase of the global ensemble. The standard deviation of $R(\cdot)$, referred as σ_R, is used to quantify the degree of metastability of the system (Shanahan (2010)).

To quantify the pairwise phase relation between two given brain regions i and k, recall that the phase locking value (4.3) is a useful tool. For convenience's sake, we report here its expression:

$$\mathrm{PLV}_{\theta_i\theta_k} = \left|\frac{1}{T}\sum_{t=1}^{T} e^{\mathrm{j}[\theta_k(t)-\theta_i(t)]}\right|,$$

whose value ranges from 0 (complete phase independence) to 1 (perfect phase locking: constant difference among θ_i and θ_k, across time). In this way a possible **FC** is directly defined as a matrix $\mathbf{FC}_{(\mathsf{PLV})} \in \mathbb{R}^{N\times N}$, whose entries are set as $[\mathbf{FC}_{(\mathsf{PLV})}]_{ij} = \mathrm{PLV}_{\theta_i\theta_j}$, for all i and j. This measure can be compared with another **FC** matrix ($\mathbf{FC}_{(\rho)}$), evaluated by means of Pearson's correlation coefficient (4.1) among the time series x_i and x_j (and not only their phases), whose entries are given by

$$\left[\mathbf{FC}_{(\rho)}\right]_{ij} = \frac{\sigma^2_{x_i x_j}}{\sigma_{x_i}\sigma_{x_j}} \in [-1,\ 1]. \tag{6.3}$$

6.3 Analysis pipeline

In order to characterize fMRI resting-state data from a synchronization point of view, we need to determine the workflow, or analysis pipeline, used to recognize the features of the measured data that we would like to reproduce by means of computational models. To design our specific pipeline, we refer to Ponce-Alvarez et al. (2015) and we adapt the proposed methods to fit our aims. Although we are focusing on a specific subset of brain areas to be coherent with the results presented in the previous chapter, in Appendix A.8 we complete the analysis by showing the results obtained by applying the same pipeline to a set of real data describing the whole brain by means of 66 brain areas.

The workflow of our analysis is composed by the following steps:

s1. data acquisition and filtering (see Section 5.2.1, restricted to the resting-state session);
s2. analytical signal representation and phase evaluation;
s3. analysis of both global and network-specific synchronization during time;
s4. characterization of the phase difference among nodes through the estimation of its probability density function (p.d.f.) (Abramowitz and Stegun (1964));
s5. definition of a functional connectivity map based on the phase locking value and comparison with the correlation matrix among the original signal;
s6. analysis of the time-varying synchronization patterns.

In the last part of this chapter, the same analysis steps are applied to the KM to perform a qualitative comparison with the real data. Specifically, we will focus on the shape of the phase difference p.d.f. function among nodes, on the dynamics of the synchronization metrics during time, and finally on the patterns of synchronized states.

Phase evaluation. In order to evaluate the phase evolution of each brain area, we applied the Hilbert transform (6.1b) to the filtered BOLD signals $x_i(\cdot)$ to obtain the associated analytical signals of the form $A_i(\cdot)e^{\mathrm{j}\theta_i(\cdot)}$, where A_i and θ_i stand for A_{x_i} and θ_{x_i}, respectively, for easiness of notation. Thus $A_i(\cdot)$ represents the evolution of the amplitude of each time series, and $\theta_i(\cdot)$ is the associated phase. Then, the first and the last ten time steps were discarded, in order to avoid border effects. The total time point of each time series hence becomes $T = 460$.

Global and network-specific synchronization The synchronization level among ROIs has been evaluated by means of the absolute value of the order parameter, $R(\cdot)$, defined as (6.2). Specifically, we considered:

$$R(t) = \left| \frac{1}{N} \sum_{i=1}^{N} e^{\mathrm{j}\theta_i(t)} \right|, \tag{6.4a}$$

$$R^{\mathsf{D}}(t) = \left| \frac{1}{N_{\mathrm{D}}} \sum_{i \in \mathrm{DAN}} e^{\mathrm{j}\theta_i(t)} \right|, \tag{6.4b}$$

$$R^{\mathsf{V}}(t) = \left| \frac{1}{N_{\mathrm{V}}} \sum_{i \in \mathrm{VIS}} e^{\mathrm{j}\theta_i(t)} \right|, \tag{6.4c}$$

$$R^{\mathsf{DV}}(t) = \left| \frac{1}{N_{\mathrm{D}} + N_{\mathrm{V}}} \sum_{i \in (\mathrm{DAN} \cup \mathrm{VIS})} e^{\mathrm{j}\theta_i(t)} \right|, \tag{6.4d}$$

where the apexes D, V and DV stand for DAN, VIS, and DAN-VIS, respectively, and the absence of the apex indicates that the order parameter has been evaluated across all the N nodes. Recall that N_{D} and N_{V} represent the number of nodes within DAN and VIS networks, and specifically we have $N = 14$, $N_{\mathsf{D}} = N_{\mathsf{V}} = 6$. In order to assess the significance of synchronization, we created a set of phase shuffled surrogates through the algorithm described in Appendix A.7. Shortly, we extracted the coefficients of the discrete Fourier transform from the original data, and we defined the Fourier coefficients for the surrogates, by preserving the same modulus and substituting the phases with uniformly distributed random numbers. Then the surrogates were exposed to the same filtering before evaluating the order parameter, used to estimate the global level of phase synchrony on the null hypothesis of absence of synchronization. The results show that phase synchronization is significantly higher ($p_{\text{val}} = 0$, t-test) than the expected accidental synchronization among surrogates. Figure 6.1(a) shows the evolution of the absolute values of the order parameters during time, related to one subject, both for the whole graph and for the specific networks. In Figure 6.1(b) instead, the probability density function of the $R(\cdot)$ value across all subjects and all time steps is reported and compared with the one obtained through surrogates. The p.d.f. restricted to DAN, VIS, or DAN-VIS configuration are reported in Figure 6.2.

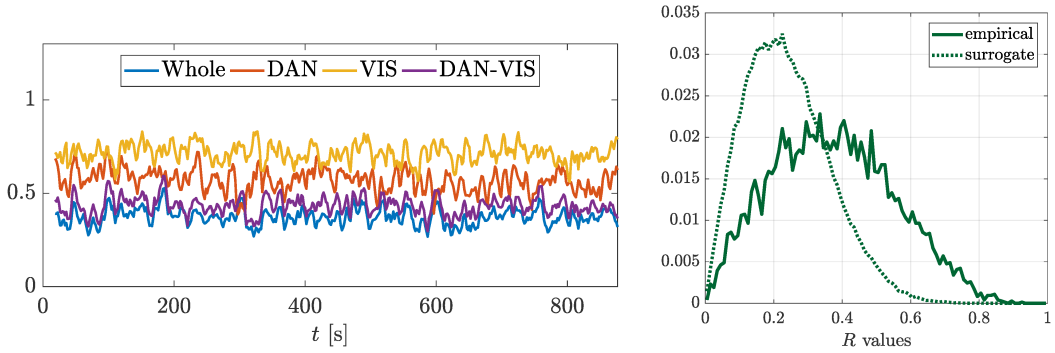

(a) Synchronization level during time (subject 1)

(b) Whole network

Figure 6.1: Phase synchronization level of the network estimated through the absolute value of the order parameters. **(a)** Evolution of (6.4) during time. **(b)** Probability density function of the absolute value of the order parameter, across all time steps and all subjects, compared with the p.d.f. of the level of phase synchrony on the null hypothesis of null synchronization (dotted line) estimated through surrogates.

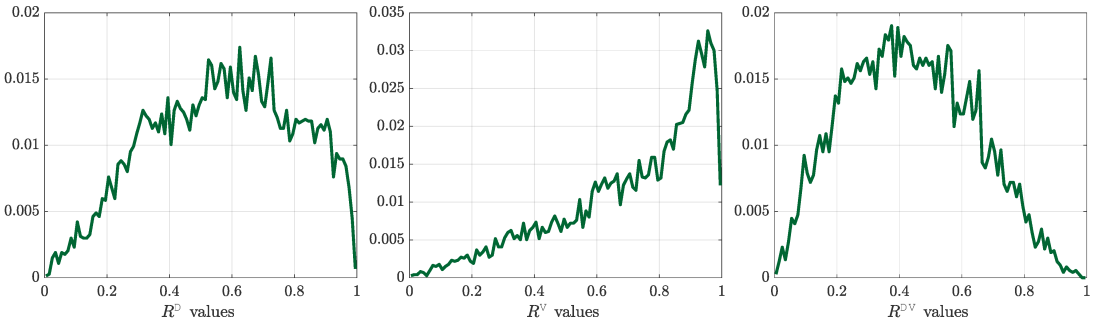

(a) p.d.f. of $R^{\mathsf{D}}(\cdot)$ (b) p.d.f. of $R^{\mathsf{V}}(\cdot)$ (c) p.d.f. of $R^{\mathsf{DV}}(\cdot)$

Figure 6.2: Probability density function of the absolute value of the order parameter restricted to the selected networks DAN **(a)**, VIS **(b)**, and DAN-VIS **(c)**, across all time steps and all subjects.

Phase difference p.d.f. For each subject, at each time point, we evaluated the difference between every pairs of nodes i and j as

$$\theta_{ij}(t) := \theta_j(t) - \theta_i(t) \in [-\pi,\ \pi], \qquad \forall\ i,\ j = 1, \ldots, N, \qquad i \neq j.$$

Observe that $\theta_{ij}(t) = -\theta_{ji}(t)$. Then, we stacked all the values into a vector, in order to estimate the probability density function of the phase difference among each pair of nodes. This measure has been used as a target function to fit the computational models with the real data. Specifically, Figure 6.3 reports the results across all pairs of brain regions, all time steps and all subjects, as well as for the cross-network DAN-VIS, which is represented by the configuration where $i \in$ DAN and $j \in$ VIS. From this figures it emerges that the p.d.f. of the phase differences assumes a bell-shape centred in zero both if the whole set of nodes is considered, and if only DAN or VIS networks are considered separately. If we focus on the DAN-VIS configuration, we can observe an interesting situation where two peaks emerge: one at zero and one at $\pm\pi$. This can suggest two explanations: we have either two separated populations, that are within-group synchronized, but between-groups desynchronized, or we have the alternation of period of synchrony and period of desynchronization among the nodes during time. A mixture of the two hypotheses can also be compelling. Indeed, as it can be observed in Figure 6.4, the p.d.f. of the phase difference is not constant during time, but periods of higher level of synchrony alternate with periods of lower synchronization. As conceivable, the shape of the p.d.f. during time is coherent with the evolution of the absolute value of the order parameter $R(\cdot)$: periods of higher $R(t)$ correspond to periods where the phase difference p.d.f. is skewed around zero.

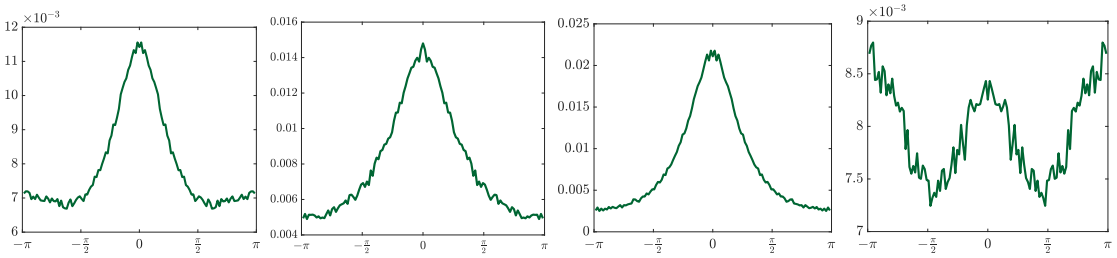

(a) Whole network (b) DAN (c) VIS (d) DAN-VIS

Figure 6.3: Probability density function (p.d.f.) of the phase differences across all pairs of brain regions, all time steps and all subjects.

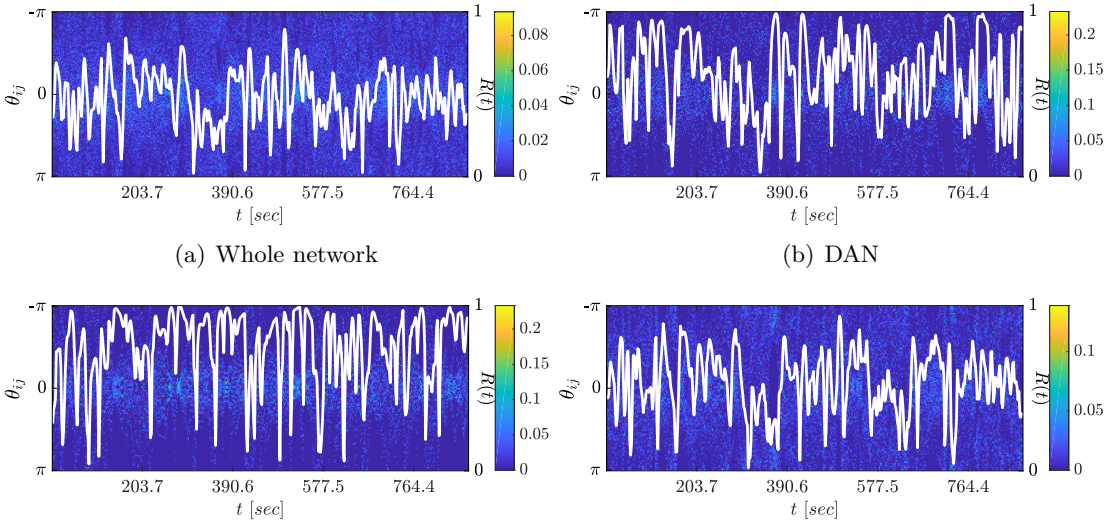

(a) Whole network (b) DAN

(c) VIS (d) DAN-VIS

Figure 6.4: Temporal evolution of the p.d.f. of the phase difference among each pair of nodes (from one subject). The colour indicates the value of the p.d.f. at each time step (left y-axis). The white lines represents the absolute value of the order parameter $R(t)$ related to the same subject (right y-axis). Subfigure **(a)** is referred to the whole graph, whereas subfigures **(b)**, **(c)** and **(d)** refer to DAN, VIS and DAN-VIS networks, respectively.

Functional connectivity maps. In this framework, the functional connectivity map is directly defined through the PLV (4.3) and it is referred as $\mathbf{FC}_{(\mathsf{PLV})} \in \mathbb{R}^{N\times N}$, as described above. Recall that the phase locking value between a pair of phases measures how much the difference among the two phases vary during time: the more constant the difference, the higher the respective PLV. Thus, a PLV equal to 1 does not mean a perfect overlapping of the phases during time, rather it means that the phases evolve with the same dynamics, preserving the same distance among them. In this way, $\mathbf{FC}_{(\mathsf{PLV})}$ and $R(\cdot)$ describe two different properties of the networks, since the latter is a measure

of the similarity among phases.

To achieve more robust measures of PLV, for each pair of brain regions, we evaluated the PLV across sliding windows of ∼40 s, and then the $\mathbf{FC}_{(\mathsf{PLV})}$ matrix has been defined as the mean over all the windows. Figure 6.5(a) shows the result. At this point, it may be interesting to compare the obtained functional map with the one given by equation (6.3), when the filtered signals are considered (rather than only their relative phases). Figure 6.5(b) show the $\mathbf{FC}_{(\rho)}$, obtained as an average across the same sliding windows used to derive $\mathbf{FC}_{(\mathsf{PLV})}$. From Figure 6.6 we can observe the relationship among the two functional measures.

Across all the subjects, the probability density function of the values of each entry of the functional connectivity matrix $\mathbf{FC}_{(\mathsf{PLV})}$ has been estimated and reported in Figure 6.7, where it is shown both with respect to the whole matrix and with respect to single sub- and cross-network. As expected, although similar, Figures 6.7, 6.1(b) and 6.2 are not congruent, thus remarking that $\mathbf{FC}_{(\mathsf{PLV})}$ and R measure two different network properties.

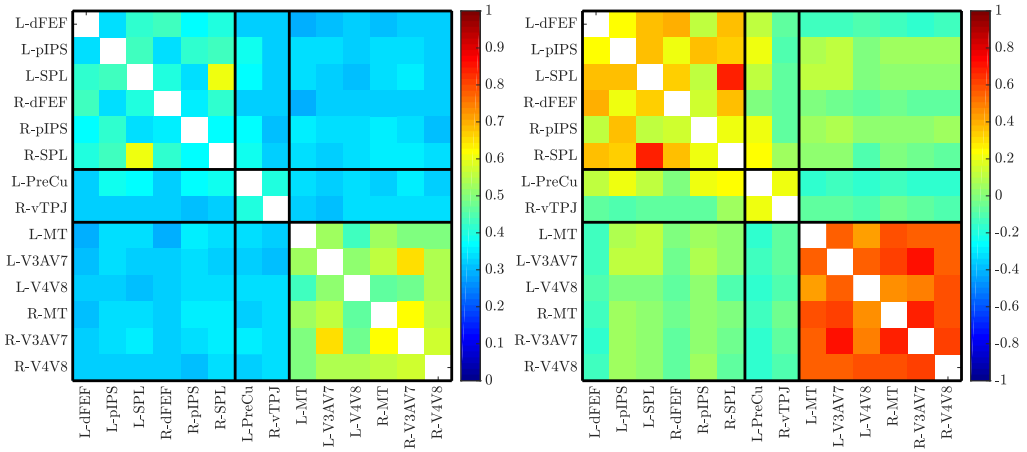

(a) $\mathbf{FC}_{(\mathsf{PLV})}$ (b) $\mathbf{FC}_{(\rho)}$

Figure 6.5: Functional connectivity maps defined through the phase locking value **(a)** and the Pearson's correlation coefficient among the filtered time series **(b)**, averaged across all the subjects. The nodes are in the same order as in Table 5.1.

Time-varying networks. We support the hypothesis that the spatio-temporal synchronization patterns, which emerge from the results reported above, reflect the formation and break up of different communities (or clusters) of synchronized brain regions. To test this hypothesis, for each subject $s = 1, \ldots, N_s$, we defined a binary tensor $\mathbf{T}_s^{\mathbf{b}} \in \mathbb{R}^{N \times N \times T}$, as described by equation (4.4), with threshold $\phi = \pi/6$, and we approximated it with the best rank-K tensor $\widetilde{\mathbf{T}}_s^{\mathbf{b}}(K) \in \mathbb{R}^{N \times N \times T}$, which can be in turn decomposed into K rank-

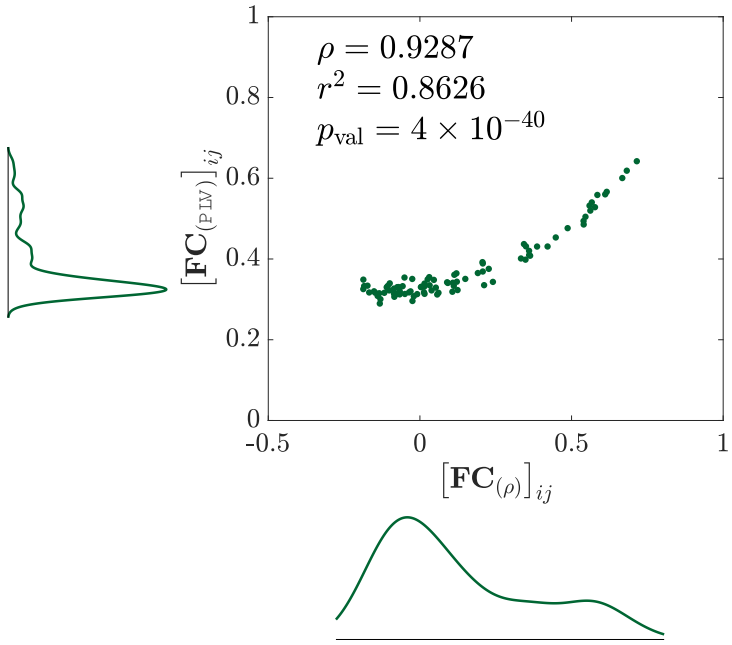

Figure 6.6: Relationship among $\mathbf{FC}_{(\text{PLV})}$ and $\mathbf{FC}_{(\rho)}$. Note that $\mathbf{FC}_{(\text{PLV})}$ assumes values within $[0,\ 1]$, while $[\mathbf{FC}_{(\text{PLV})}]_{ij} \in [-1,\ 1]$. The correlation among the two matrices and the respective significance value are given by ρ and p_{val}, respectively. r^2 instead measures the fraction of the explained variance of $\mathbf{FC}_{(\rho)}$, expressed by $\mathbf{FC}_{(\text{PLV})}$.

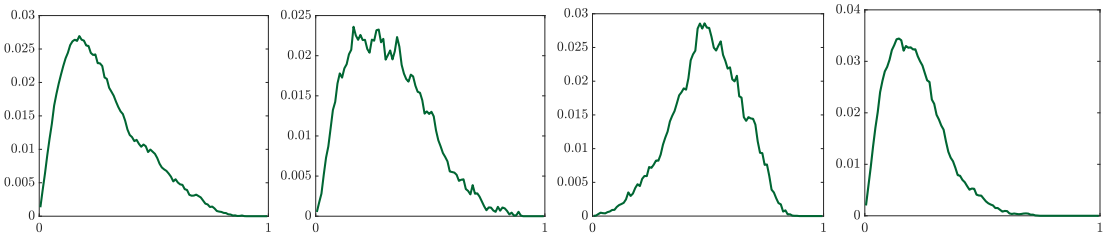

(a) Whole network (b) DAN (c) VIS (d) DAN-VIS

Figure 6.7: Probability density function (p.d.f.) of the $\mathbf{FC}_{(\text{PLV})}$ values across all pairs of brain regions and all subjects.

one positive tensor, by means of the NNTF algorithm (see Section 4.3.3.2, equations (4.6) and (4.7)). The problem of choosing the best number of components (clusters) K in order to approximate the given tensor is not easy to solve. Specifically, for each subject s and for each values of $K \in \{1, \ldots, 30\}$, we defined a fit function, as follows:

$$\text{Fit}_s(K) := 1 - \frac{\left\| \mathbf{T}_s^{\mathbf{b}} - \widetilde{\mathbf{T}}_s^{\mathbf{b}}(K) \right\|_{\text{F}}}{\|\mathbf{T}_s^{\mathbf{b}}\|_{\text{F}}} \in [0,\ 1], \qquad s = 1, \ldots, 16, \qquad K = 1, \ldots, 30. \tag{6.5}$$

Figure 6.8 shows the fit values $\text{Fit}_s(K)$ as a function of K for all the subjects, as well as the average across all of them. Although, as expected, the fit improves as the number of components K increases, the shape of the curve becomes flatter, when $K > 9$. As a trade-off between the number of the components and the goodness of the approximation, we selected $K = 9$ as the optimal number of clusters for each subject, although we tested several other choices of K, which are not reported in this work.

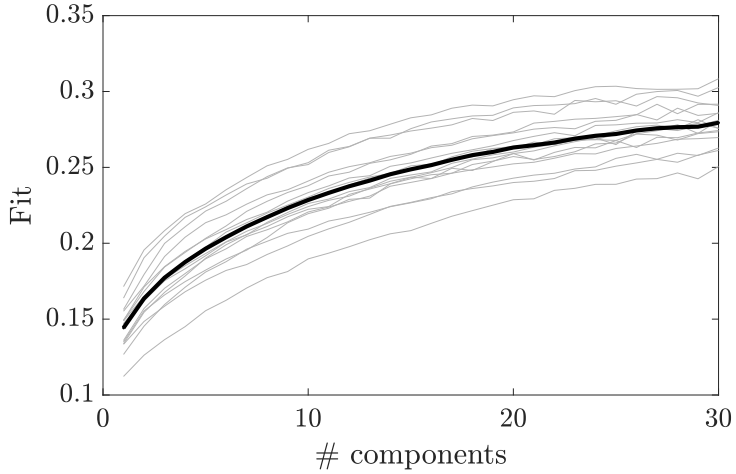

Figure 6.8: Values of the fit (6.5) as a function of the number of components K. Gray lines: fit function evaluated for each of the 16 subjects. Black thick line: average of the fit function across all the subjects.

Thus, for each subject, $K = 9$ components are extracted and the correspondent community patterns are evaluated as $\mathbf{a}_k \cdot \mathbf{a}_k{}^{\mathsf{T}}$, $k = 1, \ldots, K$, whose relative strength during time are estimated by equation (4.8). In Figure 6.9 the synchronization patterns and the respective strength during time is reported for what concerns subject number 1. What emerges from these pictures is that the strength of each community is definitively not constant during time, but there is a clear alternation among clusters, in such a way that at each interval of time a specific community dominates the other. Moreover, we can observe that, even though some communities reflect the main networks (DAN and VIS), it happens also that some nodes from DAN and VIS share the same community (see for instance the community $k = 6$).

To test our hypothesis on the relationship among the dynamics of the synchronization level during time and the formation of time varying clusters, we compared the evolution of $R(\cdot)$ with the evolution of the global strength $S(\cdot)$ as defined in equation (4.9), for each subject. From Figure 6.10, which shows this two quantities obtained from subject 1, an high level of similarity emerges among them, thus confirming our assumption.

Then, the 144 synchronization patterns (9 patterns for each of the 16 subjects) have

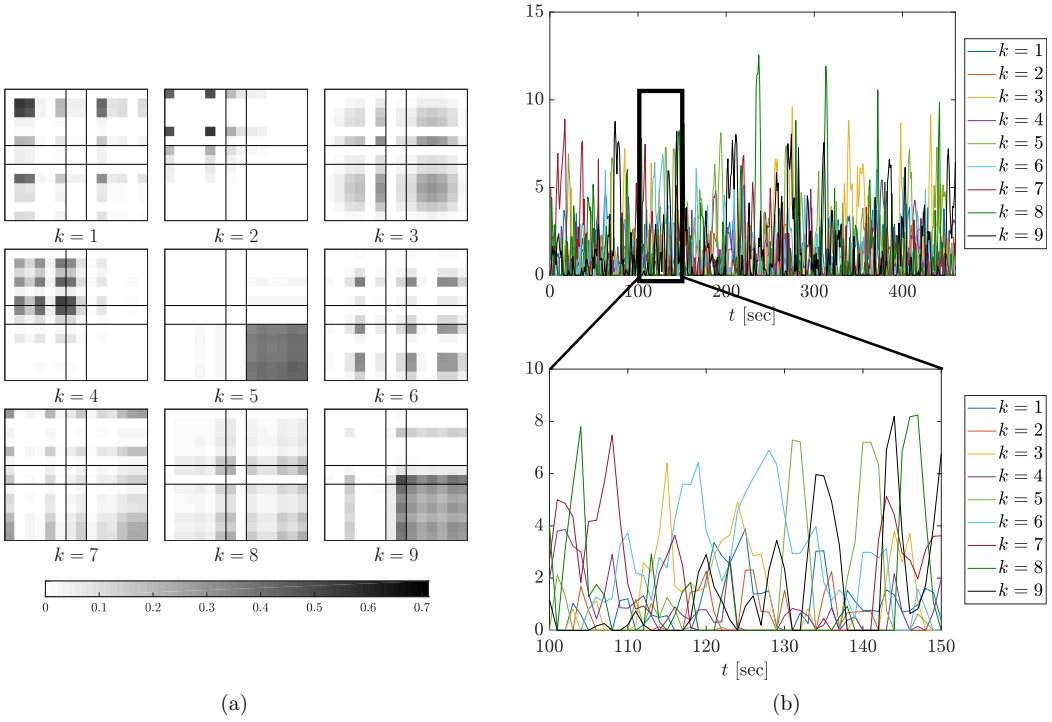

Figure 6.9: **(a)** Representation of the $K = 9$ community patterns ($\mathbf{a}_k \cdot \mathbf{a}_k{}^{\mathsf{T}}$, $k = 1, \ldots, K$) obtained from subject number 1. **(b)** Top: evolution of the strength of each community k of subject 1 during time. Bottom: enlargement of the figure above, restricted to 50 s, in order to appreciate the turnover of the clusters' activation during time.

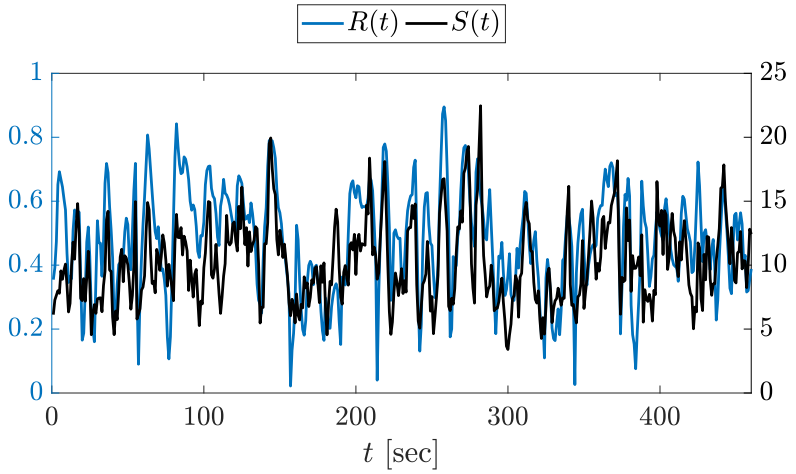

Figure 6.10: Comparison among the evolution of the absolute value $R(t)$ of the order parameter (left y-axis, blue line) and the global strength $S(t)$ (right y-axis, black line) for subject 1.

been clusterized by means of k-means in order to define $K = 9$ *global* patterns, which are representative for the entirety of the subjects. Figure 6.11 reports the obtained community patterns and the relative percentage of subjects that participate to the definition of each specific pattern. In other words, a subject s is consider as a participant to the definition of a pattern k if the k-means algorithm has assigned at least one of the patterns of s to the cluster whose centroid is k. As noted for subject 1, from the global synchronization communities it emerges again that in some cases, nodes from DAN and VIS share the same community.

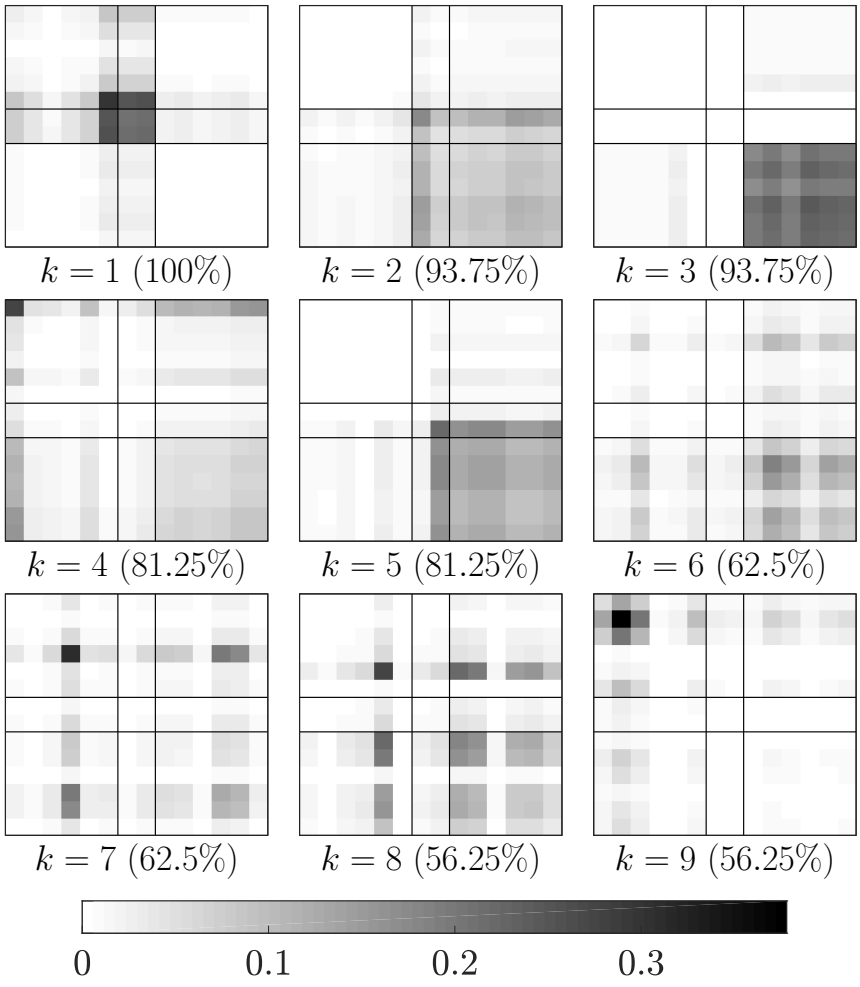

Figure 6.11: Representation of the $K = 9$ community patterns ($\mathbf{a}_k \cdot \mathbf{a}_k^{\mathsf{T}}$, $k = 1, \ldots, K$) obtained from all the subjects. To each patter a percentage value is associated, representing the percentage of subjects that participate to extract the same pattern.

6.4 Resting-state modeling by means of Kuramoto model

Among different computational models that have been used in literature to describe the RS dynamics of the brain, we have focused on a modified version (KM) of the *classic Kuramoto model* (cKM) and we have used it to simulate the qualitative behavior observed in the real data, when the structural connectivity map is available. The aim of this study is to highlight the goodness of this relatively simple mathematical model on representing the complex system of the brain. In Appendix A.3 we report a brief description of other computational models that can be used to describe resting-state dynamics. However, from our point of view, the KM stands out for its compactness and its interesting theoretical analysis (see Chapter 7).

In the following, we will first introduce Kuramoto model and a useful extended version of it, used to simulate the dynamics of the real network. Then we will apply the same analysis pipeline presented in Section 6.3 to analyze the synchronization patterns resulting from the simulated data, and we will present a qualitative comparison with the empirical results.

As a remark, a systematic identification of the KM with respect to the available real dataset is not the objective of this section. Indeed, our purpose is to emphasize the powerful of this relatively simple model to reproduce the general behavior of a network of brain areas, rather then fit exactly the specific data. These results are presented as a motivational application on the synchronization framework to the brain network, that introduce our theoretical analysis reported in Chapter 7.

6.4.1 The classic Kuramoto model (cKM) and its extension (KM)

We consider a weighted graph $\mathcal{G} = (\mathcal{V}, \mathcal{E})$, where $\mathcal{V} = \{1, \dots, N\}$ is the set of nodes representing the selected N brain areas, and $\mathcal{E} \subseteq \mathcal{V} \times \mathcal{V}$ is the set of edges, each of them connecting one node to another. The presence of the edge (i, j) indicates that nodes i and j can share information in a manner proportional to the weight associated to each link. Specifically, we consider the structural connectivity **SC** among brain areas in order to quantify these weights. Therefore, we define the weighted adjacency matrix $\mathbf{A} \in \mathbb{R}^{N \times N}$ of the graph $\mathcal{G}$ equal to a normalized version of the **SC** w.r.t. the maximum value of its entries, such that $\max_{ij}[\mathbf{A}]_{ij} = 1$. Hence, entry a_{ij} of $\mathbf{A}$ is zero if no anatomical connection among areas i and j exists. Then, by considering that two nodes i and j are neighbors if $a_{ij} \neq 0$, let $\mathcal{N}_i \subset \mathcal{V}$ be the set containing all the neighbors of node i, for each $i = 1, \dots, N$.

In order to take into account the spatial arrangement of the areas, we define a delay

matrix $\boldsymbol{\Upsilon} \in \mathbb{R}^{N\times N}$, whose entries υ_{ij}'s define the delay that affects the communication between each pair of nodes $(i,\, j)$. As in Cabral et al. (2014), we define the delay between node i and j depending on the Euclidean distance d_{ij} between the centres of the areas, and on the conduction velocity ν, so that $\upsilon_{ij} := d_{ij}/\nu$. By increasing or decreasing ν, the delays become shorter or longer, respectively, shifting the mean of the delay distribution $\bar{\upsilon}$.

Each node of the network is equipped with a constant natural frequency $\omega_i \in \mathbb{R}$, and a phase, which evolves during time. Let $\theta_i : \mathbb{R}_{\geq 0} \to \mathbb{R}$ be the map describing the phase of the i-th oscillator. The classic Kuramoto model (Kuramoto (1975)) assumes that the phase θ_i evolves as

$$\text{cKM:} \qquad \dot{\theta}_i(t) = \omega_i + \frac{C}{N}\sum_{j=1}^{N} \sin(\theta_j(t) - \theta_i(t)), \qquad i = 1, \dots, N, \qquad t \geq 0,$$

where $C \geq 0$ is the coupling strength among the oscillators.

In this work, we consider an extended version of the classical model, that enriches the model with weighted coupling strengths derived from the topology of the network, and with the delay effects on the communication among nodes, due to the spatial distance between the brain areas. Specifically, KM describes the phase dynamics of node i as

$$\text{KM:} \qquad \dot{\theta}_i(t) = \omega_i + \frac{C}{N}\sum_{j=1}^{N} a_{ij} \sin(\theta_j(t - \upsilon_{ij}) - \theta_i(t)), \qquad \forall i = 1, \dots, N, \tag{6.6a}$$

where the constant coupling factor is modulated by the strength of the anatomical connection among nodes i and j (a_{ij}), and υ_{ij} measures how late the information sent by oscillator θ_j reaches θ_i.

As mentioned in the introductive chapters, a debate is still open around the origin of the slow resting-state fluctuations. In order to investigate whether the oscillations are better described by a deterministic models, or by random activity of a low amplitude, some works in literature (see Ponce-Alvarez et al. (2015)) have compared (6.6a) with the following dynamics:

$$\dot{\theta}_i(t) = \omega + \frac{C}{N}\sum_{j=1}^{N} a_{ij} \sin(\theta_j(t - \upsilon_{ij}) - \theta_i(t)) + \eta_i(t), \qquad \forall i = 1, \dots, N, \tag{6.6b}$$

where all the natural frequencies are equal to the same value ω and the terms η_i's are uncorrelated random Gaussian noise with zero mean and variance $\sigma^2_{\eta_i}$, $\eta_i \sim \mathcal{N}(0,\, \sigma^2_{\eta_i})$. However, in line with the results presented in literature, we support the idea that the

fluctuations are not random, but well structured, and we will focus on dynamics (6.6a).

6.4.2 Distance matrix and structural connectivity map

The spatial location of each ROI in the MNI coordinates, as reported in Table 5.1 was used to evaluate the distance matrix $\mathbf{D} \in \mathbb{R}^{N\times N}$, which describes the Euclidean distance between each pair of ROIs. This matrix was then used to evaluate the delay which affects the communication among nodes, as described above.

To simulate our dynamical model, we used a structural connectivity map, that has not been estimated through the same subjects, whom the functional data belong to. Although this implies the loss of some specificity of our analysis, we believe that it is acceptable for our high-level analysis. The **SC** has been estimated by the Research Group of Professor D.S.Bassett (Department of Bioengineering, University of Pennsylvania, PA), through 705 diffusion direction data (59 min acquisition) from ten subjects. The ROIs to be used to define the **SC** has been selected as the closest match of the ROIs identified in our experiment in the 463-node Lausanne parcellation (Hagmann et al. (2008)). The nominal **SC** has been obtained by averaging the matrices of all the ten subjects. Finally, to define the weighted adjacency matrix of our system, we have normalized the anatomical map, by dividing each entry by the maximum value across all the elements of the **SC**. In this manner, each the value of each entry is bounded within $[0,\ 1]$.

Figure 6.12 shows the resulted structural connectivity (left) and the distance (right) matrices, where the diagonal elements are masked.

6.4.3 Dynamics simulation

Natural frequencies estimation. Before simulating the dynamical system, we have estimated the natural frequencies ω_i for each agent from the empirical data, as follows:

$$\omega_i^s = \frac{\theta_i^s(T) - \theta_i^s(1)}{T}, \qquad \forall\, i = 1,\dots,N, \qquad \forall\, s = 1,\dots,N_s$$
$$\widehat{\omega}_i = \frac{1}{N_s}\sum_{s=1}^{N_s} \omega_i^s, \qquad \forall\, i = 1,\dots,N,$$

where $\widehat{\omega}_i$ is the estimated natural frequency of the i-th node, T is the total number of time steps of the empirical data, and $\theta_i^s(t)$ is the unwrapped value (in radians) of the phase of node i at time step t as estimated from the data of the s-th subject.

Initial condition. The initial states for the N nodes have been evaluated by assigning a random value within $[0,\ 2\pi]$ at each node and then running the simulation for 10^3 time

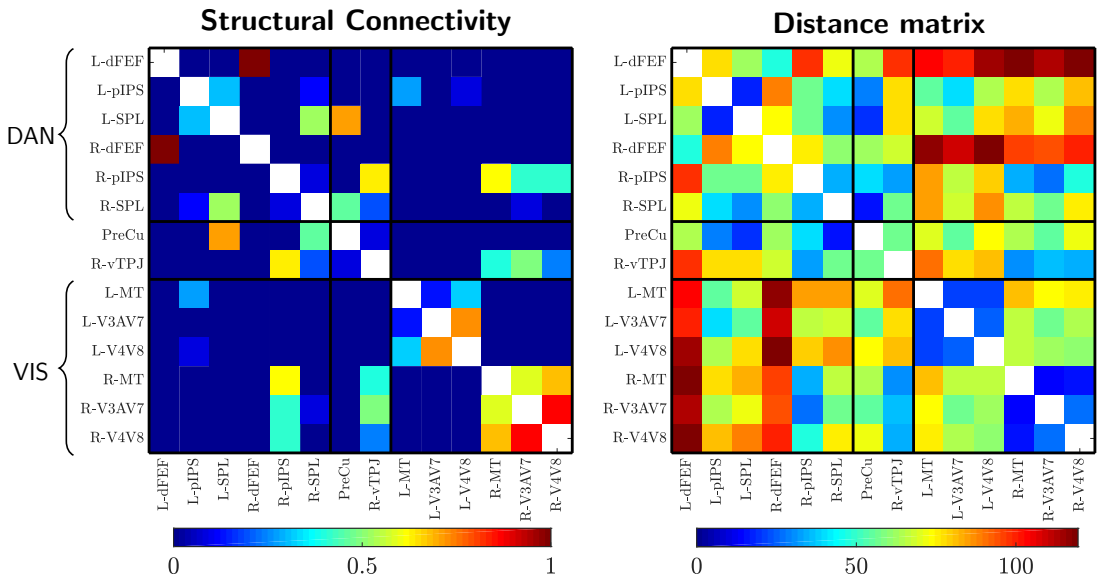

Figure 6.12: Representation of **SC** (left) and **D** (right) matrices obtained as described in the main text. **SC** is normalized w.r.t. its maximum value. The distance between each pairs of nodes is evaluated in MNI coordinates. The nodes are in the same order as in Table 5.1.

steps. The final values assumed by the phases have been set as the initial values of the simulation of interest.

The evolution of the system dynamics (6.6a) has then been simulated with the software MATLAB® 2017b, by using a time step of $1/F_s$ seconds, for about 4000 s. The first 400 s and the last 20 s were discarded, in order to avoid border effects and to be sure that the transient evolution was exhausted.

Then, the analysis steps from **s3.** to **s6.** described in Section 6.3 have been performed to compare the synthetic results with the empirical ones, previously presented. The features that we attempted to reproduce in a qualitative manner are the probability density function of the difference among pairs of phases, and the behavior of the absolute value of the order parameter (both in the whole network and in the different sub-networks) during time, which should vary as the dynamics evolves, representing periods of synchrony followed by periods of lower level of cohesion among the agents. Then, we have investigated whether the simulated $\mathbf{FC}_{(\mathsf{PLV})}$ (defined as $\widehat{\mathbf{FC}}_{(\mathsf{PLV})}$) was somehow correlated with the empirical one, reproducing the same functional networks. Finally, we tested the power of the NNTF algorithm when applied to the simulated time series, to recognized patterns of synchronized states during time.

In addition to the natural frequencies, system (6.6a) requires the definition of the two

parameters $\widetilde{C} := C/N$ and $\bar{v}$ to be completely described. Different identification tools could be implemented in order to estimate these parameters from the data. However, this goes beyond the goal of this work, that is aimed to present only a motivational example to the use of KM to describe the brain networks' dynamics. Thus, we have tested several different values of these parameters and we now report only an example to achieve our purpose. Specifically, we considered two objective functions to be maximize for different coupling values and for different conduction velocity ν: the Kullback-Lieber (KL) divergence between the p.d.f. of the phase difference among nodes of the whole network, and the correlation value among $\widehat{\mathbf{FC}}_{(\mathsf{PLV})}$ and $\mathbf{FC}_{(\mathsf{PLV})}$. From Figure 6.13, we can suddenly note that the choice of the parameters was not easy, because of a trade-off between the two objective functions: while a larger coupling strength is needed to decrease the KL divergence (and hence increase its reciprocal), a very low $\widetilde{C}$ gives a better **FC** fit.

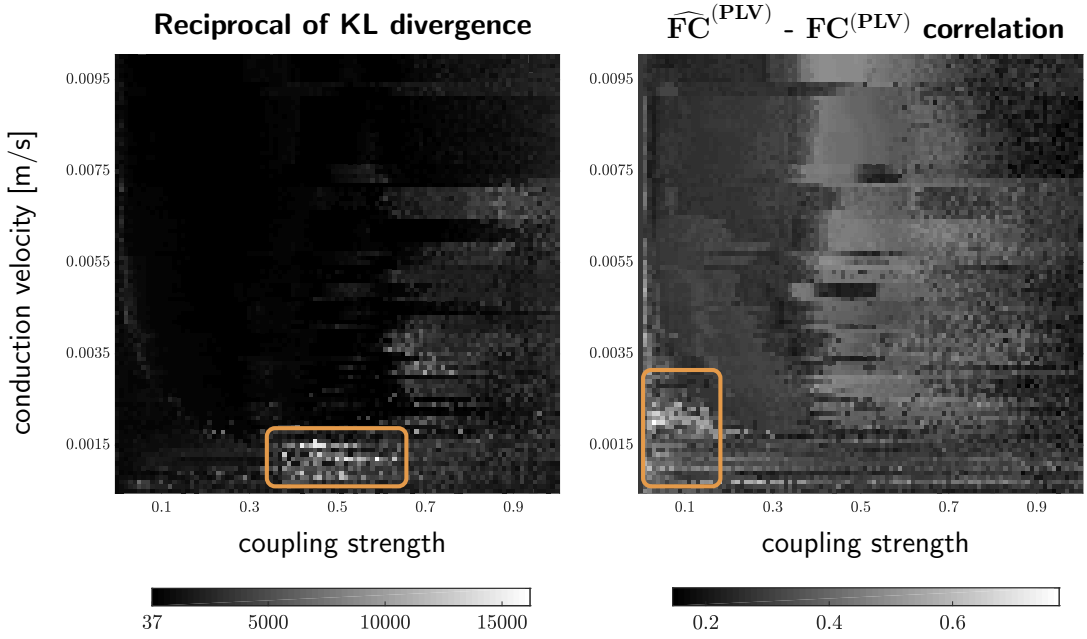

Figure 6.13: Values of the objective functions used to select the model parameters $\widetilde{C}$ (coupling strength, x-axis) and ν (conduction velocity, y-axis). **Left:** reciprocal of the Kullback-Lieber divergence among the p.d.f. of θ_{ij} on the whole network. **Right:** correlation values between the empirical and the simulated FC matrices. The orange rectangles highlight the areas with the highest (optimal) values of the objective functions. Note that the two areas do not coincide, thus introducing a trade-off on the selection of the model parameters.

However, in this place we only report the result about one specific combination of these parameters, that is $(\widetilde{C},\, \nu) = (0.46,\, 1.6 \times 10^{-3}\ \mathrm{m\,s^{-1}})$, as an example.
For instance, we can observe Figure 6.14 to compare the p.d.f. of the simulated $\theta_{ij}(\cdot)$ (green line) with the p.d.f. obtained from the real data (red line). Although the curves

are not very similar for what concerns DAN and DAN-VIS regions, the whole-network simulated phase differences have a probability density function similar to the one of the empirical data. This shape of the p.d.f. suggests that a large variability among the synchronized level among nodes (and across all the time steps) describes the simulated time series. Indeed, as reported in Figure 6.14, the absolute value of the order parameter $R(\cdot)$ is not constant at all, but, as desired, periods of higher level of synchronization (characterized by a θ_{ij}'s p.d.f. more concentrated around zero) alternate with period of desynchronization (with a more uniform shape of the p.d.f.).

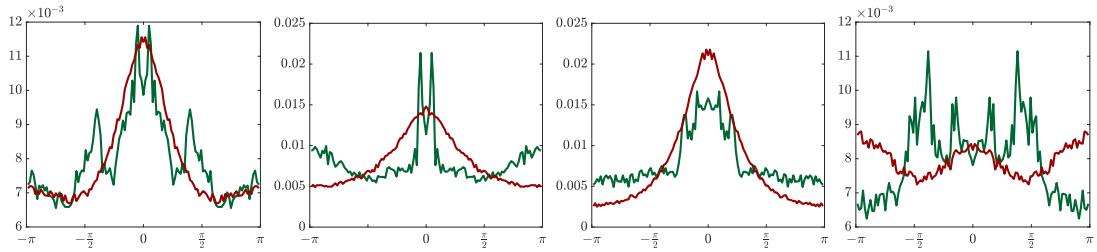

(a) Whole network (b) DAN (c) VIS (d) DAN-VIS

Figure 6.14: Comparison among the probability density function (p.d.f.) of phase differences across all pairs of brain regions, all time steps (and all subjects, for real data) obtained with the empirical data (red line) and the simulated ones (green lines). Model parameters: $(\widetilde{C},\ \nu) = (0.46,\ 1.6 \cdot 10^{-3}\ \mathrm{m\,s^{-1}})$. Subfigure **(a)** is referred to the whole graph, whereas subfigures **(b)**, **(c)** and **(d)** refer to DAN, VIS and DAN-VIS networks, respectively.

Moreover, as for the empirical data, this variability of the synchrony level can be attributed to the presence of several community patterns (we chose $K = 9$ as for the real data) with a variable strength $s_k(\cdot)$ during time. In Figure 6.16, the $K = 9$ patters are reported **(a)**, together with their strength **(c)** during a time period of less than 30 s. The strong link between the patterns' formation and the global level of synchronization within the whole network is explicitly shown in Subfigure **(b)**, where $S(\cdot)$ (black line) and $R(\cdot)$ (blue line) are compared.

Although we have selected a non-optimal combination of parameters to obtain a large correlation among the real and the simulated functional connectivities, this particular example shows a significant ($p_{\mathrm{val}} = 1.5 \times 10^{-3}$) correlation of 0.3277 between $\widehat{\mathbf{FC}}_{(\mathsf{PLV})}$ and $\mathbf{FC}_{(\mathsf{PLV})}$, which is a relatively high value, if we consider the conciseness that characterizes the computational model. Figure 6.17 reports a comparison among the two **FC**'s (left), and a scatter plot of their values (right).

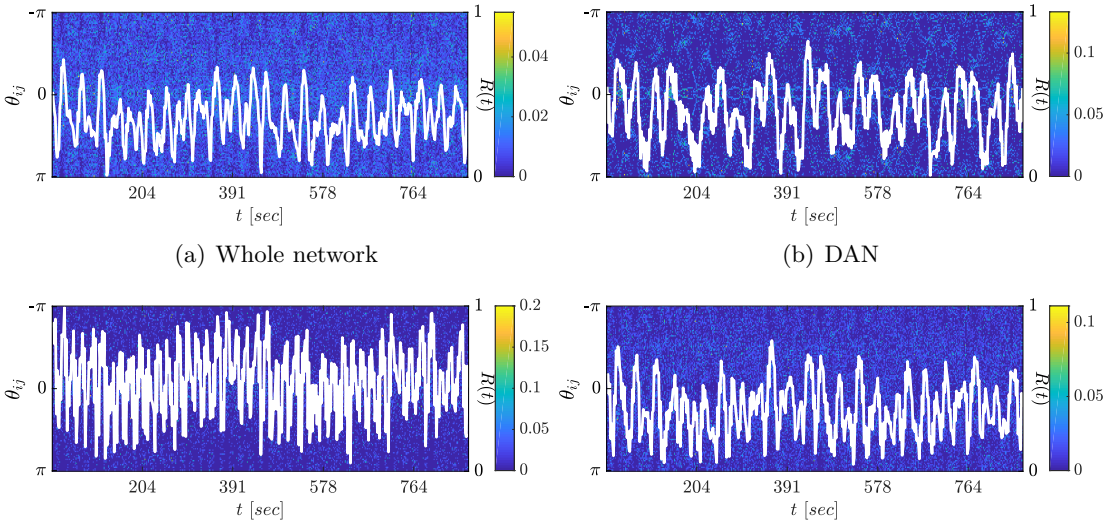

(a) Whole network (b) DAN

(c) VIS (d) DAN-VIS

Figure 6.15: Temporal evolution of the p.d.f. of the phase difference among each pair of nodes obtained with the simulation of system (6.6a) (model parameters: $(\widetilde{C},\, \nu) = (0.46,\, 1.6 \times 10^{-3}$ $\mathrm{m\,s^{-1}}$)). The color indicates the value of the p.d.f. at each time step (left y-axis). The white lines represents the absolute value of the order parameter $R(t)$ related to the same subject (right y-axis). Subfigure **(a)** is referred to the whole graph, whereas subfigures **(b)**, **(c)** and **(d)** refer to DAN, VIS and DAN-VIS networks, respectively.

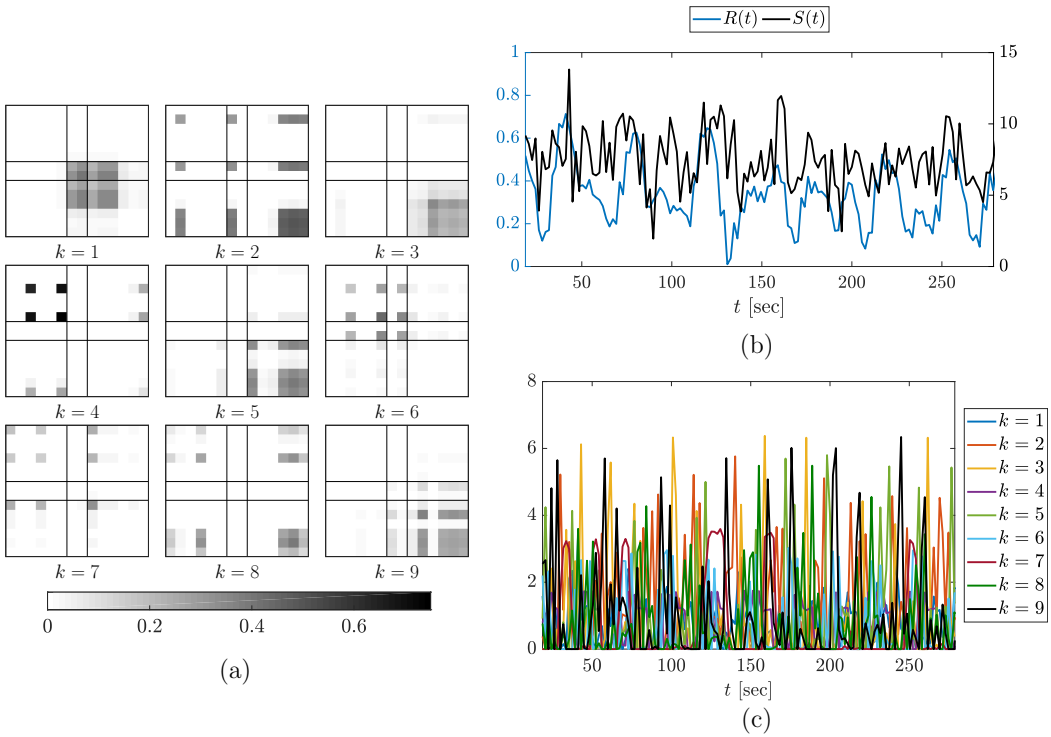

Figure 6.16: Synchronization patterns obtained from the simulated data (model parameters: $(\widetilde{C},\, v) = (0.46,\, 1.6 \times 10^{-3}\ \mathrm{m\,s^{-1}})$). **(a)** Representation of the $K = 9$ community patterns $(\mathbf{a_k} \cdot \mathbf{a_k}^{\mathsf{T}},\, i = 1, \ldots, K)$. **(b)** Comparison among the evolution of the absolute value $R(\cdot)$ of the order parameter (left y-axis, blue line) and the global strength $S(\cdot)$ (right y-axis, black line). **(c)** Evolution of the strength of each community k during time.

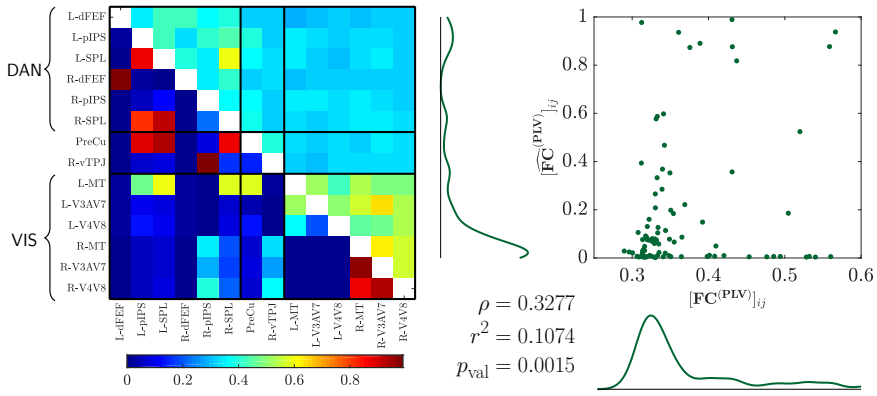

Figure 6.17: Comparison between $\widehat{\mathbf{FC}}_{(\mathsf{PLV})}$ and $\mathbf{FC}_{(\mathsf{PLV})}$ (model parameters: $(\widetilde{C},\, v) = (0.46,\, 1.6 \times 10^{-3}\ \mathrm{m\,s^{-1}})$). **Left:** Representation of the two **FC** matrices (upper triangular matrix: empirical FC, lower triangular matrix: simulated FC). **Right:** Illustration of the linear correlation among the two FC matrices. The correlation among the two matrices and the respective significance value are given by ρ and p_{val}. r^2 instead measures the explained variance (in percentage) of $\mathbf{FC}_{(\mathsf{PLV})}$, expressed by $\widehat{\mathbf{FC}}_{(\mathsf{PLV})}$.

6.5 Conclusion

In this chapter we have focused on two topics: at first, we have showed explicitly the oscillatory behavior of brain waves during resting-state, and we have reported a set of mathematical tools useful to describe the brain activity from an oscillatory point of view. Secondly, we have proposed a relatively simple computational model (an extended version of the classic Kuramoto model), which is able to reproduce the same global behavior as the real data, despite of its compact form. Specifically, it is able to highlight the metastable nature of the brain oscillations, which are characterized by periods of high level of synchrony, followed by periods of desynchronized behavior. Moreover, both in the empirical and in the simulated cases, this dynamic can be explained by means of different synchronization patters, which alternatively prevail over the others.

Therefore, this chapter highlights the power of Kuramoto model in describing the dynamics of the human brain with a low numbers of differential equations. However, throughout the sections above, it has also emerged the importance of the topology of the adjacency matrix used to simulate the model, as well as the difficulty of selecting the optimal model parameters. Driven by this challenge, our research has focused on the analytical analysis of the properties of a network of Kuramoto oscillators which determine the dynamics and the synchronization profile of the network. Indeed, a more accurate knowledge of the characteristics of Kuramoto model is required to make a proper use of this computational tool to simulate the very complex system of the brain. Despite its compactness, this model contains in fact specific non-linearities, which enable this complexity representation, but largely complicate its theoretical analysis, at the same time.

Chapter 7 is completely devoted to analytical results regarding Kuramoto models and its ability on representing fully or clustered synchronized behavior.

7

Kuramoto model and synchronization: a theoretical analysis

"Life is a constant oscillation between the sharp horns of dilemmas."
H. L. Mencken

Two main aspects emerge from the previous chapters: firstly, the human brain is a generator of oscillatory signals, whose level of synchronization determines the activity of brain regions and the co-activitation of different regions at the same time. Secondly, we have observed that Kuramoto model, a phase-model used to describe the population dynamics of a network of oscillators, is a powerful, yet relatively simple, mathematical tool to reproduce oscillatory behaviors of the brain waves.

Thus, in this chapter we address the analysis of Kuramoto model from a theoretical point of view. Our purpose consists in illustrating our analytical results on the structural and topological conditions that characterize the synchronization level of a network of Kuramoto oscillators. Specifically, we are interested in gaining new insights on the conditions necessary to achieve full or clustered synchronization, where groups of nodes evolve cohesively with the other nodes of the same group, but differently from the others.

Contents

7.1 Open questions and related work

In Section 6.1 we described the background in which Kuramoto model has emerged among other proposed oscillators' models. In this context our choice of focusing on Kuramoto model as a suitable tool to describe the complex behavior of brain networks (see Section 6.4.1) may be located. Although large part of the previous literature has been already devoted to the analysis of network of Kuramoto oscillators, several interesting questions remain open. Indeed, despite of the compactness of the dynamics' description, this mathematical model hides some obstacles, due to its non-linear nature. These difficulties emerge for instance in two scenarios, namely when also a *spatial characterization* of the oscillators has to be taken into account when describing their dynamics, and when a *clustered synchronized network* (rather that a fully synchronized phenomenon) is the object of interest.

In the former case indeed, the classical Kuramoto model's formulation is not enough complex to include the spatial location of the agents. However, from an application point of view, it may be useful to understand how the spatial displacement of the oscillators affects their mutual coupling since, intuitively, the influence between two nodes will diminish with increasing their distance. For example, in Breakspear et al. (2010) the authors state that a crucial step toward neurobiological plausibility of coupled oscillators is the incorporation of time delay effects linked to a spatial metric. The dynamics of such a model introduces connection strengths that vary with distance, and global connectivity is achieved by combining time delay effects with a finite width spatial kernel. Similarly, the importance of spatial displacement and time delay effects in biological oscillators network appears also in Cabral et al. (2011), which deals with the brain's neural activity on a network of N nodes, to study the structural connectivity in the brain in terms of connection strengths and conduction delays. Interestingly, analogous considerations regard also the study of the electric power grid dynamics where, again,

Kuramoto model proves to be an agile and useful model tool. In particular, Mangesius et al. (2012) describes a spatially embedded Kuramoto dynamics that involves a constant delay, proportional to the spatial distance between the oscillators, phase shifts caused by transmission delays and a coupling function that decreases with the distance. More in general, the basic idea that the distances among the agents affect the synchronization dynamics can be find also in Gupta et al. (2014), where the behavior of a lattice of oscillators, which interact with a power-law coupling strength, is considered.

The second obstacle, instead, refers to the fact that, while some systems require synchronization of all units to function properly (Dörfler and Bullo (2014); Chopra and Spong (2005); Gushchin et al. (2015)), recent studies have shown how neural systems, among others, depend on cluster synchronization, where populations of neurons evolve cohesively but independently from one another, and how incorrect patterns may prevent cognitive functions and characterize degenerative states such as Parkinson's and Huntington's Diseases (Hammond et al. (2007); Rubchinsky et al. (2012); Banaie et al. (2009)), and epilepsy (Lehnertz et al. (2009)). Despite recent results (Pecora et al. (2014); Sorrentino et al. (2016); Schaub et al. (2016)), methods to predict and control cluster synchronization in dynamically-changing networks remain critically lacking. Cluster synchronization has received attention only recently, and several fundamental questions remain unanswered, including the characterization of the features of the network enabling the formation of a desired pattern, and the development of control mechanisms to enforce the emergence of clusters.

Complete synchronization in networks of Kuramoto oscillators has been extensively studied, e.g., see Gómez-Gardeñes et al. (2007); Zhang et al. (2014). It has been shown that synchronization of all nodes emerges when the coupling strength among the agents is sufficiently larger than the heterogeneity of the oscillators' natural frequencies. Partial synchronization and patterns formation have received considerably less attention, with the literature being composed of only few recent works. In Pecora et al. (2014) it is shown how symmetry of the interconnections may lead to partial synchronization. Methods based on graph symmetry have also been used to find all possible clusters in networks of Laplacian-coupled oscillators (Sorrentino et al. (2016)). The relationship between clusterization and network topology has been studied in Lu et al. (2010) for unweighed interconnections. In Dahms et al. (2012), the emergence and the stability of groups of synchronized agents within a network has been studied for different classes of dynamics, like delay-coupled laser models and neuronal spiking models. Here, the approach of master stability function has been used to characterize the results. An interesting analysis for our research can be found in Schaub et al. (2016), where the authors relate cluster

synchronization to the notion of an external equitable partition in a graph. The notion of an external equitable partition can be interpreted in terms of invariant subspaces of the network adjacency matrix, a notion that we exploit in our development. However, the analysis in Schaub et al. (2016) is carried out with unweighed and undirected networks and, as we will show in our results, the conditions in Schaub et al. (2016) may not be necessary when dealing with directed and weighted networks.

Throughout the chapter, we address both the problem of the spatial characterization of phase-oscillators and the analytical analysis of the formation of clusters on nodes within the same population. Specifically, we characterize intrinsic and topological conditions that ensure fully synchronization, or the formation of desired clusters of oscillators. Although Kuramoto networks exhibit non-linear dynamics, we adopt tools from linear algebra and graph theory to characterize network conditions enabling the formation of a given synchronization pattern. Further, we design a control mechanism to perturb (a subset of) the network weights so as to enforce or prevent desired synchronization patterns.

7.2 General framework and preliminary notions

In this chapter we consider a system of N coupled oscillators, represented by a graph. A graph $\mathcal{G} = (\mathcal{V}, \mathcal{E})$ is composed of a set of nodes, $\mathcal{V} = \{1, \ldots, N\}$, consisting of the indices of the N agents of the network, and of a set of edges $\mathcal{E} \subseteq \mathcal{V} \times \mathcal{V}$, in which each edge connects one node to another (see for example, Mesbahi and Egerstedt (2010)). The edge (i, j) indicates that agent j can transmit information to agent i.

If there is a directed path from node j to i, then node i is said to be reachable from node j. If each node is reachable from all the others, then $\mathcal{G}$ is said to be *strongly connected*. Moreover, the graph is said to be *fully connected* if there exists an edge connecting each pair of nodes. Let $\mathbf{A} = [a_{ij}]$ be the weighted adjacency matrix associated to $\mathcal{G}$, where $a_{ij} \in \mathbb{R}$ if $(i, j) \in \mathcal{E}$, and $a_{ij} = 0$, otherwise. Throughout the chapter, we consider strongly connected graphs, if anything is mentioned.

Given this framework, each oscillator node i is endowed by a state that is its phase angle $\theta_i(\cdot) \in \mathbb{R}$, which obeys the dynamics

$$\dot{\theta}_i(t) = \omega_i + \frac{C}{N} \sum_{j=1}^{N} a_{ij} \sin\left(\theta_j(t) - \theta_i(t)\right), \qquad i = 1, \ldots, N, \tag{7.1}$$

which is a simplified version of Equation (6.6a), where all the delay terms ν_{ij}'s are equal to zero. Recall that $C \geq 0$ is the global coupling strength, and $\omega_i \in \mathbb{R}$ is the oscillator

natural frequency (namely: the dynamics of each isolated node is $\dot{\theta}_i(t) = \omega_i$).

7.2.1 Synchronization definitions

When analyzing the behavior of the oscillators network topologically described by a generic graph $\mathcal{G}$, there are different kinds of synchronization, which can be reached through the dynamics (7.1) (see Dörfler and Bullo (2014)):

Definition 7.2.1 (***Frequency synchronization***)**.** A subset of $N_{\mathcal{C}} \leq N$ oscillators $\mathcal{C} \subseteq \mathcal{V}$, is *frequency synchronized* if, for some initial phases $\theta_1(0), \ldots, \theta_N(0)$, it holds that

$$\dot{\theta}_i(t) = \dot{\theta}_j(t) = \omega_{\text{sync}},$$

for all times $t \in \mathbb{R}_{\geq 0}$, and $i, j \in \mathcal{C}$.

Definition 7.2.2 (***Asymptotic frequency synchronization***)**.** The subset of $N_{\mathcal{C}} \leq N$ oscillators $\mathcal{C} \subseteq \mathcal{V}$, is *asymptotically frequency synchronized* if, for some initial phases $\theta_1(0), \ldots, \theta_N(0)$, it holds that

$$\lim_{t\to\infty} \dot{\theta}_i(t) = \omega_{\text{sync}} = \frac{1}{N_{\mathcal{C}}} \sum_{i\in\mathcal{C}} \omega_i, \qquad \forall\, i \in \mathcal{C}$$

If the vector of the natural frequencies is in the orthogonal complement of the ones vector, $\begin{bmatrix} \omega_1 & \cdots & \omega_{N_{\mathcal{C}}} \end{bmatrix}^{\mathsf{T}} \in \mathbb{1}_{N_{\mathcal{C}}}^{\perp}$, then $\omega_{\text{sync}} = 0$[1].

Definition 7.2.3 (***Phase synchronization***)**.** The subset of oscillators $\mathcal{C} \subseteq \mathcal{V}$, is *phase synchronized* if, for some initial phases $\theta_1(0), \ldots, \theta_N(0)$, it holds that

$$\theta_i(t) = \theta_j(t),$$

for all times $t \in \mathbb{R}_{\geq 0}$, and $i, j \in \mathcal{C}$.

Definition 7.2.4 (***Asymptotic phase synchronization***)**.** The subset of oscillators $\mathcal{C} \subseteq \mathcal{V}$, is *asymptotically phase synchronized* if, for some initial phases $\theta_1(0), \ldots, \theta_N(0)$, it holds that

$$\lim_{t\to\infty} \theta_i(t) = \lim_{t\to\infty} \theta_j(t),$$

for all $i, j \in \mathcal{C}$.

[1] According to Dörfler and Bullo (2014), this assumption is not limiting the study since all frequencies can be expressed w.r.t. ω_{sync} as $\omega_i - \omega_{\text{sync}}$ in a rotating frame.

Definition 7.2.5 (***Phase locking***)**.** The subset of oscillators $\mathcal{C} \subseteq \mathcal{V}$, is *phase locked* if, for some initial phases $\theta_1(0), \ldots, \theta_N(0)$, it holds that

$$\text{if} \qquad \theta_i(0) - \theta_j(0) = \gamma_{ij} \qquad \text{then} \qquad \theta_i(t) - \theta_j(t) = \gamma_{ij},$$

for all times $t \in \mathbb{R}_{\geq 0}$, and $i, j \in \mathcal{C}$.

Definition 7.2.6 (***Angle invariance***)**.** For $\gamma \in [0, \pi]$, let $\Delta_N(\gamma)$ be the set of angle arrays $\boldsymbol{\theta}_i$ of dimension N, such that $|\theta_i - \theta_j| \leq \gamma$, for all θ_i, θ_j, which are elements of $\boldsymbol{\theta}_i$.

Definition 7.2.7 (***Phase cohesiveness***)**.** The subset of oscillators $\mathcal{C} \subseteq \mathcal{V}$, is *phase cohesive* if, for some initial phases $\theta_1(0), \ldots, \theta_N(0)$, it exists an angle $0 \leq \gamma \leq \pi/2$, such that

$$\text{if} \qquad \max_{i,j \in \mathcal{C}} (\theta_i(0) - \theta_j(0)) \leq \gamma \qquad \text{then} \qquad \max_{i,j \in \mathcal{C}} (\theta_i(t) - \theta_j(t)) \leq \gamma,$$

for all times $t \in \mathbb{R}_{\geq 0}$, and $i, j \in \mathcal{C}$. It is equivalent to condition:

$$\boldsymbol{\theta}_{\mathcal{C}}(0) \in \Delta_{N_{\mathcal{C}}}(\gamma) \qquad \Longrightarrow \qquad \boldsymbol{\theta}_{\mathcal{C}}(t) \in \Delta_{N_{\mathcal{C}}}(\gamma), \qquad \forall t > 0,$$

where $\boldsymbol{\theta}_{\mathcal{C}}$ is the vector of the $N_{\mathcal{C}}$ oscillators belonging to $\mathcal{C}$.

7.3 Spatially coupled oscillators network

In this section, we address the problem of embedding the spatial component in the classic Kuramoto model[2], which considers the oscillators as located on a plane (as often occurs in real world applications), and introduces a kernel function that (inversely) depends on the Euclidean distance among the oscillators. Specifically, sufficient conditions on the nominal $C \geq 0$ coupling strength and on the largest distance are obtained, which permit to achieve *frequency synchronization* and *phase cohesiveness*. More specifically, in this place, we take into account also the case in which the oscillators are influenced by different kernels, depending on their displacement in a specific area: in such a situation, the synchronization frequency changes if compared to the case where a single kernel characterizes the whole population.

Given this framework, in addition to its phase angle $\theta_i(\cdot)$ and its natural frequency ω_i, each oscillator node i is also endowed by its (static) spatial coordinates $(x_i, y_i) \in \mathbb{R}^2$.

[2] equation (7.1) formulation, with $a_{ij} = 1$, for each $i, j = 1, \ldots, N$

Thus, the dynamics of $\theta_i(\cdot)$ obeys

$$\dot{\theta}_i(t) = \omega_i - \frac{C}{N}\sum_{j=1}^{N} w(d_{ij}, p)\sin\left(\theta_i(t) - \theta_j(t)\right), \tag{7.2}$$

where $w_{ij}(\cdot,\cdot) \in]0,\ 1]$ is a coupling function that depends on the Euclidean distance d_{ij} among the agents, as follows:

$$w(d_{ij}, p) = \exp\left(-\left(\frac{d_{ij}}{p}\right)^2\right), \tag{7.3}$$

with p being a shaping parameter. In Fig. 7.1(a), it is shown an example of the shape of $w(d_{ij}, p)$ as a function of d_{ij}, and for different values of p. For sake of simplicity of the notation, we refer to w_{ij} in place of $w(d_{ij}, p)$, when p is fixed.

In summary, the dynamics (7.2) represents a modified Kuramoto model that considers also the spatial configuration of the system, i.e. the spatial displacements of the oscillatory nodes, while the interaction topology among such oscillators is modelled by graph $\mathcal{G}$ and weighed by the coupling function $w(d_{ij}, p)$.

With respect to Section 7.2.1, this study focuses on asymptotic frequency synchronization and phase cohesiveness, with phase distances $|\theta_i - \theta_j|$ limited by $\gamma < \pi/2$, which is of interest and utility for most applications (Dörfler and Bullo (2014)).

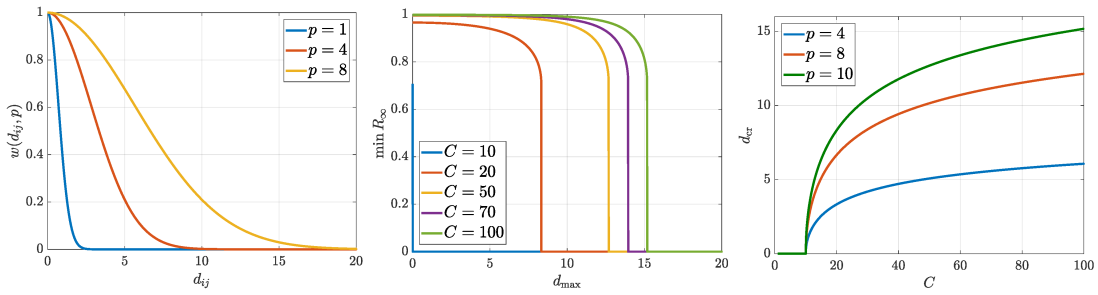

(a) $w(d_{ij}, p)$ vs. d_{ij} (b) $\min R_\infty$ vs. $d_{\max}$ (c) d_{cr} vs. C

Figure 7.1: **(a)** Shape of the kernel coupling function $w(\cdot,\cdot)$ (7.3) as a function of d_{ij} for different values of p. **(b)** Lower bound of R_∞ as a function of $d_{\max}$, for different values of C. (Parameters: $N = 100$, $p = 10$, $\omega_{\max} - \omega_{\min} = 10$). **(c)** Critical value for the Euclidean distance (d_{cr} (7.5)) as a function of C, for different values of p.

A useful metric to analyze the asymptotic level of the system synchronization is the order

parameter (6.2), which is reported here for simplicity:

$$R(t)e^{\mathrm{j}\Phi(t)} = \frac{1}{N}\sum_{i=1}^{N} e^{\mathrm{j}\theta_i(t)}.$$

Let R_∞ be limit value of $R(t)$ as t goes to the infinity, if the limits exists:

$$R_\infty = \lim_{t\to\infty} R(t).$$

Recall that $R(t)$ represents the centroid of all the phases of the oscillators at time t, when these are seen as points on the unit circle in $\mathbb{C}^1$. The magnitude $R(t) \in [0,\, 1]$ of the order parameter is a synchronization measure: if, at time t, all the oscillators are phase synchronized, then $R(t) = 1$, whereas if they are balanced (i.e. uniformly distributed over the unit circle), then $R(t) = 0$. In particular, it is useful to recall the following Lemma (Dörfler and Bullo, 2014, Lemma 3.1).

Lemma 7.3.1. ***(Minimum phase distance and order parameter)*** *Consider an array of $N \geq 2$ angles $\boldsymbol{\theta} = [\ \theta_1 \ \cdots \ \theta_N\ ]^\mathsf{T}$ and compute the magnitude $R = \frac{1}{N}\left|\sum_{i=1}^{N} e^{\mathrm{j}\theta_i}\right|$. Let γ be the length of the smallest angle such that $\boldsymbol{\theta} \in \Delta_N(\gamma)$. The following statements holds:*

1. *if $\gamma \in [0,\, \pi]$, then $R \in [\cos(\gamma/2)\,,\ 1]$;*
2. *if $\boldsymbol{\theta} \in \Delta_N(\pi)$, then $\gamma \in [2\arccos(R)\,,\ \pi]$.*

7.3.1 Single population convergence bounds

Following the results summarized in Dörfler and Bullo (2014), the interest is now to establish some explicit conditions for the modified Kuramoto model (7.2). In doing so, the following propositions extend the results in Dörfler and Bullo (2011) involving the coupling strength parameter C and the maximum $d_{\max}$ of the Euclidean distances $\{d_{ij}\}$ between the oscillators, to achieve a synchronized state for $\boldsymbol{\theta} = [\ \theta_1 \ \cdots \ \theta_N\ ]^\mathsf{T}$, namely a state where asymptotic frequency synchronization and phase cohesiveness coexist.

Proposition 7.3.2. ***(Phase cohesiveness)*** *Consider the Kuramoto model (7.2), with $N \geq 2$ oscillators, natural frequencies $\boldsymbol{\omega} \in \mathbb{1}_N^{\perp}$[3] in $[\omega_{min}, \omega_{max}]$ and coupling strength C. If the coupling strength C is higher than a critical value C_{cr}:*

$$C > C_{cr} = \frac{\omega_{max} - \omega_{min}}{e^{-\tilde{d}^2}} \quad \textit{with} \quad \tilde{d} = \frac{d_{max}}{p}, \tag{7.4}$$

[3]Recall that, according to Dörfler and Bullo (2014), this assumption is not limiting the study since all frequencies can be expressed w.r.t. ω_{sync} as $\omega_i - \omega_{sync}$ in a rotating frame.

then $\exists\, \gamma_{max} \in \,]\pi/2, \pi]$ *and* $\exists\, \gamma_{min} \in [0, \pi/2[$ *such that*

1. $\Delta_N(\gamma)$ *is positive invariant for every* $\gamma \in [\gamma_{min}, \gamma_{max}]$*, that means that each trajectory originated in* $\Delta_N(\gamma)$ *remains in* $\Delta_N(\gamma)$ *for every* $t \geq 0$ *(phase cohesiveness);*

2. $\sin(\gamma_{min}) = \sin(\gamma_{max}) = C_{cr}/C$.

Remark 7.3.3. Interestingly, in the modified Kuramoto framework introduced by (7.2), a dependence between the coupling strength C and the maximum distance $d_{\max}$ between agents can be stated. Indeed, relation (7.4) is equivalent to the following condition:

$$d_{\max} < d_{\text{cr}} := p \cdot \sqrt{-\ln\left(\frac{\omega_{\max} - \omega_{\min}}{C}\right)}. \tag{7.5}$$

In practice, if a model (7.2) is given with an imposed spatial distribution $\{d_{ij} < d_{\max}\}$, to achieve phase cohesiveness there must be exerted a coupling strength larger than C_{cr}. Conversely, if the network interactions are bounded by some coupling strength value C, the displacement among the agent should also be bounded (by d_{cr}) in order to achieve synchronization.

In Fig. 7.1(b)-7.1(c) the relation among these parameters are shown also w.r.t. the shape of the lower bound of R_∞. The reported figures are referred to a network of $N = 100$ nodes with $(\omega_{\max} - \omega_{\min}) = 10$. It is worth noticing that $d_{\max}$ shows a linear dependence on p; moreover, the upper bound for $d_{\max}$ is really restrictive for a low value of p and it remains low also if C is increased.

Proposition 7.3.4. ***(Asymptotic frequency synchronization)***
With a coupling strength $C > C_{cr}$*, model (7.2) achieves exponential frequency synchronization for all possible distributions of the natural frequencies* $\{\omega_i\}$ *on the compact interval* $[\omega_{min}, \omega_{max}]$ *and for all initial phase conditions* $\boldsymbol{\theta}(0) \in \Delta_N(\gamma_{max})$.
Moreover:

1. *the asymptotic synchronization frequency* ω_{sync} *is the average frequency* $\omega_{avg} = \frac{1}{N}\sum_{i=1}^{N}\omega_i$*;*

2. *given phase cohesiveness w.r.t.* γ *for some fixed* $\gamma < \pi/2$*, the exponential synchronization rate is no worse then* $\lambda_{fs} = Ce^{-\tilde{d}^2}\cos(\gamma)$*;*

The proofs of Propositions 7.3.2 and 7.3.4 develop along the same line as that of (Dörfler and Bullo, 2011, Theorem 4.1) and are reported in Appendix A.9 and A.10, respectively, for completeness.

Corollary 7.3.5. *Consider model (7.2) in the conditions stated by Proposition 7.3.2: the asymptotic value R_∞ of the magnitude of the order parameter (6.2) is bounded as*

$$1 \geq R_\infty \geq \cos\left(\frac{\gamma_{min}}{2}\right) = \sqrt{\frac{1+\sqrt{1-\left(\frac{\omega_{max}-\omega_{min}}{Ce^{-\tilde{d}^2}}\right)^2}}{2}}. \tag{7.6}$$

Proof of Corollary 7.3.5. As a consequence of statement 1. of Proposition 7.3.2 and Lemma 7.3.1, the asymptotic magnitude of the order parameter obeys

$$1 \geq R_\infty \geq \cos\left(\frac{\gamma_{\min}}{2}\right) = \sqrt{\frac{1+\cos\left(\gamma_{\min}\right)}{2}}. \tag{7.7}$$

From statement 2) of Proposition 7.3.2, it follows

$$\cos\left(\gamma_{\min}\right) = \sqrt{1-\left(\frac{\omega_{\max}-\omega_{\min}}{Ce^{-\tilde{d}^2}}\right)^2}, \tag{7.8}$$

and from (7.7) and (7.8), (7.6) is proved.

■

7.3.2 Two populations configuration

It is now interesting to study the case when two populations of agents with different kernels interact.

For this purpose, a configuration is considered composed by two areas ($A_{\min}$ and $A_{\max}$), populated by sets $\mathcal{A}_{\min}$ and $\mathcal{A}_{\max}$ of oscillators, characterized respectively by two different kernels $w_{\min}(\cdot)$ and $w_{\max}(\cdot)$, related to parameters $p_{\min} < p_{\max}$. In other words, it is

$$w_{\min}(d_{ij}) = w(d_{ij}, p_{\min}) \qquad \text{and} \qquad w_{\max}(d_{ij}) = w(d_{ij}, p_{\max}).$$

For the time being, the cardinality of the two populations is the same: $N/2$ oscillators belong to $\mathcal{A}_{\min}$ and the others $N/2$ to $\mathcal{A}_{\max}$.

The system dynamics becomes:

$$\dot{\theta}_i\left(t\right) = \omega_i + \frac{C}{N}\begin{cases}\sum_{j=1}^{N} w_{\min}(d_{ij})\sin\left(\theta_j\left(t\right)-\theta_i\left(t\right)\right), & i \in \mathcal{A}_{\min}\\ \sum_{j=1}^{N} w_{\max}(d_{ij})\sin\left(\theta_j\left(t\right)-\theta_i\left(t\right)\right), & i \in \mathcal{A}_{\max}\end{cases}$$

where

$$w_{\min}(d_{ij}) = e^{-\left(\frac{d_{ij}}{p_{\min}}\right)^2} < e^{-\left(\frac{d_{ij}}{p_{\max}}\right)^2} = w_{\max}(d_{ij}),$$

which yields:

$$C_{\text{cr}} = \frac{\omega_{\max} - \omega_{\min}}{e^{-\left(\frac{d_{\max}}{p_{\min}}\right)^2}}.$$

Unlike the case with a single population, in which $\omega_{\text{sync}} = \frac{1}{N}\sum_{i=1}^{N}\omega_i = 0$, in the two populations case the following lemma holds.

Lemma 7.3.6. ***(Synchronization frequency with two kernels)***
Consider a system of an even numbers $N \geq 2$ of oscillators, characterized by their spatial coordinates (x_i, y_i) and their phases $\theta_i(t)$. Let $\boldsymbol{\omega} \in \mathbb{1}_N^{\perp}$ be the vector of the natural frequencies.

If C and d_{max} are such that there is frequency synchronization among the oscillators, then, the synchronization frequency $\tilde{\omega}_{sync}$ results for $t \gg 0$:

$$\tilde{\omega}_{sync} = \frac{C}{N^2}\sum_{\substack{i\in\mathcal{A}_{min}\\ j\in\mathcal{A}_{max}}} (w_{max}(d_{ij}) - w_{min}(d_{ij}))\sin(\theta_i - \theta_j).$$

Proof of Lemma 7.3.6. Suppose $t \gg 0$ such that synchronization has been already achieved. By summing over all nodes it follows:

$$\begin{aligned}\sum_{i=1}^{N}\dot{\theta}_i = \sum_{i=1}^{N}\omega_i - \frac{C}{N}\sum_{i\in\mathcal{A}_{\min}}\sum_{j=1}^{N} w_{\min}(d_{ij})\sin(\theta_i - \theta_j) + \\ - \frac{C}{N}\sum_{i\in\mathcal{A}_{\max}}\sum_{j=1}^{N} w_{\max}(d_{ij})\sin(\theta_i - \theta_j).\end{aligned} \tag{7.9}$$

By noticing that if i, $j \in \mathcal{A}_*$ then $w_*(d_{ij}) = w_*(d_{ji})$ ($*$ being equal to min or max) and $\sin(\theta_i - \theta_j) = -\sin(\theta_j - \theta_i)$, after some calculations, (7.9) simplifies to

$$\sum_{i=1}^{N}\dot{\theta}_i = \sum_{i=1}^{N}\omega_i - \frac{C}{N}\sum_{\substack{i\in\mathcal{A}_{\min}\\ j\in\mathcal{A}_{\max}}} (w_{\min}(d_{ij}) - w_{\max}(d_{ij})\sin(\theta_i - \theta_j).$$

Hence, normalizing by the network cardinality N, it follows:

$$\tilde{\omega}_{\text{sync}} = \frac{1}{N}\sum_{i=1}^{N}\dot{\theta}_i = \omega_{\text{sync}} + \frac{C}{N^2}\sum_{\substack{i\in\mathcal{A}_{\min}\\ j\in\mathcal{A}_{\max}}} \underbrace{(w_{\max}(d_{ij}) - w_{\min}(d_{ij}))\sin(\theta_i - \theta_j)}_{B_{ij}},$$

which proves the thesis by recalling that $\omega_{\text{sync}} = 0$.

■

Namely, if the oscillator network can be described by two populations characterized by

different spatial coupling, the synchronization frequency $\tilde{\omega}_{\text{sync}}$ deviates from the null average of the natural frequencies: more specifically, this difference can be bound w.r.t. the two coupling parameters as follows.

Proposition 7.3.7. *In the hypotheses of Lemma 7.3.6, a bound $\Delta\omega_{max}$ for the difference between the synchronization frequency $\tilde{\omega}_{sync}$ and $\omega_{sync} = 0$ is given by:*

$$|\tilde{\omega}_{sync} - \omega_{sync}| \leq \frac{C}{4}\left[e^{-\left(\frac{d^*}{p_{max}}\right)^2} - e^{-\left(\frac{d^*}{p_{min}}\right)^2}\right] =: \Delta\omega_{max}, \tag{7.10}$$

where

$$d^* = p_{min}p_{max}\sqrt{\frac{2}{p_{max}^2 - p_{min}^2}\ln\left(\frac{p_{max}}{p_{min}}\right)}.$$

Proof of Proposition 7.3.7. From (7.3.2), it results

$$\tilde{\omega}_{\text{sync}} - \omega_{\text{sync}} = \frac{C}{N^2}\sum_{\substack{i\in\mathcal{A}_{\min}\\ j\in\mathcal{A}_{\max}}} \underbrace{(w_{\max}(d_{ij}) - w_{\min}(d_{ij}))\sin(\theta_i - \theta_j)}_{B_{ij}},$$

and

$$w_{\max}(d_{ij}) - w_{\min}(d_{ij}) = e^{-\left(\frac{d_{ij}}{p_{\max}}\right)^2} - e^{-\left(\frac{d_{ij}}{p_{\min}}\right)^2},$$

considering that $d_{ij} = d_{ji}$, $\forall i, j$.
To find its maximum value, the derivative is obtained:

$$\frac{\partial}{\partial d_{ij}}(w_{\max}(d_{ij}) - w_{\min}(d_{ij})) = 2d_{ij}\left[\frac{1}{p_{\min}^2}e^{-\left(\frac{d_{ij}}{p_{\min}}\right)^2} - \frac{1}{p_{\max}^2}e^{-\left(\frac{d_{ij}}{p_{\max}}\right)^2}\right],$$

which becomes zero at $d_{ij} = 0$ (trivial minimum solution) and when

$$d_{ij} = d^* = p_{\min}p_{\max}\sqrt{\frac{2}{p_{\max}^2 - p_{\min}^2}\ln\left(\frac{p_{\max}}{p_{\min}}\right)}.$$

As a consequence:

$$w_{\max}(d_{ij}) - w_{\min}(d_{ij}) \in \left[0,\ \exp\left(-\left(\frac{d^*}{p_{\max}}\right)^2\right) - \exp\left(-\left(\frac{d^*}{p_{\min}}\right)^2\right)\right],$$

and it follows that the absolute value of the quantity B_{ij} highlighted in (7.3.2) is bounded within $\left[0,\ e^{-\left(\frac{d^*}{p_{\max}}\right)^2} - e^{-\left(\frac{d^*}{p_{\min}}\right)^2}\right]$.

As a consequence

$$|\tilde{\omega}_{\text{sync}} - \omega_{\text{sync}}| \leq \frac{C}{N^2} \sum_{\substack{i \in \mathcal{A}_1 \\ j \in \mathcal{A}_2}} \left[e^{-\left(\frac{d^*}{p_{\max}}\right)^2} - e^{-\left(\frac{d^*}{p_{\min}}\right)^2} \right]$$
$$\leq \frac{C}{4} \left[e^{-\left(\frac{d^*}{p_{\max}}\right)^2} - e^{-\left(\frac{d^*}{p_{\min}}\right)^2} \right].$$

■

So far the case of two balanced populations of agents has been considered and indeed the bound (7.10) does not depend on the cardinality of the sets.
Conversely, if the two populations refer to uneven groups of oscillators, the results of Proposition 7.3.7 can be extended. Let the sets $\mathcal{A}_{\min}$ and $\mathcal{A}_{\max}$ be of different cardinalities, namely:

$$\mathcal{A}_{\min} = \{i \mid (x_i, y_i) \in A_{\min}\}, \quad |\mathcal{A}_{\min}| = N_{\min}, \tag{7.11a}$$
$$\mathcal{A}_{\max} = \{i \mid (x_i, y_i) \in A_{\max}\}, \quad |\mathcal{A}_{\max}| = N_{\max} = N - N_{\min}. \tag{7.11b}$$

In such conditions, relation (7.10) modifies to:

$$|\tilde{\omega}_{\text{sync}} - \omega_{\text{sync}}| \leq C \frac{N_{\min}(N - N_{\min})}{N^2} \left[e^{-\left(\frac{d^*}{p_{\max}}\right)^2} - e^{-\left(\frac{d^*}{p_{\min}}\right)^2} \right] = \Delta\omega_{\max}. \tag{7.12}$$

The derivative of $\omega_{\max}$ w.r.t. $N_{\min}$ is

$$\frac{\partial}{\partial N_{\min}} \Delta\omega_{\max} = C \left(\frac{N - 2N_{\min}}{N^2} \right) \left[e^{-\left(\frac{d^*}{p_{\max}}\right)^2} - e^{-\left(\frac{d^*}{p_{\min}}\right)^2} \right],$$

which equalizes to zero only at $N_{\min} = N/2$ (point of maximum); also, the minimum value for the right hand size of (7.12) is achieved at the extreme points, i.e. when the two populations are strongly unbalanced:

$$\begin{cases} N_{\min} = 1 \\ N_{\max} = N - 1 \end{cases} \quad \text{or} \quad \begin{cases} N_{\min} = N - 1 \\ N_{\max} = 1 \end{cases}.$$

In Fig. 7.2, an example of the shape of $\Delta\omega_{\max}$ as a function of $N_{\min}$ is given with $C = 50$, $p_{\min} = 3$ and $N = 50$, for different values of $p_{\max}$.

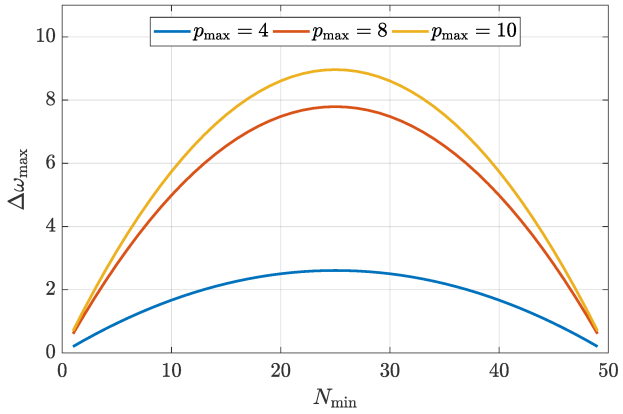

Figure 7.2: Value of $\Delta\omega_{\max}$ as a function of $N_{\min}$ with $C = 50$, $p_{\min} = 3$ and $N = 50$, for different values of $p_{\max}$.

7.3.3 Numerical results

In this section, some simulations are presented to assess and validate the previously discussed theoretical findings.

Specifically, approximately $n = 30000$ Monte Carlo realizations have been generated for a random network of oscillators spatially placed on a spherical domain (in order to avoid edge effects) and considering geodesic distances among pairs of nodes.

In this framework, the number of agents N is sampled from a uniform distribution $\mathcal{U}([10,\ 200])$ and the radius of the spherical domain is $r \sim \mathcal{U}(]0,\ 10])$; the network node position $(x_i,\ y_i,\ z_i)$ is obtained as

$$\begin{cases} x_i = r \sin(\psi_i) \cos(\varsigma_i) \\ y_i = r \sin(\psi_i) \sin(\varsigma_i) \\ z_i = r \cos(\psi_i) \end{cases}$$

as a function of the two angles $\psi_i \sim \mathcal{U}([0,\ 2\pi[)$ and $\varsigma_i \sim \mathcal{U}([0,\ 2\pi[)$.

Also, the maximum Euclidean distance among all nodes $d_{\max}$ can be calculated. As for the natural frequency distribution, for a given $N \geq 10$, the frequency vector $\boldsymbol{\omega} \in \mathbb{1}_N^{\perp}$ is constructed in two steps. Firstly, N real numbers q_i are sampled from $\mathcal{U}([-1, +1])$; then, by subtracting the average $\frac{1}{N}\sum_{i=1}^{N} q_i$, $\omega_i = q_i - \frac{1}{N}\sum_{i=1}^{N} q_i$ is defined to obtain $\boldsymbol{\omega} = [\ \omega_1 \quad \cdots \quad \omega_N\ ]^{\mathsf{T}} \in \mathbb{1}_N^{\perp}$.

Finally, a random parameter $p \in \{1, 2, \ldots, 10\}$ and a random $\gamma_{\max} \in]\pi/2, \pi]$ are chosen; $\gamma_{\min} \in [0, \pi/2, [$ is selected such that $\sin(\gamma_{\max}) = \sin(\gamma_{\min})$. Hence, a set of N oscillators $\theta_i(0)$ is generated, with $\boldsymbol{\theta}(0) \in \Delta_N(\gamma_{\max})$.

The bound gain is defined as $C_{\text{cr}} = \frac{\Delta\omega}{e^{-\left(\frac{d_{\max}}{p}\right)^2}}$, and the coupling strength C to ensure synchronization is obtained:

$$C = \frac{C_{\text{cr}}}{\sin\left(\gamma_{\max}\right)} > C_{\text{cr}}.$$

In Fig. 7.3 two simulation examples are shown. The upper row refers to **(a)** the single kernel case, where **(b)** phase cohesiveness is reached and **(c)** the Lyapunov function $V(\boldsymbol{\theta}(t))$ behaves as proved in Proposition 7.3.2. The lower row, instead, is related to **(d)** a two kernels configuration, where **(e)** phase cohesiveness is attained for the two populations and **(f)** the frequency convergence is bounded by (7.11a).

More in general, the assessment of the correctness and the accuracy of Proposition 7.3.2 for arbitrary networks is carried out by solving (7.2) for each instance and testing the assumptions:

$$\mathsf{H}_{\text{fr}}: \begin{cases} \gamma_{\max} \in \left]\pi/2, \pi\right[\\ C = \frac{C_{\text{cr}}}{\sin(\gamma_{\max})} > C_{\text{cr}} \end{cases} \implies \dot{\boldsymbol{\theta}}(t) \underset{t\to\infty}{\longrightarrow} \omega_{\text{sync}} \mathbb{1}_N,$$

$$\mathsf{H}_{\text{ph}}: \begin{cases} \gamma_{\max} \in \left]\pi/2, \pi\right[\\ C = \frac{C_{\text{cr}}}{\sin(\gamma_{\max})} > C_{\text{cr}} \end{cases} \implies \exists\, t^*, \text{ s.t. } \boldsymbol{\theta}(t^*) \in \Delta_N(\gamma_{\min}).$$

In this context, frequency synchronization is achieved if the differences among the mean values of the last 50 samples of the frequencies $\dot{\theta}_i^{(\text{avg})}$ remain below a threshold $\varepsilon_{\text{fr}} = 1.75 \times 10^{-4}\,\text{rad}\,\text{s}^{-1}$, i.e.

$$\left|\dot{\theta}_i^{(\text{avg})} - \dot{\theta}_j^{(\text{avg})}\right| < \varepsilon_{\text{fr}}, \qquad \forall\, i, j \in [1,\, N]\,.$$

Phase cohesiveness is reached at the simulation time T if

$$\left|\theta_i\left(T\right) - \theta_j\left(T\right)\right| \leq \gamma_{\min}, \qquad \forall\, i, j \in [1,\, N]\,.$$

The empirical probability $\widehat{\mathsf{P}}$ for hypotheses H_* (H_* being H_{fr} or H_{ph}) is computed. To obtain an accuracy level of $\varepsilon = 0.01$ and a confidence level of $\eta = 0.01$, that is

$$\mathsf{P}\left(\left|\mathsf{P}\left(\mathsf{H}_* \text{ is true}\right) - \widehat{\mathsf{P}}\left(\mathsf{H}_* \text{ is true}\right)\right| < \varepsilon\right) > 1 - \eta,$$

the Chernoff-Hoeffding (Chernoff (1952); Hoeffding (1963)) bound justifies the chosen number of nominal models n

$$n \geq \frac{1}{2\varepsilon^2} \ln \frac{2}{\eta} = 26492.$$

In particular, the Monte Carlo simulations in the theoretical cohesiveness and synchronization conditions stated before show that

$$\widehat{\mathrm{P}}_{\mathrm{fr}} = 85.44\% \qquad \text{and} \qquad \widehat{\mathrm{P}}_{\mathrm{ph}} = 100\%. \tag{7.13}$$

Indeed, while the value of $\widehat{\mathrm{P}}_{\mathrm{ph}}$ is really satisfactory, i.e. phase cohesiveness is obtained in every simulation, the low value of $\widehat{\mathrm{P}}_{\mathrm{fr}}$ is probably due to the threshold-based method adopted for assessing frequency synchronization and, as will be clearer later, to the high values of C (sometimes much higher than necessary), that may lead to numerical issues. In this respect, it is interesting to study the bound accuracy, i.e. to find the smallest value $C_{\min}$ that permits to achieve phase cohesiveness in $\Delta(\gamma_{\min})$.
For each sample network out of n Monte Carlo realizations, the smallest value of C leading to cohesive phases satisfying $|\max|\theta_i - \theta_j| - \gamma_{\min}| < \varepsilon_{\mathrm{ph}}$, where $\varepsilon_{\mathrm{ph}} = 8.7 \times 10^{-3}$ rad, is found iteratively by numerically integrating the dynamics (7.2): at the h-th iteration the following scheme is applied

- if $|\max|\theta_i - \theta_j| - \gamma_{\min}| < \varepsilon_{\mathrm{ph}}$, then $C^{(h)} = C_{\min}$;
- if $\max|\theta_i - \theta_j| < \gamma_{\min} - \varepsilon_{\mathrm{ph}}$, then $C^{(h+1)} = 0.9 \times C^{(h)}$;
- if $\max|\theta_i - \theta_j| > \gamma_{\min} + \varepsilon_{\mathrm{ph}}$, then $C^{(h+1)} = 1.1 \times C^{(h)}$.

This iterative process stops when the $C_{\min}$ is found or when the iterations exceed 1000. By calling $C^{(1)} = C_{\mathrm{cr}}/\sin(\gamma_{\min})$, it is expected that the ratio $C_{\min}/C^{(1)}$ is always lower than or equal to unity. Indeed, if that happens, it means that the value of C_{cr} is sufficient to achieve phase cohesiveness.
In Fig. 7.4, the statistical distribution of this ratio is shown: firstly, it can be observed that the probability of reaching phase cohesiveness as the percent number of samples with the ratio lower or equal to 1 is (of course) $\widehat{\mathrm{P}}_{\mathrm{ph}} = 100\%$.

Furthermore, by analyzing the statistical distribution, there is a significant set of sample simulations (15.95%) that yields a ratio exactly equal to 1. This fact means that the bound C_{cr} is a good bound and cannot be decreased without decreasing the probability of reaching cohesiveness. Conversely, although the adopted implementation of the iterative scheme for $C_{\min}$ leads to a sort of quantization, this plot suggests a trade-off on how much the value of C can be decreased to ensure a minimum probability of cohesiveness. In particular, it can be stated that by decreasing C tenfold, phase cohesiveness with respect to $\gamma_{\min}$ can be obtained with a probability of about 50%.

Finally, it is possible to calculate the empirical probabilities of frequency synchroniza-

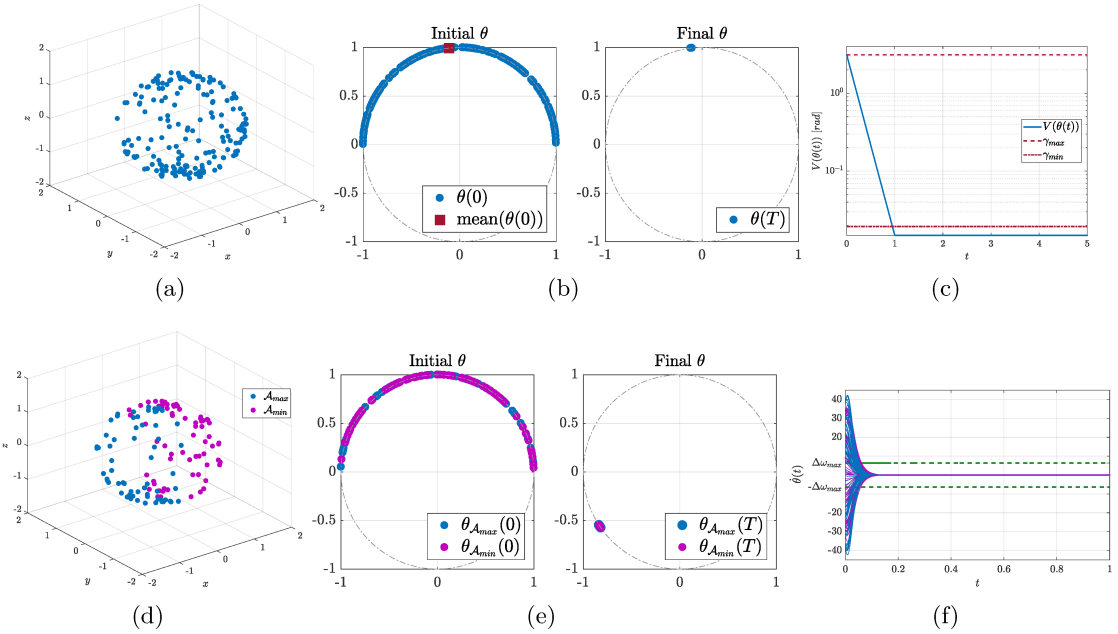

Figure 7.3: Sample realizations of a single kernel (top row) and a two kernels (bottom row) oscillators network. **Single kernel network.** Parameters: $N = 183$, $r = 1.38$, $p = 7$, $d_{\max} = 4.33$, $\gamma_{\max} = 178.9°$ - $\gamma_{\min} = 1.1°$, $C_{\text{cr}} = 2.92$ - $C = 150.31$. From left to right: spatial configuration of the agents, comparison between initial and final phases in the unit-circle, evolution of the Lyapunov function $V(\boldsymbol{\theta}(t))$ (bottom panel is a detail of the top one). **Two kernels network.** Parameters: $N = 134$ ($N_{\max} = 65$ - $N_{\min} = 69$), $r = 1.34$, $p_{\max} = 7$ - $p_{\min} = 4$, $\gamma_{\max} = 174.8°$ - $\gamma_{\min} = 5.2°$, $C_{\text{cr}} = 5.85$ - $C = 64.89$, $\omega_{\max} - \omega_{\min} = 6.3445$ - $\omega_{\text{sync}} = 0.0022$. From left to right: spatial configuration of the agents, comparison between initial and final phases in the unit-circle, evolution of the oscillators' frequencies.

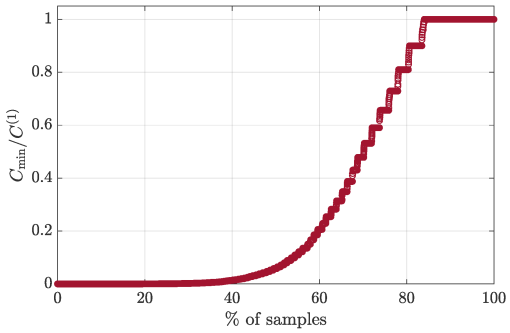

Figure 7.4: Distribution of the ratio $C_{\min}/C^{(1)}$: $C^{(1)} = C_{\text{cr}}/\sin(\gamma_{\min})$ with C_{cr} obtained by (7.4); $C_{\min}$ is the value calculated through the iterative scheme.

tion obtained with $C = C^{(1)}$ and with $C = C_{\min}$, which result in:

$$\widehat{\mathrm{P}}_{\mathrm{fr},C^{(1)}} = 85.16\% \qquad \text{and} \qquad \widehat{\mathrm{P}}_{\mathrm{fr},C_{\min}} = 99.35\%.$$

If compared with (7.13) it can be noticed that the value of $\widehat{\mathsf{P}}_{\mathrm{fr},C^{(1)}}$ is perfectly in line with that of $\widehat{\mathsf{P}}_{\mathrm{fr}}$ (taking into account the different set of Monte Carlo realizations), while $\widehat{\mathsf{P}}_{\mathrm{fr},C_{\min}}$ is much higher: in all likelihood, this is due to the fact that a lower value of C, which anyway permits to achieve phase cohesiveness, allows to reduce possible numerical issues and thus has to be preferred when using a numerical solver.

7.4 Cluster synchronization: phase cohesiveness

So far, we have investigated topological and spatial conditions required to achieve *complete* (asymptotic) frequency synchronization or phase cohesiveness in a network of Kuramoto oscillators. However, as mentioned in the introduction to this chapter, many applications refer to a condition where populations of elements evolve cohesively, but independently from the others. This condition is referred as *cluster synchronization*, in a broad sense, where, with *synchronization* one can mean different network behaviors (see Section 7.2.1).

In this section we address the problem of cluster synchronization in terms of *phase cohesiveness* among nodes belonging to the same cluster. With respect to existing notions of cluster synchronization, where the phases of the clustered oscillators are required to be equal to each other, in this section, we refer to cluster synchronization when the phase differences remain bounded over time. This definition is less stringent, and it allows us to study cluster synchronization in asymmetric oscillatory networks with general topology and parameters. We show how cluster synchronization depends on a graded combination of strong intra-cluster and weak inter-cluster connections, similarity of the natural frequencies of the oscillators within each cluster, and heterogeneity of the natural frequencies of coupled oscillators belonging to different groups. Specifically, we provide two different results for the cohesiveness of the phases of the oscillators in a cluster. The first result is based on the non-linear dynamics of the network, and it bounds from above the phase differences of the clustered oscillators. The second result uses a linear system to bound the non-linear dynamics, and it approximates the phase differences of the clustered oscillators as a function of the network parameters and natural frequencies of the oscillators. Although our second result is an approximated bound, it provides novel insights into the mechanisms enabling cluster synchronization in oscillatory networks, and it serves as a tight indication of the non-linear network evolution, as we show through a set of numerical studies.

7.4.1 Cluster synchronization in networks of Kuramoto oscillators

Throughout this section, we consider a network of N Kuramoto oscillators, represented by a weighed, undirected, and connected graph $\mathcal{G}$, as described before, whose phases' dynamics evolves as Equation (7.1), where $C = N$, that is:

$$\dot{\theta}_i(t) = \omega_i + \sum_{j=1}^{N} a_{ij} \sin(\theta_j(t) - \theta_i(t)), \qquad i = 1, \dots, N. \tag{7.14}$$

Coherently with Definition 7.2.7, a cluster of Kuramoto oscillators is defined as follows.

Definition 7.4.1 (***Cluster of oscillators***)**.** The set of oscillators $\mathcal{C} \subseteq \mathcal{V}$ is a cluster if there exists an angle $0 \leq \gamma \leq \pi$ such that, whenever $|\theta_i(0) - \theta_j(0)| \leq \gamma$ for all $i, j \in \mathcal{C}$,

$$|\theta_i(t) - \theta_j(t)| \leq \gamma,$$

for all $i, j \in \mathcal{C}$ and at all times $t \in \mathbb{R}_{\geq 0}$. □

Although Definition 7.4.1 allows a node to belong to different clusters, we will not discuss this case in this place, since our purpose is aimed at the characterization of a single cluster with respect to all the other nodes. Moreover, notice that frequencies need not be equal for nodes to belong to the same cluster. In Figure 7.5, an example of a network of clustered oscillators is depicted.

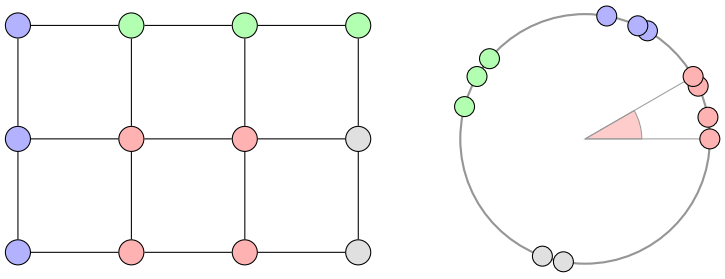

Figure 7.5: The left figure shows a network of 12 oscillators with 4 colour-coded clusters. The phases of the oscillators within each cluster evolve cohesively, as defined in Definition 7.4.1 and illustrated in the right figure.

7.4.1.1 Analysis based on non-linear cluster dynamics

Let $\mathcal{C} \subseteq \mathcal{V}$ denote a group of oscillators. From (7.1), the dynamics of each oscillator in $\mathcal{C}$ can be decomposed as

$$\dot{\theta}_i = \omega_i + \sum_{j \in \mathcal{C}} a_{ij} \sin(\theta_j - \theta_i) + \sum_{j \in \mathcal{V} \setminus \mathcal{C}} a_{ij} \sin(\theta_j - \theta_i).$$

Depending on the network parameters and oscillators' frequencies, the group $\mathcal{C}$ may behave as a cluster. In the next theorem we further characterize this relation.

Theorem 7.4.2. ***(Cluster condition based on network weights and oscillators' frequencies)***
Let $\mathcal{C} \subseteq \mathcal{V}$ and

$$\alpha_{max} = \max_{i,j \in \mathcal{C}} \left(\frac{\omega_{ij} + \sum_{k \in \mathcal{V} \setminus \mathcal{C}} (a_{jk} + a_{ik})}{2a_{ij} + \sum_{k \in \mathcal{C}} \min\{a_{ik}, a_{jk}\}} \right),$$

where $\omega_{ij} = \omega_j - \omega_i$ and a_{ij} are as in (7.1). If $\alpha_{max} \leq 1$, then $\mathcal{C}$ is a cluster with respect to the angle

$$\gamma = \arcsin(\alpha_{max}).$$

That is, if $|\theta_j(0) - \theta_i(0)| \leq \gamma$ for all $i, j \in \mathcal{C}$, then $|\theta_j(t) - \theta_i(t)| \leq \gamma$ for all $i, j \in \mathcal{C}$ and all times $t \geq 0$.

Proof of Theorem 7.4.2. Consider $\theta_{ij} = \theta_j - \theta_i$, and assume that $|\theta_{ij}(0)| \leq \gamma$ for all $i, j \in \mathcal{C}$. Notice that

$$\dot{\theta}_{ij} = \dot{\theta}_j - \dot{\theta}_i = \omega_{ij} + \sum_{k \in \mathcal{V}} a_{jk} \sin(\theta_{jk}) - a_{ik} \sin(\theta_{ik}).$$

We show that, whenever $|\theta_{ij}| = \gamma$ for some $i, j \in \mathcal{C}$, then $\frac{d|\theta_{ij}|}{dt} \leq 0$, thus proving the forward invariance of the angle γ. Assume that $\theta_{ij} = \gamma$ (the case $\theta_{ij} = -\gamma$ follows from analogous reasoning). We have

$$\dot{\theta}_{ij} = \omega_{ij} - 2a_{ij} \sin(\gamma) + \sum_{k \in \mathcal{V} \setminus \mathcal{C}} a_{jk} \sin(\theta_{jk}) - a_{ik} \sin(\theta_{ik}) + \\ + \sum_{k \in \mathcal{C} \setminus \{i,j\}} \underbrace{a_{jk} \sin(\theta_{jk}) - a_{ik} \sin(\theta_{ik})}_{f_k}.$$

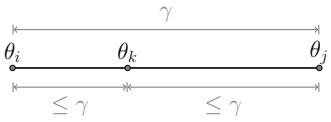

Figure 7.6: Schematic representation of the relationship among the phases related to oscillators within cluster $\mathcal{C}$. Note that $0 \leq \theta_{ik} \leq \gamma$, and $0 \leq \theta_{kj} \leq \gamma$.

Notice that for all $j, k = 1, \ldots, N$, it is

$$\theta_{jk} = \theta_k - \theta_j = \theta_i - \theta_j + \theta_k - \theta_i = \theta_{ji} + \theta_{ik} = -\gamma + \theta_{ik},$$

where $\theta_{ij} = \gamma$ by assumption (see Figure 7.6), and

$$\begin{aligned}\frac{\partial f_k}{\partial \theta_{ik}} &= a_{jk}\cos(\theta_{ik} - \gamma) - a_{ik}\cos(\theta_{ik}) \\ &= a_{jk}\cos(\theta_{ik})\cos(\gamma) + \sin(\theta_{ik})\sin(\gamma) - a_{ik}\cos(\theta_{ik}) \\ &= (a_{jk}\cos(\gamma) - a_{ik})\cos(\theta_{ik}) + \sin(\gamma)\sin(\theta_{ik}).\end{aligned}$$

Moreover,

$$\begin{cases} \frac{\partial f_k}{\partial \theta_{ik}} < 0, & \text{if } 0 \leq \theta_{ik} < \arctan\left(\frac{a_{ik} - a_{jk}\cos(\gamma)}{\sin(\gamma)}\right), \\ \frac{\partial f_k}{\partial \theta_{ik}} > 0, & \text{if } \arctan\left(\frac{a_{ik} - a_{jk}\cos(\gamma)}{\sin(\gamma)}\right) < \theta_{ik} \leq \frac{\pi}{2}. \end{cases}$$

Thus, because f_k decreases/increases monotonically in the interval $[0, \gamma]$, we have

$$\begin{aligned} f_k^{\max} = \max_{0 \leq \theta_{ik} \leq \gamma} f_k &= \max\{f_k(0), f_k(\gamma)\} \\ &= \max\{-a_{jk}\sin(\gamma), -a_{ik}\sin(\gamma)\} \\ &= -\sin(\gamma)\min\{a_{jk}, a_{ik}\}. \end{aligned}$$

The derivative $\dot{\theta}_{ij}$ can be bounded as

$$\dot{\theta}_{ij} \leq \omega_{ij} - 2a_{ij}\sin(\gamma) + \sum_{k \in \mathcal{V} \setminus \mathcal{C}} a_{jk} + a_{ik} + \sum_{k \in \mathcal{C} \setminus \{i,j\}} f_k^{\max}.$$

Finally, notice that $\dot{\theta}_{ij} \leq 0$ when the angle γ satisfies

$$\gamma \geq \arcsin\left(\max_{i,j \in \mathcal{C}}\left(\frac{\omega_{ij} + \sum_{k \in \mathcal{V} \setminus \mathcal{C}} a_{jk} + a_{ik}}{2a_{ij} + \sum_{k \in \mathcal{C}} \min\{a_{jk}, a_{ik}\}}\right)\right),$$

which concludes the proof. ∎

Theorem 7.4.2 implies that the cluster $\mathcal{C}$ is more *cohesive*, that is, it has a smaller angle γ, when the weight of the edges within the cluster increases. Similarly, the angle γ increases when (i) the weight of the edges connecting oscillators within and outside the cluster increases, and (ii) the natural frequencies of the oscillators in the cluster become more heterogeneous (ω_{ij} increases). It should be noticed that, even in the case $\mathcal{C} = \mathcal{V}$, the angle γ may remain positive, that is, the oscillators may not achieve phase synchronization, which is consistent with existing results on networks of heterogeneous oscillators (Dörfler and Bullo (2014)).

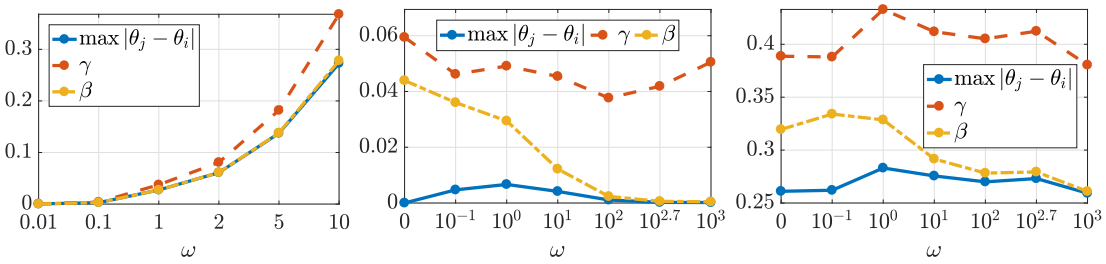

(a) $M = N$ and $\omega_i \leq \omega$, i $\in \mathcal{C}$ (b) $\omega_i = 0$, $i \in \mathcal{C}$ and $\omega_k \leq \omega$, $k \in \mathcal{V} \setminus \mathcal{C}$ (c) $\omega_i \leq 1$, $i \in \mathcal{C}$ and $\omega_k \leq \omega$, $k \in \mathcal{V} \setminus \mathcal{C}$

Figure 7.7: This figure shows the largest phase difference among the oscillators in the cluster, as described in Section 7.4.2, and the bounds γ and β derived in Theorem 7.4.2 and Theorem 7.4.6, respectively. In Figure **(a)**, the cluster comprises all nodes ($\mathcal{C} = \mathcal{V}$) and, for each value of ω, the oscillators natural frequencies are selected randomly and uniformly distributed in the interval $[0, \omega]$. In Figure **(b)**, the cluster comprises a proper subset of nodes, the oscillators in the cluster have equal frequency, while the frequencies of the oscillators outside the cluster are selected randomly and uniformly distributed in the interval $[0, \omega]$. In Figure **(c)**, the cluster comprises a proper subset of nodes, the frequencies of the oscillators in the cluster are selected randomly and uniformly distributed in the interval $[0, 1]$, while the frequencies of the oscillators outside the cluster are selected randomly and uniformly distributed in the interval $[0, \omega]$. Notice that (i) β is a tighter bound than γ, (ii) the cohesiveness of the cluster increases when the frequencies of the oscillators outside the cluster increase, and (iii) exact phase synchronization is possible only when the oscillators in the cluster have equal frequency, and the frequencies of the oscillators outside the cluster increase to infinity.

As it can be seen in Figure 7.7, the bound γ in Theorem 7.4.2 may be conservative. A more refined approximation can be obtained by accounting for the natural frequencies of the oscillators outside the cluster ($\mathcal{V} \setminus \mathcal{C}$), as we show next.

Lemma 7.4.3. ***(Linear comparison)***
Let $\mathcal{C}$ be a cluster with respect to the angle γ. Then at all times,

$$\max_{i,j\in\mathcal{C}}(\theta_j - \theta_i) \leq \max_{i,j\in\mathcal{C}}(\tilde{\theta}_j - \tilde{\theta}_i),$$

where $\tilde{\theta}_i$ satisfies $\tilde{\theta}_i(0) = \theta_i(0)$ for all $i \in \mathcal{C}$ and

$$\dot{\tilde{\theta}}_i = \omega_i + \frac{\sin(\gamma)}{\gamma}\sum_{j\in\mathcal{C}} a_{ij}(\tilde{\theta}_j - \tilde{\theta}_i) + \sum_{j\in\mathcal{V}\setminus\mathcal{C}} a_{ij}v_{ij}, \tag{7.15}$$

with $v_{ij} = \sin(\theta_j - \tilde{\theta}_i)$.

Proof of Lemma 7.4.3. The proof is divided into two parts. First, following the same procedure as in the proof of Theorem 7.4.2, it follows that $|\tilde{\theta}_{ij}| = |\tilde{\theta}_j(t) - \tilde{\theta}_i(t)| \leq \gamma$ at all times. Second, we employ the comparison lemma in Khalil (2002) to prove the claimed statement. Consider the non-negative function

$$g(t, \mathbf{x}) := \max(x_j(t) - x_i(t)),$$

where x_i denotes the i-th component of the vector $\mathbf{x}$. Proving Lemma 7.4.3 is equivalent to prove that

$$g(t, \theta) \leq g(t, \tilde{\theta}). \tag{7.16}$$

Consider

$$\mathcal{U}(t) = \{i \ : \ \theta_i(t) = \max_j \theta_j(t)\}, \qquad \widetilde{\mathcal{U}}(t) = \{i \ : \ \tilde{\theta}_i(t) = \max_j \tilde{\theta}_j(t)\},$$
$$\mathcal{M}(t) = \{i \ : \ \theta_i(t) = \min_j \theta_j(t)\}, \qquad \widetilde{\mathcal{M}}(t) = \{i \ : \ \tilde{\theta}_i(t) = \min_j \tilde{\theta}_j(t)\}.$$

Notice that

$$g(t, \boldsymbol{\theta}) = \theta_i - \theta_j \quad \text{with} \quad i \in \mathcal{U}(t) \quad \text{and} \quad j \in \mathcal{L}(t),$$
$$g(t, \tilde{\boldsymbol{\theta}}) = \tilde{\theta}_i - \tilde{\theta}_j \quad \text{with} \quad i \in \widetilde{\mathcal{U}}(t) \quad \text{and} \quad j \in \widetilde{\mathcal{M}}(t).$$

From (Lin et al., 2007, Lemma 2.2), we know that

$$D^+ g(t, \boldsymbol{\theta}) = \lim_{h\to 0} \sup \frac{g(\boldsymbol{\theta}(t+h)) - g(\boldsymbol{\theta}(h))}{h} = v_{\max}(t) - v_{\min}(t),$$

where D^+g is the right-hand derivative of $g(t,\boldsymbol{\theta})$, and

$$v_{\max}(t) = \max\{\dot{\theta}_i \ : \ i \in \mathcal{U}(t)\}, \qquad v_{\min}(t) = \min\{\dot{\theta}_i \ : \ i \in \mathcal{M}(t)\}.$$

Analogously, $D^+g(t,\tilde{\boldsymbol{\theta}}) = \tilde{v}_{\max}(t) - \tilde{v}_{\min}(t)$. From (Cao and Ren, 2011, Lemma 3.3), equation (7.16) holds if $D^+g(t,\boldsymbol{\theta})|_{\boldsymbol{\theta}=\tilde{\boldsymbol{\theta}}} \leq D^+g(t,\tilde{\boldsymbol{\theta}})$. Note that, for some i^* and j^*,

$$\begin{aligned} v_{\max} - v_{\min} = \omega_{j^*} - \omega_{i^*} &+ \sum_{k\in\mathcal{C}} a_{j^*k}\sin(\tilde{\theta}_{j^*k}) - a_{i^*k}\sin(\tilde{\theta}_{i^*k}) \\ &+ \sum_{k\in\mathcal{V}\setminus\mathcal{C}} a_{j^*k}\sin(\theta_k - \tilde{\theta}_{j^*}) - a_{i^*k}\sin(\theta_k - \tilde{\theta}_{i^*}), \end{aligned}$$

and

$$\begin{aligned} \tilde{v}_{\max} - \tilde{v}_{\min} \geq \omega_{j^*} - \omega_{i^*} &+ \frac{\sin(\gamma)}{\gamma}\sum_{k\in\mathcal{C}} a_{j^*k}\tilde{\theta}_{j^*k} - a_{i^*k}\tilde{\theta}_{i^*k} + \\ &+ \sum_{k\in\mathcal{V}\setminus\mathcal{C}} a_{j^*k}\sin(\theta_k - \tilde{\theta}_{j^*}) - a_{i^*k}\sin(\theta_k - \tilde{\theta}_{i^*}). \end{aligned}$$

Thus,

$$\begin{aligned} D^+g(t,\tilde{\boldsymbol{\theta}}) - D^+g(t,\boldsymbol{\theta})|_{\tilde{\boldsymbol{\theta}}} \geq \\ \sum_{k\in\mathcal{C}} a_{j^*k}\left(\frac{\sin(\gamma)\tilde{\theta}_{j^*k}}{\gamma} - \sin\tilde{\theta}_{j^*k}\right) - a_{i^*k}\left(\frac{\sin(\gamma)\tilde{\theta}_{i^*k}}{\gamma} - \sin\tilde{\theta}_{i^*k}\right). \end{aligned}$$

Because $\left|\tilde{\theta}_{ij}\right| \leq \gamma$, we have

$$\begin{cases} \frac{\sin(\gamma)\tilde{\theta}_{ij}}{\gamma} \leq \sin(\tilde{\theta}_{ij}), & \text{if } \tilde{\theta}_{ij} \geq 0, \\ \frac{\sin(\gamma)\tilde{\theta}_{ij}}{\gamma} \geq \sin(\tilde{\theta}_{ij}), & \text{if } \tilde{\theta}_{ij} \leq 0. \end{cases}$$

Notice that, for every $k \in \mathcal{C}$, $\tilde{\theta}_{i^*} \leq \tilde{\theta}_k \leq \tilde{\theta}_{j^*}$ and, consequently, $\tilde{\theta}_{i^*k} \geq 0$ and $\tilde{\theta}_{j^*k} \leq 0$. Thus, $D^+g(t,\tilde{\boldsymbol{\theta}}) - D^+g\,(t,\boldsymbol{\theta})\,|_{\tilde{\boldsymbol{\theta}}} \geq 0$, which concludes the proof.

■

7.4.1.2 Analysis based on approximated linear dynamics

Lemma 7.4.3 shows that the evolution of the non-linear network dynamics can be bounded by the evolution of the linear system (7.15) with bounded inputs v_{ij}. We use this observation to find a tighter approximation of the clustering angle γ. Consider a spanning tree $\mathcal{T} = (\mathcal{C}, \mathcal{E}_\mathcal{T})$ of the subgraph $(\mathcal{C}, \mathcal{E}_\mathcal{C})$, with $\mathcal{E}_\mathcal{C} = \mathcal{E} \cap \mathcal{C} \times \mathcal{C}$ (Godsil and Royle

(2013)). For $i, j \in \mathcal{C}$, let p_{ij} be the unique path on $\mathcal{T}$ from i to j[4]. Let $\tilde{\theta}_{ij} = \tilde{\theta}_j - \tilde{\theta}_i$, and notice that

$$\tilde{\theta}_{ij} = \sum_{h \in p_{ij}} \tilde{\theta}_{h+1} - \tilde{\theta}_h. \tag{7.17}$$

Let $\mathbf{x}_{\text{tree}}$ and $\mathbf{x}_{\text{cluster}}$ be the vectors of all $\tilde{\theta}_{ij}$ with $(i,j) \in \mathcal{E}_{\mathcal{T}}$ and $(i,j) \in \mathcal{C} \times \mathcal{C}$, respectively, with $j > i$. See Figure 7.8 for an illustration of these definitions. Some algebraic manipulation from (7.15) and (7.17) leads to

$$\dot{\mathbf{x}}_{\text{tree}} = \frac{\sin(\gamma)}{\gamma} \mathbf{F}\, \mathbf{x}_{\text{tree}} + \mathbf{G}\, \mathbf{u} + \boldsymbol{\Delta}_{\boldsymbol{\omega}}, \tag{7.18a}$$

$$\mathbf{x}_{\text{cluster}} = \mathbf{H}\, \mathbf{x}_{\text{tree}}, \tag{7.18b}$$

where $\mathbf{F}$, $\mathbf{G}$, and $\mathbf{H}$ are appropriately defined matrices, and $\boldsymbol{\Delta}_{\boldsymbol{\omega}}$ contains all the differences ω_{ij} with $j > i$ and $(i,j) \in \mathcal{E}_{\mathcal{T}}$. Notice that each component of $\mathbf{u}$ can be written as $u_i = \sin(\theta_p - \tilde{\theta}_q)$, for some $q \in \mathcal{C}$ and $p \in \mathcal{V} \setminus \mathcal{C}$. The following definition will be used: for the i-th component of $\mathbf{u}$, let

$$\omega_i^* = |\omega_p - \omega_q|. \tag{7.19}$$

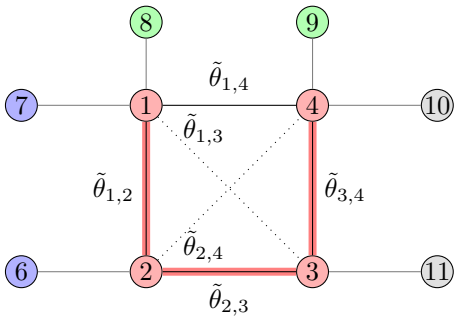

Figure 7.8: For the cluster with nodes $\mathcal{C} = \{1,2,3,4\}$ in Fig. 7.5, this figure shows a spanning tree $\mathcal{T} = (\mathcal{C}, \mathcal{E}_{\mathcal{T}})$, where $\mathcal{E}_{\mathcal{C}} = \{(1,2),(2,3),(3,4),(1,4)\}$ and $\mathcal{E}_{\mathcal{T}} = \{(1,2),(2,3),(3,4)\}$. The system (7.18) associated with the cluster $\mathcal{C}$ is in Example 7.4.4.

Example 7.4.4. ***(An example of system*** (7.18)***)***
Consider the cluster $\mathcal{C} = \{1,2,3,4\}$ of Figure 7.8 with subgraph $(\mathcal{C}, \mathcal{E}_{\mathcal{C}})$, $\mathcal{E}_{\mathcal{C}} = \{(1,2),(2,3),(3,4),(1,4)\}$. The subgraph $\mathcal{T} = (\mathcal{C}, \mathcal{E}_{\mathcal{T}})$ is a spanning tree, where $\mathcal{E}_{\mathcal{T}} = \{(1,2),(2,3),(3,4)\}$. The state

[4]A path p_{ij} on $\mathcal{E}_{\mathcal{T}}$, $i, j \in \mathcal{C}$, is a sequence of vertices of $\mathcal{C}$ such that i and j are the first and last elements of the sequence, respectively, and for any two consecutive nodes k, h it holds $(k,h) \in \mathcal{E}_{\mathcal{T}}$.

of the system (7.18) associated with $\mathcal{T}$ is

$$\mathbf{x}_{\text{tree}} = \begin{bmatrix} \tilde{\theta}_{12} & \tilde{\theta}_{23} & \tilde{\theta}_{34} \end{bmatrix}^{\mathsf{T}},$$
$$\mathbf{x}_{\text{cluster}} = \begin{bmatrix} \tilde{\theta}_{12} & \tilde{\theta}_{23} & \tilde{\theta}_{34} & \tilde{\theta}_{14} & \tilde{\theta}_{13} & \tilde{\theta}_{24} \end{bmatrix}^{\mathsf{T}}.$$

The input $\mathbf{u}$ has six components:

$$u_1 = \sin(\theta_7 - \tilde{\theta}_1), \qquad u_2 = \sin(\theta_8 - \tilde{\theta}_1), \qquad u_3 = \sin(\theta_6 - \tilde{\theta}_2),$$
$$u_4 = \sin(\theta_{11} - \tilde{\theta}_3), \qquad u_5 = \sin(\theta_9 - \tilde{\theta}_4), \qquad u_6 = \sin(\theta_{10} - \tilde{\theta}_4).$$

The matrices $\mathbf{F}$, $\mathbf{G}$, $\mathbf{H}$ and the vector $\mathbf{\Delta_\omega}$ are as follows:

$$\mathbf{F} = \begin{bmatrix} -(2a_{12} + a_{14}) & (a_{23} - a_{1,4}) & -a_{14} \\ a_{12} & -a_{23} & a_{34} \\ -a_{14} & -(a_{23} + a_{14}) & -(2a_{34} + a_{14}) \end{bmatrix},$$
$$\mathbf{G} = \begin{bmatrix} -a_{17} & -a_{18} & a_{26} & 0 & 0 & 0 \\ 0 & 0 & -a_{26} & a_{3,11} & 0 & 0 \\ 0 & 0 & 0 & -a_{3,11} & a_{49} & a_{4,10} \end{bmatrix}$$
$$\mathbf{H} = \begin{bmatrix} 1 & 0 & 0 & 1 & 1 & 0 \\ 0 & 1 & 0 & 1 & 1 & 1 \\ 0 & 0 & 1 & 1 & 0 & 1 \end{bmatrix}^{\mathsf{T}} \quad \text{and} \quad \mathbf{\Delta_\omega} = \begin{bmatrix} \omega_2 - \omega_1 \\ \omega_3 - \omega_2 \\ \omega_4 - \omega_3 \end{bmatrix}.$$

Finally, $\omega_1^* = |\omega_7 - \omega_1|$, $\omega_2^* = |\omega_8 - \omega_1|$, $\omega_3^* = |\omega_6 - \omega_2|$, $\omega_4^* = |\omega_3 - \omega_{11}|$, $\omega_5^* = |\omega_4 - \omega_9|$, and $\omega_6^* = |\omega_4 - \omega_{10}|$. □

Lemma 7.4.5. ***(Stability of*** (7.18)***)***
The system (7.18) *is stable.*

Proof of Lemma 7.4.5. Let $\tilde{\boldsymbol{\theta}}$ be the vector of $\tilde{\theta}_i$ with $i \in \mathcal{C}$, and let $\dot{\tilde{\boldsymbol{\theta}}} = -\mathbf{L}\tilde{\boldsymbol{\theta}} + \mathbf{v}$, where $\mathbf{L}$ and $\mathbf{v}$ are defined from (7.15). Notice that $\mathbf{L}$ is a Laplacian matrix (Godsil and Royle (2013)), in fact it equals the Laplacian of the subgraph of $\mathcal{G}$ with nodes $\mathcal{C}$. Thus, because the graph $\mathcal{G}$ is connected, $\mathbf{L}$ has a simple eigenvalue in the origin, with eigenvector with all equal components (Olfati-Saber et al. (2007)). Thus, the autonomous dynamics $\dot{\tilde{\boldsymbol{\theta}}} = -\mathbf{L}\tilde{\boldsymbol{\theta}}$ satisfy

$$\lim_{t\to\infty} \tilde{\theta}_j(t) - \tilde{\theta}_i(t) = 0,$$

for all $i, j \in \mathcal{C}$. As a consequence, the matrix $\mathbf{F}$ is stable because, when $\mathbf{\Delta_\omega} = \mathbb{0}$ and

$\mathbf{u} = \mathbb{0}$, the differences $\tilde{\theta}_{ij}$ converge to zero[5]. ■

Next, we exploit the frequency behavior of the system (7.18) to derive a tighter bound for the cohesiveness of the phases of the oscillators within a cluster.

Theorem 7.4.6. ***(Approximation based on linearized dynamics)*** *Let $\mathbf{G}_i$ be the i-th column of the matrix $\mathbf{G}$ in (7.18), and let ω_i^* be as in (7.19). Then, with the same notation as in Lemma 7.4.3, $\max_{ij} \theta_{ij} \leq \max_{ij} \tilde{\theta}_{ij} = \|\mathbf{x}_{cluster}\|_\infty$, and* [6]

$$\left| \|\mathbf{x}_{cluster}\|_\infty - \left\| \mathbf{H}\mathbf{F}^{-1}\mathbf{\Delta}_{\boldsymbol{\omega}} + \sum_i \mathbf{H}(\mathrm{j}\omega_i^*\mathbf{I} - \mathbf{F})^{-1}\mathbf{G}_i \right\|_\infty \right| \approx 0. \tag{7.20}$$

Proof of Theorem 7.4.6. To obtain the approximate bound in Theorem 7.4.6, we assume that, using the notation in (7.19),

$$u_i = \sin(\theta_p - \tilde{\theta}_q) \approx \sin((\omega_p - \omega_q)t) = \sin(\omega_i^* t).$$

We then exploit standard arguments from linear system theory, and in particular the harmonic response of a linear system, and the stability of (7.18) to conclude the proof.

It should be observed that our approximation is tighter as the frequencies ω_i^* grow to infinity while the natural frequencies of the oscillators in the cluster remain bounded. In fact, in this case, and with appropriate initial conditions, we have that ω_i grows to infinity, with $i \in \mathcal{V} \setminus \mathcal{C}$, and the phase θ_i evolves as $\omega_i t$:

$$\frac{\dot{\theta}_i}{\omega_i} = 1 + \underbrace{\sum_{j \in \mathcal{C}} \frac{a_{ij}}{\omega_i} \sin(\tilde{\theta}_j - \theta_i)}_{\to 0} + \underbrace{\sum_{j \in \mathcal{V} \setminus \mathcal{C}} \frac{a_{ij}}{\omega_i} \sin(\theta_j - \theta_i)}_{\to 0} = 1.$$

Then, we have that $\sin(\theta_p - \tilde{\theta}_q)$ converges to $\sin(\omega_p t)$, and the symbol $\approx$ in (7.20) can instead be replaced with $=$. ■

Theorem 7.4.6 shows how the frequency of the oscillators connected to a cluster affects the cohesiveness of the phases of its oscillators. In particular the larger ω_i^*, the less the effect of the neighboring oscillators on the cohesiveness of the cluster. In fact, in the limit when all ω_i^*'s grow to infinity, the cluster is effectively disconnected from the neighboring agents because the cluster dynamics acts as a low pass filter with respect to the frequencies ω_i^*'s. Additionally, it can be shown that, as all ω_i^*'s grow to infinity and

[5] The dimension vectors $\mathbb{0}$ are omitted, but coherent with the associated vectors.

[6] In (7.20) we have $=$ instead of $\approx$ when the cluster comprises all nodes, that is $\mathcal{C} = \mathcal{V}$, when $\mathbf{G} = 0$, or ω_i^* grow to infinity.

$\boldsymbol{\Delta_\omega}$ decreases to zero, the cluster achieves phase synchronization, that is,

$$\lim_{t\to\infty} \max_{i,j\in\mathcal{C}} (\theta_j(t) - \theta_i(t)) = 0.$$

Finally, it should be noticed that the vector $\boldsymbol{\Delta_\omega}$ is due to heterogeneity of the natural frequencies of the clustered oscillators, and it acts as a constant input to the system (7.18).

Corollary 7.4.7. ***(Equivalence of bounds when*** $|\mathcal{C}| = 2$ ***and the natural frequencies coincide)***
Let $|\mathcal{C}| = 2$ *and* $\omega_i = 0$ *for all* $i = \{1, \dots, N\}$. *Then the bounds in Theorem 7.4.2 and 7.4.6 coincide.*

Proof of Corollary 7.4.7. Without loss in generality, assume $\mathcal{C} = \{1, 2\}$. In case of $\omega_1 = \omega_2 = \omega_j = 0$ for all $j = 3, \dots, N$, from Theorem 7.4.2 it is

$$\alpha_{\max} = \sin(\gamma) = \sum_{k=3}^{n} \frac{(a_{1k} + a_{2k})}{2a_{12}}$$

Moreover, in equation (7.20), $\boldsymbol{\Delta_\omega} = [0]$, $\mathbf{H} = [1]$, $\mathbf{F} = [-2a_{12}]$, and $\mathbf{G}$ is a row vector of elements equal to $-a_{1k}$ or a_{2k}, with $k = 3, \dots, N$. Hence equation Theorem 7.4.6 says that

$$\|\mathbf{x}_{\text{cluster}}\|_\infty \approx \frac{\gamma}{\sin(\gamma)} \underbrace{\sum_{k=3}^{N} \frac{(a_{1k} + a_{2k})}{2a_{12}}}_{\sin(\gamma)} = \gamma.$$

Therefore, the two bounds coincide. ∎

7.4.2 Numerical examples

To validate the results in Section 7.4.1, we perform two sets of numerical studies. In Figure 7.7 we compare the largest phase difference within a cluster of oscillators with the bounds in Theorems 7.4.2 and 7.4.6 as a function of the oscillators' natural frequencies. We consider fully connected networks of Kuramoto oscillators, where $\mathcal{V} = \{1, \dots, N\}$ and $\mathcal{C} = \{1, \dots, N_\mathcal{C}\}$; N and $N_\mathcal{C}$ are randomly selected in the intervals $\{2, \dots, 10\}$ and $\{2, \dots, N\}$, respectively. The network weights a_{ij} are independent random variables uniformly distributed in the intervals $[0, 1]$, if $i, j \in \mathcal{C}$, and $[0, 0.01]$ otherwise. For each value of the largest natural frequency ω, we generate 100 different networks, compute the largest phase difference within the cluster, evaluate our bounds, and report the average results. The results show that the bound in Theorem 7.4.6 is tighter than the bound

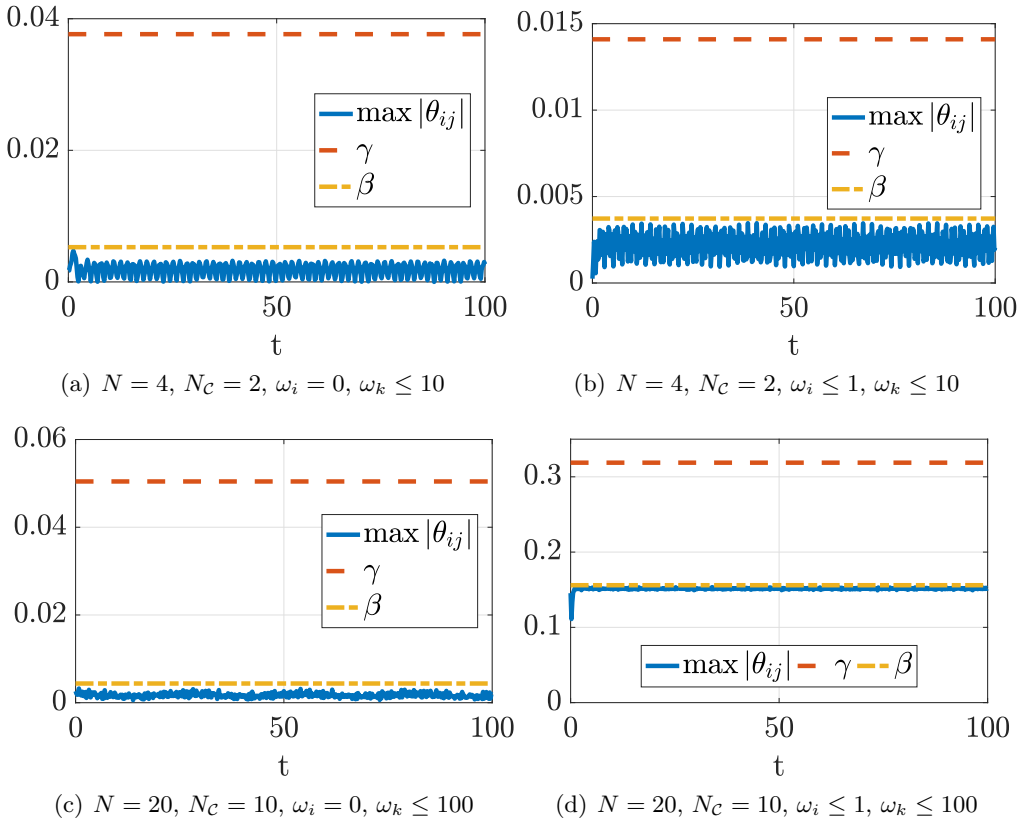

(a) $N = 4$, $N_{\mathcal{C}} = 2$, $\omega_i = 0$, $\omega_k \leq 10$

(b) $N = 4$, $N_{\mathcal{C}} = 2$, $\omega_i \leq 1$, $\omega_k \leq 10$

(c) $N = 20$, $N_{\mathcal{C}} = 10$, $\omega_i = 0$, $\omega_k \leq 100$

(d) $N = 20$, $N_{\mathcal{C}} = 10$, $\omega_i \leq 1$, $\omega_k \leq 100$

Figure 7.9: This figure shows the largest phase difference among the oscillators in the cluster over time (blue, continuous), as described in Section 7.4.2. We consider fully connected Kuramoto networks, where $\mathcal{V} = \{1, \dots, N\}$, $\mathcal{C} = \{1, \dots, N_{\mathcal{C}}\}$, $\{\omega_1, \dots, \omega_{N_{\mathcal{C}}}\}$ are selected randomly in the interval $[0, \omega_{\text{in}}^{\max}]$, and $\{\omega_{N_{\mathcal{C}}+1}, \dots, \omega_N\}$ are selected randomly in $[0, \omega_{\text{out}}^{\max}]$, with $N = 4$ in Fig. **(a)** and **(b)**, $N = 20$ in Fig. **(c)** and **(d)**, $N_{\mathcal{C}} = 2$ in Fig. **(a)** and **(b)**, $N_{\mathcal{C}} = 10$ in Fig. **(c)** and **(d)**, $\omega_{\text{in}}^{\max} = 0$ in Fig. **(a)** and **(c)**, $\omega_{\text{in}}^{\max} = 1$ in Fig. **(b)** and **(d)**, $\omega_{\text{out}}^{\max} = 10$ in Fig. **(b)**, $\omega_{\text{out}}^{\max} = 100$ in Fig. **(c)** and **(d)**. The figures highlight how heterogeneity of the natural frequencies of the oscillators in the clusters affect cluster cohesiveness. The bound from Theorem 7.4.2 is in red (dashed); the bound from Theorem 7.4.6 is in yellow (dashed-dot).

in Theorem 7.4.2, and that it captures the asymptotic behavior of the phase difference as the natural frequencies of the oscillators outside the cluster increase. Moreover, the cohesiveness of the cluster increases when the frequencies of the oscillators outside the cluster increase, and exact phase synchronization is possible only when the oscillators in the cluster have equal frequency, and the frequencies of the oscillators outside the cluster increase to infinity.

In Figure 7.9 we report the time trajectory of the largest phase difference within a cluster. We consider fully connected networks of Kuramoto oscillators, where the network weights a_{ij} are independent random variables uniformly distributed in the intervals $[0, 1]$,

if $i, j \in \mathcal{C}$, and $[0, 0.01]$ otherwise. We consider different choices of $\mathcal{V}$, $\mathcal{C}$, and of the oscillators' natural frequencies, as described in the figure caption. The results show how the phase differences inside the cluster decrease when the natural frequencies inside the cluster are homogeneous, and when the frequencies of the neighboring oscillators are sufficiently larger.

7.5 Cluster synchronization: phase Synchronization

We address now the problem of *phase synchronization* (see Definition 7.2.3) among clusters of nodes. In other words, in this section we are particularly interested in the case where the phases of groups of oscillators evolve perfectly cohesive within each group, yet independently from the phases of oscillators in different groups.

First, we consider a notion of exact cluster synchronization, where the phases of the oscillators within each cluster remain equal to each other over time, and different from the phases of the oscillators in different clusters. We derive necessary and sufficient conditions for the formation of a given synchronization pattern in directed and weighted networks of Kuramoto oscillators. In particular we show that cluster synchronization is possible if and only if **(i)** the natural frequencies are equal within each cluster, and **(ii)** for each cluster, the sum of the weights of the edges from every separate group is the same for all nodes in the cluster. Second, we leverage our characterization of cluster synchronization to develop a control mechanism that modifies the network weights so as to ensure the formation of a desired synchronization pattern. Our control method is optimal, in the sense that it determines the smallest (measured by the Frobenius norm) network perturbation for a given synchronization pattern, and it guarantees the modification of only a desired subset of the edge weights.

7.5.1 Problem setup and definitions

Consider a network of N Kuramoto oscillators described by the digraph $\mathcal{G} = (\mathcal{V}, \mathcal{E})$, as characterized in Section 7.2. The dynamics of the oscillators' phases read as (7.14). Depending on the interconnection graph $\mathcal{G}$, the adjacency matrix $\mathbf{A}$, and the oscillators natural frequencies, different oscillatory patterns are possible corresponding to (partially) synchronized or chaotic states (Mirchev et al. (2014)).

To formalize this discussion, let $\mathcal{P} = \{\mathcal{P}_1, \dots, \mathcal{P}_M\}$ be a partition of $\mathcal{V}$, that is, $\mathcal{V} = \cup_{i=1}^{M} \mathcal{P}_i$ and $\mathcal{P}_i \cap \mathcal{P}_j = \emptyset$ for all $i, j \in \{1, \dots, M\}$ with $i \neq j$. We restrict our attention to the case $M > 1$, and we will assume without loss of generality that, given $\mathcal{P} = \{\mathcal{P}_1, \dots, \mathcal{P}_M\}$, the oscillators are labelled so that $\mathcal{P}_i = \{\sum_{j=1}^{i-1} |\mathcal{P}_j| + 1, \dots, \sum_{j=1}^{i} |\mathcal{P}_j|\}$,

where $|\mathcal{P}_j|$ denotes the cardinality of the set $\mathcal{P}_j$.

Thus, we now adjust the definition of phase and frequency synchronization in Section 7.2.1, to match the specific case we are considering. Specifically, we focus our attention to the definition of phase and frequency *synchronizability*.

Definition 7.5.1 (***Phase synchronizability***)**.** For the network of oscillators $\mathcal{G} = (\mathcal{V}, \mathcal{E})$, the partition $\mathcal{P} = \{\mathcal{P}_1, \dots, \mathcal{P}_M\}$ is *phase synchronizable* if, for some initial phases $\theta_1(0), \dots, \theta_N(0)$, it holds

$$\theta_i(t) = \theta_j(t),$$

for all times $t \in \mathbb{R}_{\geq 0}$ and $i, j \in \mathcal{P}_k$, with $k \in \{1, \dots, M\}$. □

Definition 7.5.2 (***Frequency synchronizability***)**.** For the network of oscillators $\mathcal{G} = (\mathcal{V}, \mathcal{E})$, the partition $\mathcal{P} = \{\mathcal{P}_1, \dots, \mathcal{P}_M\}$ is *frequency synchronizable* if, for some initial phases $\theta_1(0), \dots, \theta_N(0)$, it holds

$$\dot{\theta}_i(t) = \dot{\theta}_j(t),$$

for all times $t \in \mathbb{R}_{\geq 0}$ and $i, j \in \mathcal{P}_k$, with $k \in \{1, \dots, M\}$. □

Clearly, phase synchronization implies frequency synchronization, while the converse statement typically fails to hold. Notice that

$$\ddot{\theta}_i = \sum_{j=1}^{N} a_{ij} \cos(\theta_j - \theta_i)(\dot{\theta}_j - \dot{\theta}_i),$$

and that the network dynamics can be written in vector form as the linear time-varying system

$$\ddot{\boldsymbol{\theta}}(t) = \mathbf{L}(t)\dot{\boldsymbol{\theta}}(t),$$

where $\mathbf{L}$ is a time-varying matrix satisfying

$$[\mathbf{L}(t)]_{ij} = \begin{cases} a_{ij} \cos(\theta_j(t) - \theta_i(t)), & \text{if } i \neq j, \\ -\sum_{k=1, k\neq i}^{N} a_{ik} \cos(\theta_k(t) - \theta_i(t)), & \text{if } i = j. \end{cases}$$

Finally, we define the characteristic matrix associated with a partition $\mathcal{P}$ of the network nodes, which will be used to derive our synchronization conditions in Section 7.5.2.

Definition 7.5.3 (***Characteristic matrix***)**.** For the network of oscillators $\mathcal{G} = (\mathcal{V}, \mathcal{E})$ and the partition $\mathcal{P} = \{\mathcal{P}_1, \dots, \mathcal{P}_m\}$, the characteristic matrix of $\mathcal{P}$ is $\mathbf{V}_\mathcal{P} \in \mathbb{R}^{N \times M}$, where

$$\mathbf{V}_\mathcal{P} = \begin{bmatrix} \mathbf{v}_1 & \mathbf{v}_2 & \cdots & \mathbf{v}_M \end{bmatrix},$$

and

$$\mathbf{v}_i^\mathsf{T} = \Big[\underbrace{0 \;\; 0 \;\; \cdots \;\; 0}_{\sum_{j=1}^{i-1} |\mathcal{P}_j|} \; \underbrace{1 \;\; 1 \;\; \cdots \;\; 1}_{|\mathcal{P}_i|} \; \underbrace{0 \;\; 0 \;\; \cdots \;\; 0}_{\sum_{j=i+1}^{N} |\mathcal{P}_j|} \Big].$$

□

To conclude this section, we illustrate our setup and the definitions given in this section with an example.

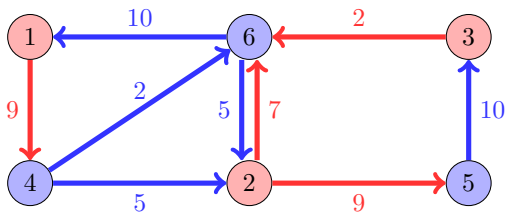

Figure 7.10: Directed network of oscillators. Nodes are partitioned as $\mathcal{P} = \{\mathcal{P}_1, \mathcal{P}_2\}$, with $\mathcal{P}_1 = \{1, 2, 3\}$ and $\mathcal{P}_2 = \{4, 5, 6\}$. Notice that, for each node i of $\mathcal{P}_1$ (resp. $\mathcal{P}_2$), the sum of the weights of all edges (i, j), with $j \in \mathcal{P}_2$ (resp. $j \in \mathcal{P}_1$), is equal. We show in Section 7.5.2 that this is a necessary condition for phase synchronization of the partition $\mathcal{P}$.

Example 7.5.4. ***(Setup and definitions)***
Consider the network of Kuramoto oscillators in Fig. 7.10, with graph $\mathcal{G} = (\mathcal{V}, \mathcal{E})$, $\mathcal{V} = \{1, 2, 3, 4, 5, 6\}$ and partition $\mathcal{P} = \{\mathcal{P}_1, \mathcal{P}_2\}$. The graph $\mathcal{G}$ and the partition $\mathcal{P}$ are described by $\mathbf{A}$ and $\mathbf{V}_\mathcal{P}$ as follows:

$$\mathbf{A} = \begin{bmatrix} 0 & 0 & 0 & 0 & 0 & 10 \\ 0 & 0 & 0 & 5 & 0 & 5 \\ 0 & 0 & 0 & 0 & 10 & 0 \\ 9 & 0 & 0 & 0 & 0 & 0 \\ 0 & 9 & 0 & 0 & 0 & 0 \\ 0 & 7 & 2 & 2 & 0 & 0 \end{bmatrix}, \qquad \mathbf{V}_\mathcal{P} = \begin{bmatrix} 1 & 0 \\ 1 & 0 \\ 1 & 0 \\ 0 & 1 \\ 0 & 1 \\ 0 & 1 \end{bmatrix}.$$

□

7.5.2 Conditions for cluster synchronization

In this section we derive necessary and sufficient conditions ensuring phase (hence frequency) synchronizability of a partition of oscillators. In particular, we show how synchronization of a partition depends both on the interconnection structure and weights, as well as on the oscillators natural frequencies. We make the following technical assumption.

(A1) For the partition $\mathcal{P} = \{\mathcal{P}_1, \dots, \mathcal{P}_M\}$ there exists an ordering of the clusters $\mathcal{P}_i$ and an interval of time $[t_1, t_2]$, with $t_2 > t_1$, such that for all times $t \in [t_1, t_2]$:

$$\max_{i \in \mathcal{P}_1} \dot{\theta}_i > \max_{i \in \mathcal{P}_2} \dot{\theta}_i > \cdots > \max_{i \in \mathcal{P}_m} \dot{\theta}_i.$$

Assumption **(A1)** requires the phases of the oscillators in different clusters to evolve with different frequencies, at least in some interval of time. This assumption is in fact not restrictive, as this is typically the case when the oscillators in different clusters have different natural frequencies. Two cases where this assumption is satisfied are presented in Fig. 7.11. A special case where Assumption **(A1)** is not satisfied is discussed at the end of this section.

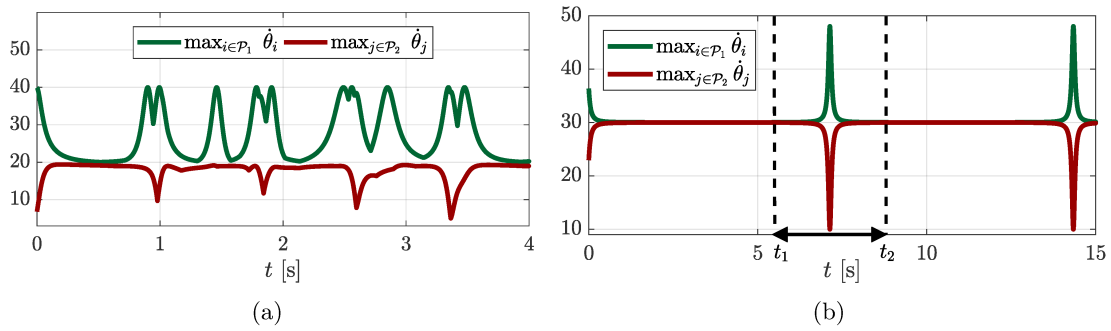

Figure 7.11: For the network in Example 7.10 with natural frequencies $\omega = [30, 30, 30, 10, 10, 10]^\mathsf{T}$ figure **(a)** shows the frequencies of the oscillators in the clusters $\mathcal{P}_1 = \{1, 2, 3\}$ and $\mathcal{P}_2 = \{4, 5, 6\}$. Notice that Assumption **(A1)** is satisfied over the entire time interval. In figure **(b)** we let $\omega = [19, 19, 19, 10, 10, 10]^\mathsf{T}$. Notice that Assumption **(A1)** is satisfied within bounded time intervals, such as $[t_1, t_2]$.

Theorem 7.5.5. ***(Cluster synchronizability)***
For the network of oscillators $\mathcal{G} = (\mathcal{V}, \mathcal{E})$, the partition $\mathcal{P} = \{\mathcal{P}_1, \dots, \mathcal{P}_M\}$ is phase synchronizable if and only if the following conditions are simultaneously satisfied:

(i) the network weights satisfy $\sum_{k\in\mathcal{P}_\ell} a_{ik} - a_{jk} = 0$ for every $i, j \in \mathcal{P}_z$ and $z, \ell \in \{1, \dots, M\}$, with $z \neq \ell$;

(ii) the natural frequencies satisfy $\omega_i = \omega_j$ for every $k \in \{1, \dots, M\}$ and $i, j \in \mathcal{P}_k$.

Proof of Theorem 7.5.5. **(If)** Let $\theta_i = \theta_j$ for all $i, j \in \mathcal{P}_k$, $k = 1, \dots, M$. Let $i, j \in \mathcal{P}_\ell$, and notice that

$$\dot\theta_i - \dot\theta_j = \sum_{z\neq\ell}\sum_{k\in\mathcal{P}_z} a_{ik}\sin(\theta_k - \theta_i) - a_{jk}\sin(\theta_k - \theta_j) = \sum_{z\neq\ell} s_{z\ell} \sum_{k\in\mathcal{P}_z} a_{ik} - a_{jk} = 0,$$

where we have used conditions (i) and (ii), and where s_{zl} is a parameter that depends on the clusters z and ℓ, but not on the indices i, j, k. We conclude that, when conditions (i) and (ii) are satisfied, $\boldsymbol{\theta} \in \mathrm{Im}(\mathbf{V}_\mathcal{P})$ implies $\dot{\boldsymbol{\theta}} \in \mathrm{Im}(\mathbf{V}_\mathcal{P})$, so that the subspace $\mathrm{Im}(\mathbf{V}_\mathcal{P})$ is invariant and the network is phase synchronizable (simply select $\boldsymbol{\theta}(0) \in \mathrm{Im}(\mathbf{V}_\mathcal{P})$).

(Only if) We first show that condition (i) is necessary for phase synchronization. Assume that the network is phase synchronized, and notice that it is also frequency synchronized. Let $i, j \in \mathcal{P}_\ell$. Because the network is phase synchronized, we must have at all times that

$$\begin{aligned} 0 = \ddot\theta_i - \ddot\theta_j &= \sum_{z\neq\ell}\sum_{k\in\mathcal{P}_z} a_{ik}\cos(\theta_k - \theta_i)(\dot\theta_k - \dot\theta_i) + \\ &\quad - \sum_{z\neq\ell}\sum_{k\in\mathcal{P}_z} a_{jk}\cos(\theta_k - \theta_j)(\dot\theta_k - \dot\theta_j) \qquad (7.21a) \\ &= \sum_{z\neq\ell} c_{z\ell}v_{z\ell} \underbrace{\sum_{k\in\mathcal{P}_z} a_{ik} - a_{jk}}_{d_z}, \qquad (7.21b) \end{aligned}$$

where $c_{z\ell}$ and $v_{z\ell}$ depends on the clusters z and ℓ, but not on the indices i, j, k. From Assumption **(A1)**, possibly after reordering the clusters, in some non-trivial interval we have

$$\max_{i\in\mathcal{P}_1}\dot\theta_i > \max_{i\in\mathcal{P}_2}\dot\theta_i > \cdots > \max_{i\in\mathcal{P}_m}\dot\theta_i.$$

Thus, (7.21) implies that, either $d_z = 0$ for all z (thus implying condition (i)), or the functions $c_{zl}v_{zl}$ must be linearly dependent at all times in the interval. Assume by contradiction that the functions $c_{zl}v_{zl}$ are linearly dependent at all times in the above

interval. Then it must hold that

$$\sum_{z\neq\ell} d_z \frac{d^n}{dt^n} c_{z\ell} v_{z\ell} = 0,$$

for every non-negative integer n, where $\frac{d^n}{dt^n}$ denotes n-times differentiation. In other words, not only the functions $c_{zl}v_{zl}$ must be linearly dependent, but also all their derivatives, at some times in the above interval. Let $d_1 \neq 0$ (if $d_1 = 0$, simply select the first non-zero coefficient), and $i, j \notin \mathcal{P}_1$. Notice that, because of assumption **(A1)**, there exists an integer n such that $d_1 \frac{d^N}{dt^N} c_{1\ell} v_{1\ell} \gg d_z \frac{d^n}{dt^n} c_{z\ell} v_{z\ell}$, for all $z \neq 1$. Thus, the functions $c_{zl}v_{zl}$ cannot be linearly dependent. We conclude that statement (i) is necessary for phase synchronization.

We now prove that, when the network is phase synchronized, statement (i) implies statement (ii). This shows that statement (ii) is necessary for phase synchronization. Let the network be phase synchronized, and let $i, j \in \mathcal{P}_\ell$. We have

$$0 = \dot{\theta}_i - \dot{\theta}_j = \omega_i - \omega_j + \sum_{z\neq\ell} s_{z\ell} \underbrace{\sum_{k\in\mathcal{P}_z} a_{ik} - a_{jk}}_{=0},$$

where $s_{z\ell}$ is a parameter that depends on the clusters z and ℓ, but not on the indices i, j, k, and where we have used the fact that statement (i) is necessary for phase synchronization. Thus, $\omega_i = \omega_j$, and statement (ii) is also necessary for phase synchronization. This concludes the proof. ■

Remark 7.5.6. ***(Necessity of assumption (A1))***
Consider a network of oscillators with adjacency matrix

$$\mathbf{A} = \begin{bmatrix} 0 & a_{12} & 0 & 0 \\ a_{21} & 0 & a_{23} & 0 \\ 0 & a_{32} & 0 & a_{34} \\ 0 & 0 & a_{43} & 0 \end{bmatrix},$$

and natural frequencies $\omega_i = \bar{\omega}$ for all $i \in \{1, \ldots, 4\}$. Notice that condition (i) in Theorem 7.5.5 is not satisfied. Let $\theta_1(0) = \theta_2(0)$ and $\theta_3(0) = \theta_4(0) = \theta_1(0) + \pi$, and notice that $\dot{\theta}_i = \bar{\omega}$ at all times and for all $i \in \{1, \ldots, 4\}$ (Assumption **(A1)** is not satisfied). In other words, the partition $\mathcal{P} = \{\mathcal{P}_1, \mathcal{P}_2\}$, with $\mathcal{P}_1 = \{1, 2\}$ and $\mathcal{P}_2 = \{3, 4\}$ is phase synchronized, independently of the interconnection weights among the oscillators. Thus, condition (i) in Theorem may not be necessary when Assumption **(A1)** is not

satisfied.

□

Let $\mathbf{A} \odot \mathbf{B}$ denote the Hadamard product between $\mathbf{A}$ and $\mathbf{B}$ (Horn and Johnson (1990)), and $\mathrm{Im}(\mathbf{V}_{\mathcal{P}})^{\perp}$ the orthogonal subspace to $\mathrm{Im}(\mathbf{V}_{\mathcal{P}})$.

Corollary 7.5.7. ***(Matrix condition for synchronization)***
Condition (i) *in Theorem 7.5.5 is equivalent to* $\bar{\mathbf{V}}_{\mathcal{P}}^{\mathsf{T}} \bar{\mathbf{A}} \mathbf{V}_{\mathcal{P}} = \mathbb{0}_{N-M,N-M}$, *where* $\bar{\mathbf{V}}_{\mathcal{P}} \in \mathbb{R}^{N \times (N-M)}$ *satisfies* $\mathrm{Im}(\bar{\mathbf{V}}_{\mathcal{P}}) = \mathrm{Im}(\mathbf{V}_{\mathcal{P}})^{\perp}$, *and*

$$\bar{\mathbf{A}} = \mathbf{A} - \mathbf{A} \odot \mathbf{V}_{\mathcal{P}} \mathbf{V}_{\mathcal{P}}^{\mathsf{T}}. \tag{7.22}$$

Proof of Corollary 7.5.7. Let $\bar{\mathbf{A}} = [\bar{a}_{ij}]$ and $\mathbf{A} = [a_{ij}]$. Notice that $\bar{a}_{ij} = a_{ij}$ when i and j belong to different clusters, and $\bar{a}_{ij} = 0$ when i and j belong to the same cluster. Thus,

$$[\bar{\mathbf{A}} \mathbf{V}_{\mathcal{P}}]_{ij} = \begin{cases} \sum_{k \in \mathcal{P}_j} a_{ik}, & \text{if } i \notin \mathcal{P}_j, \\ 0, & \text{if } i \in \mathcal{P}_j. \end{cases}$$

Select $\bar{\mathbf{V}}_{\mathcal{P}}$ so that $\bar{\mathbf{V}}_{\mathcal{P}} = [\bar{\mathbf{v}}_1 \cdots \bar{\mathbf{v}}_{N-M}]$ and $\bar{\mathbf{v}}_i^{\mathsf{T}} \mathbf{x} = x_r - x_s$, with $r, s \in \mathcal{P}_\ell$, for a vector $\mathbf{x}$ of compatible dimension. Then,

$$[\bar{\mathbf{V}}_{\mathcal{P}}^{\mathsf{T}} \bar{\mathbf{A}} \mathbf{V}_{\mathcal{P}}]_{ij} = \begin{cases} \sum_{k \in \mathcal{P}_j} a_{rk} - a_{sk}, & r, s \notin \mathcal{P}_j, \\ 0, & r, s \in \mathcal{P}_j, \end{cases}$$

where r, s are the non-zero indices of $\bar{v}_i$. ■

7.5.3 Control of cluster synchronization

In the previous section we derive conditions on the network of oscillators to guarantee phase and frequency synchronization. These conditions are rather stringent, and are typically not satisfied for arbitrary partitions and interconnection weights. To complement our analysis, in this section we develop a control mechanism to modify the oscillators' interconnection weights so as to guarantee synchronization of a given partition. Specifically, we study the following minimization problem:

$$\min_{\boldsymbol{\Delta}} \ \|\boldsymbol{\Delta}\|_F^2 \tag{7.23a}$$

$$\text{s.t. } \bar{\mathbf{V}}_{\mathcal{P}}^{\mathsf{T}} \left[\bar{\mathbf{A}} + \boldsymbol{\Delta} \right] \mathbf{V}_{\mathcal{P}} = \mathbb{0}_{N-M,M} \tag{7.23b}$$

$$\boldsymbol{\Delta} \in \mathcal{H} \tag{7.23c}$$

where $\|\mathbf{\Delta}\|_F$ denotes the Frobenius norm of the matrix $\mathbf{\Delta}$, $\bar{\mathbf{A}}$ is as in (7.22), and $\mathcal{H}$ encodes a desired sparsity pattern of the perturbation matrix $\mathbf{\Delta}$. For example, $\mathcal{H}$ may represent the set of matrices compatible with the graph $\mathcal{G} = (\mathcal{V}, \mathcal{E})$, that is, $\mathcal{H} = \{\mathbf{M} \ : \ \mathbf{M} \in \mathbb{R}^{|\mathcal{V}|\times|\mathcal{V}|} \text{ and } m_{ij} = 0 \text{ if } (i,j) \notin \mathcal{E}\}$. The constraint (7.23b) reflects the invariance condition in Corollary 7.5.7 and, together with condition (ii) in Theorem 7.5.5, ensures synchronization of the partition $\mathcal{P}$. Thus, the minimization problem (7.23) determines the smallest perturbation of the interconnection weights that guarantees synchronization of a partition $\mathcal{P}$ and satisfies desired sparsity constraints. It should be observed that, given the solution $\mathbf{\Delta}^*$ to (7.23), the modified adjacency matrix is $\mathbf{A} + \mathbf{\Delta}^*$ even if the constraint (7.23b) is expressed in terms of $\bar{\mathbf{A}}$. This follows from the fact that connections among nodes of the same cluster do not affect the synchronization properties of the partition $\mathcal{P} = \{\mathcal{P}_1, \dots, \mathcal{P}_M\}$ (see Corollary 7.5.7).

To solve the minimization problem (7.23), we define the following minimization problem by including the sparsity constraints (7.23c) into the cost function:

$$\min_{\mathbf{\Delta}} \ \|\mathbf{\Delta} \oslash \mathbf{H}\|_F^2 \tag{7.24a}$$

$$\text{s.t. } \ \bar{\mathbf{V}}_{\mathcal{P}}^{\mathsf{T}} \left[\bar{\mathbf{A}} + \mathbf{\Delta}\right] \mathbf{V}_{\mathcal{P}} = \mathbb{0}_{N-M,N-M} \tag{7.24b}$$

where $\oslash$ denotes elementwise division, and $\mathbf{H}$ satisfies $h_{ij} = 1$ if there exists a matrix $\mathbf{M} \in \mathcal{H}$ such that $m_{ij} \neq 0$, and $h_{ij} = 0$ otherwise. Clearly, the minimization problems (7.23) and (7.24) are equivalent, in the sense that $\mathbf{\Delta}^*$ is a (feasible) solution to (7.23) if and only if it has finite cost in (7.24).

Theorem 7.5.8. ***(Synchronization via structured perturbation)*** *Let* $\mathbf{T} = [\mathbf{V}_{\mathcal{P}} \ \bar{\mathbf{V}}_{\mathcal{P}}]$, *and let*

$$\begin{bmatrix} \tilde{\mathbf{A}}_{11} & \tilde{\mathbf{A}}_{12} \\ \tilde{\mathbf{A}}_{21} & \tilde{\mathbf{A}}_{22} \end{bmatrix} = \mathbf{T}^{-1} \bar{\mathbf{A}} \mathbf{T}.$$

The minimization problem (7.23) *has a unique solution if and only if there exists a matrix* $\mathbf{\Lambda}$ *satisfying*

$$\mathbf{X} = (\bar{\mathbf{V}}_{\mathcal{P}} \mathbf{\Lambda} \mathbf{V}_{\mathcal{P}}^{\mathsf{T}}) \odot \mathbf{H}, \qquad \textit{and} \qquad \tilde{\mathbf{A}}_{21} = \bar{\mathbf{V}}_{\mathcal{P}}^{\mathsf{T}} \mathbf{X} \mathbf{V}_{\mathcal{P}}.$$

Moreover, if it exists, the solution $\mathbf{\Delta}^*$ *to* (7.23) *is*

$$\mathbf{\Delta}^* = \mathbf{T} \begin{bmatrix} \tilde{\mathbf{\Delta}}_{11}^* & \tilde{\mathbf{\Delta}}_{12}^* \\ \tilde{\mathbf{\Delta}}_{21}^* & \tilde{\mathbf{\Delta}}_{22}^* \end{bmatrix} \mathbf{T}^{-1},$$

where $\tilde{\mathbf{\Delta}}_{11}^* = -\mathbf{V}_{\mathcal{P}}^{\mathsf{T}} \mathbf{X} \mathbf{V}_{\mathcal{P}}$, $\tilde{\mathbf{\Delta}}_{12}^* = -\mathbf{V}_{\mathcal{P}}^{\mathsf{T}} \mathbf{X} \bar{\mathbf{V}}_{\mathcal{P}}$, $\tilde{\mathbf{\Delta}}_{21}^* = -\tilde{\mathbf{A}}_{21}$, *and* $\tilde{\mathbf{\Delta}}_{22}^* = -\bar{\mathbf{V}}_{\mathcal{P}}^{\mathsf{T}} \mathbf{X} \bar{\mathbf{V}}_{\mathcal{P}}$.

Proof of Theorem 7.5.8. Notice that the problem (7.23) is convex, therefore if the solution exists, $\boldsymbol{\Delta}^*$ is unique. We adopt the method of Lagrange multipliers to derive optimality conditions for the problem (7.24). The Lagrangian is

$$\mathcal{L}(\boldsymbol{\Delta}, \boldsymbol{\Lambda}) = \sum_{i=1}^{N}\sum_{j=1}^{N} \delta_{ij}^2 h_{ij}^{-1} + \sum_{i=1}^{M} \boldsymbol{\lambda}_i^\mathsf{T} \bar{\mathbf{V}}_\mathcal{P}^\mathsf{T} (\bar{\mathbf{A}} + \boldsymbol{\Delta}) \mathbf{v}_i,$$

where $\boldsymbol{\Lambda} = [\boldsymbol{\lambda}_1, \dots, \boldsymbol{\lambda}_M] \in \mathbb{R}^{(N-M)\times M}$ is a matrix collecting vectors of Lagrange multipliers, and $\mathbf{v}_i \in \mathbb{R}^N$ is the i-th column of $\mathbf{V}_\mathcal{P}$. By equating the partial derivatives of $\mathcal{L}$ to zero we obtain the following optimality conditions:

$$\frac{\partial \mathcal{L}}{\partial \boldsymbol{\lambda}_i} = 0 \qquad \Longrightarrow \qquad \bar{\mathbf{V}}_\mathcal{P} (\bar{\mathbf{A}} + \boldsymbol{\Delta}) \mathbf{v}_i = \mathbb{0}_N, \tag{7.25a}$$

$$\frac{\partial \mathcal{L}}{\partial \delta_{ij}} = 0 \qquad \Longrightarrow \qquad 2\delta_{ij} h_{ij}^{-1} + \sum_{k=1}^{M} \boldsymbol{\lambda}_k^\mathsf{T} \bar{\mathbf{v}}_i^\mathsf{T} v_{jk} = 0, \tag{7.25b}$$

where $\bar{\mathbf{v}}_i$ is the i-th row of $\bar{\mathbf{V}}_\mathcal{P}$ and v_{jk} is the entry (j,k) of the matrix $\mathbf{V}_\mathcal{P}$. Finally, (7.25a) and (7.25b) can be rewritten in matrix form as

$$\bar{\mathbf{V}}_\mathcal{P}^\mathsf{T} (\bar{\mathbf{A}} + \boldsymbol{\Delta}) \mathbf{V}_\mathcal{P} = \mathbb{0}_{N-M,M}, \tag{7.26a}$$

$$\boldsymbol{\Delta} \oslash \mathbf{H} + \bar{\mathbf{V}}_\mathcal{P} \boldsymbol{\Lambda} \mathbf{V}_\mathcal{P}^\mathsf{T} = \mathbb{0}_N, \tag{7.26b}$$

where a factor 2 of (7.25b) has been included into the Lagrange multipliers. Applying the change of coordinates $\mathbf{T} = [\mathbf{V}_\mathcal{P}\ \bar{\mathbf{V}}_\mathcal{P}]$, $\tilde{\mathbf{A}} = \mathbf{T}\bar{\mathbf{A}}\mathbf{T}^{-1}$ and $\boldsymbol{\Delta} = \mathbf{T}\tilde{\boldsymbol{\Delta}}\mathbf{T}^{-1}$, denoting with $\mathbb{I}_d$ the identity matrix of dimension d, equation (7.26a) becomes

$$\begin{aligned}\bar{\mathbf{V}}_\mathcal{P}^\mathsf{T} \mathbf{T} (\tilde{\mathbf{A}} + \tilde{\boldsymbol{\Delta}}) \mathbf{T}^{-1} \mathbf{V}_\mathcal{P} &= \begin{bmatrix} \mathbb{0}_{N-M,M} & \mathbb{I}_{N-M} \end{bmatrix} \begin{bmatrix} \tilde{\mathbf{A}}_{11} + \tilde{\boldsymbol{\Delta}}_{11} & \tilde{\mathbf{A}}_{12} + \tilde{\boldsymbol{\Delta}}_{12} \\ \tilde{\mathbf{A}}_{21} + \tilde{\boldsymbol{\Delta}}_{21} & \tilde{\mathbf{A}}_{22} + \tilde{\boldsymbol{\Delta}}_{22} \end{bmatrix} \begin{bmatrix} \mathbb{I}_M \\ \mathbb{0}_{N-M,M} \end{bmatrix} \\ &= \mathbb{0}_{N-M,M},\end{aligned}$$

which leads to

$$\tilde{\boldsymbol{\Delta}}_{21}^* = -\tilde{\mathbf{A}}_{21}. \tag{7.27}$$

Equation (7.26b) is equivalent to

$$\boldsymbol{\Delta} + (\bar{\mathbf{V}}_\mathcal{P} \boldsymbol{\Lambda} \mathbf{V}_\mathcal{P}^\mathsf{T}) \odot \mathbf{H} = \mathbb{0}_N,$$

which can be decomposed as follows:

$$\underbrace{\begin{bmatrix}\mathbf{V}_{\mathcal{P}} & \bar{\mathbf{V}}_{\mathcal{P}}\end{bmatrix}}_{\mathbf{T}}\begin{bmatrix}\tilde{\mathbf{\Delta}}_{11} & \tilde{\mathbf{\Delta}}_{12}\\ \tilde{\mathbf{\Delta}}_{21} & \tilde{\mathbf{\Delta}}_{22}\end{bmatrix}\underbrace{\begin{bmatrix}\mathbf{V}_{\mathcal{P}}^{\mathsf{T}}\\ \bar{\mathbf{V}}_{\mathcal{P}}^{\mathsf{T}}\end{bmatrix}}_{\mathbf{T}^{-1}}+(\bar{\mathbf{V}}_{\mathcal{P}}\mathbf{\Lambda}\mathbf{V}_{\mathcal{P}}^{\mathsf{T}})\odot\mathbf{H}=\mathbb{0}_N,$$

from which we obtain

$$\left(\mathbf{V}_{\mathcal{P}}\tilde{\mathbf{\Delta}}_{11}\mathbf{V}_{\mathcal{P}}^{\mathsf{T}}-\bar{\mathbf{V}}_{\mathcal{P}}\tilde{\mathbf{A}}_{12}\mathbf{V}_{\mathcal{P}}^{\mathsf{T}}+\mathbf{V}_{\mathcal{P}}\tilde{\mathbf{\Delta}}_{12}\bar{\mathbf{V}}_{\mathcal{P}}^{\mathsf{T}}+\bar{\mathbf{V}}_{\mathcal{P}}\tilde{\mathbf{\Delta}}_{22}\bar{\mathbf{V}}_{\mathcal{P}}^{\mathsf{T}}\right)+\left(\bar{\mathbf{V}}_{\mathcal{P}}\mathbf{\Lambda}\mathbf{V}_{\mathcal{P}}^{\mathsf{T}}\right)\odot\mathbf{H}=\mathbb{0}_N,\quad(7.28)$$

where the constraint (7.27) has already been incorporated.

Let $\mathbf{X}=(\bar{\mathbf{V}}_{\mathcal{P}}\mathbf{\Lambda}\mathbf{V}_{\mathcal{P}}^{\mathsf{T}})\odot\mathbf{H}$. Recall that $\bar{\mathbf{V}}_{\mathcal{P}}^{\mathsf{T}}\bar{\mathbf{V}}_{\mathcal{P}}=\mathbb{I}_{N-M}$, $\mathbf{V}_{\mathcal{P}}^{\mathsf{T}}\mathbf{V}_{\mathcal{P}}=\mathbb{I}_M$, and $\bar{\mathbf{V}}_{\mathcal{P}}^{\mathsf{T}}\mathbf{V}_{\mathcal{P}}=\mathbb{0}_{N-M,M}$. By pre-multiplying equation (7.28) by $\bar{\mathbf{V}}_{\mathcal{P}}^{\mathsf{T}}$ and post-multiplying it by $\mathbf{V}_{\mathcal{P}}$, we obtain

$$-\tilde{\mathbf{A}}_{21}+\bar{\mathbf{V}}_{\mathcal{P}}^{\mathsf{T}}\mathbf{X}\mathbf{V}_{\mathcal{P}}=\mathbb{0}_{N-M,M},$$

which is a system of linear equations, that can be solved with respect to the unknown $\mathbf{\Lambda}$. Following the same reasoning of above, we can obtain the following other three equations that entirely determine the solution $\tilde{\mathbf{\Delta}}_{11}$, $\tilde{\mathbf{\Delta}}_{12}$, and $\tilde{\mathbf{\Delta}}_{22}$:

$$\begin{aligned}\tilde{\mathbf{\Delta}}_{11}+\mathbf{V}_{\mathcal{P}}^{\mathsf{T}}\mathbf{X}\mathbf{V}_{\mathcal{P}}&=\mathbb{0}_{M,M},\\ \tilde{\mathbf{\Delta}}_{12}+\mathbf{V}_{\mathcal{P}}^{\mathsf{T}}X\bar{\mathbf{V}}_{\mathcal{P}}&=\mathbb{0}_{M,N-M},\\ \tilde{\mathbf{\Delta}}_{22}+\bar{\mathbf{V}}_{\mathcal{P}}^{\mathsf{T}}\mathbf{X}\bar{\mathbf{V}}_{\mathcal{P}}&=\mathbb{0}_{N-M,N-M}.\end{aligned}$$

Finally, the optimal matrix $\mathbf{\Delta}^*$, solution to the problem (7.24), is given in original coordinates as

$$\mathbf{\Delta}^*=\mathbf{T}\begin{bmatrix}\tilde{\mathbf{\Delta}}_{11}^* & \tilde{\mathbf{\Delta}}_{12}^*\\ -\tilde{\mathbf{A}}_{21} & \tilde{\mathbf{\Delta}}_{22}^*\end{bmatrix}\mathbf{T}^{-1}.$$

■

Theorem 7.5.8 characterizes the smallest (measured by the Frobenius norm) structured network perturbation that ensures synchronization of a given partition. When the perturbation is not constrained, that is, $\mathcal{H}=\{\mathbf{M}\ :\ m_{ij}\neq 0 \text{ for all } i \text{ and } j\}$ in (7.23), the optimal perturbation has a straightforward expression.

Corollary 7.5.9. ***(Unconstrained minimization problem)***
Let $\mathcal{H} = \{\mathbf{M} \ : \ m_{ij} \neq 0$ *for all* i *and* $j\}$. *The minimization problem* (7.23) *is always feasible, and its solution is*

$$\boldsymbol{\Delta}^* = -\bar{\mathbf{V}}_{\mathcal{P}}\bar{\mathbf{V}}_{\mathcal{P}}^{\mathsf{T}}\bar{\mathbf{A}}\mathbf{V}_{\mathcal{P}}\mathbf{V}_{\mathcal{P}}^{\mathsf{T}}.$$

Proof of Corollary 7.5.9. First, notice that $h_{ij} = 1$ for all i and j. As a consequence, the optimality equations (7.26) can be rewritten in a way that (7.26a) is unchanged, and (7.26b) becomes:

$$\boldsymbol{\Delta} + \bar{\mathbf{V}}_{\mathcal{P}}\boldsymbol{\Lambda}\mathbf{V}_{\mathcal{P}}^{\mathsf{T}} = \mathbb{0}_N.$$

We now pre- and post-multiply both sides by $\bar{\mathbf{V}}_{\mathcal{P}}^{\mathsf{T}}$ and $\mathbf{V}_{\mathcal{P}}$, respectively, and obtain

$$\begin{aligned}\boldsymbol{\Lambda} &= \bar{\mathbf{V}}_{\mathcal{P}}^{\mathsf{T}}\bar{\mathbf{A}}\mathbf{V}_{\mathcal{P}},\\ \boldsymbol{\Delta}^* &= -\bar{\mathbf{V}}_{\mathcal{P}}\bar{\mathbf{V}}_{\mathcal{P}}^{\mathsf{T}}\bar{\mathbf{A}}\mathbf{V}_{\mathcal{P}}\mathbf{V}_{\mathcal{P}}^{\mathsf{T}},\end{aligned}$$

where we use (7.26a), $\mathbf{V}_{\mathcal{P}}^{\mathsf{T}}\mathbf{V}_{\mathcal{P}} = \mathbb{I}_M$, and $\bar{\mathbf{V}}_{\mathcal{P}}^{\mathsf{T}}\bar{\mathbf{V}}_{\mathcal{P}} = \mathbb{I}_{N-M}$. ■

We now present an example where we adjust the network weights to ensure synchronization of a desired partition.

Example 7.5.10. ***(Enforcing synchronization of a partition)***
Consider the network in Figure 7.12 **(a)**. The dashed edges and the solid edges represent constrained and unconstrained edges, respectively. The corresponding matrices $\bar{\mathbf{A}}$ and $\mathbf{H}$ read as

$$\bar{\mathbf{A}} = \begin{bmatrix} 0 & 0 & 0 & 0 & 0 & 12\\ 0 & 0 & 0 & 5 & 0 & 5\\ 0 & 0 & 0 & 0 & 10 & 0\\ 9 & 0 & 0 & 0 & 0 & 0\\ 0 & 9 & 0 & 0 & 0 & 0\\ 0 & 7 & 2 & 0 & 0 & 0 \end{bmatrix}, \qquad \mathbf{H} = \begin{bmatrix} 0 & 1 & 1 & 0 & 0 & 0\\ 1 & 0 & 1 & 0 & 1 & 0\\ 1 & 1 & 0 & 0 & 1 & 1\\ 0 & 1 & 1 & 0 & 1 & 1\\ 1 & 1 & 1 & 1 & 0 & 1\\ 1 & 0 & 0 & 1 & 1 & 0 \end{bmatrix}.$$

Notice that $\mathbf{H}$ allows only a subset of interconnections to be modified, specifically, those corresponding to its unit entries.

It can be shown that, because condition (i) in Theorem 7.5.5 is not satisfied (equivalently $\bar{\mathbf{V}}_{\mathcal{P}}^{\mathsf{T}}\bar{\mathbf{A}}\mathbf{V}_{\mathcal{P}} \neq \mathbb{0}_{N-M,M}$), the network is not phase synchronizable (see Figures 7.12 **(b)** and **(c)** for the evolution of the oscillators' phases and frequencies). From Theorem 7.5.8

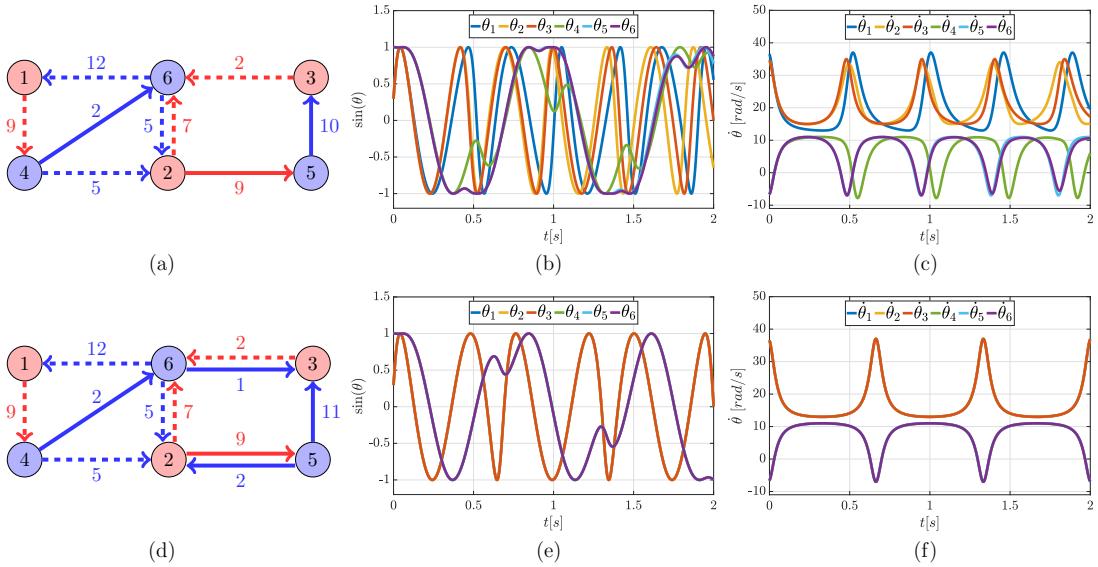

Figure 7.12: Figure **(a)** shows the network in Example 7.5.10, where the dashed (resp. solid) edges correspond to the zero (resp. unit) entries of $\mathbf{H}$. The partition $\mathcal{P} = \{\mathcal{P}_1, \mathcal{P}_2\}$, with $\mathcal{P}_1 = \{1, 2, 3\}$ and $\mathcal{P}_2 = \{4, 5, 6\}$, is not synchronizable (see Theorem 7.5.5). This can be seen, for instance, by verifying that the weight of the incoming edge to nodes 1 and 2 is different. Figures **(b)** and **(c)** show a particular evolution of the phases and frequencies of the oscillators. Figure **(d)** shows the modified network as obtained from Theorem 7.5.8. It can be verified that condition (i) in Theorem 7.5.5 is now verified, and the partition $\mathcal{P}$ is synchronizable when the natural frequencies are selected as in condition (ii) in Theorem 7.5.5. Particular evolutions of the phases and frequencies of the oscillators are in Figure **(e)** and **(f)**, where the synchronization pattern is clearly visible.

we obtain the optimal perturbation that ensures synchronization, which leads to the network in Figure 7.12 **(d)**. Notice that the network in Figure 7.12 **(d)** satisfies condition (i) in Theorem 7.5.5. In fact, when the natural frequencies are equal within each cluster (condition (ii) in Theorem 7.5.5), the clusters evolve cohesively; see Figures 7.12 **(e)** and **(f)**. □

7.6 Conclusion

In this chapter we addressed the problem of characterizing different conditions of synchronization within a network of Kuramoto oscillators. First, motivated by applications in biological field and by the study of power network dynamics, we have investigated complete synchronization within oscillators, coupled through a distance-dependent kernel function. In this framework, a critical bound was derived for strength global coupling among nodes, in order to achieve asymptotic frequency synchronization and phase cohesiveness. This bound has been validated in terms of correctness and accuracy by means

of numerical simulations on a general spatial configuration, where the interacting agents are distributed on a spherical domain. Statistical figures have been obtained that confirm the validity of the approach. A trade-off between the value of the coupling strength and the probability of convergence was suggested to relax the strength bound. Then, the complete synchronization in a configuration where two populations of oscillators (with different kernel parameters) interact has been considered. In such scenario, we have characterized the new synchronization frequency, when compared with the one obtained when only one population is considered.

Secondly, we focused on cluster synchronization in networks of Kuramoto oscillators, by means of phase cohesiveness among nodes in the same group. Specifically, we characterized the formation of such clusters as a function of the network weights and oscillators intrinsic parameters. We showed how cluster synchronization depends on a graded combination of strong intra-cluster and weak inter-cluster connections, similarity of the natural frequencies of the oscillators within each cluster, and heterogeneity of the natural frequencies of coupled oscillators belonging to different groups.

Finally, we considered clusters of Kuramoto oscillators, which are perfectly phase-synchronized. We adopted tools from linear algebra and graph theory to characterize network conditions enabling the formation of a given synchronization pattern. Additionally, we developed a control mechanism to modify the edges of a network to ensure the formation of desired clusters. Our control method is optimal, as it determines the smallest perturbation (measured in terms of Frobenius norm) for a desired synchronization pattern that is compatible with a pre-specified set of structural constraints.

8

Conclusions

Throughout this work, we made an excursus on the intricate tie existing among the activity of the human brain, the functioning of mitochondria in our cells, and the continuous requirement of energy that governs this complex relationship. We exploit several theoretical and empirical tools in order to explore this topic from various points of view and to highlight the power of computational models as an helpful instrument to reproduce the basic principles that lie under observed behaviors.

In this chapter we hence take stock of the results presented in the previous chapters, and we propose some research lines, for future developments.

First, we have introduced the main evidences suggesting the existence of a strong relation between the brain activity and a proper working effective activity of the house of power of our body, namely the mitochondria. Researches on neurodegenerative diseases have played a main role in the unearthing this reciprocal dependence. The coexistence of both mitochondrial and neuronal dysfunction have been in fact found in various neurological disorders, such as Parkinson's, or Huntinghton's Diseases (Chapter 1).

After a description of the biological background involving mitochondria and mitochondrial dynamics (that refers to the continuous change of organelles' shape), we have proposed a mathematical model useful to reproduce the main processes involved in mitochondrial dynamics (fusion and fission), together with other fundamental phenomena,

such as mitophagy, biogenesis, and damage. Most importantly, we have introduced a bioenergetic regulation of this dynamical systems by means of a feedback control effected by the available quantity of ATP level within the cell (Chapters 2 and 3).

From Chapter 4, the objective of our analysis shifted and focused on the description of brain activity during both conditions of rest or task-doing. We introduced the characterization of the brain as a graph of nodes at various scales, whose dynamics depend on the communication among agents. Thus, we reported some mathematical tools used to characterize the brain networks' topology, both anatomically and functionally, and we discussed the existence of different non-invasive techniques implemented to record experimental signals from the brain (see Chapter 5). Specifically, part of the experimental contribution of this manuscript can be found in Chapter 5, where we investigated different hypotheses on the role of ongoing activity of the brain during rest, and on the questionable relationship between different measurement techniques, such as fMRI and MEG.

In Chapter 6 instead, we proposed a different approach to characterize the activity of the brain, as the behavior emerged from a population of oscillatory elements. To this aim, we explored the oscillatory properties of an experimental dataset of fMRI signals, in order to define the main features characterising the observed resting-state fluctuations and to quantify the synchronization level among brain areas during time. These main features have been used later to guide the simulation of a synthetic brain network, described by an extended version of the classical Kuramoto model, whose design and analysis are one contribution of this work.

Attracted by the large amount of various behaviors (from complete synchronization, to chaos, passing through a metastability condition), describable by different parametrizations of Kuramoto model, we devoted Chapter 7 to report our analytical results on the analysis and control of networks of Kuramoto oscillators. Specifically, we focused on the network and intrinsic conditions required to achieve a clustered configuration, where groups of nodes evolve cohesively with the members of the same group, but differently from the others.
In light of the fact that the human brain may be described as a network of brain areas, characterized by high level of clustering and modularity, this theoretical analysis can be very helpful to investigate the open questions on the activity of brain networks.

Despite the large amount of effort used by scientists from all-over the world to explore the human brain and its complex activity in the last decades, a lot of observed behaviors remain mysteries for our minds. The actual role of the resting-state fluctuations, as well as the (possible) relationship between RSNs and behavioral networks is not fully understood, so far. Different hypotheses have been tested through computational models

at different time and spatial scales, but a clear answer has not been formulated. Even more open problems regard the bidirectional relationship between brain and mitochondria, because of the serious difficulties existing to obtain empirical data required to analyze and investigate controversial theories.

We believe that our population modeling approach may be a suitable tool not only to analyze complex systems, as population of mitochondria, or ensembles of neurons, but also to predict and control such systems. So far, Deep Brain Stimulation (DBS) methods are sometimes applied during the course of PD; although it may ease symptoms, it has not been proven to change the underlying course of disease, and many mechanisms are still unknown.

The formulation of network-based hypotheses, coupled with the growing potential to modulate neural function across many spatial (and population) scales, brings with it important engineering challenges. Network control indeed combines estimates of network connectivity with models of system dynamics to predict the optimal location to inject energy in order to push the system toward a desired target state or target dynamics. Through this theory, we may have the opportunity to better understand cognitive control, optimize stimulation for neurological disorders, and inform surgical or stimulation-based interventions. Hence, future efforts should be spent in using network population models for furnishing even more concrete instruments to predict and treat neurological diseases.

From our point of view, the collaboration among different research fields is the most promising way in order to achieve new insights about one of the most broaden mystery of our human being. Thus, our interest on integrating the discipline of automation engineering with system biology, neurology, and medicine is becoming even more relevant for our research.

A

Appendix

Contents

A.1 Nullclines (3.10) analysis

In this section we provide some computational details, helpful to derive interesting observations on the dynamic evolution of systems (3.1). In particular, in this place we report the analysis of the sign of the nullclines.

$\mathbf{x_f}$-nullcline

$$\frac{\partial \bar{x}_\mathrm{f}}{\partial \bar{x}_\mathrm{h}} = \frac{\varphi \bar{x}_\mathrm{d}}{\psi_1 + \psi_2} \geq 0, \qquad \frac{\partial \bar{x}_\mathrm{f}}{\partial \bar{x}_\mathrm{d}} = \frac{\varphi \bar{x}_\mathrm{h}}{\psi_1 + \psi_2} \geq 0$$

x_ATP-nullcline

$$\frac{\partial \bar{x}_\mathrm{ATP}}{\partial \bar{x}_\mathrm{h}} = \left(\beta + \frac{\eta\varphi \bar{x}_\mathrm{d}}{\psi_1 + \psi_2}\right)\frac{1}{\bar{u}} \geq 0, \quad \frac{\partial \bar{x}_\mathrm{ATP}}{\partial \bar{x}_\mathrm{d}} = \left(\varepsilon + \frac{\eta\varphi \bar{x}_\mathrm{h}}{\psi_1 + \psi_2}\right)\frac{1}{\bar{u}} \geq 0,$$
$$\frac{\partial \bar{x}_\mathrm{ATP}}{\partial \bar{x}_\mathrm{f}} = \frac{\eta}{\bar{u}} \geq 0, \qquad \frac{\partial \bar{x}_\mathrm{ATP}}{\partial \bar{u}} = -\left(\beta \bar{x}_\mathrm{h} + \varepsilon \bar{x}_\mathrm{d} + \eta\varphi \frac{\bar{x}_\mathrm{h}\bar{x}_\mathrm{d}}{\psi_1 + \psi_2}\right)\frac{1}{\bar{u}^2} \leq 0$$

$\mathbf{x_d}$-nullcline

$$\frac{\partial \bar{x}_\mathrm{d}}{\partial \bar{x}_\mathrm{h}} = \frac{(\psi_1 + \psi_2)^2 \, \delta\mu}{\left[(\psi_1 + \psi_2)\,\mu + \varphi\psi_1 \bar{x}_\mathrm{h}\right]^2} > 0$$
$$\lim_{\bar{x}_\mathrm{h} \to +\infty} \bar{x}_\mathrm{d} = (\psi_1 + \psi_2)\,\frac{\delta}{\varphi\psi_1}$$

$\mathbf{x_h}$-nullcline

$$\lim_{\bar{x}_\mathrm{d} \to 0} \bar{x}_\mathrm{h} = \frac{u\,(\alpha_1 - \delta k)}{\delta\beta}, \qquad \lim_{\bar{x}_\mathrm{d} \to +\infty} \bar{x}_\mathrm{h} = -\,(\psi_1 + \psi_2)\,\frac{\varepsilon}{\varphi\eta} < 0$$

A.2 Measures to define dynamic functional networks in the brain

Cross-Coherence While correlation is defined in time domain, **cross-coeherence** (Coh) measures relationships in frequency domain. Specifically, the squared coefficient of coherence can be interpreted as the proportion of the power in one of the two time series (at a selected frequency), which can be explained by its linear regression to the other time course. At frequency f, the coherence between any two time series $x_i(\cdot)$ and $x_j(\cdot)$ is given by

$$\mathrm{Coh}_{x_i x_j}(f) = \left| \frac{S_{x_i x_j}(f)}{\sqrt{S_{x_i x_i}(f) S_{x_j x_j}(f)}} \right|,$$

where $S_{x_i x_i}(\cdot)$ and $S_{x_j x_j}(\cdot)$ are power spectral densities of signals x_i and x_j, respectively, and $S_{x_i x_j}(\cdot)$ is the cross-spectral density among the signals. Coherence is an even positive function ($\mathrm{Coh}_{x_i x_j}(-f) = \mathrm{Coh}_{x_i x_j}(f)$), bounded within 0 and 1.

Independent component analysis (ICA) An other measure used to estimate functional networks during resting-state consists in the **independent component analysis** (ICA), which is a computational technique for identifying hidden statistically independent sources from multivariate data. The assumption under this approach is that each signal is the result of the linear combination of independent spatial signals $\mathrm{IC}_k(t)$, $k = 1, \ldots, K$:

$$x_i(t) = \sum_{k=1}^{K} c_{i,k} \mathrm{IC}_k(t), \qquad \forall\, i = 1, \ldots, N,$$

where K is the number of sources that generate independent signals. As ICA does not reduce the dimension of the data ($K = N$), before ICA it is usually applied a *principal components analysis* (PCA), in order to reduce the complexity of the data, by selecting the $K \leq N$ components, which explain most of the variance of the data. Specifically, ICA can be applied both temporal or spatially, meaning that it is evaluated optimizing temporal or spatial independence between components, respectively. While spatial ICA maps areas that are consistently active at the same time, temporal ICA finds the regions in the brain that mostly contribute to a given temporal signal.

Mutual information (MI) An other functional connectivity measure, which, unlike the previous ones, is non-linear, is the **mutual information** (MI), which is a simple but robust method of detecting shared information between two signals. It is computed

based on the distributions of values within variables and the joint distribution of two (or more) variables

$$\mathrm{MI}_{x_i x_j} = h(x_i) + h(x_j) - h(x_i, x_j),$$

where $h(x(\cdot))$ is the entrophy od $x(\cdot)$, and $h(x, y)$ is the joined entropy between $x(\cdot)$ and $y(\cdot)$. The main advantages of MI are that, as mentioned before, it can detect different kinds of relation, both linear and non-linear, and that it has a long tradition of use and development in engineering and information technology. However some drawbacks have to be mentioned. First of all, it does not provide information as to whether a relationship linear or non-linear, or positive or negative. Furthermore, MI can be very computationally intensive, particularly if used for exploratory analyses, and it can be sensitive to the discretization method used to estimate it. Finally, more importantly, it is not linked to a clear neurophysiological interpretation (Cohen (2014)).

Granger causality (GC) When a directed connectivity is needed, **Granger causality** (GC) technique can be implemented to infer FC. Specifically, GC tests whether variance in one signal can be predicted from variance in another signal earlier in time. The general concept of Granger causality is based on the core idea that the cause precedes its effect. One possible approach to quantify this notion refers to the principle of predictability, that is: a variable x_i Granger-causes another variable x_j of the same multivariate process, if the knowledge of x_i's past improves the forecast of x_j (Granger (1969)). The main advantages of Granger prediction are that it tests for and can dissociate directional connectivity; however it is sensitive to violations of stationarity, and it can be computationally time-consuming to perform.

A.3 Other computational models to simulate RS dynamics in the brain

Far from being an exhaustive collection of computational models used to describe the dynamics of brain networks, we report here a set of models that we consider as a good sample of heterogeneous systems, used to describe empirical functional data in resting-state.

A.3.1 Rulkov neuron model (RN)

Rulkov neuron model (Rulkov (2001)) is a discrete-time bursting model, where each node's dynamics is described by a two dimensional state $\mathbf{x}_i = [\ x_{i,1} \quad x_{i,2}\ ]^\mathsf{T}$, whose dynamics obeys the following equation:

$$x_{i,1}(t+1) = \frac{\alpha_i}{1+(x_{i,1}(t))^2} + x_{i,2}(t) + C\sum_{j=1}^{N} a_{ij}(t-\upsilon_{ij})$$
$$x_{i,2}(t+1) = x_{i,2}(t) - \gamma x_{i,1}(t) - \beta.$$

This computational model is usually adopted to describe the dynamics of a single neuron. Specifically, $x_{i,1}$ represents the membrane potential (fast variable), while $x_{i,2}$ is the slow dynamics, modulated by the slower ions currents. However, in this place, we consider each node representative for an entire ROI, whose elements are characterized by a very similar bursting pattern. The spiking time of the fast variable is parametrized by the parameter α_i, that causes irregular sequences of spikes if bounded within $[4.1,\ 4.3]$. Parameters β and γ, used to describe the slow dynamics, are usually set at a very slow value (e.g. 0.001). C, a_{ij} and υ_{ij} as the same meaning as in Equation (6.6a).

A.3.2 FitzHugh-Nagumo model (FHN)

FitzHugh-Nagumo model (FitzHugh (1961); Nagumo et al. (1962)) is a continuous-time bursting model that simplifies the previous Hodgkin-Huxley model (Hodgkin and Huxley (1952)). As the Rulkov neuron model, it is usually used to describe the dynamics of each single neuron through a two dimensional state variable $\mathbf{v}_i = [\ v_{i,1} \quad v_{i,2}\ ]^\mathsf{T}$, which models the fast membrane potential's dynamics ($v_{i,1}$), and the slow recovery potential ($v_{i,2}$). In

particular, for each $i = 1, \dots, N$, the system dynamics obeys the following law:

$$\dot{v}_{i,1}(t) = c\left[v_{i,2}(t) + v_{i,1}(t) - \frac{v_{i,1}(t)^3}{3}\right] + C\sum_{j=1}^{N}(v_{i,1}(t) - v_{j,1}(t - \upsilon_{ij}))$$
$$\dot{v}_{i,2}(t) = -\frac{v_{i,1}(t) - a + bv_{i,2}(t)}{c},$$

where C, a_{ij}, and υ_{ij} have the same meaning as before, and a, b, and c are other tunable parameters.

For what concerns RN and FHN models, the phase is used to be defined through the local maxima of the slow variables (which correspond to the onset of bursting behavior, or peak in the fast variable) as follows:

$$\theta(t) := 2\pi\ell + 2\pi\frac{t - t_\ell}{t_{\ell+1} - t_\ell}, \qquad t_\ell \le t \le t_{\ell+1}, \tag{A.6}$$

where t_ℓ is the instant of time at which the ℓ-th burst begins. A definition of the bursting frequency comes directly from (A.6) and is given by

$$\omega := \lim_{t\to+\infty}\frac{\theta(t) - \theta(0)}{t}.$$

A.3.3 Greenberg-Hastings model (GH)

Greenberg-Hastings model (Greenberg and Hastings (1978)) differs from all the previously introduced ones, since it is a simple discrete state dynamical model, where at each node $i = 1, \dots, N$ it is assigned one of three states: quiescent Q, excited E, or refractory R, such that each state variable x_i has a discrete domain: $x_i(t) \in \{Q, E, R\}$. The transition rules, which determines the dynamics can be summarized as follows:

t1. $Q \to E$ with probability $r_1 \sim 1/N$ or if $\sum_{j=1}^{N}\tilde{a}_{ij}\mathbf{1}_{x_j}(S) > T_a$, otherwise $Q \to Q$,

t2. $E \to R$ always,

t3. $R \to Q$ with probability $r_2 \sim 100\ r_1$,

where $\tilde{a}_{ij}$ is equal to a_{ij} (anatomical coupling) if the Euclidean distance d_{ij} among nodes i and j is less than a threshold $T_d \ge 0$, and zero otherwise, $T_a \ge 0$ is a constant threshold, which regulates the activation rate, and $\mathbf{1}_v(\cdot)$ is the indicator function of variable v,

defined as:

$$\mathbf{1}_v(x) = \begin{cases} 1, & \text{if } v = x, \\ 0, & \text{if } v \neq x. \end{cases}$$

Following the same workflow of Haimovici et al. (2013), for the numerical simulation, the time series of each node is binarized into $\tilde{x}_i(t)$, assigning $\tilde{x}_i(t) = 1$, if $x_i(t) = E$, and $\tilde{x}_i(t) = 0$, otherwise. Then, it is convolved with a standard hemodynamic response function (Friston et al. (1995)), to mime the fMRI signal.

Although being very simple, this model has been proved to be very powerful to describe brain networks dynamics, when it works near a critical point (Haimovici et al. (2013)). It is worth noting that, even though the delay term υ_{ij} is not directly included into the dynamics, the threshold T_d can be tuned in order to avoid the communication among distant areas. In summary, the tunable parameters of this model are the transition probability r_1 and r_2, and the two threshold T_d and T_a.

A.4 Measures and algorithm in brain networks analysis

A.4.1 Hierarchical algorithms

Agglomerative hierarchical clustering Agglomerative hierarchical clustering starts setting each data point in a separate cluster and it aggregates points into larger sets of similar observations. As a similarity measure, it is often used the FC map derived from the time series. Given a similarity matrix, this algorithm groups nodes such that the similarity within clusters is high and the similarity between clusters is low, usually by implementing a greedy approach. The result of this method is a tree-like structure (called dendrogram), which describes the hierarchical relations between clusters. Different levels of this tree hence define different number of clusters. Despite being very popular and flexible, this algorithm has the disadvantage of being biased toward grouping together the core nodes of a community at the expense of peripheral nodes (Newman and Girvan (2004)).

Divisive hierarchical clustering Divisive hierarchical clustering is a method proposed in Girvan and Newman (2002), which starts with a connectivity matrix, and defines communities based on the ordered removal of edges according to their betweenness centrality, evaluated as the number of the shortest paths that go through the considered edge. Removing the edge with the highest betweenness centrality at each step of the algorithm causes the graph to fragment, and the connected components that remain represent putative modules of the network. As with hierarchical clustering, the result is a dendrogram that reveals the nested community structure of the graph. Each level of the dendrogram corresponds to a point at which the removal of an edge fragments one of the graph's components.

Hierarchical clustering algorithms however do not give any information to determine whether the clustering solution obtained at one level is more valid or reliable than another. To overcome this problem, in Newman and Girvan (2004) a modularity-based approach has been proposed.

Modularity clustering The *modularity index* Q can be evaluated through the following equation, once a nodes partition $\mathcal{P}$ has been defined:

$$Q(\mathcal{P}) = \frac{1}{\ell} \sum_{i=1}^{N} \sum_{j=1}^{N} \left[a_{ij} - \frac{d_i d_j}{\ell} \right] \delta(c_i, c_j),$$

where a_{ij} is the entry $(i,\ j)$ of the (weighted) adjacency matrix of the network, c_i and c_j are the clusters containing nodes i and j, respectively, $\delta(c_i,\ c_j)$ is the Kronecker delta function and equals one if $c_i = c_j$, and zero otherwise, and finally ℓ and d_i are the number of links and the node degree indices, defined as

$$\ell = \sum_{i,j=1}^{N} a_{ij}, \qquad\qquad d_i = \sum_{j=1}^{N} a_{ij}, \quad \forall i = 1, \ldots, N.$$

In case of weighted graph, ℓ is the sum of the weights of all links, and d_i is the weighted degree (or *strength*) of node i. Similarly, a *directed modularity* is defined as (Leicht and Newman (2008))

$$Q^{\rightarrow}(\mathcal{P}) = \frac{1}{\ell} \sum_{i,j=1}^{N} \left[a_{ij} - \frac{d_i^{\text{out}} d_j^{\text{in}}}{\ell} \right] \delta(c_i, c_j),$$

where d_i^{out} is the sum over the weights of all the edges that exit from node i, and d_j^{in} is the sum over the weights of all the edges that enter into node j.

Among several computational algorithms that have been proposed to implement a method to identify directly the best partition of a graph, the Louvain algorithm (Blondel et al. (2008)) is one of the most widely used methods, thanks to its computational low cost and accuracy.

A.4.2 Centroid-based clustering

The most common centroid-based clustering method is k-means (Lloyd (1982)), an iterative algorithm aimed to define $1 \leq K \leq N$ centroids (one for each cluster) and to assign each node to the cluster which has the *nearest* (with respect to a predefined distance measure) centroid. Specifically, it is initialized by guessing K centroids positions, and assigning each node to the group that has the closest centroid. When all nodes have been assigned, it updates the positions of the K centroids, and repeat the assignment. These steps are repeated until the centroid position (or the nodes' assignment) does not move any more. The need of a priori information about the number of cluster K is one of the main drawbacks of this algorithm. However some quality measures, like the *silhouette* measure (Rousseeuw (1987)), can be used to evaluate the optimal number of community within a graph, given a measure of similarity (or dissimilarity) used during the clusterization steps. The second limitation of k-means is the sensitivity of the result with respect to the initial guess of the centroids' position. Thus, a typical approach to overcome this limitation is to re-run the algorithm multiple times, starting with different

initial clusters to reduce the possibilities of local solution, and then choose the best configuration, with respect to a selected performance function.

A.5 Additional results of Chapter 5

A.6 Inter-subject FC analysis

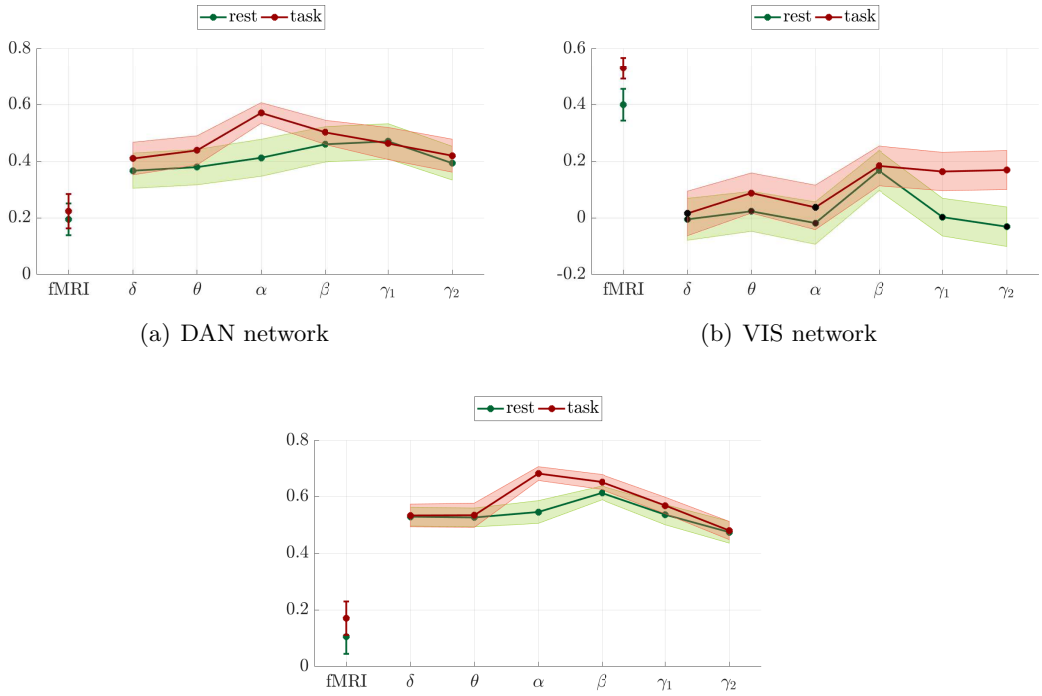

(a) DAN network

(b) VIS network

(c) DAN-VIS network

Figure A.1: Intra-modality coherence among subjects: average and confidence interval of the Pearson's correlation coefficients evaluated between the vectorized **FC** of each pair of subjects in the DAN network **(a)**, VIS network **(b)**, and DAN-VIS cross-network **(c)**. Colored markers represents significantly positive (or negative) values, while black markers stand for non significant results.

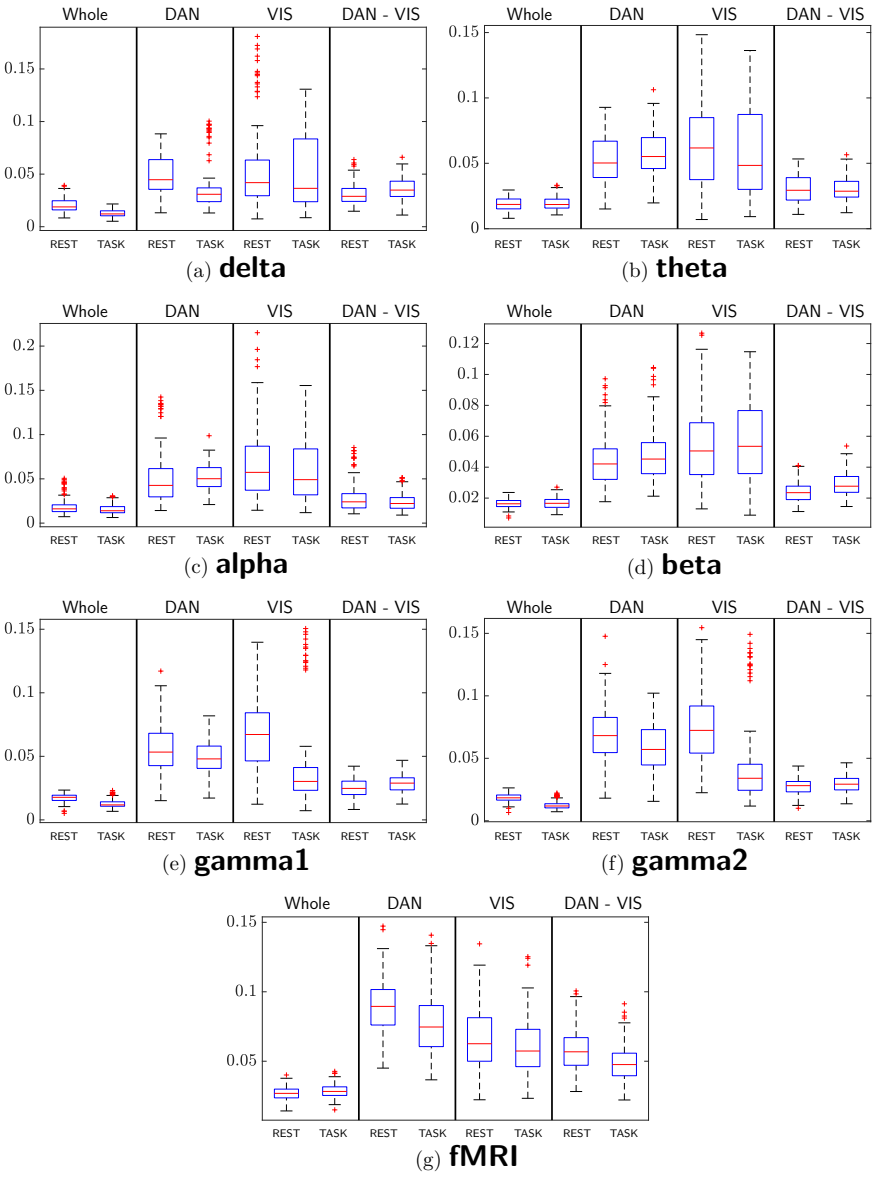

Figure A.2: Boxplots of the Frobenius norm of the difference among each pair of **FC** matrices (normalized w.r.t. to the maximum value of the entries among all the population) derived from different subjects, normalized by the number of the entries of the matrix.

A.6.1 Network matrices density

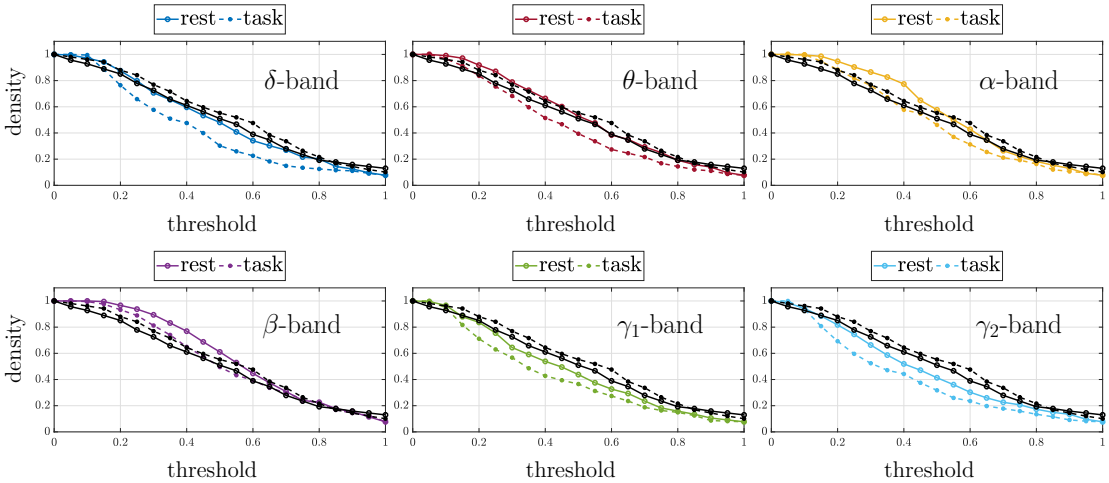

Figure A.3: Density of the **FC** sub-matrices related to the DAN sub-network, estimated as described in Section 5.2.1, as a function of the threshold vector $\mathbf{t_r}$. Each plot represents the density of $\mathbf{FC}^{\mathsf{D}}_{\mathrm{MEG}}$ of a specific frequency band evaluated during rest (colored continuous line) and during task (colored dotted line), compared with the density of $\mathbf{FC}^{\mathsf{D}}_{\mathrm{fMRI}}(\mathsf{R})$ (black continuous line) and $\mathbf{FC}^{\mathsf{D}}_{\mathrm{fMRI}}(\mathsf{T})$ (black dotted line).

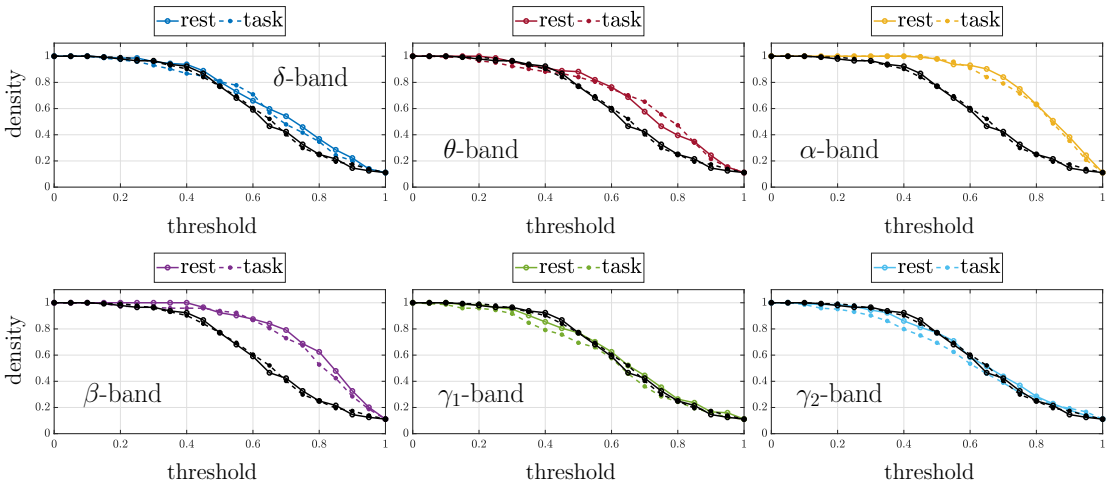

Figure A.4: Density of the **FC** sub-matrices related to the VIS sub-network, estimated as described in Section 5.2.1, as a function of the threshold vector $\mathbf{t_r}$. Each plot represents the density of $\mathbf{FC}^{\mathsf{V}}_{\mathrm{MEG}}$ of a specific frequency band evaluated during rest (colored continuous line) and during task (colored dotted line), compared with the density of $\mathbf{FC}^{\mathsf{V}}_{\mathrm{fMRI}}(\mathsf{R})$ (black continuous line) and $\mathbf{FC}^{\mathsf{V}}_{\mathrm{fMRI}}(\mathsf{T})$ (black dotted line).

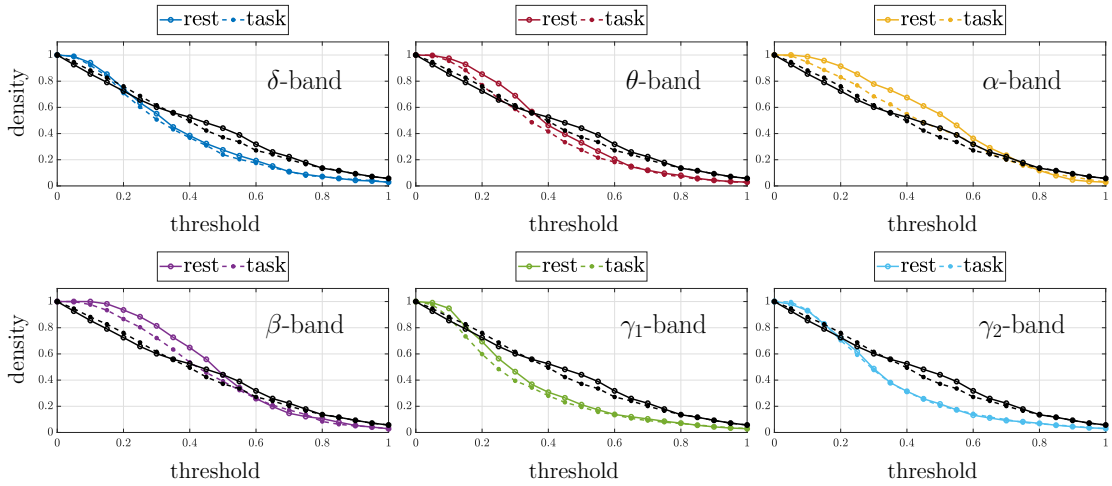

Figure A.5: Density of the **FC** sub-matrices related to the DAN-VIS cross-network, estimated as described in Section 5.2.1, as a function of the threshold vector $\mathbf{t_r}$. Each plot represents the density of $\mathbf{FC}^{\mathsf{DV}}_{\mathrm{MEG}}$ of a specific frequency band evaluated during rest (colored continuous line) and during task (colored dotted line), compared with the density of $\mathbf{FC}^{\mathsf{DV}}_{\mathrm{fMRI}}(\mathsf{R})$ (black continuous line) and $\mathbf{FC}^{\mathsf{DV}}_{\mathrm{fMRI}}(\mathsf{T})$ (black dotted line).

A.6.2 Hamming distance between FC matrices

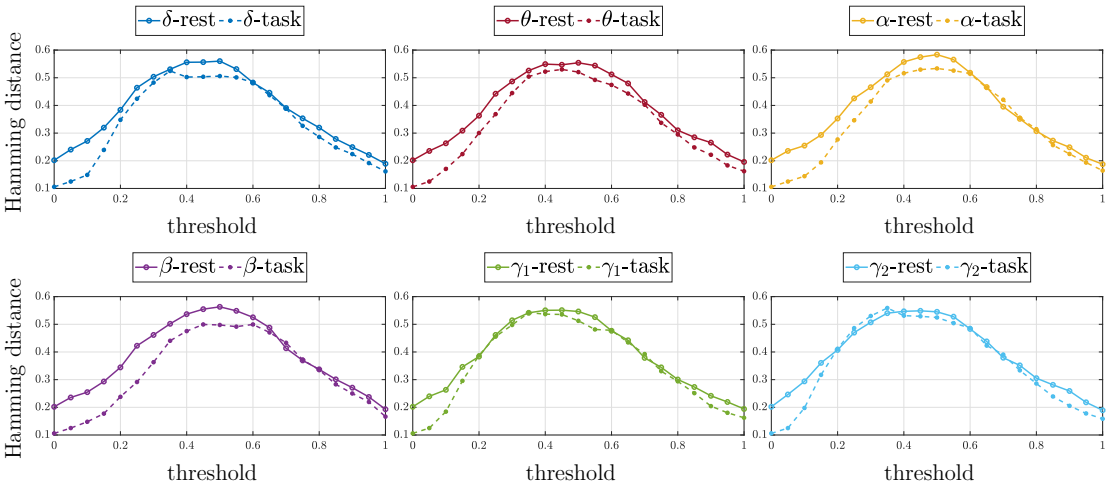

Figure A.6: Hamming distance between $\mathbf{FC}^{\mathrm{D}}_{\mathrm{fMRI}}$ and $\mathbf{FC}^{\mathrm{D}}_{\mathrm{MEG}}$ in resting-state (continuous line) and during task (dashed line), evaluated as described in Section 5.2.1, as a function of the threshold vector $\mathbf{t_r}$. The different boxes and colors represent different frequency bands. In this figure, the case of the DAN sub-network is represented.

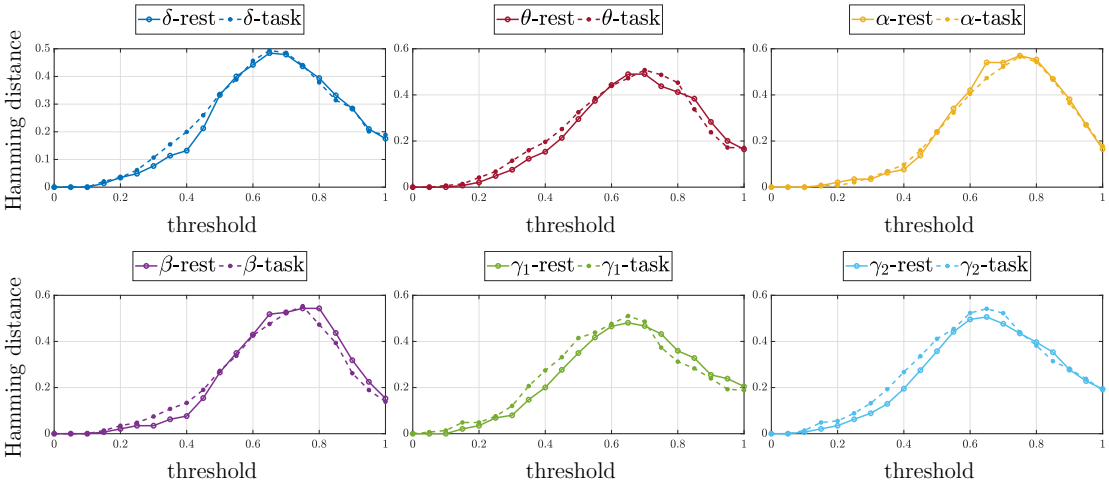

Figure A.7: Hamming distance between $\mathbf{FC}^{\mathrm{V}}_{\mathrm{fMRI}}$ and $\mathbf{FC}^{\mathrm{V}}_{\mathrm{MEG}}$ in resting-state (continuous line) and during task (dashed line), evaluated as described in Section 5.2.1, as a function of the threshold vector $\mathbf{t_r}$. The different boxes and colors represent different frequency bands. In this figure, the case of the VIS sub-network is represented.

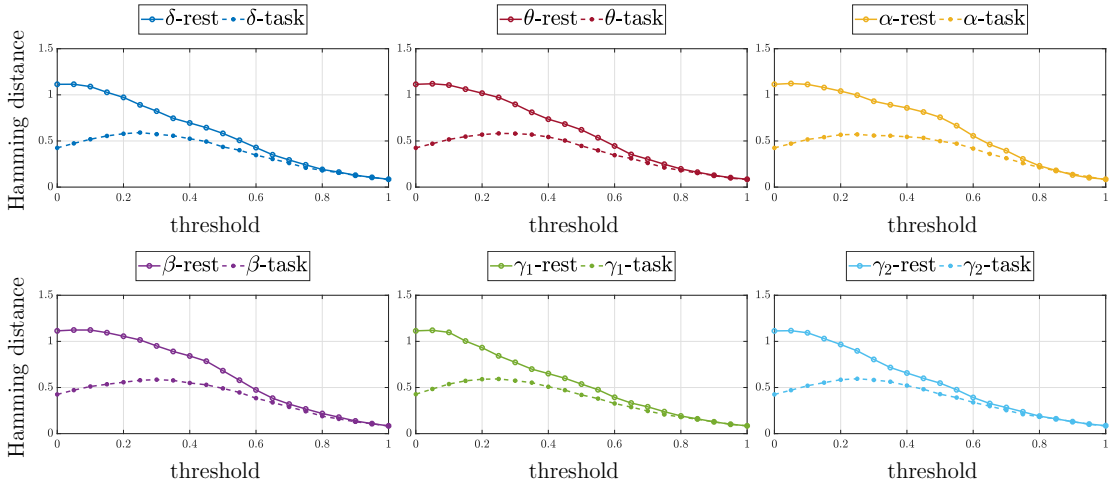

Figure A.8: Hamming distance between $\mathbf{FC}^{\mathrm{DV}}_{\mathrm{fMRI}}$ and $\mathbf{FC}^{\mathrm{DV}}_{\mathrm{MEG}}$ in resting-state (continuous line) and during task (dashed line), evaluated as described in Section 5.2.1, as a function of the threshold vector $\mathbf{t_r}$. The different boxes and colors represent different frequency bands. In this figure, the case of the DAN-VIS cross-network is represented.

A.7 Phase randomized surrogates

The significance of synchronization in Section 6.3 is obtained by estimated a distribution of the synchronization level under the null hypothesis of zero synchronization. To this aim, a set of phase-randomized surrogates has been generated with Algorithm 1. Shortly, we extracted the coefficients of the discrete Fourier transform from the original data, and we defined the Fourier coefficients for the surrogates, by preserving the same modulus and substituting the phases with uniformly distributed random numbers. Then the surrogates were exposed to the same filtering used for real data. From filtered surrogates, we extracted the phase evolution by means of Hilbert transform, and we evaluated the order parameter for the obtained phases. Finally, the level of synchrony is estimated as the absolute value of the order parameter for each time instant ($t = 1, \ldots, T$). We used this algorithm ten times for each subjects, to obtain a pull of values for the synchronization level used to estimate the probability density function of the global level of phase synchrony on the null hypothesis of zero synchronization.

Algorithm 1 Surrogates generation and synchronization level evaluation

$\mathbf{R}^{\text{surr}} = \mathbb{0}_{10 \times N_s \times T}$ ▷ initialization
for iter $= \{1, \ldots, 10\}$ **do**
  for $i_s = \{1, \ldots, N_s\}$ **do** ▷ iterate across subjects
    for $i = \{1, \ldots, N\}$ **do**
      $\tilde{x}_i(f) \leftarrow$ estimated Fourier transform of fMRI data $x(t)$
      $\boldsymbol{\varphi} = [\ \varphi_1 \quad \cdots \quad \varphi_{(T/2-1)}\ ]^{\mathsf{T}}$, with $\varphi_k \sim \mathcal{U}([-\pi, \pi])$
      $\boldsymbol{\varphi} \leftarrow [\ -\boldsymbol{\varphi} \quad 0 \quad \boldsymbol{\varphi}\ ]^{\mathsf{T}}$
      $x_i^{\text{surr}}(t) = \frac{1}{T} \sum_{k=1}^{T} |\tilde{x}_i(k)|\, e^{-\mathrm{j}\left(\frac{2\pi k t}{T} + \varphi_k\right)}$ ▷ generate surrogate time series
      $x_{\text{fil},i}^{\text{surr}}(t) \leftarrow$ filtered surrogate data
      $a_i^{\text{surr}}(t) = x_{\text{fil},i}^{\text{surr}}(t) + \mathrm{j}\mathcal{H}[x_{\text{fil},i}^{\text{surr}}(t)]$ ▷ analytic surrogate signal
      $\theta_i^{\text{surr}}(t) = \angle(a_i^{\text{surr}}(t))$ ▷ phase of surrogate signal
    end for
    $R^{\text{surr}}(t) e^{\mathrm{j}\Phi^{\text{surr}}(t)} = \frac{1}{N} \sum_{i=1}^{N} e^{\mathrm{j}\theta_i^{\text{surr}}(t)}$ ▷ surrogates' order parameter
    $[\mathbf{R}^{\text{surr}}]_{\text{iter},i_s,t} \leftarrow R^{\text{surr}}(t)$ ▷ save data
  end for
end for

A.8 Full brain synchronization analysis

To complete the analysis presented in Section 6.3, we report here the results obtained through a synchronization analysis of a full-brain network, as described in Ponce-Alvarez et al. (2015).

Specific, we use a fully available database (Ponce-Alvarez et al., 2015, Supporting Information), which consists on the time series of resting BOLD activity measured in 24 right-handed healthy young volunteers (age range 20-31 years). Each subject underwent two scanning runs of 10 min (with a sampling time $dt = 2$ s), in a resting-state condition. The brain parcellation consists on $N = 66$ areas (33 cortical regions per hemisphere), described in Hagmann et al. (2008).

Using the same pipeline as described in Section 6.3, we filter the original data and extract the phases' time series for each of the N regions. Since the analysis is the same as described in the main text, in this site we report only some figures of the results of this full-brain analysis, neglecting the details. These results may be compared with the ones reported in Ponce-Alvarez et al. (2015). This can be interpreted as a control test in order to verify the goodness of the implemented pipeline.

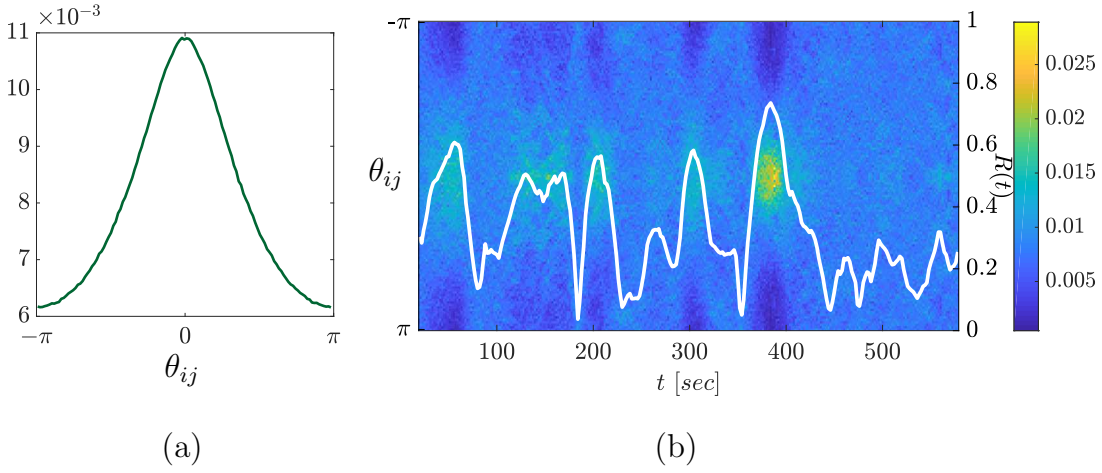

Figure A.9: Analysis of the distribution of the phase difference θ_{ij}. **(a)** Probability density function (p.d.f.) of phase differences across all pairs of brain regions, all time steps and all subjects. **(b)** Temporal evolution of the p.d.f. of the phase difference among each pair of nodes (from one subject). The colour indicates the value of the p.d.f. at each time step (left y-axis). The white line represents the absolute value of the order parameter $R(t)$ related to the same subject (right y-axis).

	Label	Brain region		Label	Brain region
1.	rBSTS	Bank of the superior temporal sulcus (right)	34.	lCMF	Caudal middle frontal cortex (left)
2.	rST	Superior temporal cortex (right)	35.	lFP	Frontal pole (left)
3.	rTT	Transverse temporal cortex (right)	36.	lIP	Inferior parietal cortex (left)
4.	lBSTS	Bank of the superior temporal sulcus (left)	37.	lMOF	Medial orbitofrontal cortex (left)
5.	lST	Superior temporal cortex (left)	38.	lPTRI	Pars triangularis (left)
6.	lTT	Transverse temporal cortex (left)	39.	rMT	Middle temporal cortex (right)
7.	rCAC	Caudal anterior cingulate cortex (right)	40.	rPARH	Parahippocampal cortex (right)
8.	rPOPE	Pars opercularis (right)	41.	rTP	Temporal pole (right)
9.	rPORB	Pars orbitalis (right)	42.	lMT	Middle temporal cortex (left)
10.	lCAC	Caudal anterior cingulate cortex (left)	43.	lPARH	Parahippocampal cortex (left)
11.	lPOPE	Pars opercularis (left)	44.	lTP	Temporal pole (left)
12.	lPORB	Pars orbitalis (left)	45.	rPARC	Paracentral lobule (right)
13.	rRAC	Rostral anterior cingulate cortex (right)	46.	rPREC	Precentralgyrus (right)
14.	rRMF	Rostral middle frontal cortex (right)	47.	rPSTC	Postcentralgyrus (right)
15.	rSMAR	Supramarginalgyrus (right)	48.	lPARC	Paracentral lobule (left)
16.	lRAC	Rostral anterior cingulate cortex (left)	49.	lPREC	Precentralgyrus (left)
17.	lRMF	Rostral middle frontal cortex (left)	50.	lPSTC	Postcentralgyrus (left)
18.	lSMAR	Supramarginalgyrus (left)	51.	rLOF	Lateral orbitofrontal cortex (right)
19.	rISTC	Isthmus of the cingulate cortex (right)	52.	lLOF	Lateral orbitofrontal cortex (left)
20.	rPC	Posterior cingulate cortex (right)	53.	rCUN	Cuneus (right)
21.	rPCUN	Precuneus (right)	54.	rENT	Entorhinal cortex (right)
22.	rSF	Superior frontal cortex (right)	55.	rFUS	Fusiform gyrus (right)
23.	lISTC	Isthmus of the cingulate cortex (left)	56.	rIT	Inferior temporal cortex (right)
24.	lPC	Posterior cingulate cortex (left)	57.	rLING	Lingual gyrus (right)
25.	lPCUN	Precuneus (left)	58.	rLOCC	Lateral occipital cortex (right)
26.	lSF	Superior frontal cortex (left)	59.	rPCAL	Pericalcarine cortex (right)
27.	rSP	Superior parietal cortex (right)	60.	lCUN	Cuneus (left)
28.	lSP	Superior parietal cortex (left)	61.	lENT	Entorhinal cortex (left)
29.	rCMF	Caudal middle frontal cortex (right)	62.	lFUS	Fusiform gyrus (left)
30.	rFP	Frontal pole (right)	63.	lIT	Inferior temporal cortex (left)
31.	rIP	Inferior parietal cortex (right)	64.	lLING	Lingual gyrus (left)
32.	rMOF	Medial orbitofrontal cortex (right)	65.	lLOCC	Lateral occipital cortex (left)
33.	rPTRI	Pars triangularis (right)	66.	lPCAL	Pericalcarine cortex (left)

Table A.1: Names and abbreviations of the brain regions used in this analysis (Hagmann et al. (2008)), in the same order used to produce Figures A.10 and A.11.

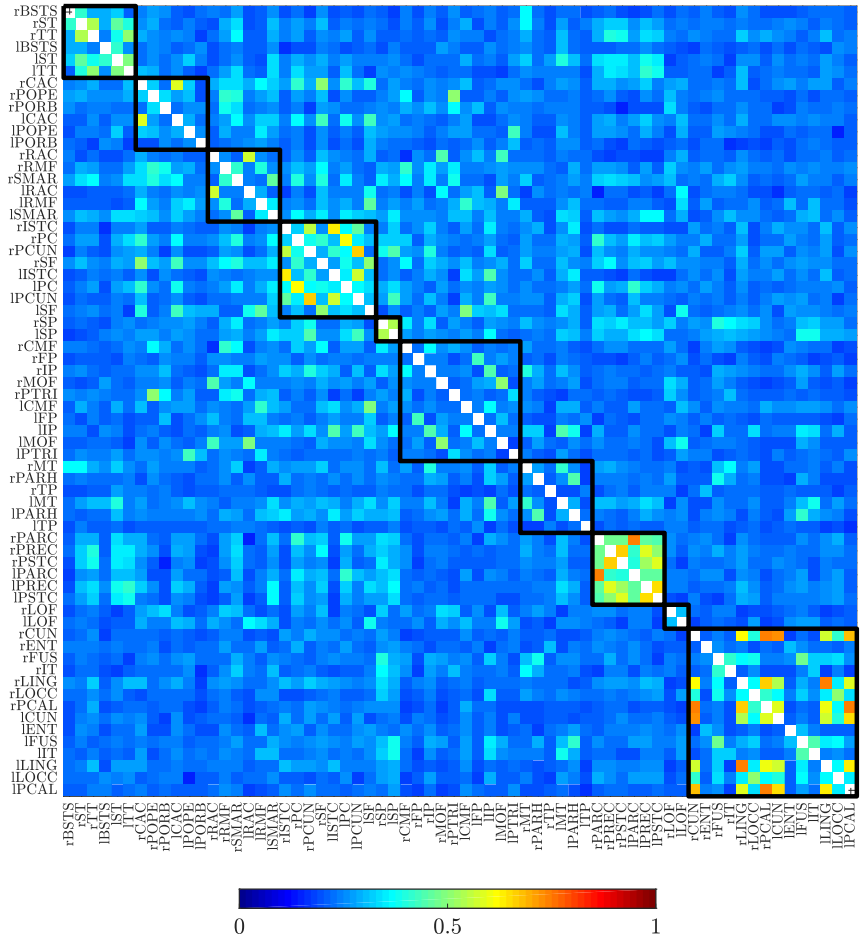

(a)

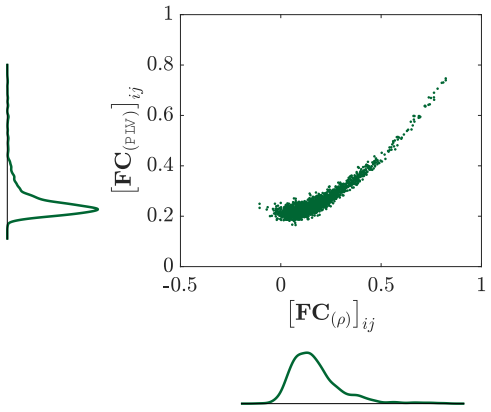

(b)

Figure A.10: Functional connectivity map analysis. **(a)** FC map defined through the phase locking value $\mathbf{FC}_{(\mathsf{PLV})}$. The labels of ROIs are in the same order as in Table A.1. The black lines highlight cognitive modules. **(b)** Relationship among $\mathbf{FC}_{(\mathsf{PLV})}$ and $\mathbf{FC}_{(\rho)}$. Note that $\mathbf{FC}_{(\rho)}$ assumes values within $[0, 1]$, while $[\mathbf{FC}_{(\mathsf{PLV})}]_{ij} \in [-1,\ 1]$.

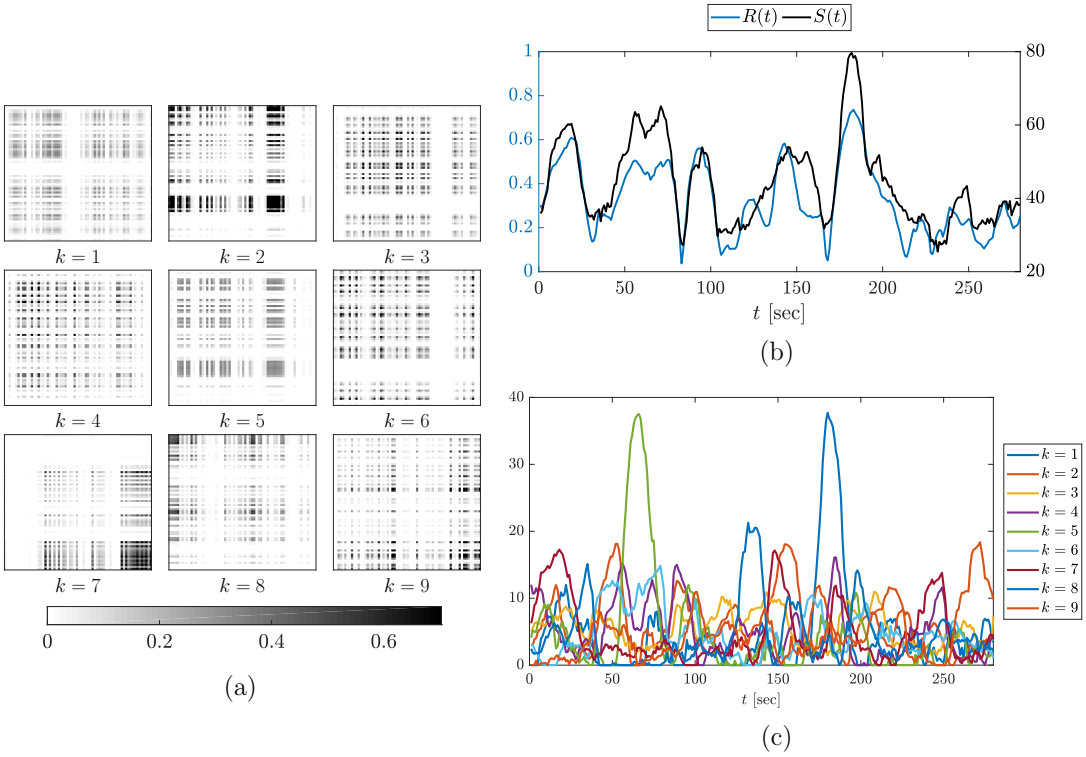

Figure A.11: Synchronization patterns obtained from the phase evolutions during time. **(a)** Representation of the $K = 9$ community patterns ($\mathbf{a}_k \cdot \mathbf{a}_k^\mathsf{T}$, $k = 1, \ldots, K$) obtained from all the 24 subjects. The ROIs are in the same order as in Table A.1. **(b)** Comparison among the evolution of the absolute value $R(\cdot)$ of the order parameter (left y-axis, blue line) and the global strength $S(\cdot)$ (right y-axis, black line) of one subject. **(c)** Evolution of the strength of each community k during time for the same subject.

A.9 Proof of Proposition 7.3.2

Proposition. ***(Phase cohesiveness)***
Consider the Kuramoto model (7.2), with $N \geq 2$ oscillators, natural frequencies $\boldsymbol{\omega} \in \mathbb{1}_N^{\perp}$, in $[\omega_{min}, \omega_{max}]$ and coupling strength C. If the coupling strength C is higher than a critical value C_{cr}:

$$C > C_{cr} = \frac{\omega_{max} - \omega_{min}}{e^{-\tilde{d}^2}} \quad with \quad \tilde{d} = \frac{d_{max}}{p}$$

then $\exists\, \gamma_{max} \in \,]\pi/2, \pi]$ and $\exists\, \gamma_{min} \in [0, \pi/2[$ such that

1. *$\Delta_N(\gamma)$ is positive invariant for every $\gamma \in [\gamma_{min}, \gamma_{max}]$, that means that each trajectory originated in $\Delta_N(\gamma)$ remains in $\Delta_N(\gamma)$ for every $t \geq 0$ (phase cohesiveness);*
2. *$\sin(\gamma_{min}) = \sin(\gamma_{max}) = C_{cr}/C$.*

Proof. To prove the positive invariance of $\Delta_N(\gamma)$, i.e. the phase cohesiveness in $\Delta_N(\gamma)$ for some $\gamma \in [0,\ \pi]$, the function $V : \mathbb{T}^N \to [0,\ \pi]$ is introduced as

$$V(\boldsymbol{\theta}) = \max\{|\theta_i - \theta_j| \text{ s.t. } i,\ j \in \{1,\ \ldots,\ N\}\}.$$

The angle containing all the initial phases $\theta_i(0)$ has a maximum and a minimum: be $I_{\max}(\boldsymbol{\theta})$ and $I_{\min}(\boldsymbol{\theta})$ the sets of indices of angles $\{\theta_1,\ \ldots,\ \theta_N\}$ equal to the maximum and the minimum, respectively. It follows:

$$V(\boldsymbol{\theta}) = |\theta_{m'} - \theta_{l'}|, \qquad \forall\, m' \in I_{\max}(\boldsymbol{\theta}), \qquad \forall\, l' \in I_{\min}(\boldsymbol{\theta}).$$

Assuming $\theta_i(0) \in \Delta_N(\gamma)$, it is now to show that this condition remains $\forall t > 0$, which can happen if and only if $V(\boldsymbol{\theta}) \leq \gamma \leq \pi$. It follows that $\Delta_N(\gamma)$ is positively invariant if and only if $V(\boldsymbol{\theta})$ does not increase at any time t such that $V(\boldsymbol{\theta}(t)) = \gamma$. The upper Dini derivative of $V(\boldsymbol{\theta})$ is given by Dörfler and Bullo (2011):

$$V'_+(\boldsymbol{\theta}) = \lim_{h \to 0} \sup \frac{V(\boldsymbol{\theta}(t+h)) - V(\boldsymbol{\theta}(t))}{h} = \dot{\theta}_m(t) - \dot{\theta}_l(t), \tag{A.7}$$

where $m \in I_{\max}(\boldsymbol{\theta}(t))$ and $l \in I_{\min}(\boldsymbol{\theta}(t))$ are such that $\dot{\theta}_m(t) = \max\left\{\dot{\theta}_{m'}(t) \mid m' \in I_{\max}(\boldsymbol{\theta}(t))\right\}$ and $\dot{\theta}_l(t) = \max\left\{\dot{\theta}_{l'}(t) \mid l' \in I_{\min}(\boldsymbol{\theta}(t))\right\}$. Along the system dynamics (7.2), (A.7) can be written as follows:

$$V'_+(\boldsymbol{\theta}) = \omega_m - \omega_l - \frac{C}{N}\sum_{i=1}^{N} w_{mi}\sin(\theta_m - \theta_i) + -\frac{C}{N}\sum_{i=1}^{N} w_{li}\sin(\theta_i - \theta_l),$$

where all phases $\boldsymbol{\theta}$'s are time-dependent, and this explicit dependence is henceforth omitted for simplicity of notation.

From $V(\boldsymbol{\theta}) = \gamma$, it follows that $\theta_m - \theta_l = \gamma$ and

$$\begin{cases} \theta_m - \theta_i \in [0, \gamma] \subseteq [0, \pi] \implies \sin(\theta_m - \theta_i) \geq 0 \\ \theta_i - \theta_l \in [0, \gamma] \subseteq [0, \pi] \implies \sin(\theta_i - \theta_l) \geq 0 \end{cases} . \tag{A.8}$$

Moreover the kernel property stands

$$w_{ij} \in \left[e^{-\tilde{d}^2},\ 1\right] \subseteq]0,\ 1], \qquad \forall\ i, j = 1, \ldots, N,$$

where $\tilde{d} = \frac{d_{\max}}{p}$, which yields

$$V'_+(\boldsymbol{\theta}) \leq \omega_m - \omega_l - \frac{Ce^{-\tilde{d}^2}}{N} \sum_{i=1}^{N} (\sin(\theta_m - \theta_i) + \sin(\theta_i - \theta_l)) . \tag{A.9}$$

By means of prosthaphaeresis formulas applied to $\theta_m - \theta_i$ and $\theta_i - \theta_l$, the summation in (A.9) results

$$\sum_{i=1}^{N} 2 \sin\left(\frac{\theta_m - \theta_l}{2}\right) \cos\left(\frac{\theta_m - \theta_i}{2} - \frac{\theta_i - \theta_l}{2}\right)$$

and through the relations (A.8) it is:

$$\begin{aligned} &\sin\left(\frac{\theta_m - \theta_l}{2}\right) = \sin\left(\frac{\gamma}{2}\right), \\ &\cos\left(\frac{\theta_m - \theta_i}{2} - \frac{\theta_i - \theta_l}{2}\right) \geq \cos\left(\frac{\theta_m - \theta_l}{2}\right) = \cos\left(\frac{\gamma}{2}\right). \end{aligned}$$

Going back to the derivative (A.9), it follows:

$$\begin{aligned} V'_+(\boldsymbol{\theta}) &\leq \omega_m - \omega_l - \frac{C}{N} e^{-\tilde{d}^2} \sum_{i=1}^{N} 2 \sin\left(\frac{\gamma}{2}\right) \cos\left(\frac{\gamma}{2}\right) \\ &\leq \omega_m - \omega_l - Ce^{-\tilde{d}^2} \sin(\gamma). \end{aligned}$$

The length of the arc formed by the phases is non-increasing in $\Delta_N(\gamma)$ if for any pair $\{m,\ l\}$ it holds that

$$Ce^{-\tilde{d}^2} \sin(\gamma) \geq \max(\boldsymbol{\omega}) - \min(\boldsymbol{\omega}) \qquad \Longrightarrow \qquad V'_+(\boldsymbol{\theta}) \leq 0. \tag{A.10}$$

For $\gamma \in [0,\ \pi]$, the left member of (A.10) is a concave function, whose maximum is at

$\gamma^* = \pi/2$. Thus, there exists an open set of arc lengths $\gamma \in [0,\ \pi]$ satisfying (A.10) if and only if

$$Ce^{-\tilde{d}^2} > \max(\boldsymbol{\omega}) - \min(\boldsymbol{\omega}),$$

which corresponds to the equivalent relations (7.4) and (7.5).
It follows that $\forall\gamma \in [\gamma_{\min}, \gamma_{\max}]$, $V(\boldsymbol{\theta})$ is non-increasing and it is strictly decreasing for $\gamma \in\ ]\gamma_{\min},\ \gamma_{\max}[$. As a consequence of that, the set $\Delta_N(\gamma)$ is positive invariant $\forall\gamma \in [\gamma_{\min}, \gamma_{\max}]$, and each trajectory starting in $\Delta_N(\gamma_{\max})$ approaches asymptotically $\Delta_N(\gamma_{\min})$ (*phase cohesiveness*).
Furthermore, if (7.4) holds and hence (A.10) is true, there exists a unique $\gamma_{\min} \in [0,\ \pi/2[$ and a unique $\gamma_{\max} \in\ ]\pi/2,\ \pi]$, which obey (A.10) with the equality sign:

$$\sin(\gamma_{\min}) = \sin(\gamma_{\max}) = \frac{1}{C}\frac{\Delta\omega}{e^{-\tilde{d}^2}} = \frac{C_{\text{cr}}}{C}.$$

■

A.10 Proof of Proposition 7.3.4

Proposition. ***(Frequency synchronization)***
With a coupling strength $C > C_{cr}$, model (7.2) achieves exponential frequency synchronization for all possible distributions of the natural frequencies $\{\omega_i\}$ on the compact interval $[\omega_{min}, \omega_{max}]$ and for all initial phase conditions $\boldsymbol{\theta}(0) \in \Delta_N(\gamma_{max})$.
Moreover:

1. *the asymptotic synchronization frequency ω_{sync} is the average frequency $\omega_{avg} = \frac{1}{N}\sum_{i=1}^{N}\omega_i$;*

2. *given phase cohesiveness w.r.t. γ for some fixed $\gamma < \pi/2$, the exponential synchronization rate is no worse then $\lambda_{fs} = Ce^{-\tilde{d}^2}\cos(\gamma)$;*

Proof. From Kuramoto model (7.2) written as

$$f_i(\theta) = \omega_i + \sum_{j=1}^{N} a_{ij}\sin(\theta_i - \theta_j),$$

with $a_{ij} = \frac{C}{N}w_{ij}$, it follows that

$$\frac{\partial f_i}{\partial \theta_i} = \sum_{j=1}^{N} a_{ij}\cos(\theta_i - \theta_j), \qquad \frac{\partial f_i}{\partial \theta_j} = -a_{ij}\cos(\theta_i - \theta_j).$$

This implies that the Jacobian $\mathbf{J}(\boldsymbol{\theta})$ satisfies

$$\mathbf{J}(\boldsymbol{\theta}) = -\mathbf{B}\mathrm{diag}\left(\{\tilde{a}_{ij}\}_{\{i,j\}\in\mathcal{E}}\right)\mathbf{B}^{\mathsf{T}},$$

where $\mathbf{B}$ is the incidence matrix of the graph $\mathcal{G}$ with $\tilde{a}_{ij} = a_{ij}\cos(\theta_i - \theta_j) > 0$, since $|\theta_i - \theta_j| < \gamma_{\min} < \pi/2$ for the phase cohesiveness. Moreover, $\mathbf{J}(\boldsymbol{\theta})$ is negative semidefinite and equal to the graph Laplacian $\mathbf{L}_{\mathcal{G}}$. Hence, by differentiating the phase dynamics (7.2), the frequency dynamics is obtained as

$$\frac{d\dot{\theta}_i}{dt} = -\sum_{j=1}^{N}\tilde{a}_{ij}(t)\left(\dot{\theta}_i - \dot{\theta}_j\right) \qquad i = 1,\ldots,N, \tag{A.11}$$

or, equivalently,

$$\frac{d\dot{\boldsymbol{\theta}}}{dt} = -\mathbf{L}_{\mathcal{G}}(t)\,\dot{\boldsymbol{\theta}}.$$

Since $\ker(\mathbf{L}_{\mathcal{G}}) = \mathrm{Im}(\mathbb{1}_N)$, it follows

$$\mathbb{1}_N^{\mathsf{T}} \frac{d}{dt}\dot{\boldsymbol{\theta}} = 0 \qquad \Longrightarrow \qquad \sum_{i=1}^{N} \dot{\theta}_i(t) = \sum_{i=1}^{N} \omega_i = N\,\omega_{\mathrm{avg}}.$$

The dynamics (A.11) can be regarded as a *linear consensus protocol* with time-varying strictly-positive weights and, according to Dörfler and Bullo (2011)[Theorem 4.1], all frequencies $\dot{\theta}_i(t)$ synchronize exponentially:

$$\left\| \dot{\boldsymbol{\theta}}(t) - \omega_{\mathrm{sync}}\mathbb{1}_N \right\|_2 \leq \left\| \dot{\boldsymbol{\theta}}(0) - \omega_{\mathrm{sync}}\mathbb{1}_N \right\|_2 e^{-\lambda_{\mathrm{fs}} t},$$

with $\lambda_{fs} = \lambda_2(\mathbf{L}_{\mathcal{G}})\cos(\gamma) \geq Ce^{-\tilde{d}^2}\cos(\gamma)$, where $\lambda_2(\mathbf{L}_{\mathcal{G}})$ is the Fiedler value of $\mathbf{L}_{\mathcal{G}}$ (Gershgorin disc Theorem)[1]. Therefore, if $C > C_{\mathrm{cr}}$, exponential convergence of the frequencies $\dot{\theta}_i(t)$ to ω_{sync} is attained.

■

[1] The Fiedler value, or Fiedler eigenvalue, of a graph $\mathcal{G}$ is the second-smallest eigenvalue of the Laplacian matrix of $\mathcal{G}$.

Bibliography

Aarsland, D., Bronnick, K., Williams-Gray, C., Weintraub, D., Marder, K., Kulisevsky, J., Burn, D., Barone, P., Pagonabarraga, J., Allcock, L., et al. (2010). Mild cognitive impairment in parkinson disease a multicenter pooled analysis. *Neurology*, 75(12):1062–1069.

Abou-Sleiman, P. M., Muqit, M. M., and Wood, N. W. (2006). Expanding insights of mitochondrial dysfunction in parkinson's disease. *Nature reviews. Neuroscience*, 7(3):207.

Abramowitz, M. and Stegun, I. A. (1964). *Handbook of mathematical functions: with formulas, graphs, and mathematical tables*, volume 55. Courier Corporation.

Acebrón, J. A., Bonilla, L. L., Vicente, C. J. P., Ritort, F., and Spigler, R. (2005). The kuramoto model: A simple paradigm for synchronization phenomena. *Reviews of modern physics*, 77(1):137.

Ahlfors, S. P. and Simpson, G. V. (2004). Geometrical interpretation of fmri-guided meg/eeg inverse estimates. *NeuroImage*, 22(1):323–332.

Allen, E. A., Damaraju, E., Plis, S. M., Erhardt, E. B., Eichele, T., and Calhoun, V. D. (2014). Tracking whole-brain connectivity dynamics in the resting state. *Cerebral cortex*, 24(3):663–676.

Archer, S. L. (2013). Mitochondrial dynamics—mitochondrial fission and fusion in human diseases. *New England Journal of Medicine*, 369(23):2236–2251.

Arfanakis, K., Cordes, D., Haughton, V. M., Moritz, C. H., Quigley, M. A., and Meyerand, M. E. (2000). Combining independent component analysis and correlation analysis to probe interregional connectivity in fmri task activation datasets. *Magnetic resonance imaging*, 18(8):921–930.

Arieli, A., Sterkin, A., Grinvald, A., and Aertsen, A. (1996). Dynamics of ongoing activity: explanation of the large variability in evoked cortical responses. *Science*, 273(5283):1868.

Attwell, D., Buchan, A. M., Charpak, S., Lauritzen, M., MacVicar, B. A., and Newman, E. A. (2010). Glial and neuronal control of brain blood flow. *Nature*, 468(7321):232.

Attwell, D. and Laughlin, S. B. (2001). An energy budget for signaling in the grey matter of the brain. *Journal of Cerebral Blood Flow & Metabolism*, 21(10):1133–1145.

Bach, D., Naon, D., Pich, S., Soriano, F. X., Vega, N., Rieusset, J., Laville, M., Guillet, C., Boirie, Y., Wallberg-Henriksson, H., et al. (2005). Expression of mfn2, the charcot-marie-tooth neuropathy type 2a gene, in human skeletal muscle. *Diabetes*, 54(9):2685–2693.

Baloh, R. H. (2008). Mitochondrial dynamics and peripheral neuropathy. *The Neuroscientist*, 14(1):12–18.

Banaie, M., Sarbaz, Y., Pooyan, M., Gharibzadeh, S., and Towhidkhah, F. (2009). Modeling huntington's disease considering the theory of central pattern generators (cpg). *Advances in Computational Intelligence*, pages 11–19.

Bender, A., Krishnan, K. J., Morris, C. M., Taylor, G. A., Reeve, A. K., Perry, R. H., Jaros, E., Hersheson, J. S., Betts, J., Klopstock, T., et al. (2006). High levels of mitochondrial dna deletions in substantia nigra neurons in aging and parkinson disease. *Nature genetics*, 38(5):515.

Betti, V., Della Penna, S., de Pasquale, F., Mantini, D., Marzetti, L., Romani, G. L., and Corbetta, M. (2013). Natural scenes viewing alters the dynamics of functional connectivity in the human brain. *Neuron*, 79(4):782–797.

Betts, J., College, O., Desaix, P., Johnson, J., Johnson, E., Korol, O., Kruse, D., Poe, B., Wise, J., Womble, M., et al. (2013). *Anatomy and Physiology*. Open Textbooks. OpenStax College.

Blekhman, I. I. (1988). *Synchronization in science and technology*. American Society of Mechanical Engineers.

Blondel, V. D., Guillaume, J.-L., Lambiotte, R., and Lefebvre, E. (2008). Fast unfolding of communities in large networks. *Journal of statistical mechanics: theory and experiment*, 2008(10):P10008.

Boissan, M., Montagnac, G., Shen, Q., Griparic, L., Guitton, J., Romao, M., Sauvonnet, N., Lagache, T., Lascu, I., Raposo, G., et al. (2014). Nucleoside diphosphate kinases fuel dynamin superfamily proteins with gtp for membrane remodeling. *Science*, 344(6191):1510–1515.

Boland, M. L., Chourasia, A. H., and Macleod, K. F. (2013). Mitochondrial dysfunction in cancer. *Frontiers in oncology*, 3.

Bradshaw, T. Y., Romano, L. E., Duncan, E. J., Nethisinghe, S., Abeti, R., Michael, G. J., Giunti, P., Vermeer, S., and Chapple, J. P. (2016). A reduction in drp1-mediated fission compromises mitochondrial health in autosomal recessive spastic ataxia of charlevoix saguenay. *Human molecular genetics*, 25(15):3232–3244.

Brainard, D. H. (1997). The psychophysics toolbox. *Spatial vision*, 10:433–436.

Breakspear, M., Heitmann, S., and Daffertshofer, A. (2010). Generative models of cortical oscillations: neurobiological implications of the kuramoto model. *Frontiers in human neuroscience*, 4.

Brookes, M. J., Hale, J. R., Zumer, J. M., Stevenson, C. M., Francis, S. T., Barnes, G. R., Owen, J. P., Morris, P. G., and Nagarajan, S. S. (2011). Measuring functional connectivity using meg: methodology and comparison with fcmri. *Neuroimage*, 56(3):1082–1104.

Bullmore, E. and Sporns, O. (2009). Complex brain networks: graph theoretical analysis of structural and functional systems. *Nature reviews. Neuroscience*, 10(3):186.

Bullmore, E. and Sporns, O. (2012). The economy of brain network organization. *Nature reviews. Neuroscience*, 13(5):336.

Cabral, J., Hugues, E., Sporns, O., and Deco, G. (2011). Role of local network oscillations in resting-state functional connectivity. *Neuroimage*, 57(1):130–139.

Cabral, J., Kringelbach, M. L., and Deco, G. (2014). Exploring the network dynamics underlying brain activity during rest. *Progress in neurobiology*, 114:102–131.

Cao, Y. and Ren, W. (2011). Distributed multi-agent coordination: A comparison lemma based approach. In *American Control Conference (ACC), 2011*, pages 1618–1623. IEEE.

Capotosto, P., Tosoni, A., Spadone, S., Sestieri, C., Perrucci, M. G., Romani, G. L., Della Penna, S., and Corbetta, M. (2013). Anatomical segregation of visual selection mechanisms in human parietal cortex. *Journal of Neuroscience*, 33(14):6225–6229.

Cenedese, A. and Favaretto, C. (2015). On the synchronization of spatially coupled oscillators. In *2015 54th IEEE Conference on Decision and Control (CDC)*, pages 4836–4841.

Cenedese, A., Favaretto, C., and Occioni, G. (2016). Multi-agent swarm control through kuramoto modeling. In *2016 IEEE 55th Conference on Decision and Control (CDC)*, pages 1820–1825.

Chan, F., Lax, N. Z., Davies, C. H., Turnbull, D. M., and Cunningham, M. O. (2016). Neuronal oscillations: A physiological correlate for targeting mitochondrial dysfunction in neurodegenerative diseases? *Neuropharmacology*, 102:48–58.

Chauhan, A., Vera, J., and Wolkenhauer, O. (2014). The systems biology of mitochondrial fission and fusion and implications for disease and aging. *Biogerontology*, 15(1):1–12.

Chen, C.-C., Kiebel, S. J., Kilner, J. M., Ward, N. S., Stephan, K. E., Wang, W.-J., and Friston, K. J. (2012). A dynamic causal model for evoked and induced responses. *Neuroimage*, 59(1):340–348.

Chernoff, H. (1952). A measure of asymptotic efficiency for tests of a hypothesis based on the sum of observations. *The Annals of Mathematical Statistics*, pages 493–507.

Cherry, A. D. and Piantadosi, C. A. (2015). Regulation of mitochondrial biogenesis and its intersection with inflammatory responses. *Antioxidants & redox signaling*, 22(12):965–976.

Chinnery, P. F., Samuels, D. C., Elson, J., and Turnbull, D. M. (2002). Accumulation of mitochondrial dna mutations in ageing, cancer, and mitochondrial disease: is there a common mechanism? *The Lancet*, 360(9342):1323–1325.

Cho, D.-H., Nakamura, T., Fang, J., Cieplak, P., Godzik, A., Gu, Z., and Lipton, S. A. (2009). S-nitrosylation of drp1 mediates β-amyloid-related mitochondrial fission and neuronal injury. *Science*, 324(5923):102–105.

Chopra, N. and Spong, M. W. (2005). On synchronization of kuramoto oscillators. In *Decision and Control, 2005 and 2005 European Control Conference. CDC-ECC'05. 44th IEEE Conference on*, pages 3916–3922. IEEE.

Clarke, J. and Braginski, A. (2006). *The SQUID Handbook: Applications of SQUIDs and SQUID Systems*. John Wiley & Sons.

Clay, H. B., Sillivan, S., and Konradi, C. (2011). Mitochondrial dysfunction and pathology in bipolar disorder and schizophrenia. *International Journal of Developmental Neuroscience*, 29(3):311–324.

Cohen, M. X. (2014). *Analyzing neural time series data: theory and practice*. MIT Press.

Cole, M. W., Bassett, D. S., Power, J. D., Braver, T. S., and Petersen, S. E. (2014). Intrinsic and task-evoked network architectures of the human brain. *Neuron*, 83(1):238–251.

Cuesta, A., Pedrola, L., Sevilla, T., García-Planells, J., Chumillas, M. J., Mayordomo, F., LeGuern, E., Marín, I., Vílchez, J. J., and Palau, F. (2002). The gene encoding ganglioside-induced differentiation-associated protein 1 is mutated in axonal charcot-marie-tooth type 4a disease. *Nature genetics*, 30(1).

Dahms, T., Lehnert, J., and Schöll, E. (2012). Cluster and group synchronization in delay-coupled networks. *Physical Review E*, 86(1):016202.

Dalmasso, G., Zapata, P. A. M., Brady, N. R., and Hamacher-Brady, A. (2017). Agent-based modeling of mitochondria links sub-cellular dynamics to cellular homeostasis and heterogeneity. *PloS one*, 12(1):e0168198.

Damoiseaux, J. S. and Greicius, M. D. (2009). Greater than the sum of its parts: a review of studies combining structural connectivity and resting-state functional connectivity. *Brain Structure and Function*, 213(6):525–533.

De Pasquale, F., Della Penna, S., Snyder, A. Z., Lewis, C., Mantini, D., Marzetti, L., Belardinelli, P., Ciancetta, L., Pizzella, V., Romani, G. L., et al. (2010). Temporal dynamics of spontaneous meg activity in brain networks. *Proceedings of the National Academy of Sciences*, 107(13):6040–6045.

De Tommaso, M., De Carlo, F., Difruscolo, O., Massafra, R., Sciruicchio, V., and Bellotti, R. (2003). Detection of subclinical brain electrical activity changes in huntington's disease using artificial neural networks. *Clinical neurophysiology*, 114(7):1237–1245.

Deco, G., Jirsa, V. K., Robinson, P. A., Breakspear, M., and Friston, K. (2008). The dynamic brain: from spiking neurons to neural masses and cortical fields. *PLoS computational biology*, 4(8):e1000092.

Della Penna, S., Pizzella, V., and Romani, G. L. (2014). Impact of squids on functional imaging in neuroscience. *Superconductor Science and Technology*, 27(4):044004.

Disatnik, M.-H., Hwang, S., Ferreira, J. C., and Mochly-Rosen, D. (2015). New therapeutics to modulate mitochondrial dynamics and mitophagy in cardiac diseases. *Journal of molecular medicine*, 93(3):279–287.

Dominy, J. E. and Puigserver, P. (2013). Mitochondrial biogenesis through activation of nuclear signaling proteins. *Cold Spring Harbor perspectives in biology*, 5(7):a015008.

Dörfler, F. and Bullo, F. (2011). On the critical coupling for kuramoto oscillators. *SIAM Journal on Applied Dynamical Systems*, 10(3):1070–1099.

Dörfler, F. and Bullo, F. (2014). Synchronization in complex networks of phase oscillators: A survey. *Automatica*, 50(6):1539–1564.

Duvezin-Caubet, S., Jagasia, R., Wagener, J., Hofmann, S., Trifunovic, A., Hansson, A., Chomyn, A., Bauer, M. F., Attardi, G., Larsson, N.-G., et al. (2006). Proteolytic processing of opa1 links mitochondrial dysfunction to alterations in mitochondrial morphology. *Journal of Biological Chemistry*, 281(49):37972–37979.

Ehses, S., Raschke, I., Mancuso, G., Bernacchia, A., Geimer, S., Tondera, D., Martinou, J.-C., Westermann, B., Rugarli, E. I., and Langer, T. (2009). Regulation of opa1 processing and mitochondrial fusion by m-aaa protease isoenzymes and oma1. *The Journal of cell biology*, 187(7):1023–1036.

Engel, A. K., Gerloff, C., Hilgetag, C. C., and Nolte, G. (2013). Intrinsic coupling modes: multiscale interactions in ongoing brain activity. *Neuron*, 80(4):867–886.

Exner, N., Lutz, A. K., Haass, C., and Winklhofer, K. F. (2012). Mitochondrial dysfunction in parkinson9s disease: molecular mechanisms and pathophysiological consequences. *The EMBO journal*, 31(14):3038–3062.

Favaretto, C., Bassett, D. S., Cenedese, A., and Pasqualetti, F. (2017a). Bode meets kuramoto: Synchronized clusters in oscillatory networks. In *2017 American Control Conference (ACC)*, pages 2799–2804.

Favaretto, C. and Cenedese, A. (2016). On brain modeling in resting-state as a network of coupled oscillators. In *2016 IEEE 55th Conference on Decision and Control (CDC)*, pages 4190–4195.

Favaretto, C., Cenedese, A., and Pasqualetti, F. (2017b). Cluster synchronization in networks of kuramoto oscillators. In *IFAC World Congress*.

Ferrari, F. A., Viana, R. L., Lopes, S. R., and Stoop, R. (2015). Phase synchronization of coupled bursting neurons and the generalized kuramoto model. *Neural Networks*, 66:107–118.

Figge, M. T., Reichert, A. S., Meyer-Hermann, M., and Osiewacz, H. D. (2012). Deceleration of fusion–fission cycles improves mitochondrial quality control during aging. *PLoS computational biology*, 8(6):e1002576.

FitzHugh, R. (1961). Impulses and physiological states in theoretical models of nerve membrane. *Biophysical journal*, 1(6):445–466.

Flippo, K. H. and Strack, S. (2017). Mitochondrial dynamics in neuronal injury, development and plasticity. *J Cell Sci*, 130(4):671–681.

Fornito, A., Harrison, B. J., Zalesky, A., and Simons, J. S. (2012). Competitive and cooperative dynamics of large-scale brain functional networks supporting recollection. *Proceedings of the National Academy of Sciences*, 109(31):12788–12793.

Fornito, A., Zalesky, A., and Breakspear, M. (2013). Graph analysis of the human connectome: promise, progress, and pitfalls. *Neuroimage*, 80:426–444.

Fornito, A., Zalesky, A., and Bullmore, E. (2016). *Fundamentals of brain network analysis*. Academic Press.

Forsaa, E. B., Larsen, J. P., Wentzel-Larsen, T., Goetz, C. G., Stebbins, G. T., Aarsland, D., and Alves, G. (2010). A 12-year population-based study of psychosis in parkinson disease. *Archives of Neurology*, 67(8):996–1001.

Fransson, P. (2006). How default is the default mode of brain function?: Further evidence from intrinsic bold signal fluctuations. *Neuropsychologia*, 44(14):2836–2845.

Friston, K. J. (2011). Functional and effective connectivity: a review. *Brain connectivity*, 1(1):13–36.

Friston, K. J., Frith, C. D., Turner, R., and Frackowiak, R. S. (1995). Characterizing evoked hemodynamics with fmri. *Neuroimage*, 2(2):157–165.

Friston, K. J., Harrison, L., and Penny, W. (2003). Dynamic causal modelling. *Neuroimage*, 19(4):1273–1302.

Friston, K. J., Kahan, J., Biswal, B., and Razi, A. (2014). A dcm for resting state fmri. *Neuroimage*, 94:396–407.

Gao, W., Gilmore, J. H., Alcauter, S., and Lin, W. (2013). The dynamic reorganization of the default-mode network during a visual classification task. *Frontiers in systems neuroscience*, 7.

Garcés, P., Pereda, E., Hernández-Tamames, J. A., Del-Pozo, F., Maestú, F., and Ángel Pineda-Pardo, J. (2016). Multimodal description of whole brain connectivity: A comparison of resting state meg, fmri, and dwi. *Human brain mapping*, 37(1):20–34.

Giardina, I. (2008). Collective behavior in animal groups: theoretical models and empirical studies. *HFSP journal*, 2(4):205–219.

Girard, M., Larivière, R., Parfitt, D. A., Deane, E. C., Gaudet, R., Nossova, N., Blondeau, F., Prenosil, G., Vermeulen, E. G., Duchen, M. R., et al. (2012). Mitochondrial dysfunction and purkinje cell loss in autosomal recessive spastic ataxia of charlevoix-saguenay (arsacs). *Proceedings of the National Academy of Sciences*, 109(5):1661–1666.

Girvan, M. and Newman, M. E. (2002). Community structure in social and biological networks. *Proceedings of the national academy of sciences*, 99(12):7821–7826.

Godsil, C. and Royle, G. F. (2013). *Algebraic graph theory*, volume 207. Springer Science & Business Media.

Gómez-Gardeñes, J., Moreno, Y., and Arenas, A. (2007). Synchronizability determined by coupling strengths and topology on complex networks. *Physical Review E*, 75(6):066106.

Granger, C. W. (1969). Investigating causal relations by econometric models and cross-spectral methods. *Econometrica: Journal of the Econometric Society*, pages 424–438.

Greenberg, J. M. and Hastings, S. (1978). Spatial patterns for discrete models of diffusion in excitable media. *SIAM Journal on Applied Mathematics*, 34(3):515–523.

Greicius, M. D., Krasnow, B., Reiss, A. L., and Menon, V. (2003). Functional connectivity in the resting brain: a network analysis of the default mode hypothesis. *Proceedings of the National Academy of Sciences*, 100(1):253–258.

Greicius, M. D., Supekar, K., Menon, V., and Dougherty, R. F. (2009). Resting-state functional connectivity reflects structural connectivity in the default mode network. *Cerebral cortex*, 19(1):72–78.

Gu, M., Gash, M., Mann, V., Javoy-Agid, F., Cooper, J., and Schapira, A. (1996). Mitochondrial defect in huntington's disease caudate nucleus. *Annals of neurology*, 39(3):385–389.

Guo, X., Disatnik, M.-H., Monbureau, M., Shamloo, M., Mochly-Rosen, D., and Qi, X. (2013). Inhibition of mitochondrial fragmentation diminishes huntington's disease–associated neurodegeneration. *The Journal of clinical investigation*, 123(12):5371.

Gupta, S., Campa, A., and Ruffo, S. (2014). Kuramoto model of synchronization: equilibrium and nonequilibrium aspects. *Journal of Statistical Mechanics: Theory and Experiment*, 2014(8):R08001.

Gushchin, A., Mallada, E., and Tang, A. (2015). Synchronization of heterogeneous kuramoto oscillators with arbitrary topology. In *American Control Conference (ACC), 2015*, pages 637–644. IEEE.

Hagmann, P. (2005). From diffusion mri to brain connectomics.

Hagmann, P., Cammoun, L., Gigandet, X., Meuli, R., Honey, C. J., Wedeen, V. J., and Sporns, O. (2008). Mapping the structural core of human cerebral cortex. *PLoS biology*, 6(7):e159.

Haimovici, A., Tagliazucchi, E., Balenzuela, P., and Chialvo, D. R. (2013). Brain organization into resting state networks emerges at criticality on a model of the human connectome. *Physical review letters*, 110(17):178101.

Hall, E. L., Robson, S. E., Morris, P. G., and Brookes, M. J. (2014). The relationship between meg and fmri. *Neuroimage*, 102:80–91.

Hammond, C., Bergman, H., and Brown, P. (2007). Pathological synchronization in parkinson's disease: networks, models and treatments. *Trends in neurosciences*, 30(7):357–364.

Hari, R. and Parkkonen, L. (2015). The brain timewise: how timing shapes and supports brain function. *Phil. Trans. R. Soc. B*, 370(1668):20140170.

Harris, J. J., Jolivet, R., and Attwell, D. (2012). Synaptic energy use and supply. *Neuron*, 75(5):762–777.

Haun, F., Nakamura, T., Shiu, A. D., Cho, D.-H., Tsunemi, T., Holland, E. A., La Spada, A. R., and Lipton, S. A. (2013). S-nitrosylation of dynamin-related protein 1 mediates mutant huntingtin-induced mitochondrial fragmentation and neuronal injury in huntington's disease. *Antioxidants & redox signaling*, 19(11):1173–1184.

Henson, R. N., Flandin, G., Friston, K. J., and Mattout, J. (2010). A parametric empirical bayesian framework for fmri-constrained meg/eeg source reconstruction. *Human brain mapping*, 31(10):1512–1531.

Hervias, I., Beal, M. F., and Manfredi, G. (2006). Mitochondrial dysfunction and amyotrophic lateral sclerosis. *Muscle & nerve*, 33(5):598–608.

Hipp, J. F., Hawellek, D. J., Corbetta, M., Siegel, M., and Engel, A. K. (2012). Large-scale cortical correlation structure of spontaneous oscillatory activity. *Nature neuroscience*, 15(6):884–890.

Hodgkin, A. L. and Huxley, A. F. (1952). A quantitative description of membrane current and its application to conduction and excitation in nerve. *The Journal of physiology*, 117(4):500–544.

Hoeffding, W. (1963). Probability inequalities for sums of bounded random variables. *Journal of the American statistical association*, 58(301):13–30.

Hoitzing, H., Johnston, I. G., and Jones, N. S. (2015). What is the function of mitochondrial networks? a theoretical assessment of hypotheses and proposal for future research. *Bioessays*, 37(6):687–700.

Horn, R. A. and Johnson, C. R. (1990). Matrix analysis. corrected reprint of the 1985 original.

Horton, T., Graham, B., Corral-Debrinski, M., Shoffner, J., Kaufman, A., Beal, M., and Wallace, D. (1995). Marked increase in mitochondrial dna deletion levels in the cerebral cortex of huntington's disease patients. *Neurology*, 45(10):1879–1883.

Huygens, C. (1897). *Œuvres complètes de Christiaan Huygens: Tome VII Correspondance 1670-1675*, volume 1. Martinus Nijhoff.

Hwang, S., Disatnik, M.-H., and Mochly-Rosen, D. (2015). Impaired gapdh-induced mitophagy contributes to the pathology of huntington9s disease. *EMBO molecular medicine*, 7(10):1307–1326.

Hyde, B. B., Twig, G., and Shirihai, O. S. (2010). Organellar vs cellular control of mitochondrial dynamics. In *Seminars in cell & developmental biology*, volume 21, pages 575–581. Elsevier.

Hyder, F., Rothman, D. L., and Bennett, M. R. (2013). Cortical energy demands of signaling and nonsignaling components in brain are conserved across mammalian species and activity levels. *Proceedings of the National Academy of Sciences*, 110(9):3549–3554.

Hyder, F., Rothman, D. L., and Shulman, R. G. (2002). Total neuroenergetics support localized brain activity: implications for the interpretation of fmri. *Proceedings of the National Academy of Sciences*, 99(16):10771–10776.

Ishihara, N., Jofuku, A., Eura, Y., and Mihara, K. (2003). Regulation of mitochondrial morphology by membrane potential, and drp1-dependent division and fzo1-dependent fusion reaction in mammalian cells. *Biochemical and biophysical research communications*, 301(4):891–898.

Jäger, S., Handschin, C., Pierre, J. S., and Spiegelman, B. M. (2007). Amp-activated protein kinase (ampk) action in skeletal muscle via direct phosphorylation of pgc-1α. *Proceedings of the National Academy of Sciences*, 104(29):12017–12022.

Ježek, P. and Plecitá-Hlavatá, L. (2009). Mitochondrial reticulum network dynamics in relation to oxidative stress, redox regulation, and hypoxia. *The international journal of biochemistry & cell biology*, 41(10):1790–1804.

Ježek, P., Plecitá-Hlavatá, L., Smolková, K., and Rossignol, R. (2010). Distinctions and similarities of cell bioenergetics and the role of mitochondria in hypoxia, cancer, and embryonic development. *The international journal of biochemistry & cell biology*, 42(5):604–622.

Jones, R. (2010). The roles of pink1 and parkin in parkinson's disease. *PLoS biology*, 8(1):e1000299.

Jornayvaz, F. R. and Shulman, G. I. (2010). Regulation of mitochondrial biogenesis. *Essays in biochemistry*, 47:69–84.

Khalil, H. K. (2002). Nonlinear systems, 3rd. *New Jewsey, Prentice Hall*, 9.

Kim, J., Moody, J. P., Edgerly, C. K., Bordiuk, O. L., Cormier, K., Smith, K., Beal, M. F., and Ferrante, R. J. (2010). Mitochondrial loss, dysfunction and altered dynamics in huntington's disease. *Human molecular genetics*, 19(20):3919–3935.

Kleiner, M., Brainard, D., Pelli, D., Ingling, A., Murray, R., Broussard, C., et al. (2007). What's new in psychtoolbox-3. *Perception*, 36(14):1.

Koch, M. A., Norris, D. G., and Hund-Georgiadis, M. (2002). An investigation of functional and anatomical connectivity using magnetic resonance imaging. *Neuroimage*, 16(1):241–250.

Kowald, A. and Kirkwood, T. B. (2011). Evolution of the mitochondrial fusion–fission cycle and its role in aging. *Proceedings of the National Academy of Sciences*, 108(25):10237–10242.

Kuramoto, Y. (1975). Self-entrainment of a population of coupled non-linear oscillators. In *International Symposium on Mathematical Problems in Theoretical Physics*, volume 39 of *Lecture Notes in Physics*, pages 420–422. Springer Berlin Heidelberg.

Legros, F., Lombès, A., Frachon, P., and Rojo, M. (2002). Mitochondrial fusion in human cells is efficient, requires the inner membrane potential, and is mediated by mitofusins. *Molecular biology of the cell*, 13(12):4343–4354.

Lehnertz, K., Bialonski, S., Horstmann, M.-T., Krug, D., Rothkegel, A., Staniek, M., and Wagner, T. (2009). Synchronization phenomena in human epileptic brain networks. *Journal of neuroscience methods*, 183(1):42–48.

Leicht, E. A. and Newman, M. E. (2008). Community structure in directed networks. *Physical review letters*, 100(11):118703.

Levy, R., Hutchison, W. D., Lozano, A. M., and Dostrovsky, J. O. (2000). High-frequency synchronization of neuronal activity in the subthalamic nucleus of parkinsonian patients with limb tremor. *Journal of Neuroscience*, 20(20):7766–7775.

Levy, R., Hutchison, W. D., Lozano, A. M., and Dostrovsky, J. O. (2002). Synchronized neuronal discharge in the basal ganglia of parkinsonian patients is limited to oscillatory activity. *Journal of Neuroscience*, 22(7):2855–2861.

Lewis, F. L., Zhang, H., Hengster-Movric, K., and Das, A. (2014). Introduction to synchronization in nature and physics and cooperative control for multi-agent systems on graphs. In *Cooperative Control of Multi-Agent Systems*, pages 1–21. Springer.

Lin, Z., Francis, B., and Maggiore, M. (2007). State agreement for continuous-time coupled nonlinear systems. *SIAM Journal on Control and Optimization*, 46(1):288–307.

Liu, X., Chang, C., and Duyn, J. H. (2013). Decomposition of spontaneous brain activity into distinct fmri co-activation patterns. *Frontiers in systems neuroscience*, 7.

Liu, X. and Duyn, J. H. (2013). Time-varying functional network information extracted from brief instances of spontaneous brain activity. *Proceedings of the National Academy of Sciences*, 110(11):4392–4397.

Lloyd, S. (1982). Least squares quantization in pcm. *IEEE transactions on information theory*, 28(2):129–137.

Lord, L.-D., Expert, P., Huckins, J. F., and Turkheimer, F. E. (2013). Cerebral energy metabolism and the brain's functional network architecture: an integrative review. *Journal of Cerebral Blood Flow & Metabolism*, 33(9):1347–1354.

Losón, O. C., Song, Z., Chen, H., and Chan, D. C. (2013). Fis1, mff, mid49, and mid51 mediate drp1 recruitment in mitochondrial fission. *Molecular biology of the cell*, 24(5):659–667.

Lu, B. (2011). *Mitochondrial Dynamics and Neurodegeneration*. Springer Science & Business Media.

Lu, W., Liu, B., and Chen, T. (2010). Cluster synchronization in networks of coupled nonidentical dynamical systems. *Chaos: An Interdisciplinary Journal of Nonlinear Science*, 20(1):013120.

MacAskill, A. F., Brickley, K., Stephenson, F. A., and Kittler, J. T. (2009). Gtpase dependent recruitment of grif-1 by miro1 regulates mitochondrial trafficking in hippocampal neurons. *Molecular and Cellular Neuroscience*, 40(3):301–312.

Magistretti, P. J. (2006). Neuron–glia metabolic coupling and plasticity. *Journal of Experimental Biology*, 209(12):2304–2311.

Magistretti, P. J. and Allaman, I. (2015). A cellular perspective on brain energy metabolism and functional imaging. *Neuron*, 86(4):883–901.

Mangesius, H., Hirche, S., and Obradovic, D. (2012). Quasi-stationarity of electric power grid dynamics based on a spatially embedded kuramoto model. In *American Control Conference (ACC), 2012*, pages 2159–2164. IEEE.

Marzetti, L., Della Penna, S., Snyder, A. Z., Pizzella, V., Nolte, G., de Pasquale, F., Romani, G. L., and Corbetta, M. (2013). Frequency specific interactions of meg resting state activity within and across brain networks as revealed by the multivariate interaction measure. *Neuroimage*, 79:172–183.

McKenna, M., Gruetter, R., Sonnewald, U., Waagepetersen, H., and Schousboe, A. (2006). Energy metabolism of the brain. *Basic neurochemistry*, 8:200–31.

Mesbahi, M. and Egerstedt, M. (2010). *Graph theoretic methods in multiagent networks*. Princeton University Press.

Mihaylova, M. M. and Shaw, R. J. (2011). The ampk signalling pathway coordinates cell growth, autophagy and metabolism. *Nature cell biology*, 13(9):1016–1023.

Mirchev, M., Basnarkov, L., Corinto, F., and Kocarev, L. (2014). Cooperative phenomena in networks of oscillators with non-identical interactions and dynamics. *IEEE Transactions on Circuits and Systems I: Regular Papers*, 61(3):811–819.

Mishra, P. and Chan, D. C. (2016). Metabolic regulation of mitochondrial dynamics. *J Cell Biol*, pages jcb–201511036.

Misko, A. L., Sasaki, Y., Tuck, E., Milbrandt, J., and Baloh, R. H. (2012). Mitofusin2 mutations disrupt axonal mitochondrial positioning and promote axon degeneration. *Journal of Neuroscience*, 32(12):4145–4155.

Mitra, A. and Raichle, M. E. (2016). How networks communicate: propagation patterns in spontaneous brain activity. *Phil. Trans. R. Soc. B*, 371(1705):20150546.

Moncada, S. and Erusalimsky, J. D. (2002). Opinion: Does nitric oxide modulate mitochondrial energy generation and apoptosis? *Nature reviews. Molecular cell biology*, 3(3):214.

Moreira, P. I., Carvalho, C., Zhu, X., Smith, M. A., and Perry, G. (2010). Mitochondrial dysfunction is a trigger of alzheimer's disease pathophysiology. *Biochimica et Biophysica Acta (BBA)-Molecular Basis of Disease*, 1802(1):2–10.

Mouli, P. K., Twig, G., and Shirihai, O. S. (2009). Frequency and selectivity of mitochondrial fusion are key to its quality maintenance function. *Biophysical journal*, 96(9):3509–3518.

Mukamel, R., Gelbard, H., Arieli, A., Hasson, U., Fried, I., and Malach, R. (2005). Coupling between neuronal firing, field potentials, and fmri in human auditory cortex. *Science*, 309(5736):951–954.

Muthukumaraswamy, S. D. and Singh, K. D. (2008). Spatiotemporal frequency tuning of bold and gamma band meg responses compared in primary visual cortex. *Neuroimage*, 40(4):1552–1560.

Nagumo, J., Arimoto, S., and Yoshizawa, S. (1962). An active pulse transmission line simulating nerve axon. *Proceedings of the IRE*, 50(10):2061–2070.

Newman, M. E. and Girvan, M. (2004). Finding and evaluating community structure in networks. *Physical review E*, 69(2):026113.

Niemann, A., Wagner, K. M., Ruegg, M., and Suter, U. (2009). Gdap1 mutations differ in their effects on mitochondrial dynamics and apoptosis depending on the mode of inheritance. *Neurobiology of disease*, 36(3):509–520.

Nilsson, L. I. H., Pettersen, I. K. N., Nikolaisen, J., Micklem, D., Dale, H. A., Røsland, G. V., Lorens, J., and Tronstad, K. J. (2015). A new live-cell reporter strategy to

simultaneously monitor mitochondrial biogenesis and morphology. *Scientific reports*, 5:17217.

Nishikawa, T. and Motter, A. E. (2015). Comparative analysis of existing models for power-grid synchronization. *New Journal of Physics*, 17(1):015012.

Nordenfelt, A., Used, J., and Sanjuán, M. A. (2013). Bursting frequency versus phase synchronization in time-delayed neuron networks. *Physical Review E*, 87(5):052903.

Okatsu, K., Koyano, F., Kimura, M., Kosako, H., Saeki, Y., Tanaka, K., and Matsuda, N. (2015). Phosphorylated ubiquitin chain is the genuine parkin receptor. *J Cell Biol*, pages jcb–201410050.

Olfati-Saber, R., Fax, J. A., and Murray, R. M. (2007). Consensus and cooperation in networked multi-agent systems. *Proceedings of the IEEE*, 95(1):215–233.

Oliveira, J. (2010). Nature and cause of mitochondrial dysfunction in huntington's disease: focusing on huntingtin and the striatum. *Journal of neurochemistry*, 114(1):1–12.

Painold, A., Anderer, P., Holl, A. K., Letmaier, M., Saletu-Zyhlarz, G. M., Saletu, B., and Bonelli, R. M. (2010). Comparative eeg mapping studies in huntington's disease patients and controls. *Journal of neural transmission*, 117(11):1307–1318.

Papoulis, A. (1960). Fourier integral and its applications.[the].

Pasqualetti, F., Favaretto, C., Zhao, S., and Zampieri, S. (2018). Fragility and controllability tradeoff in complex networks. [submitted to ACC 2018].

Patel, P. K., Shirihai, O., and Huang, K. C. (2013). Optimal dynamics for quality control in spatially distributed mitochondrial networks. *PLoS computational biology*, 9(7):e1003108.

Pecora, L. M., Sorrentino, F., Hagerstrom, A. M., Murphy, T. E., and Roy, R. (2014). Cluster synchronization and isolated desynchronization in complex networks with symmetries. *Nature communications*, 5.

Pelli, D. G. (1997). The videotoolbox software for visual psychophysics: Transforming numbers into movies. *Spatial vision*, 10(4):437–442.

Pfurtscheller, G. and Da Silva, F. L. (1999). Event-related eeg/meg synchronization and desynchronization: basic principles. *Clinical neurophysiology*, 110(11):1842–1857.

Pikovsky, A., Rosenblum, M., and Kurths, J. (2003). *Synchronization: a universal concept in nonlinear sciences*, volume 12. Cambridge university press.

Pizzella, V., Marzetti, L., Della Penna, S., de Pasquale, F., Zappasodi, F., and Romani, G. L. (2014). Magnetoencephalography in the study of brain dynamics. *Functional neurology*, 29(4):241.

Polidori, M. C., Mecocci, P., Browne, S. E., Senin, U., and Beal, M. F. (1999). Oxidative damage to mitochondrial dna in huntington's disease parietal cortex. *Neuroscience letters*, 272(1):53–56.

Ponce-Alvarez, A., Deco, G., Hagmann, P., Romani, G. L., Mantini, D., and Corbetta, M. (2015). Resting-state temporal synchronization networks emerge from connectivity topology and heterogeneity. *PLoS computational biology*, 11(2):e1004100.

Prando, G., Zorzi, M., Bertoldo, A., and Chiuso, A. (2017). Estimating effective connectivity in linear brain network models. *arXiv preprint arXiv:1703.10363*.

Pyakurel, A., Savoia, C., Hess, D., and Scorrano, L. (2015). Extracellular regulated kinase phosphorylates mitofusin 1 to control mitochondrial morphology and apoptosis. *Molecular cell*, 58(2):244–254.

Qi, X., Qvit, N., Su, Y.-C., and Mochly-Rosen, D. (2013). A novel drp1 inhibitor diminishes aberrant mitochondrial fission and neurotoxicity. *J Cell Sci*, 126(3):789–802.

Raichle, M. E. (2003). Functional brain imaging and human brain function. *Journal of Neuroscience*, 23(10):3959–3962.

Raichle, M. E. and Gusnard, D. A. (2002). Appraising the brain's energy budget. *Proceedings of the National Academy of Sciences*, 99(16):10237–10239.

Rangaraju, V., Calloway, N., and Ryan, T. A. (2014). Activity-driven local atp synthesis is required for synaptic function. *Cell*, 156(4):825–835.

Rousseeuw, P. J. (1987). Silhouettes: a graphical aid to the interpretation and validation of cluster analysis. *Journal of computational and applied mathematics*, 20:53–65.

Routh, E. J. (1877). *A treatise on the stability of a given state of motion: particularly steady motion*. Macmillan and Company.

Rubchinsky, L. L., Park, C., and Worth, R. M. (2012). Intermittent neural synchronization in parkinson's disease. *Nonlinear dynamics*, 68(3):329–346.

Rubinov, M. and Sporns, O. (2010). Complex network measures of brain connectivity: uses and interpretations. *Neuroimage*, 52(3):1059–1069.

Rulkov, N. F. (2001). Regularization of synchronized chaotic bursts. *Physical Review Letters*, 86(1):183.

Santos, D., Esteves, A. R., Silva, D. F., Januário, C., and Cardoso, S. M. (2015). The impact of mitochondrial fusion and fission modulation in sporadic parkinson's disease. *Molecular neurobiology*, 52(1):573–586.

Schaub, M. T., O'Clery, N., Billeh, Y. N., Delvenne, J.-C., Lambiotte, R., and Barahona, M. (2016). Graph partitions and cluster synchronization in networks of oscillators. *Chaos: An Interdisciplinary Journal of Nonlinear Science*, 26(9):094821.

Semedo, D. (2015). Researchers reduce mutated mitochondrial genomes implicated in mitochondrial diseases. https://mitochondrialdiseasenews.com/2015/04/24/researchers-reduce-mutated-mitochondrial-genomes-implicated-mitochondrial-diseases/.

Shanahan, M. (2010). Metastable chimera states in community-structured oscillator networks. *Chaos: An Interdisciplinary Journal of Nonlinear Science*, 20(1):013108.

Shirendeb, U. P., Calkins, M. J., Manczak, M., Anekonda, V., Dufour, B., McBride, J. L., Mao, P., and Reddy, P. H. (2011). Mutant huntingtin's interaction with mitochondrial protein drp1 impairs mitochondrial biogenesis and causes defective axonal transport and synaptic degeneration in huntington's disease. *Human molecular genetics*, 21(2):406–420.

Shulman, G. L., Corbetta, M., Buckner, R. L., Raichle, M. E., Fiez, J. A., Miezin, F. M., and Petersen, S. E. (1997). Top-down modulation of early sensory cortex. *Cerebral cortex (New York, NY: 1991)*, 7(3):193–206.

Shutt, T., Geoffrion, M., Milne, R., and McBride, H. M. (2012). The intracellular redox state is a core determinant of mitochondrial fusion. *EMBO reports*, 13(10):909–915.

Siegel, M., Donner, T. H., and Engel, A. K. (2012). Spectral fingerprints of large-scale neuronal interactions. *Nature Reviews Neuroscience*, 13(2):121–134.

Sivera, R., Espinós, C., Vílchez, J. J., Mas, F., Martínez-Rubio, D., Chumillas, M. J., Mayordomo, F., Muelas, N., Bataller, L., Palau, F., et al. (2010). Phenotypical features of the p. r120w mutation in the gdap1 gene causing autosomal dominant charcot-marie-tooth disease. *Journal of the Peripheral Nervous System*, 15(4):334–344.

Smith, A. J., Blumenfeld, H., Behar, K. L., Rothman, D. L., Shulman, R. G., and Hyder, F. (2002). Cerebral energetics and spiking frequency: the neurophysiological basis of fmri. *Proceedings of the National Academy of Sciences*, 99(16):10765–10770.

Smith, S. M., Fox, P. T., Miller, K. L., Glahn, D. C., Fox, P. M., Mackay, C. E., Filippini, N., Watkins, K. E., Toro, R., Laird, A. R., et al. (2009). Correspondence of the brain's functional architecture during activation and rest. *Proceedings of the National Academy of Sciences*, 106(31):13040–13045.

Smith, S. M., Miller, K. L., Salimi-Khorshidi, G., Webster, M., Beckmann, C. F., Nichols, T. E., Ramsey, J. D., and Woolrich, M. W. (2011). Network modelling methods for fmri. *Neuroimage*, 54(2):875–891.

Soikkeli, R., Partanen, J., Soininen, H., Pääkkönen, A., and Riekkinen, P. (1991). Slowing of eeg in parkinson's disease. *Electroencephalography and clinical neurophysiology*, 79(3):159–165.

Song, W., Chen, J., Petrilli, A., Liot, G., Klinglmayr, E., Zhou, Y., Poquiz, P., Tjong, J., Pouladi, M. A., Hayden, M. R., et al. (2011). Mutant huntingtin binds the mitochondrial fission gtpase dynamin-related protein-1 and increases its enzymatic activity. *Nature medicine*, 17(3):377–382.

Song, W., Song, Y., Kincaid, B., Bossy, B., and Bossy-Wetzel, E. (2013). Mutant sod1 g93a triggers mitochondrial fragmentation in spinal cord motor neurons: neuroprotection by sirt3 and pgc-1α. *Neurobiology of disease*, 51:72–81.

Sorrentino, F., Pecora, L. M., Hagerstrom, A. M., Murphy, T. E., and Roy, R. (2016). Complete characterization of the stability of cluster synchronization in complex dynamical networks. *Science advances*, 2(4):e1501737.

Spadone, S., Della Penna, S., Sestieri, C., Betti, V., Tosoni, A., Perrucci, M. G., Romani, G. L., and Corbetta, M. (2015). Dynamic reorganization of human resting-state networks during visuospatial attention. *Proceedings of the National Academy of Sciences*, 112(26):8112–8117.

Sporns, O., Tononi, G., and Kötter, R. (2005). The human connectome: a structural description of the human brain. *PLoS computational biology*, 1(4):e42.

Starr, P. A., Kang, G. A., Heath, S., Shimamoto, S., and Turner, R. S. (2008). Pallidal neuronal discharge in huntington's disease: support for selective loss of striatal cells originating the indirect pathway. *Experimental neurology*, 211(1):227–233.

Stevenson, C. M., Brookes, M. J., and Morris, P. G. (2011). β-band correlates of the fmri bold response. *Human brain mapping*, 32(2):182–197.

Stevenson, C. M., Wang, F., Brookes, M. J., Zumer, J. M., Francis, S. T., and Morris, P. G. (2012). Paired pulse depression in the somatosensory cortex: associations between meg and bold fmri. *Neuroimage*, 59(3):2722–2732.

Strogatz, S. H. (2000). From kuramoto to crawford: exploring the onset of synchronization in populations of coupled oscillators. *Physica D: Nonlinear Phenomena*, 143(1):1–20.

Sturrock, A. and Leavitt, B. R. (2010). The clinical and genetic features of huntington disease. *Journal of Geriatric Psychiatry and Neurology*, 23(4):243–259. PMID: 20923757.

Sukhorukov, V. M., Dikov, D., Reichert, A. S., and Meyer-Hermann, M. (2012). Emergence of the mitochondrial reticulum from fission and fusion dynamics. *PLoS computational biology*, 8(10):e1002745.

Tagliazucchi, E., Balenzuela, P., Fraiman, D., and Chialvo, D. R. (2012). Criticality in large-scale brain fmri dynamics unveiled by a novel point process analysis. *Frontiers in physiology*, 3.

Talairach, J. and Tournoux, P. (1988). Co-planar stereotaxic atlas of the human brain. 3-dimensional proportional system: an approach to cerebral imaging.

Tallon-Baudry, C. and Bertrand, O. (1999). Oscillatory gamma activity in humans and its role in object representation. *Trends in cognitive sciences*, 3(4):151–162.

Tam, Z. Y., Gruber, J., Halliwell, B., and Gunawan, R. (2013). Mathematical modeling of the role of mitochondrial fusion and fission in mitochondrial dna maintenance. *PloS one*, 8(10):e76230.

Tam, Z. Y., Gruber, J., Halliwell, B., and Gunawan, R. (2015). Context-dependent role of mitochondrial fusion-fission in clonal expansion of mtdna mutations. *PLoS computational biology*, 11(5):e1004183.

Tiberi, L., Favaretto, C., Innocenti, M., Bassett, D. S., and Pasqualetti, F. (2017). Synchronization patterns in networks of kuramoto oscillators: A geometric approach for analysis and control. *arXiv preprint arXiv:1709.06193*. [accepted for CDC 2017].

Toga, A. W. (2015). *Brain mapping: An encyclopedic reference*. Academic Press.

Tondera, D., Grandemange, S., Jourdain, A., Karbowski, M., Mattenberger, Y., Herzig, S., Da Cruz, S., Clerc, P., Raschke, I., Merkwirth, C., et al. (2009). Slp-2 is required for stress-induced mitochondrial hyperfusion. *The EMBO journal*, 28(11):1589–1600.

Toyama, E. Q., Herzig, S., Courchet, J., Lewis, T. L., Losón, O. C., Hellberg, K., Young, N. P., Chen, H., Polleux, F., Chan, D. C., et al. (2016). Amp-activated protein kinase mediates mitochondrial fission in response to energy stress. *Science*, 351(6270):275–281.

Twig, G., Hyde, B., and Shirihai, O. S. (2008). Mitochondrial fusion, fission and autophagy as a quality control axis: the bioenergetic view. *Biochimica et Biophysica Acta (BBA)-Bioenergetics*, 1777(9):1092–1097.

Van Den Heuvel, M. P., Mandl, R. C., Kahn, R. S., Pol, H., and Hilleke, E. (2009a). Functionally linked resting-state networks reflect the underlying structural connectivity architecture of the human brain. *Human brain mapping*, 30(10):3127–3141.

Van Den Heuvel, M. P. and Pol, H. E. H. (2010). Exploring the brain network: a review on resting-state fmri functional connectivity. *European neuropsychopharmacology*, 20(8):519–534.

Van Essen, D. C. (2005). A population-average, landmark-and surface-based (pals) atlas of human cerebral cortex. *Neuroimage*, 28(3):635–662.

Ventura-Clapier, R., Garnier, A., and Veksler, V. (2008). Transcriptional control of mitochondrial biogenesis: the central role of pgc-1α. *Cardiovascular research*, 79(2):208–217.

Wellstead, P. and Cloutier, M. (2012). *Systems biology of Parkinson's disease*. Springer Science & Business Media.

Wen, H. and Liu, Z. (2016). Broadband electrophysiological dynamics contribute to global resting-state fmri signal. *Journal of Neuroscience*, 36(22):6030–6040.

Winfree, A. T. (1967). Biological rhythms and the behavior of populations of coupled oscillators. *Journal of theoretical biology*, 16(1):15–42.

Winterer, G., Carver, F. W., Musso, F., Mattay, V., Weinberger, D. R., and Coppola, R. (2007). Complex relationship between bold signal and synchronization/desynchronization of human brain meg oscillations. *Human Brain Mapping*, 28(9):805–816.

Xia, M., Wang, J., and He, Y. (2013). Brainnet viewer: a network visualization tool for human brain connectomics. *PloS one*, 8(7):e68910.

Zalesky, A., Fornito, A., and Bullmore, E. (2012). On the use of correlation as a measure of network connectivity. *Neuroimage*, 60(4):2096–2106.

Zanna, C., Ghelli, A., Porcelli, A. M., Karbowski, M., Youle, R. J., Schimpf, S., Wissinger, B., Pinti, M., Cossarizza, A., Vidoni, S., et al. (2007). Opa1 mutations associated with dominant optic atrophy impair oxidative phosphorylation and mitochondrial fusion. *Brain*, 131(2):352–367.

Zatorre, R. J., Fields, R. D., and Johansen-Berg, H. (2012). Plasticity in gray and white: neuroimaging changes in brain structure during learning. *Nature neuroscience*, 15(4):528.

Zhang, Z., Sarlette, A., and Ling, Z. (2014). Synchronization of kuramoto oscillators with non-identical natural frequencies: a quantum dynamical decoupling approach. In *Decision and Control (CDC), 2014 IEEE 53rd Annual Conference on*, pages 4585–4590. IEEE.

Züchner, S., Mersiyanova, I. V., Muglia, M., Bissar-Tadmouri, N., Rochelle, J., Dadali, E. L., Zappia, M., Nelis, E., Patitucci, A., Senderek, J., et al. (2004). Mutations in the mitochondrial gtpase mitofusin 2 cause charcot-marie-tooth neuropathy type 2a. *Nature genetics*, 36(5):449–451.

Zumer, J. M., Brookes, M. J., Stevenson, C. M., Francis, S. T., and Morris, P. G. (2010). Relating bold fmri and neural oscillations through convolution and optimal linear weighting. *Neuroimage*, 49(2):1479–1489.